GENERAL RELATIVISTIC RADIATION MAGNETOHYDRODYNAMICS, WITH APPLICATIONS TO BLACK HOLE ACCRETION DISKS

BY

BENJAMIN RANSOM RYAN

DISSERTATION

Submitted in partial fulfillment of the requirements
for the degree of Doctor of Philosophy in Astronomy
in the Graduate College of the
University of Illinois at Urbana-Champaign, 2018

Urbana, Illinois

Doctoral Committee:

Professor Charles Gammie, Chair
Professor Eliot Quataert
Professor James Stone
Professor Athol Kemball
Professor Brian Fields

Abstract

Electron temperatures in the inner region of accretion disks around black holes are set by the balance of advection, viscous heating, and radiative interactions. At the lowest accretion rates, radiative processes may be safely ignored, and electrons are nearly virial. Advection carries the lion's share of this internal energy through the event horizon. At near-Eddington accretion rates, *advection* may be safely ignored, as energy generated from viscous heating is quickly radiated away. What, then, of intermediate accretion rates for which advection, heating, and radiative cooling timescales are all comparable? After all, a large fraction of all known black hole candidates (low-luminosity active galactic nuclei and quiescent black hole X-ray binaries) live in this region of parameter space. In this work we specialize to low accretion rate supermassive black holes subject to synchrotron and Compton losses.

The dynamics of accretion are set by angular momentum transport. A leading picture for this process has an instability of magnetic fields threading a differentially rotating fluid, the magnetorotational instability (MRI), driving turbulence that leads to diffusive angular momentum transport. The need to capture this process self-consistently in the near-horizon regime motivated the development of numerical methods for general relativistic magnetohydrodynamics (GRMHD). However, even the local details of MRI-driven turbulence simulations are still not completely understood. Along the way, this work considers a central issue with modeling the MRI: whether the resulting stress is independent of the numerics when resistivity and viscosity are neglected (as they almost always are in GRMHD simulations).

GRMHD simulations are now a standard tool for modeling black hole accretion flows, but do not include radiative processes, limiting their application to very low accretion rates. To address this problem we developed the `bhlight` scheme, which couples proven methods for flux-conservative general relativistic magnetohydrodynamics to covariant Monte Carlo radiation transport to produce a frequency-dependent, full transport general relativistic radiation magnetohydrodynamics (GRRMHD) scheme. This code is robust and accurate across a range of test problems, and computationally efficient on our problem of interest: very sub-Eddington black hole accretion flows for which radiative cooling is still crucial.

The turbulent heating rate of the electrons in these (at least somewhat) Coulomb-collisionless flows is

crucial to accurately capturating radiative interactions. We subsequently extended `bhlight` to incorporate the electron heating model of Ressler et al. (2015); the resulting method we term `ebhlight`. We first apply `ebhlight` to a study of accretion onto a $M/M_\odot = 10^8$, $a_\star = 0.5$ black hole for a range of accretion rates. We find that by $\dot{m} \sim 10^{-5}$ radiative cooling significantly reduces the radiative efficiency relative to a non-cooling accretion flow. Coulomb heating far from the black hole leads to a significant enhancement in luminosity due to inverse Compton scattering. With increasing $\dot{m}$, the high energy spectrum evolves from a steep series of Compton bumps to a smooth power law over many decades in frequency. These are the first self-consistent models of radiatively cooled LLAGN using frequency-depedent full transport, and extend from the fully radiatively inefficient regime to near ($\sim 1\%$) thin disk efficiencies.

We then use `ebhlight` to study M87, a classic LLAGN source. M87 is one of the two principal targets for the Event Horizon Telescope's campaign to image black hole event horizons. Previous GRMHD studies of M87 have had difficulty achieving self-consistency; radiative cooling appears to be required. Here we include this radiative cooling over a suite of models with different black hole masses and spins (matching the 230 GHz flux of Doeleman et al. 2012), and find that it (together with Coulomb heating) is indeed critical to the thermodynamics of the flow. We also find a Compton y parameter of order unity in all cases. We produce synthetic images from these models in support of upcoming EHT measurements.

Acknowledgments

Whom should I acknowledge? First, Charles Gammie. Given the respect I hold for and the various professional debts I owe to my advisor, I imagine that in developing any expression of recognition or gratitude I should immediately indulge in vulgar excesses of bumptious pseudoliterary pretension, purposeless baroque ornamentation, and saccharine fawning. Instead, let me borrow from a more sober writer while restricting myself to merely noting that I consider his words here entirely appropriate.

> I observed that everybody believed that he thought as he spoke, and that in all that he did he never had any bad intention; and he never showed amazement and surprise, and was never in a hurry, and never put off doing a thing, nor was perplexed nor dejected, nor did he ever laugh to disguise his vexation, nor, on the other hand, was he ever passionate or suspicious. He was accustomed to do acts of beneficence, and was ready to forgive, and was free from all falsehood; and he presented the appearance of a man who could not be diverted from right, rather than of a man who had been improved. I observed, too, that no man could ever think that he was despised by [Charles], or ever venture to think himself a better man. He had also the art of being humorous in an agreeable way.
>
> - Marcus Aurelius

It is a pleasure to thank my collaborators. Josh Dolence's steady, skeptical eye routinely kept me from going off the rails, and let us not forget that one may find in his own thesis the kernel of the `bhlight` algorithm. Sean Ressler has been a valuable influence on my work on accretion disks. In particular, his method for calculating electron temperatures played a large role in my work, and he identified and fixed several serious bugs in `bhlight`. Sasha Tchekhovskoy has made numerous valuable comments and suggestions over the course of my career. Eliot Quataert has been an inexhaustible source of perspicacity, inspiration, and general good nature and goodwill. Sebastien Fromang & Pierre Kestener were encouraging and insightful; in particular, I learned a lot, perhaps most of what I know, about working with supercomputers from Pierre.

Jim Stone and the rest of the TCAN collaboration have provided great advice, and it has been a rare

privilege to be exposed to such a group of luminaries as a larval-stage graduate student. Stu Shapiro's (and Charles') journal club, in which I had to regularly and rapidly select, digest, and defend articles from the literature, was a critical stage in my development. The members of my thesis committee not already named, Athol Kemball and Brian Fields, have provided valuable comments and criticisms that have done much to improve my work. Many other researchers in the field have at one time or another provided me with valuable advice, but Mani Chandra deserves special recognition. Our graduate careers were remarkably symmetric, and it was to my great advantage that I got to advance in graduate coursework and research in cooperation with someone so bright, industrious, selfless, and optimistic. His absurdly generous donation of an espresso machine to the department as he left the country is in no small part responsible for the existence of this thesis. I also want to thank You-Hua Chu for her advice, support, and delicious baked goods, Jeri Cochran for her perpetual friendship (as I write this she is about to take me out to lunch), and Judy Whittington and Cory Holt for protecting me from logistical challenges against which I am hopelessly inept.

Prior to graduate school I had several important influences in physics. Fabian Heitsch introduced me to numerical astrophysics and guided me towards my graduate career. Hugon Karwowski introduced me to numerical physics and gave me the opportunity to measure my enthusiasm for laboratory work. Jon Bennett introduced me to research physics. John Kolena introduced me to physics, and in his lectures provided a toolkit for clearheaded thinking.

Gratitude and love to my mother Amy, father Morgan, and sister Bailey for their support and humor. Regular evacuations to North Carolina to eat Utz popcorn, build papercraft models, watch Black Adder, play with a horde of cats and dogs, and generally put responsiblity on hold kept me refreshed.

And now one last, best show of gratitude and admiration for my fiancée, Courtney. But first, an aside. The moment Courtney "got" my research methodology was when an episode of the television series *Forensic Files* described the use of computational fluid dynamics to explain the unexpectedly rapid evolution of a burning wooden escalator that resulted in the King's Cross Fire. The cause is now known as the trench effect, in which the Coandă effect (flowing gas is pushed against hard surfaces by necessarily higher ambient pressure) and flashover combine to rapidly move a fire up an inclined surface of flammable material. This effect was discovered in part through numerical simulations performed to explain the fire. Seeing the flame lie along the trench, the researchers at first worried that they had made a sign error in their code's gravitational source terms. While I can sympathize with this worry in my research, I am happy to say that I have no such concern about the sign of my affection for Courtney. I can't wait to move forward together and share the gradual, lifelong construction of a state of wonder and serenity.

Table of Contents

List of Tables

List of Figures

Chapter 1

Introduction

Consider a black hole of mass M and angular momentum J embedded in a weakly magnetized, rotating fluid with specific angular momentum $l \gg GM/c$ such that the material is centrifugally supported against inflow. What then? This outcome is sensitive to the mass of the black hole M, the dimensionless spin parameter of the black hole $a_\star = cJ/(GM^2) \in (-1, 1)$, and the density of the fluid, more usefully interpreted as an accretion rate $\dot{m} = \dot{M}/\dot{M}_{\rm Edd}$ where $\dot{M}_{\rm Edd}$ is the Eddington mass accretion rate[1]. Other parameters, such as the angle made by the black hole and disk orbital angular momenta, and the topology of the magnetic field, may play significant roles, but they exceed the scope of this work.

For supermassive black holes, the black hole influences the surrounding medium wherever the absolute gravitational potential energy of the gas exceeds its thermal energy. This occurs inside the Bondi radius $R_B \sim GM/c_s^2$, where c_s is the sound speed of the surrounding fluid. For stellar mass black holes, material is supplied by a companion star. Non-axisymmetric motion in the fluid is quickly dissipated by collisions, and the flow settles into a nearly Keplerian disk inside some circularization radius $R_c = l^2/(GM)$. In order to be accreted inside of R_c, fluid elements must lose angular momentum. While external torques applied by coherent magnetic fields may extract angular momentum vertically (e.g. Blandford & Payne 1982), a standard view is that turbulence inside the disk leads to friction between differentially rotating disk annuli that in turn expels angular momentum radially. This angular momentum flux then controls accretion.

In this work we specialize to the inner region of accretion flows where most of the gravitational potential energy is liberated, $r \lesssim 100$ where $r \equiv R/R_g$ with $R_g \equiv GM/c^2$ the gravitational radius. Throughout this work we assume disk accretion in this region. For $\dot{m} \ll 1$, radiative losses are negligible over an inflow time, and temperatures are nearly virial. For $10^{-2} \lesssim \dot{m} \lesssim 1$, the disk is radiatively efficient and becomes cold relative to its orbital kinetic energy. For $\dot{m} \gtrsim 1$, photon trapping makes advective cooling important again. These different classes of disks (radiatively inefficient accretion flows, thin disks, and slim or super-Eddington disks, respectively) exhibit quite different radiative properties, probably accounting for much of the phenomenology observed in accreting black holes.

[1]Throughout, we adopt a nominal efficiency $\eta = 0.1$ when evaluating $\dot{M}_{\rm Edd} \equiv 4\pi GMm_p/(\eta\sigma_T c)$, i.e. $\dot{M}_{\rm Edd} = 2.2 \times 10^{-8}(M/M_\odot)M_\odot{\rm yr}^{-1} = 1.4 \times 10^{18}(M/M_\odot){\rm g\ s}^{-1}$.

The magnetized turbulent state often invoked to drive accretion is difficult to capture self-consistently with analytic or time-averaged methods. Instead, more researchers are turning to numerical simulations, especially general relativistic magnetohydrodynamics (GRMHD) in which magnetized fluid is integrated on a background black hole spacetime. Not only do these simulations provide first-principals realizations of the statistics of black hole accretion disks, but allow for post-processing with radiative transfer methods to produce synthetic images and spectra for comparison with observations.

Such GRMHD simulations, however, assume negligible radiative cooling. In contrast, most real accreting black holes are subject to radiative cooling, or even dynamically significant radiation pressure. While it is straightforward to introduce optically thin cooling functions to GRMHD simulations, other processes like absorption and scattering require solving the equation of radiative transport. Particularly in relativity, where photons follow nontrivial geodesics, this has proved challenging to implement; the field of general relativistic *radiation* magnetohydrodynamics (GRRMHD) is still developing.

1.1 Black Holes

A black hole is any object with an event horizon, a surface inside of which null geodesics (usually, rays of light) will remain for all time. This concept is relatively far from everyday experience, and received opposition following its appearance from theoretical studies of general relativity. Arthur Eddington, upon confronting the apparent inevitability of gravitational collapse of a sufficiently compact star to a black hole, declared, "I think that there should be a law of Nature to prevent the star from behaving in this absurd way." Nonetheless, black holes are now considered a standard feature of our Universe, and have also found wide utility in theoretical physics. Here, we review the basic properties of astrophysical black holes.

Black holes candidate masses are distributed approximately bimodally, either as stellar-mass black holes (commonly termed X-ray binaries, or XRBs; $M/M_\odot \sim 6 - 100$) or supermassive black holes (SMBHs; $M/M_\odot \sim 10^6 - 10^{10}$). Stellar-mass black holes are the products of high-mass supernovae, and normal galaxies at redshift $z = 0$, including our own, may each host $\sim 10^8$ such black holes (e.g. Brown & Bethe 1994, Elbert et al. 2018). The origins of supermassive black holes are somewhat less certain, as they are sensitive to the astrophysics of the early universe. However, there is now compelling evidence that essentially all normal galaxies host at least one supermassive black hole at their center (e.g. Magorrian et al. 1998, Ho 1999, Kormendy & Ho 2013). Indeed, SMBHs may play a role in normal galaxy evolution (Ferrarese & Merritt 2000).

The distribution and intrinsic properties of astrophysical black holes can be difficult to pin down ob-

servationally. On the other hand, black holes emerge at once from the theory of general relativity upon consideration of a point particle with mass M and angular momentum[2] J. While the solution to Einstein's equations for $J = 0$, the Schwarzschild metric, was identified almost immediately in 1915 (in the context of the external field of a spherical star), the general case resisted analytic treatment for a considerable time until Kerr (1963). This solution, the Kerr metric, was subsequently shown to have properties close to uniqueness (Carter 1971)[3]. Beginning with Oppenheimer & Snyder (1939), event horizons were also shown to emerge from dynamical collapse.

The Einstein field equations of general relativity are challenging to solve for nonstationary distributions of mass-energy. This can be sidestepped, however, by assuming that the gravitational potential is dominated everywhere by the central black hole. It turns out that in all astrophysically relevant scenarios (except compact object mergers), the fluid density ρ is sufficiently small ($\rho R_g^3/M \ll 1$) that the fluid experiences no self-gravity. For supermassive black holes, $\rho R_g^3/M \sim 10^{-7}$, and for stellar mass black holes, $\rho R_g^3/M \sim 10^{-15}$. Throughout this work, we assume a stationary spacetime (the Kerr metric) as the background on which we evolve non-self-gravitating plasma and radiation.

It is often convenient to describe the Kerr solution in coordinates that are regular across the event horizon; here, we adopt Kerr-Schild coordinates (t, r, θ, ϕ) (related to Boyer-Lindquist coordinates by a transformation of the time coordinate) and units such that $GM = c = 1$. The metric tensor is then

$$g_{\mu\nu} = \begin{pmatrix} -\left(1 - \frac{2r}{\rho^2}\right) & \frac{2r}{\rho^2} & 0 & -\frac{2a_\star r \sin^2\theta}{\rho^2} \\ \frac{2r}{\rho^2} & 1 + \frac{2r}{\rho^2} & 0 & -a_\star \sin^2\theta \left(1 + \frac{2r}{\rho^2}\right) \\ 0 & 0 & \rho^2 & 0 \\ -\frac{2a_\star r \sin^2\theta}{\rho^2} & -a_\star \sin^2\theta \left(1 + \frac{2r}{\rho^2}\right) & 0 & \sin^2\theta \left(\rho^2 + a_\star^2 \sin^2\theta \left(1 + \frac{2r}{\rho^2}\right)\right) \end{pmatrix} \tag{1.1}$$

where $\rho^2 = r^2 + a_\star^2 \cos^2\theta$. These coordinates are stationary and axisymmetric (symmetric in t and ϕ). The event horizon is a surface of constant r, $r_{\rm eh} = 1 + \sqrt{1 - a_\star^2}$; $r_{\rm eh}$ decreases from 2 for a nonspinning black hole to 1 for a maximally spinning black hole. Kerr black holes also possess an ergoregion between $r_{\rm ergo} = 1 + \sqrt{1 - a_\star^2 \cos^2\theta}$ and $r_{\rm eh}$, inside of which a timelike observer must rotate with the spacetime.

[2] An electric charge Q is also permissible, but irrelevant in astrophysical scenarios because any dynamically important charge would be rapidly neutralized. In addition to neutralization by ambient plasma, one possible route to charge neutralization is pair breakdown, in which electromagnetic energy is transformed into electron-positron pair rest mass. Blandford & Znajek (1977) showed that this occurs for a black hole in vacuum when $Q/M \gtrsim 10^{-13} a_\star^{-1/2} (M/M_\odot)^{1/2}$ and $a_\star \gtrsim 10^{-12} (M_\odot/M)$.

[3] The full story is a bit technical and not entirely airtight: all uncharged, stationary, axisymmetric black holes belong to one of a set of disjoint families. The Kerr solution is one such family, and no other families of black holes parameterized by (M, J) are known. The only way around the uniqueness of the Kerr solution would be a new family of black holes with, say, coffee cup-shaped event horizons. However, assuming real analyticity of spacetime, one can show that all cross sections of spinning black holes are 2-spheres (Hawking & Ellis 1973, at which point the Kerr solution would be unique (with additional consideration for nondegenerate event horizons; Robinson 1975). One can also add additional fields not part of general relativity or electomagnetism, e.g. Herdeiro & Radu (2014), although such a procedure will probably introduce additional parameters beyond (M, J).

Additional structure appears when considering test particle motion in the Kerr geometry (Bardeen et al. 1972). Keplerian orbits around Kerr black holes are in some ways quite similar to those around point masses in Newtonian gravity; in particular,

$$\Omega = d\phi/dt = \pm\frac{1}{r^{3/2} \pm a_\star} \tag{1.2}$$

where, throughout this section, $\pm$ selects between prograde (+) and retrograde (−) orbits. A major qualitative difference, however, is that for black holes, there is an innermost stable circular orbit (ISCO) for Keplerian motion in the equatorial plane. The ISCO radius is given by

$$\begin{aligned} r_{\rm ISCO} &= 3 + z_2 \mp \sqrt{(3-z_1)\,(3+z_1+2z_2)}, \\ z_1 &= 1 + \left(1-a_\star^2\right)^{1/3}\left[(1+a_\star)^{1/3} + (1-a_\star)^{1/3}\right], \\ z_2 &= \sqrt{3a_\star^2 + z_1^2}. \end{aligned}$$

For $a_\star = 0$, $r_{\rm ISCO} = 6$. Note that for $a_\star \gtrsim 0.94$, $r_{\rm ISCO} < r_{\rm ergo}$ with potential consequences for torques on the inner boundary (e.g. Gammie 1999). A particle of mass m slowly drifting inwards along Keplerian orbits down to the ISCO also generates energy efficiently, 5.7% to 42% of m depending on the spin of the black hole (e.g. Shapiro & Teukolsky 1983; note that this efficiency is lower for counterrotating disks with $a_\star < 0$); compare to the efficiency of hydrogen fusion, 0.73%.

Additionally, in relativity photons possess (unstable) bound orbits. In the equatorial plane this is known as the photon ring, with radius

$$r_{\rm ph} = 2\left(1 + \cos\left(\frac{2}{3}\cos^{-1}\left(\mp a_\star\right)\right)\right); \tag{1.3}$$

for a non-spinning black hole, $r_{\rm ph} = 3$. The photon ring may appear as a bright structure in images of optically thin accretion flows; geodesics passing near this structure will traverse relatively long pathlengths through radiating plasma.

1.1.1 Evidence for Astrophysical Black Holes

The search for black holes in astronomy has historically been largely synonymous with the search for event horizons. Not only should we not expect to make measurements *inside* an event horizon, but event horizons and hard surfaces have very different radiative properties. However, this field of research has recently changed qualitatively with the detection at 09:50:45 UTC on September 14, 2015 of gravitational radiation from a

binary black hole merger (Abbott et al. 2016a). Here we briefly review the history of demonstrating the existence of black holes in nature in a roughly chronological fashion, concluding with the state of the field in the era of gravitational wave observatories. This is a relatively high-level overview; more details of some individual black hole candidates of special interest for constraining accretion theory will be presented after the fundamentals of this theory are introduced. The search for black holes is also interwoven with measuring black hole mass, so along the way we will review the major techniques for making such measurements. A tremendous amount of work has gone into this field, and the references in this section should in no way be considered comprehensive (for reviews, see e.g. Kormendy & Richstone 1995, Ferrarese & Ford 2005, Kormendy & Ho 2013).

Black holes were first invoked to explain the enormous luminosities of distant sources with optical spectra that resembled ordinary stars. Schmidt (1963) begins, "The only objects seen on a 200-in. plate near the positions of the components of the radio source 3C 273 reported by Hazard, Mackey and Shimmins in the preceding article are a star of about thirteenth magnitude and a faint wisp or jet. [...] The close correlation between the radio structure and the star with the jet is suggestive and intriguing." The simultaneous large redshifts and narrow widths further argued against a compact galactic source with exotic gravitational redshifting. Lynden-Bell (1969) then argued that the inferred luminosities required gravitational binding energies large enough that the object could not help but collapse to a black hole (see also Salpeter 1964). Rees (1984) subsequently showed that any scenario that could produce quasar-like emission should ultimately produce a supermassive black hole. Quasar abundances and luminosities suggest that at $z = 0$ a typical galaxy will host a $\gtrsim 10^7 M_\odot$ SMBH (Soltan 1982, Chokshi & Turner 1992).

While active galactic nuclei presented strong circumstantial evidence for black holes, the large distances to these sources prohibited straightforward dynamical measurement. The first direct evidence for black holes was instead provided by Cygnus X-1, a galactic high mass X-ray binary. Webster & Murdin (1972) found evidence through velocity redshifts and X-ray variability for a compact object of mass $2.5 \lesssim M/M_\odot \lesssim 6$[4] in an eclipsing orbit with a $\sim 10 M_\odot$ main sequence star (see also Bolton 1972). These inferences continue to be confirmed, more recently by a series of papers combining accurate VLBA parallax measurements of distance (Reid et al. 2011), historical spectroscopic and photometric observations (Orosz et al. 2011), and disk continuum fitting (Gou et al. 2011) to find a black hole of mass $M/M_\odot = 14.8 \pm 1$.

While active galactic nuclei are typically quite distant ($\gtrsim$ Mpc), the Milky Way's own Sagittarius A* is an exception. For this system, only ~ 8 kpc away, the trajectories of individual stars orbiting this source are resolvable, first through speckle imaging (e.g. Eckart & Genzel 1997, Ghez et al. 1998) and later with adaptive

[4]Masses for neutron stars, the most compact generally accepted object without an event horizon, cap out at $2 - 3 M_\odot$, e.g. Kalogera & Baym 1996.

optics (e.g. Ghez et al. 2005). The result (Ghez et al. 2008, Gillessen et al. 2009) is a mass $M \sim 4.2 \times 10^6 M_\odot$ inside a radius $\sim 100\text{AU} \sim 2400GM/c^2$. This compaction virtually guarantees a black hole, or at least an exotic object with very similar properties.

For a Keplerian disk, knowledge of the radius and orbital frequency constrain the interior mass. Therefore, by constructing models of disks satisfying radial velocity measurements made close to the black hole (and accounting for radial pressure gradients and disk warps), one may measure the black hole mass; this is the gas-dynamical measurement method (e.g. Harms et al. 1994, Macchetto et al. 1997, Barth et al. 2001, and Kormendy & Ho 2013 for a review). In practice, nebular line emission in the optical is usually readily detectable, and the velocity structure of a collisional disk is nearly trivial. One then uses such a model to match measured velocities, velocity dispersions, and surface brightness, However, the mass-to-light ratio must be assumed in order to provide the galaxy's contribution to the gravitational potential, one must check independently that the inner region of the galaxy has indeed relaxed to a disk-like configuration, disk inclination must be known precisely, and dust absorption may render the disk opaque.

Stars in galaxies generally interact exclusively with the galactic gravitational potential. Motions of stars near a supermassive black hole should be sensitive to the mass of that black hole; inferring this mass from bulk stellar motion is the stellar-dynamical measurement method (see Kormendy & Richstone 1995 for a review). While one cannot resolve individual stars in other galaxies, one can measure projected brightness, velocities, and velocity dispersions. Models of stellar distributions are then projected and used to interpret the observations (e.g. Kormendy 1988, Dressler & Richstone 1988). This process is subject to a number of subtleties, including triaxiality (van den Bosch & de Zeeuw 2010), eccentric orbits (Shen & Gebhardt 2010), and structure in the mass-to-light ratio (Gebhardt & Thomas 2009). The tradeoff between stellar-dynamical and gas-dynamical measurements is that, while stars only feel gravity, one is projecting a solution to the collisionless Boltzmann equation rather than to the much lower dimensional collisional fluid equations. Unfortunately, comparison measurements between the two techniques have only been made in about ten galaxies, and it is currently not clear why the methods commonly disagree by a (systematic) factor ~ 2.

Reverberation mapping (Blandford & McKee 1982) considers the accreting black hole as a compact, variable continuum source surrounded by a region of $\sim 10^4$ K clouds that produce broad line emission. This broad line region is challenging to resolve; instead, one may identify lags between the central continuum and broad line emission and use the speed of light to measure distances inside the disk. Combined with line widths and an assumed disk structure, this provides an enclosed mass (e.g. Peterson et al. 2004, and Peterson 2014 for a review). However, the structure and inclination of the broad line region must then be assumed. In addition, radiation pressure on the broad line region is challenging to disentangle from gravity.

When masers (molecular clouds of sufficiently low density that population inversions are possible, leading to negative absorption coefficients) are present near active galactic nuclei, one can extract the mass of the black hole to high accuracy, as in the $\sim 3.8 \times 10^7 M_\odot$ black hole at the center of NGC 4258 (Herrnstein et al. 2005)[5]. Such masers are especially valuable because they probe the accretion disk rotation curve on tenths of parsec scales (e.g. Greene et al. 2010, Kuo et al. 2011, and Lo (2005) for a review).

Broderick et al. (2009) directly approached the question of whether an event horizon is present in Sgr A*. Supposing that the central object has a hard surface, any gravitational binding energy not radiated prior to accreting matter impacting this surface will be converted into thermal radiation (see also e.g. Narayan & Heyl 2002). The relative radio and IR luminosities of Sgr A* render this scenario essentially impossible in the current framework of accretion theory (Sgr A*'s accretion flow would have to be very nearly perfectly radiatively efficient).

The measurements just described all use electromagnetic observations. One might prefer to instead measure gravity directly; merging black holes, for example, should emit an order unity fraction of their mass in gravitational waves. Such gravitational wave detections have recently been obtained for six compact object mergers by the Laser Inteferometer Gravitational-Wave Observatory (LIGO), beginning with Abbott et al. (2016a). In unobjectionable agreement within errors with predictions from general relativity, these observations have neatly resolved the question of whether black holes exist astrophysically in an essentially loophole-free way. LIGO has even helped rule out nearly-but-not-quite black hole models, like gravastars (where support against collapse comes from spacetime degeneracy pressure) which were shown to be inconsistent with LIGO measurements by Chirenti & Rezzolla (2016). Such objects would be very difficult or impossible to rule out by measurements of spectra from accreting black holes because they are akin to rearranging mass inside the event horizon.

1.1.2 Constraints on Black Hole Spin

For supermassive black holes, the Bondi radius may be $\sim 10^6 R_g$; the monopolar contribution of gravity is felt far from the event horizon. The spin, however, produces a quadrupole moment in the gravitational potential (e.g. Misner et al. 1973), which decays with R more rapidly than the gravitational monopole ($\sim R^{-3}$ rather than $\sim R^{-1}$). Spin is therefore significant over a much smaller range of radii, typically only for $R \lesssim 10 R_g$. Measurements of black hole spin are consequently more challenging than measurements of black hole mass.

Black hole spin is probably the source of free energy tapped by relativistic jets (Blandford & Znajek 1977); the power of such jets is sensitive to $a_\star$ (McKinney & Gammie 2004, Tchekhovskoy et al. 2012). The

[5]In this case, maser activity also exposed a warp in the accretion disk. Warps may have important consequences for accretion, e.g. Fragile et al. 2007, Liska et al. 2018

Source	$M/M_\odot$	$a_\star$ (Fit)	$a_\star$ (FeK)	$a_\star$ (GW)	References
Cyg X-1	14.8 ± 1.0	> 0.95	> 0.95		MNS14, R14
LMC X-1	10.9 ± 1.4	$0.92^{+0.05}_{-0.07}$	> 0.55		MNS14, R14
M33 X-7	15.65 ± 1.45	0.84 ± 0.05			MNS14
GRS 1915+105	10.1 ± 0.6	> 0.95	> 0.97		MNS14, R16
4U 1543-475	9.4 ± 1.0	0.80 ± 0.1	0.3 ± 0.1		MNS14
GRO J1655-40	6.3 ± 0.5	0.70 ± 0.1			MNS14
XTE J1550-564	9.1 ± 0.6	$0.34^{+0.20}_{-0.28}$	$0.33 - 0.77$		MNS14, R14
H1743-322	~ 8	0.2 ± 0.3			MNS14
LMC X-3	7.6 ± 1.6	< 0.3			MNS14
GX339-4			0.94 ± 0.02		R14
A0620-00	6.6 ± 0.25	0.12 ± 0.19			MNS14
MAXI J1836-194			0.88 ± 0.03		R14
SAX J1711.6-3808			$0.6^{+0.2}_{-0.4}$		R14
Swift J1753.5-0127			$0.76^{+0.11}_{-0.15}$		R14
XTE J1650-500			0.79 ± 0.01		R14
XTE J1652-453			0.45 ± 0.02		R14
XTE J1752-223			0.52 ± 0.11		R14
XTE J1908+094			0.75 ± 0.09		R14
GW150914	62^{+4}_{-4}			$0.67^{+0.05}_{-0.07}$	Abbott et al. (2016a)
GW151226	$20.8^{+6.1}_{-1.7}$			$0.74^{+0.06}_{-0.06}$	Abbott et al. (2016b)
GW170104	$48.7^{+5.7}_{-4.6}$			$0.64^{+0.09}_{-0.2}$	Abbott et al. (2017a)
GW170608	$18.0^{+4.8}_{-0.9}$			$0.69^{+0.04}_{-0.05}$	Abbott et al. (2017b)
GW170814	$53.2^{+3.2}_{-2.5}$			$0.70^{+0.07}_{-0.05}$	Abbott et al. (2017c)

Source	$M/(10^6 M_\odot)$	$a_\star$ (Fit)	$a_\star$ (FeK)	$a_\star$ (GW)	References
Mrk335	14.2 ± 3.7		$0.83^{+0.09}_{-0.13}$		R14
IRAS 00521-7054			> 0.84		R14
Tons180	~ 8.1		$0.92^{+0.03}_{-0.11}$		R14
Fairall 9	255 ± 56		$0.52^{+0.19}_{-0.15}$		R14
Mrk359	~ 1.1		$0.66^{+0.3}_{-0.54}$		R14
Mrk1018	~ 140		$0.58^{+0.36}_{-0.74}$		R14
1H0419-577	~ 340		> 0.89		R14
Ark120	150 ± 19		$0.64^{+0.19}_{-0.11}$		R14
Swift J0501.9-3239			> 0.99		R14
1H0707-495	~ 2.3		> 0.97		R14
Mrk79	52.4 ± 14.4		> 0.987		R14
MCG-6-30-15	$2.9^{+1.8}_{-1.6}$		> 0.98		R14
Mrk841	~ 79		> 0.52		R14
Swift J2127.4+5654	~ 1.5		0.6 ± 0.2		R14
Ark564	~ 1.1		$0.96^{+0.01}_{-0.11}$		R14

Table 1.1: Available measurements of black hole spin for stellar-mass and supermassive black holes. MNS14 denotes continuum-fitting (Fit) measurements from McClintock et al. (2014) and references therein. R14 denotes broad iron line (FeK) measurements from Reynolds (2014) and references therein. There is some disagreement between these two methods. GW denotes detection by gravitational waves. For LIGO sources, only final spins of the post-merger black hole are given, as pre-merger spins are not as strongly constrained. All GW signals shown are for binary BH mergers. The sole detected binary neutron star merger, GW170817, did not constrain the final BH spin as strongly. Note that systematic uncertainties in Fit and FeK methods are probably larger than for the GW method.

phenomenology of relativisic jets is one of the major active research areas in high energy astrophysics. Table 1.1 provides currently known black hole spins.

There are two leading methods for measuring black hole spin. First, thermal continuum fitting, introduced by Zhang et al. (1997) (see McClintock et al. 2014 for a recent review), assumes that near-Eddington accretion disks are geometrically thin, optically thick, and emit like blackbodies[6]. X-ray spectra are then used to constrain the accretion rate and spin by fixing the location of the ISCO once the mass, inclination angle, and observer distance are known.

Continuum fitting relies on the accretion disk being sharply truncated at the ISCO. In accretion theory this is not unreasonable; the inflow time is $\sim 100T_g$ at the ISCO, whereas the ballistic infall time is $\sim {T_g}^7$. Also to our benefit is that $r_{\rm ISCO}$ scales *at least* linearly with $a_\star$. Additionally, there is strong circumstantial evidence from observations for an ISCO-like feature in accretion disks. In particular, when fitting XRB spectra the inner edge parameter can remain quite stable while fitting black hole spectra over large changes in flux (Tanaka & Lewin 1995, Steiner et al. 2010). Note, however, that a common assumption in disk modeling (zero torque at the ISCO) is not always precisely valid (Gammie 1999; Agol & Krolik 2000).

The consequences of radiative transport through the vertical structure of the disk, especially spectral hardening, are also important to capture. For example, for thermal emission one would expect $L \sim T^4$; this does not quite hold, however, in measurements of XRBs (e.g. McClintock et al. 2009). Once color correction is included (commonly using the method of Davis & Hubeny 2006), however, the $L \sim T^4$ trend re-emerges to good precision. Modeling is also useful in this case because typically observations do not provide an independent constraint on spectral hardening (McClintock et al. 2014).

The second leading technique is inner disk reflection modeling. Originally proposed by Fabian et al. (1989), the technique (see Miller 2007 and Reynolds 2014 for reviews) relies on a $\sim$ keV temperature accretion disk being illuminated by external higher energy power-law emission. These impinging X rays then excite spectral lines (for astrophysical metallicities, Fe K transitions around $\sim 2-10$ keV are typically favored). The observed shape of such a line is then compared to its rest frame shape to infer the geometry of the accretion flow. Larger spins and inclinations lead to more broadening. Inclination is an output of this technique, and along with mass and distance not being inputs, some frequently significant uncertainties are avoided with this method.

Just as with continuum fitting, broad line spectroscopy relies on little dissipation and low densities inside the ISCO. It also generally assumes a lamppost model for continuum emission incident on the accretion

[6]Specifically, this technique assumes that luminous, thermal accretion disks are described by the axisymmetric, stationary Novikov & Thorne (1973) solution, to which we will return in a later section, embedded in a hot corona.

[7]This is supported by simulations, e.g. Shafee et al. 2008 for a thin magnetized disk around a non-spinning black hole.

disk; this is not clearly supported by theory. Finally, the iron line is identified after a subtraction operation accounting for soft excess, line-of-sight absorption, and X-ray fluorescence by cold material far from the black hole. Errors in producing the residual, intrinsic iron line can contaminate spin measurements.

Along with enhancing fundamental understanding of BHs, LIGO has given us a new handle on black hole spin. Although this technique provides probably the best available constraints on final spin, there are currently no examples of post-merger BHs with detected accretion disks; LIGO spin values are less useful to accretion theory. Black hole spin following a binary merger may also not be representative of spins following long periods of disk accretion.

1.2 Black Hole Accretion Disks

Should a stellar mass black hole find itself in a close binary with a normal star, or a supermassive black hole be embedded in the interstellar medium at the center of a galaxy, they will begin accreting gas at detectable rates. In both scenarios there is a superabundance of angular momentum in the gas reservoir, and the resulting barrier in the effective potential eventually retards accretion, at which point the flow circularizes into an accretion disk. This generally occurs far from the black hole, whereas this work concerns the structure of accretion in the inner ~ 100 gravitational radii where most of the gravitational energy is liberated. Therefore, here we consider accretion purely in the picture of pseudo-Keplerian disks.

1.2.1 Kinematics

In examining accretion in a Keplerian flow, we first ask: is hydrodynamic Keplerian flow stable to perturbations? With some caveats, yes, even in the nonlinear regime. This is perhaps counterintuitive at first glance; astrophysical black hole accretion disks generally have very large Reynolds numbers ($\mathrm{Re} \equiv vL/\nu$, $v \sim c_s$ and $L \sim H$), and high Reynolds numbers generally lead to turbulence. Additionally, viscous Cartesian shear flows are unstable, both theoretically (Orszag & Kells 1980) and experimentally (Davies & White 1928). A crucial difference, however, obtains in Keplerian or Keplerian-like flows in which angular momentum and angular velocity gradients have opposite sign: epicyclic motion stabilizes the flow (Balbus et al. 1996, Balbus & Hawley 1998). Evidence points to hydrodynamic pseudo-Keplerian flows being nonlinearly stable (Stone & Balbus 1996, Ji et al. 2006). However, there may be still be instabilities present in more complex systems, such as the vertical shear instability (Nelson et al. 2013), the subcritical baroclinic instability (e.g. Lesur & Papaloizou 2010), and the zombie vortex instability (Marcus et al. 2015, but see Lesur & Latter 2016).

Molecular viscosity will still act to transport angular momentum in laminar flow. However, for astro-

physical accretion disks this effect is generally far too small to explain observed accretion rates (Pringle 1981). We are then left, despite the robust hydrodynamic stability of Keplerian flows, to consider a turbulent viscosity. Turbulent states can produce correlations in r and ϕ components of vectors, leading to a net $r-\phi$ stress, which in turn can transport angular momentum[8]. Early disk modeling parameterized this turbulent viscosity with a dimensionless constant α; $\nu = \alpha c_s H$ (Shakura & Sunyaev 1973). Forty-five years ago Novikov & Thorne (1973) wrote, "Someday, perhaps ten years hence, when one understands the magnetic and turbulent viscosities better, one can insert in the formalism a reliable value of α."

Magnetized Keplerian flows turn out to be unstable to the magnetorotational instability (Balbus & Hawley 1991), a local, axisymmetric instability of vertical magnetic fields through a differentially rotating plasma[9]. There is a profitable analogy between this system and two point masses on a spring (Balbus & Hawley 1998). Magnetic tension acts as a spring connecting fluid elements along a magnetic field line. Following a radial perturbation with wavenumber $\mathbf{k} = k\hat{\mathbf{z}}$, there is a mismatch in rotational frequencies between those fluid elements. As they separate, magnetic tension transfers angular momentum to the outer fluid element, and they separate faster; the system is unstable.

The MRI is a powerful instability. For a Keplerian disk, the maximum growth rate and corresponding wavelength are

$$\omega_{\max} = \frac{3}{4}\Omega \tag{1.4}$$

$$k_{\max} = \frac{\sqrt{15}}{4}\frac{\Omega}{v_{\rm A}}. \tag{1.5}$$

In particular, notice that $\omega_{\max} \sim \Omega$. For an instability drawing free energy from differential rotation, there is no faster timescale in the problem than $1/\Omega$; it is not clear that another instability could grow much faster than the MRI (e.g. Balbus & Hawley 1998). It is also ubiquitous. Not only does its local nature exempt it from any requirements of special global circumstances, but it acts for any rotational profile such that

$$\frac{d\Omega^2}{d\log R} < 0, \tag{1.6}$$

a condition of course satisfied by Keplerian rotation. Finally, the MRI is purely Alfvénic, and collisionality is not required[10] so long as the plasma is moderately thermal. In a collisionless plasma, the MRI keeps the

[8] Balbus & Hawley (1998) point out that turbulence by itself does not guarantee angular momentum transport. In shear flows, energy is transferred from the background flow into turbulent motions via vortex stretching, which *does* correlate u^r and u^ϕ.

[9] We require a highly conductive (fully ionized) plasma such that magnetic fields are "frozen in" to the fluid (but see Gammie 1996 when this does not obtain globally). Note also that purely toroidal magnetic fields are susceptible to a similar instability.

[10] Alfvén modes are unaffected by particle collisions.

same instability criterion, and has somewhat *faster* fastest growing mode growth rates when plasma $\beta \gg 1$ (Quataert et al. 2002).

However, the classical weak-field MRI breaks down once $v_{\rm A} \sim c_s \sim H\Omega$. Consider Equation 1.5: for $v_{\rm A} \gg R\Omega$, $k_{\rm max} \ll 1/R$, i.e. the fastest growing mode no longer fits inside the disk! Really such a system is qualitatively different; magnetic energy dominates orbital kinetic energy. Such a situation is now often termed a Magnetically Arrested Disk (MAD; Narayan et al. 2003). The strong magnetization even in the midplane of MADs leads them to behave and radiate quite differently from their less-magnetized counterparts[11]. We do not consider MADs in this work, but they are an exciting future direction for radiation MHD.

The MRI is often likely to act; we now ask how it saturates. Here, local numerical simulations[12] have taken the fore, beginning with Hawley et al. (1995). Studying a local box for different (conserved) initial field strengths of uniform vertical or azimuthal field, the authors produced saturation predictors for the magnetic field strength[13]

$$\left\langle \frac{B^2}{8\pi} \right\rangle = \begin{cases} (1.21 \pm 0.29)\rho_0(L_z\Omega)(\lambda_c\Omega) \text{ if } \mathbf{B}_0 = B_0\mathbf{z} \\ (0.012 \pm 0.002)\rho_0(L_y\Omega)(\lambda_c\Omega) \text{ if } \mathbf{B}_0 = B_0\mathbf{y} \end{cases} \tag{1.7}$$

where ρ_0 is the mean density, L_z and L_y are the box dimensions in z and y, respectively, and $\lambda_c = 9.18\beta_0^{-1/2}$ where β_0 is that for the initial magnetic field. Further work including vertical gravity (Stone et al. 1996, Miller & Stone 2000) showed the formation of a hot magnetically-dominated corona; above $z \sim 2H$, the solution changes qualitatively. Guan & Gammie (2011) provided fits to the density and magnetic energy density in this *stratified* model with zero net field:

$$\langle \rho \rangle = \begin{cases} 0.93\rho_0 \exp\left(-\frac{z^2}{2H}\right) \text{ if } |z| \leq 2.55H \\ 0.036\rho_0 \exp\left(-\frac{|z|-2.6H}{0.44H}\right) \text{ else} \end{cases} \tag{1.8}$$

$$\left\langle \frac{B^2}{8\pi} \right\rangle = \begin{cases} 0.012\rho_0 c_s^2 \text{ if } |z| \leq 2.55H \\ 0.012\rho_0 c_s^2 \exp\left(-\frac{|z|-2.6H}{0.64H}\right) \text{ else} \end{cases} \tag{1.9}$$

These quantities inform the turbulent stresses (the Maxwell stress, $B^x B^y/(4\pi)$, and the subdominant Reynolds stress, $\rho v^x v^y$). A major open question is what the mean amplitude of MRI-driven turbulence is in the absence of mean fields, to which we will return in a later chapter (Ryan et al. 2017a).

Although the complete picture of MRI-driven turbulent stresses is still lacking, local numerical simulations

[11] Frequently termed SANE, for Standard and Normal Evolution

[12] Called "shearing boxes" for their Cartesian-like coordinates (x, y, z) related to global (r, ϕ, z) coordinates, shear-periodic radial boundary conditions, and the presence of Coriolis and tidal forces.

[13] See also Brandenburg et al. 1995 and Matsumoto & Tajima 1995.

generally agree on certain quantitative results. The $r-\phi$ stress is related to correlations in the magnetic field; the scalar magnetic field autocorrelation function exhibits a tilt relative to the y axis of $\sim 18^\circ$ (Davis et al. 2010, Ryan et al. 2017a). The height-integrated Maxwell stress is a factor ~ 4 greater than the height-integrated Reynolds stress (Ryan et al. 2017a). The viscosity parameter can be estimated from the midplane magnetization: $\alpha \approx 1/(2\beta)$.

Angular momentum transport through magnetorotational turbulence driven by the MRI is a leading candidate for the mechanism governing accretion in many astrophysical accretion disks[14]. However, there is as yet a lack of irrefutable evidence that this process is active in real accretion flows.

1.2.2 Radiative Processes

As the mass accretion rate is increased from very low values, what are the first radiative processes to become important in the inner region of RIAFs? Here, typical electron temperatures $\Theta_e \equiv k_B T_e/(m_e c^2) \gtrsim 1$, surface densities are such that the Thomson depth $\tau_T \lesssim 1$, and magnetic fields are such that the plasma $\beta = 8\pi n_e k_B T/B^2 \sim 10$. The most energetic processes are synchrotron emission and Compton upscattering (e.g. Mahadevan 1997). In particular, note that, for hot electrons, the ratio of bremsstrahlung to synchrotron emission (e.g. Rybicki & Lightman 1979) is

$$\frac{J_b}{J_s} \approx \frac{\alpha\beta g_{ff}}{\frac{T_p}{T_e}\Theta_e^{3/2}} \tag{1.10}$$

where $\alpha \approx 1/140$ is the fine structure constant, $\beta \approx 10$ for MRI-driven turbulence, the Gaunt factor $g_{ff} \approx 1$, and we take $T_p/T_e \lesssim 10$. For $\Theta_e \gtrsim 1$, synchrotron emission dominates bremsstrahlung. Throughout this work, we consider radiative losses due to synchrotron and Compton only.

Radiative properties of plasmas are sensitive to the distribution functions of the radiating particles. In particular, nonthermal electrons may dramatically change the spectra of black hole accretion disks (Coppi 1999). We consider only thermal electron distributions in this work, but generalizing these results to non-thermal distributions is an interesting future direction (e.g. Chael et al. 2017).

Synchrotron emission is the result of relativistic electrons accelerating around magnetic field lines as they move along their helical trajectories. Generically, synchrotron emission peaks around the synchrotron frequency,

$$\nu_s = \frac{2}{9}\nu_c \Theta_e^2 \sin\theta, \tag{1.11}$$

[14]Magnetic fields can transport angular momentum even without driving turbulence. For example, vertical fields can transport angular momentum vertically (Blandford & Znajek 1977).

where $\nu_c = q_e B/(2\pi m_e c)$ is the cyclotron frequency, $\Theta_e \equiv k_B T_e/(m_e c^2)$, and θ is the angle relative to the magnetic field. At lower frequencies the plasma is optically thick to thermal self-absorption, and at higher frequencies the emissivity falls off. Extensive work has been done to evaluate the emissivity resulting from this process for a thermal distribution of electrons. However, the modestly relativistic regime in which we are interested is particularly challenging. Throughout, we adopt the transrelativistic fitting formula of Leung et al. (2011):

$$j_\nu = n_e \frac{\sqrt{2}\pi q_e^2 \nu_s}{3K_2(1/\Theta_e)c}\left(X^{1/2} + 2^{11/12}X^{1/6}\right)^2 \exp\left(-X^{1/3}\right) \tag{1.12}$$

where $X = \nu/\nu_s$, and K_2 is a modified Bessel function of the second kind. Note the following limits:

$$K_2(1/\Theta_e) \approx \left(\frac{\pi\Theta_e}{2}\right)^{1/2} \exp\left(-\frac{1}{\Theta_e}\right) \text{ for } \Theta_e \ll 1 \tag{1.13}$$

$$K_2(1/\Theta_e) \approx 2\Theta_e^2 \text{ for } \Theta_e \gg 1 \tag{1.14}$$

Also, Equation 1.12 is not valid for $\Theta_e \ll 1$. For this reason, together with the relative unimportance of synchrotron contributions from lower temperature regions, we generally ignore synchrotron emission when $\Theta_e < 0.3$.

Compton scattering ($e^- + \gamma \rightarrow e^- + \gamma$) is the relativistic extension of Thomson scattering, in which the electron and photon can exchange energy as well as momentum. For a comprehensive set of results, including Monte Carlo calculations, see Pozdnyakov et al. (1983). Of particular interest here is what happens when a soft photon ($h\nu \ll k_B T_e$) encounters a relativistic electron (i.e. $\Theta_e \gtrsim 1$). This reaction, in which the photon takes energy from the electron, is called *inverse Compton scattering* or *Compton upscattering*. Compton upscattering off a thermal distribution is often described in terms of a mean amplification factor $A \equiv \langle \Delta\nu/\nu \rangle + 1$. For one collision (Padmanabhan 2000) the angle-averaged fractional change in photon frequency is

$$\frac{\langle \Delta\nu \rangle}{\nu} = \frac{4}{3}\gamma^2\beta^2, \tag{1.15}$$

and the mean amplification factor for a thermal electron distribution is

$$A = \int d\gamma \frac{\langle \Delta\nu \rangle}{\nu}\frac{dN}{d\gamma}, \tag{1.16}$$

where

$$\frac{dN}{d\gamma} = \frac{\gamma(\gamma^2-1)^{1/2}}{\Theta_e K_2(1/\Theta_e)} \exp\left(-\frac{\gamma}{\Theta_e}\right) \tag{1.17}$$

is the Maxwell-Jüttner distribution function (relativistic, classical, non-interacting particles in thermal equilibrium). The amplification factor is then

$$A = \frac{4\Theta_e K_3(1/\Theta_e)}{K_2(1/\Theta_e)} + 1 \tag{1.18}$$

or approximately (C. Gammie, private communication, but see e.g. Rybicki & Lightman (1979) for a derivation of a similar but slightly less accurate formula bridging low and high temperature limits)

$$A \approx 1 + 4\Theta_e - 2\Theta_e^{3/2} + 16\Theta_e^2. \tag{1.19}$$

Evidently Compton upscattering can be a dramatic process; for $\Theta_e = 10$, mm wavelengths will upscatter into the optical band in a single interaction, and for $\Theta_e = 100$, into the X-ray band.

The interaction rate for Compton scattering is set by the Klein-Nishina cross section (Klein & Nishina 1929), the relativistic extension of the Thomson cross section $\sigma_{\rm T}$. The full expression is

$$\sigma_{\rm KN} = \sigma_{\rm T}\frac{3}{4\epsilon^2}\left(2 + \frac{\epsilon^2(1+\epsilon)}{(1+2\epsilon)^2} + \frac{\epsilon^2-2\epsilon-2}{2\epsilon}\log(1+2\epsilon)\right) \tag{1.20}$$

where $\epsilon = h\nu\gamma(1-\beta\cos\theta)$ is the photon energy in the rest frame of the electron in units of the electron rest mass energy. For $\epsilon \gg 1$,

$$\sigma_{\rm KN} \approx \sigma_{\rm T}\frac{3}{8\epsilon}\log(2\epsilon); \tag{1.21}$$

higher energy photons (in the electron rest frame!) are less susceptible to scattering. The corresponding differential cross section (for all ϵ) is

$$\frac{d\sigma_{\rm KN}}{d\epsilon'} = \frac{\sigma_{\rm T}}{2\pi\epsilon^2}\left(\frac{\epsilon}{\epsilon'} + \frac{\epsilon'}{\epsilon} - 1 + \cos^2\theta\right) \tag{1.22}$$

where ϵ' is the photon energy after scattering.

The electron rest frame energy dependence of $\sigma_{\rm KN}$ motivates the introduction of a "hot cross section" $\sigma_{\rm H}$ (e.g. Dolence et al. 2009) in which one integrates the cross section over an electron distribution in the

rest frame of that distribution such that the specific absorptivity takes the convenient form $\alpha_\nu = n_e \sigma_{\rm H}$:

$$\sigma_{\rm H} = \frac{1}{n_e} \int d^3p \frac{dn_e}{d^3p} (1 - \beta \cos\theta) \sigma_{\rm KN}. \tag{1.23}$$

where θ is the angle between electron and photon momenta as measured in the fluid rest frame.

A useful quantity for interpreting the role of Compton scattering both in modifying spectra and in importance for cooling is the Compton y parameter, $y = \langle N_s \rangle (A-1)$ where $\langle N_s \rangle \sim \max(\tau_s, \tau_s^2)$ is the mean number of scatterings per photon. For $y \sim 1$, Compton scattering is making an order unity contribution to the radiation field.

Other radiative processes may be important, particularly at higher accretion rates than we consider here. Bremsstrahlung (e.g. Rybicki & Lightman 1979) dominates synchrotron at the higher densities and lower temperatures of near-Eddington disks. γ-γ pair production may play an important role (Guilbert et al. 1983, Fabian et al. 2015), but is sensitive to details of the accretion flow and background radiation and requires further study (Wong, Ryan & Gammie 2018). The double Compton process, $e^- + \gamma \rightarrow e^- + \gamma + \gamma$ (e.g. Thorne 1981, McKinney et al. 2017), may also play a role even at low accretion rates. Once the radiation field begins to approach the Planck distribution, stimulated scattering becomes important (e.g. Sincell & Krolik 1994). Hadronic processes such as proton synchrotron (e.g. Aharonian 2000) may also play a role in blazar emission, where jet temperatures and magnetizations may be enormous.

1.2.3 Cold Accretion Disks

One of the first and most successful accretion disk models is the radiatively efficient, thin disk solution of Shakura & Sunyaev (1973), and the subsequent relativistic generalization of Novikov & Thorne (1973). This solution relies on a few key assumptions: (1) internal energy due to dissipative heating is radiated away locally as a blackbody (2) an anomalous α viscosity is present such that $\nu = \alpha c_s H$ (3) the orbital motion is Keplerian (4) the solution is stationary (5) $H/R \ll 1$, i.e. we can vertically integrate the solution while neglecting terms of second order or higher in H/R (6) the stress vanishes at the inner boundary, corresponding to the innermost stable circular orbit. In addition, the solution has different regions in radius depending on whether the flow is gas pressure-dominated or radiation-pressure dominated, and whether the opacity is dominated by Thomson scattering or bremsstrahlung absorption.

The thin disk solution conveniently takes power-law form, produced here to provide values in my preferred units for $r = R/R_g$, $m = M/M_\odot$, and $\dot{m} = \dot{M}/\dot{M}_{\rm Edd}$, along with using $c_s^2 = \gamma P/\rho$. For the inner region

$P_r >> P_g$, $\kappa = \kappa_s$:

$$T = 4.7 \times 10^7 \ \alpha^{-1/4} m^{1/4} r^{-3/8} \text{ K} \tag{1.24}$$

$$\Sigma = 3.8 \times 10^{-1} \ \alpha^{-1} \dot{m}^{-1} \mathcal{F}^{-1} r^{3/2} \text{ g cm}^{-2} \tag{1.25}$$

$$\rho = 9.6 \times 10^{-8} \ \alpha^{-1} m^{-1} \dot{m}^{-2} \mathcal{F}^{-2} r^{3/2} \text{ g cm}^{-3} \tag{1.26}$$

$$H = 2.0 \times 10^6 \ m \dot{m} \mathcal{F} \text{ cm} \tag{1.27}$$

$$v^r = 4.0 \times 10^{12} \ \alpha \dot{m}^2 \mathcal{F} r^{-5/2} \text{ cm s}^{-1} \tag{1.28}$$

$$F = 6.9 \times 10^{27} \ m^{-1} \dot{m} \mathcal{F} r^{-3} \text{ erg cm}^{-2} \text{ s}^{-1} \tag{1.29}$$

$$\tau_s = 1.5 \times 10^{-1} \ \alpha^{-1} \dot{m}^{-1} \mathcal{F}^{-1} r^{3/2} \tag{1.30}$$

$$\tau_{ff} = 3.5 \times 10^{-12} \ \alpha^{-9/8} m^{-1/8} \dot{m}^{-3} \mathcal{F}^{-3} r^{69/16} \tag{1.31}$$

$$\tau_* = 7.2 \times 10^{-7} \ \alpha^{-17/16} m^{-1/16} \dot{m}^{-2} \mathcal{F}^{-2} r^{93/32} \tag{1.32}$$

$$\beta_r = 1.6 \times 10^7 \ \alpha^{1/4} m^{1/4} \dot{m}^2 \mathcal{F}^2 r^{-21/8} \tag{1.33}$$

For the middle region $P_g >> P_r$, $\kappa = \kappa_s$:

$$T = 1.3 \times 10^9 \ \alpha^{-1/5} m^{-1/5} \dot{m}^{2/5} \mathcal{F}^{2/5} r^{-9/10} \text{ K} \tag{1.34}$$

$$\Sigma = 2.2 \times 10^5 \ \alpha^{-4/5} m^{1/5} \dot{m}^{3/5} \mathcal{F}^{3/5} r^{-3/5} \text{ g cm}^{-2} \tag{1.35}$$

$$\rho = 3.7 \times 10^1 \ \alpha^{-7/10} m^{-7/10} \dot{m}^{2/5} \mathcal{F}^{2/5} r^{-33/20} \text{ g cm}^{-3} \tag{1.36}$$

$$H = 2.9 \times 10^3 \ \alpha^{-1/10} m^{9/10} \dot{m}^{1/5} \mathcal{F}^{1/5} r^{21/20} \text{ cm} \tag{1.37}$$

$$v^r = 7.0 \times 10^6 \ \alpha^{4/5} m^{-1/5} \dot{m}^{2/5} \mathcal{F}^{-3/5} r^{-2/5} \text{ cm s}^{-1} \tag{1.38}$$

$$F = 6.9 \times 10^{27} \ m^{-1} \dot{m} \mathcal{F} r^{-3} \text{ erg cm}^{-2} \text{ s}^{-1} \tag{1.39}$$

$$\tau_s = 8.6 \times 10^4 \ \alpha^{-4/5} m^{1/5} \dot{m}^{3/5} \mathcal{F}^{3/5} r^{-3/5} \tag{1.40}$$

$$\tau_{ff} = 7.0 \times 10^{-3} \ \alpha^{-4/5} m^{1/5} \dot{m}^{-2/5} \mathcal{F}^{-2/5} r^{9/10} \tag{1.41}$$

$$\tau_* = 2.5 \times 10^1 \ \alpha^{-4/5} m^{1/5} \dot{m}^{1/10} \mathcal{F}^{1/10} r^{3/20} \tag{1.42}$$

$$\beta_r = 8.5 \times 10^2 \ \alpha^{1/10} m^{1/10} \dot{m}^{4/5} \mathcal{F}^{4/5} r^{-21/20} \tag{1.43}$$

For the outer region $P_g >> P_r$, $\kappa = \kappa_{ff}$:

$$T = 2.5 \times 10^8 \ \alpha^{-1/5} m^{-1/5} \dot{m}^{3/10} \mathcal{F}^{3/10} r^{-3/4} \ \mathrm{K} \tag{1.44}$$

$$\Sigma = 1.1 \times 10^6 \ \alpha^{-4/5} m^{1/5} \dot{m}^{7/10} \mathcal{F}^{7/10} r^{-3/4} \ \mathrm{g\ cm^{-2}} \tag{1.45}$$

$$\rho = 4.3 \times 10^2 \ \alpha^{-7/10} m^{-7/10} \dot{m}^{11/20} \mathcal{F}^{11/20} r^{-15/8} \ \mathrm{g\ cm^{-3}} \tag{1.46}$$

$$H = 1.3 \times 10^3 \ \alpha^{-1/10} m^{9/10} \dot{m}^{3/20} \mathcal{F}^{3/20} r^{9/8} \ \mathrm{cm} \tag{1.47}$$

$$v^r = 1.4 \times 10^6 \ \alpha^{4/5} m^{-1/5} \dot{m}^{3/10} \mathcal{F}^{-7/10} r^{-1/4} \ \mathrm{cm\ s^{-1}} \tag{1.48}$$

$$F = 6.9 \times 10^{27} \ m^{-1} \dot{m} \mathcal{F} r^{-3} \ \mathrm{erg\ cm^{-2}\ s^{-1}} \tag{1.49}$$

$$\tau_s = 4.4 \times 10^5 \ \alpha^{-4/5} m^{1/5} \dot{m}^{7/10} \mathcal{F}^{7/10} r^{-3/4} \tag{1.50}$$

$$\tau_{ff} = 1.3 \times 10^2 \ \alpha^{-4/5} m^{1/5} \dot{m}^{1/5} \mathcal{F}^{1/5} \tag{1.51}$$

$$\beta_r = 5.5 \times 10^{-1} \ \alpha^{1/10} m^{1/10} \dot{m}^{7/20} \mathcal{F}^{7/20} r^{-3/8} \tag{1.52}$$

where $\mathcal{F} = 1 - (r/6)^{-1/2}$ ($6 = r_{\mathrm{ISCO}}$ for a non-spinning black hole) encodes our assumption of a stress-free inner boundary.

This problem has three important timescales. First, the orbital timescale $t_{\mathrm{orb}} \sim 1/\Omega$, the time taken to complete one orbit. Second, the thermal timescale $t_{\mathrm{thermal}} \sim 1/(\alpha\Omega)$, the time taken by energy dissipated at the midplane to escape vertically as radiation (Lightman 1974a). Third, the viscous timescale $t_{\mathrm{viscous}} \sim 1/(\alpha\Omega(H/R)^2)$ is the time taken for the α viscosity to accrete matter radially inwards[15] (e.g. Lightman 1974b). Note that for thin disks, $t_{\mathrm{viscous}} \gg t_{\mathrm{thermal}}$.

The thermal timescale is connected to a critical and still poorly understood issue: the thermal instability of radiation pressure-dominated thin disks (Shakura & Sunyaev 1976) caused by mismatched temperature dependencies of the viscous heating (Q_+) and radiative cooling (Q_-) rates. Generally, an α disk will be thermally unstable when (Piran 1978)

$$\frac{\partial \log Q_+}{\partial P}\Big|_\Sigma > \frac{\partial \log Q_-}{\partial P}\Big|_\Sigma \tag{1.53}$$

with Σ the surface density and P the thermal pressure. In the radiation pressure-dominated regime, $Q_+ \sim P^2$ whereas $Q_- \sim P$. This result is borne out by local dynamical models of radiation pressure-dominated disks, even when the α viscosity is replaced by self-consistent magnetorotationally driven turbulence (Jiang et al. 2013b). This is surprising because observed near-Eddington accretion disks show variability only at the few

[15]The viscous timescale also appears in the diffusion coefficient for the time-dependent expression for surface density in thin disks.

percent level (e.g. Remillard & McClintock 2006).

1.2.4 Hot Accretion Disks

The success of the thin disk model is not universal across observed accreting black holes. In particular, many show highly nonthermal spectra and low luminosities. This requires relaxing assumptions from the previous section about geometrical thinness and radiatively efficient blackbody emission. Additionally, the ions and electrons might also not be in equilibrium, and the plasma could be two-temperature (Shapiro et al. 1976).

This class of solutions, radiatively inefficient accretion flows (RIAFs; Ichimaru 1977, or also advection-dominated accretion flows or ADAFS; Narayan & Yi 1994) trades radiative cooling for advective cooling. All energy liberated through viscous dissipation is advected inwards with the flow, and ultimately through the event horizon. The result is a self-similar, nearly virial accretion flow, and $H \sim R$ rather than $H/R \ll 1$. See Yuan & Narayan (2014) for a recent review. Additionally, note that radiative cooling may be included semi-analytically, e.g. Narayan et al. 1997.

The ADAF solution (Narayan & Yi 1994 is given by (and expressed in cgs units for $\gamma = 1.5$, $f = 1$, and $\alpha = 0.05$):

$$c_s = R\Omega_K \left[\frac{2(5+2\epsilon)g}{9\alpha^2}\right]^{1/2} = 1.8 \times 10^{10}\ r^{-1/2}\ \text{cm s}^{-1} \tag{1.54}$$

$$T = \frac{m_p g 2(2\epsilon+5)}{18\alpha^2\gamma k_b} R^2\Omega_K^2 = 1.3 \times 10^{12}\ r^{-1}\ \text{K} \tag{1.55}$$

$$H = \left[\frac{2\epsilon+5}{\epsilon(2\epsilon+5)}\right]^{1/2} R = 2.6 \times 10^5\ mr\ \text{cm} \tag{1.56}$$

$$v^\phi = R\Omega_K \left[\frac{2\epsilon(5+2\epsilon)g}{9\alpha^2}\right]^{1/2} = 2.3 \times 10^{10}\ r^{-1/2}\ \text{cm s}^{-1} \tag{1.57}$$

$$v^r = -\frac{(2\epsilon+5)g}{3\alpha} R\Omega_K = -8.0 \times 10^8\ r^{-1/2}\ \text{cm s}^{-1} \tag{1.58}$$

$$\rho = \frac{3\dot{M}\alpha\sqrt{2\epsilon\,(2\epsilon+5)}}{4\pi R^3 g\Omega_K(5+2\epsilon)(10+4\epsilon)^{1/2}} = 3.7 \times 10^{-3}\ \dot{m}m^{-1}r^{-3/2}\ \text{g cm}^{-3} \tag{1.59}$$

$$\tau_s \sim H\kappa_s\rho = 3.8 \times 10^2\ \dot{m}r^{-1/2} \tag{1.60}$$

$$g = \left(1 + \frac{18\alpha^2}{(5+2\epsilon)^2}\right)^{1/2} - 1 \tag{1.61}$$

where $\epsilon = (5/3-\gamma)/((\gamma-1)f)$ and $f \in [0,1]$ is the fraction of heat that is lost through advection. Notice that when $\gamma = 5/3$, $v^\phi = 0$ (accretion is purely radial) along with other pathologies, such as $H \to \infty$. This is because $P = K\rho^\gamma$ and self-similarity together require purely radial inflow for $\gamma = 5/3$.

Hot, advection-dominated accretion flows turn out to be unstable to convection in the radial direction:

entropy increases as one moves down the potential well, and sub-Keplerian motion cannot stabilize this (Begelman & Meier 1982, Narayan & Yi 1994, Igumenshchev et al. 1996, Igumenshchev & Abramowicz 1999, Stone et al. 1999). Convection in shear flows may transport angular momentum inwards, opposite the behavior of a usual turbulent viscosity (Ryu & Goodman 1992, Stone & Balbus 1996, Balbus et al. 1996). This motivates one to ask what happens when convection dominates over an alpha viscosity (in the sense that $\alpha \ll 1$), or a convection-dominated accretion flow (CDAF; Narayan et al. 2000, Quataert & Gruzinov 2000). The eddy turnover time for convection is $\sim$ dynamical time, rather than the much longer viscous time for α transport. One then might consider a configuration that is marginally stable to convection[16].

This solution gives (assuming stationary energy flux, i.e. the n parameter from Quataert and Gruzinov 2000 is $n = 1/2$). Scalings are evaluated for $\gamma = 5/3$:

$$c_s = R\Omega_K \left(\frac{\gamma+1}{\gamma-1} - n\right)^{-1/2} = 1.6 \times 10^{10} r^{-1/2} \text{ cm s}^{-1} \tag{1.62}$$

$$T = \frac{m_p}{2\gamma k_B} \frac{R^2\Omega_K^2}{\frac{\gamma+1}{\gamma-1} - n} = 9.3 \times 10^{11} r^{-1} \text{ K} \tag{1.63}$$

$$v^\phi = R\Omega_K \left[\frac{2\left(\frac{1}{\gamma-1} - n\right)}{\frac{\gamma+1}{\gamma-1} - n}\right]^{1/2} = 2.3 \times 10^{10} r^{-1/2} \text{ cm s}^{-1} \tag{1.64}$$

$$v^r = -\frac{\dot{M}}{2\pi\Sigma R} = -1.6 \times 10^{10} r^{-3/2} \text{ cm s}^{-1} \tag{1.65}$$

$$\rho \propto R^{-n} (\sin\theta)^{2\left[\frac{1}{\gamma-1} - n\right]} = 3.2 \times 10^{-4} \dot{m} m^{-1} r^{-1/2} \sin^2\theta \text{ g cm}^{-3} \tag{1.66}$$

$$\tau_s \sim R\kappa_s\rho = 19\dot{m} r^{1/2} \tag{1.67}$$

Normalizing ρ to an accretion rate presents an obvious challenge in that $\dot{M}(\rho) = 0$ in the CDAF model (note the absence of an α viscosity). However, the accretion rate $\dot{M} = -4\pi R^2 \rho v^r$ may be estimated (Quataert and Gruzinov 2000) by studying the solution where self-similarity is violated; that is, at the ISCO, $v^r \sim -c_s$. $\dot{m}$ and m then specify the solution (although $v^r(r)$ is probably overestimated).

At low accretion rates, these solutions are Coulomb collisionless (i.e. $t_{\text{Coulomb}} \gg t_{\text{inflow}}$; Mahadevan & Quataert 1997 for ADAFs). A leading view is that the ions are probably not thermal, but exhibit a bounded degree of pressure anisotropy (the ratio of pressures perpendicular and parallel to the magnetic field $P_\perp/P_\parallel$) due to kinetic instabilities. For $P_\perp - P_\parallel < -B^2$, the plasma is susceptible to the firehose instability (e.g. Matteini et al. 2006), whereas for $P_\perp - P_\parallel > (B^2/2)(P_\parallel/P_\perp)$ the plasma is susceptible to the mirror instability (Chandrasekhar et al. 1958, Parker 1958). Kinetic simulations suggest that in shearing magnetic fields, the plasma tends to assume a configuration marginally stable to these instabilities (Kunz et al. 2014, Riquelme et

[16]However, see Balbus & Hawley 2002 for several criticisms of the CDAF.

al. 2015). This persists in a more realistic local simulation of kinetic magnetorotationally-driven turbulence (Kunz et al. 2016), with ions favoring the threshold for mirror instability and adopting a κ distribution (e.g. Livadiotis & McComas 2013). This pressure anisotropy, although it should produce an $r-\phi$ stress in Keplerian accretion disks, does not appear to significantly alter flow statistics in numerical simulations (Foucart et al. 2017).

The electrons may similarly adopt a pressure-anisotropic κ distribution. However, kinetic dissipation (i.e. wave-particle interactions) may heat protons and electrons differently as a function of local plasma properties (Quataert & Gruzinov 1999). The basic picture is that protons act like a high-pass filter on electromagnetic waves cascading to smaller scales, and increasing the plasma magnetization will increase the fraction of waves at high enough frequencies such that the ions are transparent to them. However, the electron larmor radius is the smallest length scale, and electrons will sap energy from all waves ignored by ions. Consequently, for $\beta \gg 1$ most of the heat is dissipated into ions, and vice versa (e.g. Howes 2010, for which the critical β below which electrons are preferentially heated is ~ 2.5).

Radiation governs the thermodynamics of thin disks, whereas it plays no role at all in RIAFs. A first question to ask, in pursuit of a smooth intermediate regime between these two extremes, is where and when radiative losses become significant to the inner region of RIAFs. Here we evaluate cooling times due to synchrotron emission (t_s; Equation 1.12 for $\Theta_e \gg 1$ integrated over frequency) and Compton upscattering t_c[17] for RIAF and CDAF models, along with Compton y. For the ADAF, $t_s/t_{\rm inflow} \sim \dot{m}^{-1} r$, $t_c/t_{\rm inflow} \sim \dot{m}^{-2} r^{3/2}$, and $y \sim \dot{m} r^{-5/2}$. For the CDAF, $t_s/t_{\rm inflow} \sim \dot{m}^{-1} r^{-1}$, $t_c/t_{\rm inflow} \sim \dot{m}^{-2} r^{1/2}$, and $y \sim \dot{m} r^{-3/2}$. Note especially the qualitative difference; ADAFs first cool off at small r, whereas CDAFs first cool off at large r. The relative contributions of Compton upscattering are also different between models. Evidently an accurate model for the accretion flow is important to accurately modeling such intermediate accretion flows. This is a powerful motivation for including radiation in numerical MHD models.

Note that at somewhat higher accretion rates, $\dot{m} \gtrsim 1$, optical depths become large enough that photon trapping is non-negligible, and energy is again advected radially. The disk then becomes a geometrically slim, marginally radiatively inefficient flow (or a slim disk; Abramowicz et al. 1988), similar to the hot accretion flows just discussed.

1.2.5 Outflows

Accretion in the disk midplane does not prohibit vertical outflows. Such outflows may be particularly important in active galactic nuclei, as they may affect galaxy evolution on cosmological timescales (see

[17]For the luminosity of Compton scattering at a given radius, we take $L_{\rm C}(r) = y L_{\rm s}(r)$, where $L_{\rm s}(r)$ is the synchrotron luminosity inside r, i.e. we are assuming a lightbulb model for synchrotron emission and only single upscatterings.

Kormendy & Ho 2013 for a review). Outflows from black hole accretion disks are generally divided into two categories: jets and disk winds.

Black hole jets, as commonly understood, are the result of dipolar fields threading the black hole tapping the rotational energy of the black hole in the ergoregion (Blandford & Znajek 1977). This process can be powerful; for a dipolar magnetic field aligned with the black hole spin axis and $a_\star \lesssim 0.95$, the fourth-order expansion of the Blandford-Znajek power is (Tchekhovskoy et al. 2012)

$$P_{\rm BZ} = \frac{\kappa}{4\pi c}\Phi^2\Omega_H^2\left(1 + 1.38\left(\frac{\Omega_{\rm H}R_g}{c}\right)^2 - 9.2\left(\frac{\Omega_{\rm H}R_g}{c}\right)^4\right) \tag{1.68}$$

where $\kappa \sim 0.05$ depends on the detailed geometry of the magnetic field, Φ is the magnetic flux through the event horizon, and $\Omega_{\rm H} = a_\star c/(2R_g(1+\sqrt{1-a_\star^2}))$ is the angular frequency of the black hole. This power taps a potentially large energy reserve; the free energy in spin is (e.g. Misner et al. 1973, McKinney & Gammie 2004)

$$E_{\rm spin} = 5.3\times10^{61}\left(\frac{M}{10^8 M_\odot}\right)\ {\rm erg}. \tag{1.69}$$

This process is also efficient in units of accreted rest mass energy. Φ is necessarily related to $\dot{M}$, both through its effect on the strength of magnetorotationally driven turbulence and the suppression of the MRI by strong vertical fields (additionally, a supervirial magnetic field would unbind the accretion disk). McKinney & Gammie 2004 found, for a particular Φ, a %-level jet efficiency (electromagnetic energy flux out of the event horizon over mass accretion flux into the event horizon) of $\epsilon = 0.068(2-(1+\sqrt{1-a_\star^2}))$. Tchekhovskoy et al. (2011) subsequently identified a Φ for which $\epsilon > 100\%$ (the magnetically arrested disk). Tchekhovskoy et al. (2012) studied maximum $\phi = \Phi/\sqrt{\dot{M}R_g^2 c}$ as a function of spin (typically, $\phi \sim 50$).

There is also free energy available from the rotation of the gas disk itself. Blandford & Payne (1982) showed that vertical magnetic fields through a thin accretion disk can lead to an outflow of matter, as well as a vertical flux of angular momentum, driving accretion. Whether similar results apply in hot, geometrically thick disks is an open question; the gas internal energy in ADAFs is such that the material is or nearly is unbound (e.g. Narayan & Yi 1995). Blandford & Begelman (1999) proposed an extension to the ADAF model in which the torque due to the α viscosity drives outflows when transporting liberated binding energy to larger radii.

1.3 Observed Accretion Disks Around Black Holes

We now return to observational results, with a stronger emphasis on the electromagnetic signatures of accretion disks. We emphasize the evidence for accretion flows at intermediate $\dot{m}$ such that they are not cleanly described by either RIAFs or thin disks. Some special attention is also paid to Sagittarius A* and M87, the principal sources for the Event Horizon Telescope.

1.3.1 Stellar-Mass Black Holes

Our galaxy probably contains many millions of stellar-mass black holes (e.g. Brown & Bethe 1994). However, these are generally only detectable if they are accreting rapidly, and this situation requires a close binary with a normal star; the interstellar medium is too tenuous to support observable accretion. However, for the purposes of studying accretion disks, only the rapidly accreting systems (X-ray binaries, or XRBs) are interesting to us.

XRBs may receive matter either through stellar winds or Roche lobe overflows; the former are termed high-mass XRBs, and the latter low-mass XRBs, because high-mass stars produce much stronger winds. This may lead to qualitative differences in the accretion flow structure onto the black hole; at least for Roche lobe overflow, accretion streams may drive spiral shocks throughout the accretion disk (Ju et al. 2016) that in some cases may provide angular momentum transport comparable to MRI-driven turbulence (Ju et al. 2017).

There are about 20 known stellar mass black holes (Remillard & McClintock 2006; their reported systems are reproduced in Table 1.1). XRBs perhaps differ most from accreting SMBHs in that they show dramatic variability. T_g is a factor $\sim 10^5 - 10^9$ shorter in XRBs, and one academic career encompasses many viscous times of an XRB disk. The crown jewel of this variability is the state transition, a persistent mystery in accretion disk theory. Most systems trace out a similar path in X-ray hardness-intensity space (e.g. Fender et al. 2004) exhibiting marked hysteresis, which may be related to disk magnetization (e.g. Begelman & Armitage 2014).

McClintock & Remillard (2006) divide observed XRB states in five. In order of increasing mass accretion rate, these five states are (1) quiescent; very low luminosity dominated by power-law emission, in which most XRBs spend most of their lives, and which are well fit by ADAF models (2) low/hard; more luminous than the quiescent state but still faint, and highly variable (3) intermediate; the catch-all for combinations of properties of low/hard and high/soft states (4) high/soft; thermal emission with only %-level variability (5) very high; near-Eddington X-ray luminosities with a power-law index steeper than in the hard state.

The intermediate state is a particular challenge; not only is it difficult to cleanly relate such states

between sources, but it is not a clean match for existing analytic models. Méndez & van der Klis (1997) captured GX 339-4 in such an intermediate state, with luminosity squarely between low/hard and high/soft states and spectra with both "hard" and "soft" features. Esin et al. (1997) argue that such intermediate states may be due to a truncated disk, where only the innermost region of the flow is radiatively inefficient. It is likely that radiative cooling acting globally is important to the intermediate disk.

1.3.2 Supermassive Black Holes

The rich phenomenology of AGN has led to the development of many observational classes; Rees (1978) wrote, "Indeed the catalogues contain a whole zoo of objects with a confusing array of names." Happily, theory and observation have gradually been converging. Urry & Padovani (1995) argued that observer angle with respect to the black hole spin axis is largely responsible for spectral differences in AGN, by showing that it was consistent with expected population statistics. Additionally, the accretion rate in Eddington units is believed to further account for many remaining differences (Shen & Ho 2014). Consistent with earlier evidence that most normal galaxies host a supermassive black hole, about half of nearby galaxies have detectable evidence of AGN in emission lines (Ho et al. 1997).

In broad strokes, AGN are either quasars/Seyfert galaxies or Low-luminosity Active Galactic Nuclei (LLAGN). The former are much more abundant at higher redshift; presumably, galaxy evolution feeds mass into AGN at higher rates when $z > 0$. These systems are extremely (near-Eddington) luminous, with near thermal spectra and broad emission lines. LLAGN (e.g. Ho 2008), on the other hand, are a significant fraction of AGN in the local universe and have radiative efficiencies much below thin disk values (Ho 2009). Seyferts and LLAGN are often distinguished by line intensity ratio plots (Veilleux & Osterbrock 1987).

Two LLAGN of particular interest are Sagittarius A* and M87, the two event horizons resolvable on the sky with earth-scale mm interferometry. Not only do decades of observations exist for both these sources, but the Event Horizon Telescope (EHT; e.g. Wagner et al. 2015) will soon image these accretion flows on horizon scales. The EHT is a yearly campaign of about seven 230 GHz radio telescopes scattered around the world. The diffration-limited resolution for this system is

$$\theta \approx 1.22\frac{\lambda}{D} \approx 25\left(\frac{\lambda}{1.3\text{ mm}}\right)\left(\frac{D}{12742\text{ km}}\right)^{-1}\ \mu\text{as} \tag{1.70}$$

As the earth rotates these telescopes map out the UV plane of the source. The time to take an image is ~ 1 day, and the result is event horizon-scale resolution near the synchrotron frequency for these sources.

1.3.3 Sagittarius A*

The Milky Way's Sagittarius A* (Sgr A*) has a mass $M/M_\odot \sim 4.6 \times 10^6$ and is one of the slowest accreting ($\dot{m} \sim 10^{-8}$, e.g. Marrone et al. 2006) SMBHs known. As such, it is an excellent laboratory to study hot accretion physics in the absence of radiative cooling (which may be safely neglected, e.g. Dibi et al. 2012). As discussed previously, our proximity to Sgr A* allows a unique opportunity to resolve the dynamics of individual stars around this supermassive black hole, and so we have an especially clear understanding of both the black hole mass and the environment on Bondi radius scales.

Sgr A* displays intrinsic variability. In particular, it shows approximately one X-ray flare per day, each lasting $\sim 10^2 - 10^4$ seconds with intensities distributed as a power law, $dN/dL \sim L^{-1.9}$ (Neilsen et al. 2013). All such X-ray flares appear to have a NIR counterpart, although not all NIR variability is correlated with X-ray activity (Morris et al. 2012 for a review). There is currently not clear evidence for radio counterparts to X-ray flares (Capellupo et al. 2017).

Fish et al. (2011), using VLBI, found near-horizon variability in Sgr A*, a powerful motivation for relativistic time-dependent modeling. Note, however, that this variability occurred with a timescale of order the EHT imaging timescale. This exposes a difficulty with using the EHT to study Sgr A*; the light crossing time for the event horizon of Sgr A* is short compared to a day. In addition, Sgr A* suffers from an electron scattering screen between it and us (Bower et al. 2006) that blurs images on EHT scales.

1.3.4 M87

M87, however, has a mass $M/M_\odot \sim 3.3 - 6.2 \times 10^9$ (Gebhardt et al. 2011, Walsh et al. 2013). M87 is a prototypical LLAGN, 16.7 Mpc away at the center of the Virgo cluster. This system was one of the first detected relativistic jets, and yielded the first dynamical measurement of a SMBH (Sargent et al. 1978). M87 is also a nearly face-on source (observer angle $\lesssim 25\,\mathrm{deg}$, e.g. Heinz & Begelman 1997). The much longer T_g and lack of significant interstellar scattering relative to Sgr A* make M87 a valuable alternative source for EHT observations, even if its event horizon may be slightly smaller on the sky. Doeleman et al. 2012 already placed constraints on the source size with VLBI, suggesting a compact jet launching region.

M87 exhibits a quasi-flat spectrum across almost ten decades in frequency, in contrast to the steep Compton bumps common to RIAF models (e.g. Mościbrodzka et al. 2009). Variability decreases towards longer wavelengths; the mm peak is hardly variable at all (Prieto et al. 2016). M87 also shows rapid (~ 1 day $\sim$ few T_g) TeV variability (e.g. Aharonian et al. 2006).

Flux from M87 contains polarization information; Kuo et al. (2014) recently detected %-level linear polarization and a rotation measure $\mathrm{RM} \in [-7.5 \times 10^5, 3.4 \times 10^5]$ rad m^{-2}. Together with a simplified

accretion disk model, this implies an accretion rate about two orders of magnitude below the accretion rate at the Bondi radius, and is a useful constraint for disk models. We will return to M87 in detail in a later chapter.

1.4 Numerical Models of Hot Accretion Disks, or GRMHD

Analytic models have proven to be powerful tools for understanding accretion onto black holes. But real accretion disks are fundamentally time-dependent, with turbulent eddies on scales $\sim H$. Especially when $H \sim R$ in RIAFs, with long-range correlations potentially introduced by magnetic fields, and with general relativity, a global self-consistent model is called for. Prior to global numerical calculations, Pringle (1981) lamented that, due to the parameterization of α, "The main failing of accretion disk theory is that it has no predictive power except in certain limiting circumstances." Here we outline the successes of numerical modeling of hot relativistic accretion flows; see Yuan & Narayan (2014) for a review.

Early global modeling employed viscous hydrodynamics in a pseudo-Newtonian potential[18] (e.g. Igumenshchev & Abramowicz 1999, McKinney & Gammie 2002; the latter authors also note that the absence of an event horizon makes the numerical solution very sensitive to the position of the inner boundary). General relativistic magnetohydrodynamic, or GRMHD, methods were subsequently introduced (Koide et al. 1999, De Villiers & Hawley 2003a, Gammie et al. 2003), and have become a standard tool for modeling RIAFs.

GRMHD simulations usually agree on some generic disk properties. The torus is largely axisymmetric (although see e.g. Fragile et al. 2007 for the effects of non-axisymmetric disk tilts). This, together with finite computational resources, has motivated global albeit axisymmetric simulations. This procedure is not without issues, however. In the absence of net magnetic fields, which will be perenially susceptible to the MRI, the anti-dynamo theorem requires that the plasma magnetization decay with time. Additionally, turbulence in 2D is qualitatively different than in 3D; in 2D vortices are stable, and power cascades towards larger scales. However, there is still a profitable analogy to be made to axisymmetric magnetized shear flows (Guan & Gammie 2008). Subgrid models for a magnetic dynamo have also been introduced (Sądowski et al. 2015a), although the degree of disagreement relative to 3D flows is not completely clear. 3D GRMHD simulations (e.g. Shiokawa et al. 2012, Narayan et al. 2012) remain the gold standard.

However, 3D simulations are expensive, particularly because the viscous time $t_{\rm viscous} \sim r^{3/2}$; at large radii, the time to achieve inflow equilibrium is many light crossing times for the black hole. With current computational resources, simulations cover only a dynamic range of at most a factor ~ 100 in radius (e.g.

[18] Usually the Pacynski-Wiita potential (Paczyński & Wiita 1980), which impersonates the Schwarzschild geometry remarkably well; in particular, it has an innermost stable circular orbit at $6R_g$!

Narayan et al. 2012). This makes certain questions, such as the scaling of density with radius, challenging to answer because the gas is only in equilibrium near the black hole where the effects of the ISCO and black hole are felt most strongly. One also wishes to remove effects due to the finite extent of the disk and outer radial boundary. As a result, the surface density profile of RIAFs is still something of an open question.

GRMHD simulations without cooling produce thick disks; $H/R \lesssim 1$, and roughly constant with radius. $H/R \sim 0.3$ is typical (e.g. Shiokawa et al. 2012), but see Penna et al. (2013) for discussion of a possible dependence on the Bernoulli parameter of the initial conditions. These disks (e.g. McKinney & Gammie 2004) are generally gas pressure-dominated in the midplane, surrounded by a more strongly magnetized (plasma $\beta \sim 1$) corona, and a magnetically dominated funnel region ($b^2/\rho > 1$). In magnetically arrested disks, however (e.g. Tchekhovskoy et al. 2011, McKinney et al. 2012), the disk is much more strongly magnetized everywhere, orbital angular velocities are less, and the funnel region is larger (see also Narayan et al. 2012 for a direct comparison).

1.5 Radiative Post-Processing of GRMHD Simulations

GRMHD simulations provide the statistics of the fluid only; they do not describe observable radiation. For radiatively inefficient flows, this may be evaluated by post-processing the fluid data. Generally, this is done either through relativistic raytracing to a pinhole camera[19] (e.g. Noble et al. 2007, Vincent et al. 2011, Chan et al. 2013, Dexter 2016, Mościbrodzka & Gammie 2018) or calculating the specific intensity globally with Monte Carlo or characteristics methods (e.g. Dolence et al. 2009, Schnittman & Krolik 2013, Narayan et al. 2016).

These methods have been widely used to interpret very low accretion rate black holes, particularly Sagittarius A*[20] (Mościbrodzka et al. 2009, Dexter et al. 2010, Dolence et al. 2012, Shcherbakov et al. 2012, Mościbrodzka et al. 2014, Chan et al. 2015, Ressler et al. 2017). They allow for direct comparison to VLBI imaging, polarimetric measurements, observed fluxes, and variability information. Additionally, these methods can confirm expectations for the emission structure, such as most X-ray emission from Compton upscattering being produced near the black hole (e.g. Mościbrodzka et al. 2009).

[19] Scattering is generally neglected in such methods, although they often employ *polarized* transport.
[20] Due to both the EHT and negligible radiative cooling.

1.6 GRRMHD Accretion Disk Simulations

For most accretion disks, radiative cooling plays at least a perturbative role. Recently, much effort has been spent extending the successes of GRMHD modeling into these higher accretion rates through general relativistic radiation MHD[21], or GRRMHD. This work, with the goal of identifying thermal equilibrium states at all $\dot{m}$, is largely divided into two different approaches: proceeding downwards in $\dot{m}$ from super-Eddington rates, and proceeding upwards in $\dot{m}$ from highly sub-Eddington (aka nonradiative GRMHD) rates. A classic early study of radiating MHD accretion disks (Ohsuga et al. 2009), however, more holistically showed that the same model can produce RIAF, thin disk, and slim disk torii just by varying accretion rate.

At very high accretion rates, optical depths are large; radiation is transported diffusively, and is nearly thermal. Consequently, one may to good approximation evolve frequency-integrated moment closures rather than the frequency-dependent radiative transfer equation. Typically this moment closure is either flux-limited diffusion (or the relativistic generalization; Farris et al. 2008) or the M1 closure (Levermore 1984). While M1 conserves radiation momentum as well as radiation energy, it assumes there is a frame in which the radiation is isotropic: the radiation is self-interacting, and impinging beams of radiation will collide unphysically.

Relativistic M1 methods (McKinney et al. 2014, Fragile et al. 2014, Sądowski et al. 2014) have generally found consistency with the slim disk picture: large optical depths, $H \lesssim R$, and radiative efficiencies lower than nominal thin disk values[22]. McKinney et al. (2015) subsequently studied super-Eddington MAD accretion and found total efficiencies significantly exceeding thin disk values. Radiation pressure may also drive outflows in super-Eddington systems (Sądowski & Narayan 2015b). Jiang et al. (2014a) introduced a method for solving the gray, time-dependent transfer equation to order v/c and subsequently applied this scheme to super-Eddington disks (Jiang et al. 2014b Jiang et al. 2017).

At low accretion rates, however, optical depths are much lower ($\tau_s \ll 1$). The radiation may no longer *a priori* be assumed to be thermal or diffusive. In particular, Compton scattering globally couples the flow through the radiative transfer equation. Some work has directly applied gray moment closures to very sub-Eddington systems (Sądowski et al. 2017, Sądowski & Gaspari 2017). This thesis is primarily concerned with the development and application of a full transport GRRMHD method, `bhlight`.

[21] Other work has examined radiative cooling in simulations via local cooling functions (e.g. Fragile & Meier 2009, Dibi et al. 2012, Wu et al. 2016), but we do not review that avenue of investigation here.

[22] Total efficiencies can be similar to those in nonradiative GRMHD simulations, as one would expect for $\dot{m} \to \infty$.

Chapter 2

Resolution Dependence of Magnetorotational Turbulence in the Isothermal Stratified Shearing Box

2.1 Summary

Magnetohydrodynamic (MHD) turbulence driven by the magnetorotational instability can provide diffusive transport of angular momentum in astrophysical disks, and a widely studied computational model for this process is the ideal, stratified, isothermal shearing box. Here we report results of a convergence study of such boxes up to a resolution of $N = 256$ zones per scale height, performed on `blue waters` at NCSA with `ramses-gpu`. We find that the time and vertically integrated dimensionless shear stress $\overline{\alpha} \sim N^{-1/3}$, i.e. the shear stress is resolution dependent. We also find that the magnetic field correlation length decreases with resolution, $\lambda \sim N^{-1/2}$. This variation is strongest at the disk midplane. We show that our measurements of $\overline{\alpha}$ are consistent with earlier studies. We discuss possible reasons for the lack of convergence[1].

2.2 Introduction

Astrophysical disks form in galaxies and around black holes, neutron stars, white dwarfs, main sequence stars, and planets because the angular momentum of the parent plasma is approximately conserved while kinetic energy in noncircular or non-coplanar motion is easily dissipated and radiated away. Disk evolution is therefore governed by angular momentum transport, which can take the form of external torques (e.g. from magnetized winds) or internal transport.

Diffusive internal transport of angular momentum has been fruitfully described with the phenomenological anomalous viscosity, or α, model (Shakura & Sunyaev 1973; Lynden-Bell & Pringle 1974), which attributes transport to localized turbulence. No general driver of turbulence in non-self-gravitating Keplerian disks was known until the discovery by Balbus & Hawley (1991) of the magnetorotational instability (MRI), a local, linear instability of weakly magnetized disks. Subsequent nonlinear numerical studies convincingly demonstrated that the MRI leads to turbulence and outward angular momentum transport (see the

[1]This work appeared in publication as Ryan et al. (2017a).

review of Balbus & Hawley, 1998). Later work has uncovered purely hydrodynamical instabilities including the zombie vortex (Marcus et al. 2015, but see Lesur & Latter 2016), the vertical shear instability (Urpin 2003, Nelson et al. 2013), the baroclinic instability (Klahr & Bodenheimer, 2003; Petersen et al., 2007a,b; Lesur & Papaloizou, 2010), and convective overstability (Klahr & Hubbard 2014). Nonetheless, MRI-driven turbulence remains the leading candidate for driving disk evolution in many astrophysical settings.

Our paper probes numerical convergence of MHD turbulence in a particular disk model. By convergence, we mean resolution and dissipation-scale independence in average quantities like the angular momentum flux. We begin by reviewing the various classes of numerical models used to study MHD turbulence in disks, and describing the claims of convergence or nonconvergence made for each class.

Numerical simulations of disk turbulence can be divided into local and global models. In a *local model* (or shearing box; Goldreich & Lynden-Bell 1965, Hawley et al. 1995), the equations of motion are expanded to lowest order in the ratio of the scale height H to the local radius r in a co-orbiting Keplerian frame. Differential rotation manifests as a linear shear flow. The shearing box boundary conditions then make it possible to model the disk in a shear-periodic, rectangular box. The local model is highly symmetric and cannot, for example, distinguish between the inward and outward directions (it is symmetric under a rotation by π around the z axis). In a *global model*, by contrast, one simulates some radial range within a disk without requiring $H \ll r$. Global models do not have the inward-outward symmetry of the local model.

The vertical (z) component of gravitational acceleration in the local model is $-\Omega^2 z$, where $\Omega \equiv$ orbital frequency. *Unstratified* local models turn off the vertical component of gravity, begin with a uniform vertical density profile, and typically use periodic vertical boundary conditions. *Stratified* local models turn on the vertical component of gravity, begin with a z-dependent vertical density profile, and use a variety of vertical boundary conditions.

For most boundary conditions, local simulations conserve one or more components of the mean magnetic field. For example, unstratified local models with periodic vertical boundary conditions conserve the mean vertical and toroidal field if the mean radial field vanishes.[2] Numerical investigations show that the mean field can have a profound effect on the saturated turbulent state, so we need to distinguish between *zero mean field* models, where all the currents that sustain the field are contained within the simulation volume and can therefore decay, and *mean field* models, where one or more components of the field is fixed by the boundary conditions and cannot decay.

Turbulence leads to dissipation. In *explicit dissipation* models (or *direct numerical simulations*) dissipation is incorporated directly in the model, for example by a scalar viscosity ν and resistivity η that are

[2] A nonvanishing mean radial field is conserved, but it causes the toroidal field to vary linearly in time. See Hawley et al. (1995).

dimensionlessly parameterized by the Reynolds numbers and their ratio, the magnetic Prandtl number:

$$Re \equiv \frac{c_s H}{\nu} \qquad Re_M \equiv \frac{c_s H}{\eta} \qquad Pr_M \equiv \frac{\nu}{\eta}. \tag{2.1}$$

In *implicit large eddy simulation* (ILES) models there is no explicit dissipation, and dissipation is provided by the numerical scheme through truncation error at the grid scale. Notice that for ILES models run with a conservative scheme, lost kinetic and magnetic energy is entirely captured as plasma thermal energy. In this sense reconnection can be "included" in an ILES model, although the reconnection rate and dynamics may be incorrect.

The consequences of using ILES to study high Reynolds number hydrodynamic turbulence are fairly well understood (e.g. Sagaut 2006): if there is sufficient dynamic range (large enough zone number) then the character of dissipation at small scales has little influence on turbulent structures at large scales. It is large-scale structures that often determine the flow properties of greatest astrophysical interest, such as turbulent momentum flux. The consequences of using ILES to study high Reynolds numbers magnetohydrodynamic (MHD) turbulence are less well understood (Miesch et al. 2015). It is fair to say that many disk simulators (including us) have frequently *assumed* that with enough dynamic range MHD ILES would converge to the astrophysically relevant high Reynolds numbers result (but see Lesur & Longaretti 2007, Fromang et al. 2007, Longaretti & Lesur 2010, Meheut et al. 2015, Walker et al. 2016).

Finally, disk simulations can be subdivided according to their treatment of heating and cooling of the plasma. Direct simulation of the interaction of radiation with matter has, until recently, been expensive in comparison to available computational resources. Most disk simulations have therefore used simplified treatments of plasma thermodynamics, with phenomenological cooling and heating, or assumed an isothermal equation of state with pressure $P = \rho c_s^2$, and c_s constant in time and space. Isothermal models are relevant to disks heated by external illumination, such as disks around compact objects at many gravitational radii, where the thermal timescale can be short compared to the dynamical timescale.

Local models also depend on the box dimensions which are purely numerical parameters. Changes in box sizes are known to produce qualitative changes in shearing box models (e.g. Simon et al. 2012, Ross et al. 2016, Shi et al. 2016). Even the largest domains find correlations on the scale of the box, at least in the corona (Guan & Gammie 2011). Two related questions emerge. Does the shearing box model converge as the box sizes goes to infinity? Does shearing box evolution match global behavior as the box size goes to infinity? These questions are challenging to answer numerically.

Much is now understood about convergence of the gross, time-averaged properties of MRI-driven tur-

bulence (e.g. α) in every corner of the five dimensional disk model parameter space: local/global, stratified/unstratified, mean/zero net field, ILES/explicit dissipation, isothermal/nonisothermal. A summary of previous calculations emphasizing convergence is given in Table 2.1.

Geometry	Stratified	Net Flux	Dissipation	Isothermal	Convergent	Maximum Resolution	References
local	no	zero	ILES	yes	no	$256/H$	(1) (2) (3) (4)
local	no	zero	explicit	yes	yes	$512/H$	(5)
local	no	mean	ILES	yes	yes	$256/H$	(6) (2) (3)
local	no	mean	explicit	yes	yes	$800/H$	(7)
local	no	mean	ILES	no	yes	$64/H$	(8)
local	yes	zero	ILES	yes	this work	$256/H$	(9) (10) (11)
local	yes	zero	ILES	no	unclear	$64/H$	(12) (13)
local	yes	zero	explicit	yes	unclear	$128/H$	(14) (15)
local	yes	mean	ILES	yes	unclear	$48/H$	(16) (17)
local	yes	zero	ILES	no	unclear	$64/H$	(18) (19)
global	no	zero	ILES	yes	unclear	$480 \times 1920 \times 128$	(20)
global	yes	zero	ILES	no	unclear	$768 \times 256 \times 256$	(21) (22) (23)
global	yes	mean	ILES	no	unclear	$288 \times 128 \times 128$	(24) (25) (26)

Table 2.1: For convergence (stress with respect to dissipative scale), *no* and *yes* indicate clear, consistent, persuasive findings in the literature. This table is incomplete: it focuses on studies that consider convergence, and omits some combinations of parameters. A global unstratified simulation has cylindrical geometry and neglects vertical gravity. $H \equiv c_s/\Omega$. (1) Fromang et al. (2007); (2) Simon et al. (2009); (3) Guan et al. (2009); (4) Bodo et al. (2011); (5) Fromang (2010); (6) Hawley et al. (1995); (7) Meheut et al. (2015); (8) Jiang et al. (2013a); (9) Davis et al. (2010); (10) Bodo et al. (2014); (11) Nauman & Blackman (2014); (12) Shi et al. (2010); (13) Bodo et al. (2015) (14) Simon et al. (2011); (15) Oishi & Mac Low (2011) (16) Bai & Stone (2013); (17) Fromang et al. (2013); (18) Jiang et al. (2013b); (19) Bodo et al. (2015); (20) Sorathia et al. (2012); (21) Shiokawa et al. (2012); (22) Hawley et al. (2013); (23) Parkin & Bicknell (2013); (24) Tchekhovskoy et al. (2011); (25) McKinney et al. (2012); (26) Beckwith et al. (2009)

Zero net field, local, unstratified, isothermal, ILES models are particularly interesting: Fromang et al. (2007) showed that these models are nonconvergent (see also Pessah et al. 2007), and this has been independently confirmed (Simon et al. 2009, Guan et al. 2009). With N the number of resolution elements along one axis, with zone aspect ratios fixed, nonconvergence appears as $\alpha \propto N^{-1}$ (but see Bodo et al. 2011) and magnetic correlation length $\lambda \propto N^{-1}$ (i.e. correlation length is proportional to zone size). But this is not the full story: Shi et al. (2016) have recently found convergence if the vertical extent of the model is large compared to the radial extent. In this case MHD turbulence excites waves that travel vertically, and this may be connected to the butterfly oscillations seen in stratified models. However, the connection between these tall boxes and traditional unstratified (and stratified) shearing boxes is still uncertain, and we consider it premature to change the relevant conclusion for convergence in Table 2.1.

Unstratified models converge, however, if either explicit dissipation (Fromang 2010, but see Bodo et al.

2011) or a mean magnetic field (Simon et al. 2009, Guan et al. 2009) are added. When a mean field is added α increases proportional to the mean field strength (Hawley et al. 1995, Salvesen et al. 2016).

What about stratified models? One might think that stratification would lead to magnetically driven convection which could organize the field on the scale of the convective eddies, leading to convergence. But the numerical evidence for convergence of zero net field, local, stratified, isothermal ILES models is contradictory. The work of Davis et al. (2010), using the `athena` code, is consistent with convergence, while the work of Bodo et al. (2014), using the `pluto` code, shows a sharp drop in Maxwell stress at the highest accessible resolution of $200/\sqrt{2} \simeq 141$ zones per scale height. The question of convergence for stratified, isothermal ILES models is particularly pressing because they are sometimes used to interpret observations in both local (e.g. Simon et al. 2015) and global (e.g. Mościbrodzka et al. 2009, Flock et al. 2015) forms.

This paper therefore returns to study the convergence of zero net field, local, stratified, isothermal ILES models at high resolutions made newly accessible by the combination of NCSA's `blue waters` machine and the `ramses-gpu` code. In Section 2 we present the physical model and numerical method. Section 3 contains the results of our calculations. Section 4 discusses the implications of our results and future directions. Section 5 concludes.

2.3 Model

2.3.1 Governing Equations

The local model expands the equations of motion to lowest nontrivial order around a Keplerian orbit at $R = R_0, \phi = \phi_0 + \Omega t, z = 0$ and defines the local Cartesian coordinates

$$(x, y, z) = (R - R_0, R_0 (\phi - \Omega t - \phi_0), z) . \tag{2.2}$$

In the local model for a Keplerian disk the equations of ideal MHD, with an isothermal equation of state ($P = \rho c_s^2$; $P \equiv$ pressure, $\rho \equiv$ density, $c_s \equiv$ sound speed, which is assumed constant), are

$$\frac{\partial \rho}{\partial t} = -\nabla \cdot (\rho \boldsymbol{v}) , \tag{2.3}$$

$$\frac{\partial \rho \boldsymbol{v}}{\partial t} = -\nabla \cdot (\rho \boldsymbol{v}\boldsymbol{v}) + (\boldsymbol{B} \cdot \nabla) \boldsymbol{B} - \nabla \left(\frac{\boldsymbol{B} \cdot \boldsymbol{B}}{2} + P \right) - 2 \rho \Omega \hat{\boldsymbol{e}}_z \times \boldsymbol{v} + \rho \nabla \left(-\frac{3}{2} \Omega^2 x^2 + \frac{1}{2} \Omega^2 z^2 \right) , \tag{2.4}$$

$$\frac{\partial \boldsymbol{B}}{\partial t} = \nabla \times (\boldsymbol{v} \times \boldsymbol{B}) , \tag{2.5}$$

where $\boldsymbol{v} \equiv$ velocity in the local frame and $\boldsymbol{B} \equiv$ magnetic field, subject to the constraint

$$\nabla \cdot \boldsymbol{B} = 0. \tag{2.6}$$

Equation (2.4) includes Coriolis and tidal forces. Notice that there is no explicit dissipation (resistivity or viscosity) and that R_0 does not appear in the governing equations.

For $\boldsymbol{B} = 0$ these equations admit the equilibrium

$$\rho = \rho_0 \exp\left(-\frac{z^2}{2H^2}\right), \tag{2.7}$$

$$\boldsymbol{v} = -\frac{3}{2} x \Omega \hat{\boldsymbol{e}}_y. \tag{2.8}$$

Here $H = c_s/\Omega$. Notice that others (e.g. Davis et al. 2010, Bodo et al. 2014) define the scale height as $\sqrt{2}c_s/\Omega$. This implies that their resolution should be multiplied by $1/\sqrt{2}$ for comparison with ours. The initial conditions for our model are the unmagnetized equilibrium (2.7)-(2.8), seeded with a uniform toroidal field at $|z| < 2H$; $\mathbf{B} = 0$ elsewhere. The initial plasma $\beta \equiv 2P/B^2 = 50$ at the midplane.

Hereafter we set

$$c_s = 1 \qquad \Omega = 1 \qquad \rho_0 = 1 \tag{2.9}$$

which together imply that $H = 1$ and the surface density $\Sigma = \sqrt{2\pi}$. The mass, length, and time units are thus $\rho_0 H^3$, H, and Ω^{-1}, respectively. Occasionally we reinsert these units for clarity.

For the x and y boundaries we use *shearing box boundary conditions* (see Hawley et al., 1995). With these boundary conditions the model is translation-invariant in the $x - y$ plane, and also invariant under rotations by π around the z axis. In addition, the vertical magnetic flux $\Phi_z \equiv \int dxdy B_z$ (integral taken over the entire $x - y$ domain at any z) is conserved. Our initial conditions have $\Phi_z = 0$, and our model extends over $-L_x/2 < x < L_x/2$, with $L_x = 3$, and over $-L_y/2 < y < L_y/2$, with $L_y = 4$.

At least three different z boundary conditions have been used for stratified shearing boxes. Beginning with Stone et al. (1996), many have used outflow boundary conditions. Davis et al. (2010) used periodic boundary conditions, which have the advantage that all three components of the mean magnetic field are conserved in exchange for altering the domain topology. Several authors (Brandenburg et al. 1995, Bodo et al. 2014) adopt impenetrable, stress-free boundaries that set $\partial v_x/\partial z = \partial v_y/\partial z = v_z = 0$ and $B_x = B_y = \partial B_z/\partial z = 0$ (or the equivalent conditions on the magnetic vector potential). The effect of boundary condition choice has not been systematically studied at modern resolution, although Stone et al. (1996) found that an artificial resistive layer at $2 < |z| < 3$ did not affect midplane dynamics significantly, and Oishi & Mac Low (2011)

demonstrate similar behavior in three runs that differ only by choice of vertical boundary conditions. For finite thermal diffusivity, Gressel (2013) find a significant change in energy transport between outflow and impenetrable vertical boundaries. For a discussion of the effects of very large vertical extents, see Suzuki et al. (2010).

We chose outflow boundary conditions and a large vertical extent to minimize the influence of the vertical boundaries on the body of the disk. Formally, outflow boundary conditions are $\partial \mathbf{B}/\partial z = 0$ and $\partial \mathbf{v}/\partial z = 0$, and $-(1/\rho)\partial(c_s^2\rho)/\partial z - \Omega^2 z = 0$, consistent with hydrostatic equilibrium. Our model extends over $-L_z/2 < z < L_z/2$ with $L_z = 12$.

Outflow boundary conditions imply that fluid mass in the computational domain is not conserved. The characteristic outflow timescale $\tau_{\rm out} \equiv \Sigma/\dot{\Sigma}$. Assuming sonic outflow at the boundaries, $\dot{\Sigma} \approx 2\rho(|z| = L_z/2)c_s$. Using the density profile fit from Guan & Gammie (2011) that takes account of magnetic support of the disk atmosphere, $\tau_{\rm out} \approx 6\times10^4\Omega^{-1}$. This is long compared to our integration times. Outflow boundary conditions also imply that the radial and toroidal magnetic flux are not conserved.

The domain size $(L_x, L_y, L_z) = (3, 4, 12)H$ may influence the turbulent state. Guan & Gammie (2011) and Simon et al. (2012) provide numerical evidence that angular momentum transport and variability may depend on structures large compared to H, but such large domains are currently inaccessible at our target resolution. Simon et al. (2012) demonstrate a transition to anomalous behavior as L_x goes from 2 to 0.5. The minimum L_x that avoids these pathologies is known to be less than $L_x = 3$; the results of Davis et al. (2010) suggest that this minimum is less than $L_x = \sqrt{2}$.

Finally, the integration time Δt should be long enough that average values for α and other quantities of interest can be measured with reasonable signal to noise. Our typical integration time is $\approx 300\Omega^{-1}$ (see the Appendix for a discussion of measurement errors).

2.3.2 Numerical Methods

We integrate the model with `ramses-gpu` (Fromang et al., 2006; Kestener et al., 2010, 2014), a modern astrophysical MHD code with support for GPU acceleration[3]. `ramses-gpu` is a second-order finite volume MUSCL scheme. Fluxes are evaluated with the HLLD approximate Riemann solver (Miyoshi & Kusano 2005). The constraint $\nabla \cdot \mathbf{B} = 0$ is preserved via constrained transport with face-centered magnetic fields (Evans & Hawley 1988).

Numerical resolution is characterized by

$$N = \frac{H}{\Delta x} \tag{2.10}$$

[3]Freely available: `http://www.maisondelasimulation.fr/projects/RAMSES-GPU/html/`

i.e. the number of zones per scale height in the radial direction. We take $\Delta x : \Delta y : \Delta z = 1 : 2 : 1$, so this is also the number of zones per scale height in the vertical direction, and twice the number of zones per scale height in the azimuthal direction. Hawley et al. (2011) showed that for MRI growth the azimuthal direction is typically better resolved than the vertical direction by a factor of a few in shearing boxes, as did Parkin & Bicknell (2013). Guan et al. (2009) showed that the autocorrelation function of the magnetic field in unstratified, isothermal shearing box models is anisotropic and approximately in the ratio $1 : 4 : 1$ in the radial, azimuthal, and vertical directions, suggesting that near the midplane the y direction is slightly better resolved than x and z in our model.

The mean azimuthal velocity $\overline{v}_y = -(3/2)\Omega x$. Truncation error depends on the velocity of the fluid with respect to the grid, and therefore if $\overline{v}_y$ is the dominant component of the velocity field the truncation error will vary systematically with x. This problem can be solved by using orbital advection (also known as "FARGO"; Masset 2000) for the MHD equations (Johnson et al. 2008, and references therein). We do not use orbital advection, but the shear velocity at the edge of our boxes is only $1.5c_s$, and we have checked that the Maxwell and Reynolds stresses do not vary significantly with x.

We start preliminary models from smooth initial conditions. These were seeded with white noise, with $\delta v_i \sim 0.01 c_s$ and $\delta\rho \sim 0.01\rho_0$ to excite a spectrum of unstable modes. We used late-time snapshots from these models to initialize our production models. Each run at resolution $2N$ was initialized with a snapshot from the final (or near-final) state of a model with resolution N using a divergence-free prolongation operator (Fromang et al., 2006). While this avoids running high resolution models through an initial transient phase (and allows our model to forget the initial net azimuthal magnetic flux), it does introduce a potential bias by coupling the initial state of one simulation to the final (or near-final) state of a lower resolution model.

Stratified shearing box models have high Alfvén speeds in the upper atmosphere ($v_A \sim \rho^{-1/2}$), which via the Courant condition can demand an impractically small timestep. This is a standard problem in numerical MHD, and can be solved by applying a density floor, or re-introducing a displacement current that limits the Alfvén speed to a maximum speed (Boris, 1970). In shearing box models, Miller & Stone (2000) used a version of the Boris fix with speed of light $v_{A,max} = (1, 4, 8)c_s$. Guan & Gammie (2011), by contrast, impose a density floor of $10^{-5}\rho_0$. We impose a density floor such that $v_A < v_{A,max} = 10c_s$. Our $v_{A,max}$ is higher than the expected v_A at $z = 6$ (as deduced from the fit to averaged stratified shearing box properties of Guan & Gammie 2011) but small enough to limit the integration to a practical timestep.

In characterizing the saturated state, we use the following averages: an average over volume

$$\langle f \rangle \equiv \frac{\int dxdydz\, f}{\int dxdydz}, \tag{2.11}$$

Label	N = Zones/H	$t_0(\Omega^{-1})$	$\Delta t(\Omega^{-1})$
`r32`	32	1800	300
`r64`	64	2100	300
`r128`	128	2400	300
`r256`	256	2648	288

Table 2.2: Model parameters.

Label	$\overline{\alpha}$	$\overline{\langle -B^x B^y \rangle}$	$\overline{\langle \rho v^x \delta v^y \rangle}$	$\Delta M/M_0$	$\sigma_\alpha/\overline{\alpha}$	$\lambda_{\rm minor}$	$\lambda_{\rm major}$	$\theta_{\rm tilt}$
`r32`	0.039	0.0061	0.0017	0.69%	0.24	0.12	0.61	16.0°
`r64`	0.034	0.0053	0.0015	0.65%	0.37	0.085	0.40	17.8°
`r128`	0.025	0.0039	0.0011	0.55%	0.26	0.060	0.27	18.6°
`r256`	0.019	0.0029	0.0008	0.40%	0.23	0.043	0.20	19.0°

Table 2.3: $\lambda_{\rm minor}$, $\lambda_{\rm major}$, and $\theta_{\rm tilt}$ are averaged over $|z| < 2H$.

an average over x and y

$$[f] \equiv \frac{\int dxdy\, f}{\int dxdy}, \tag{2.12}$$

and an average over time

$$\overline{f} \equiv \frac{\int dt\, f}{\int dt}. \tag{2.13}$$

The height-integrated Shakura-Sunyaev α parameter is

$$\alpha \equiv \frac{\langle \rho v^x \delta v^y - B^x B^y \rangle}{\langle P \rangle}. \tag{2.14}$$

This definition does not depend explicitly on box size. It is the average used in height-integrated disk evolution models (e.g. King et al. 2007) for comparison with observation.

2.4 Results

We consider four models, marching forward in linear resolution by factors of two from $N = 32$ to $N = 256$. Each model is started using late-time data from the preceding lower-resolution model. All share a common coordinate time t. The runs and their linear resolution, initial time t_0, and duration Δt are given in Table 2.3.2. We define t' for each run as $t - t_0$. Poloidal slices from all four resolutions are shown in Figure 2.1.

For $L_z = 12H$ about 0.5% of the disk mass is lost per $300\Omega^{-1}$ after accounting for mass added via the density floor (see Table 2.3.2; M_0 is the mass of the disk at the start of that run).

We now turn to the effects of resolution on one- and two-point statistics of the saturated state. Section 2.4.1 considers volume- and area-averaged quantities over the domain. Section 2.4.2 presents the correlation

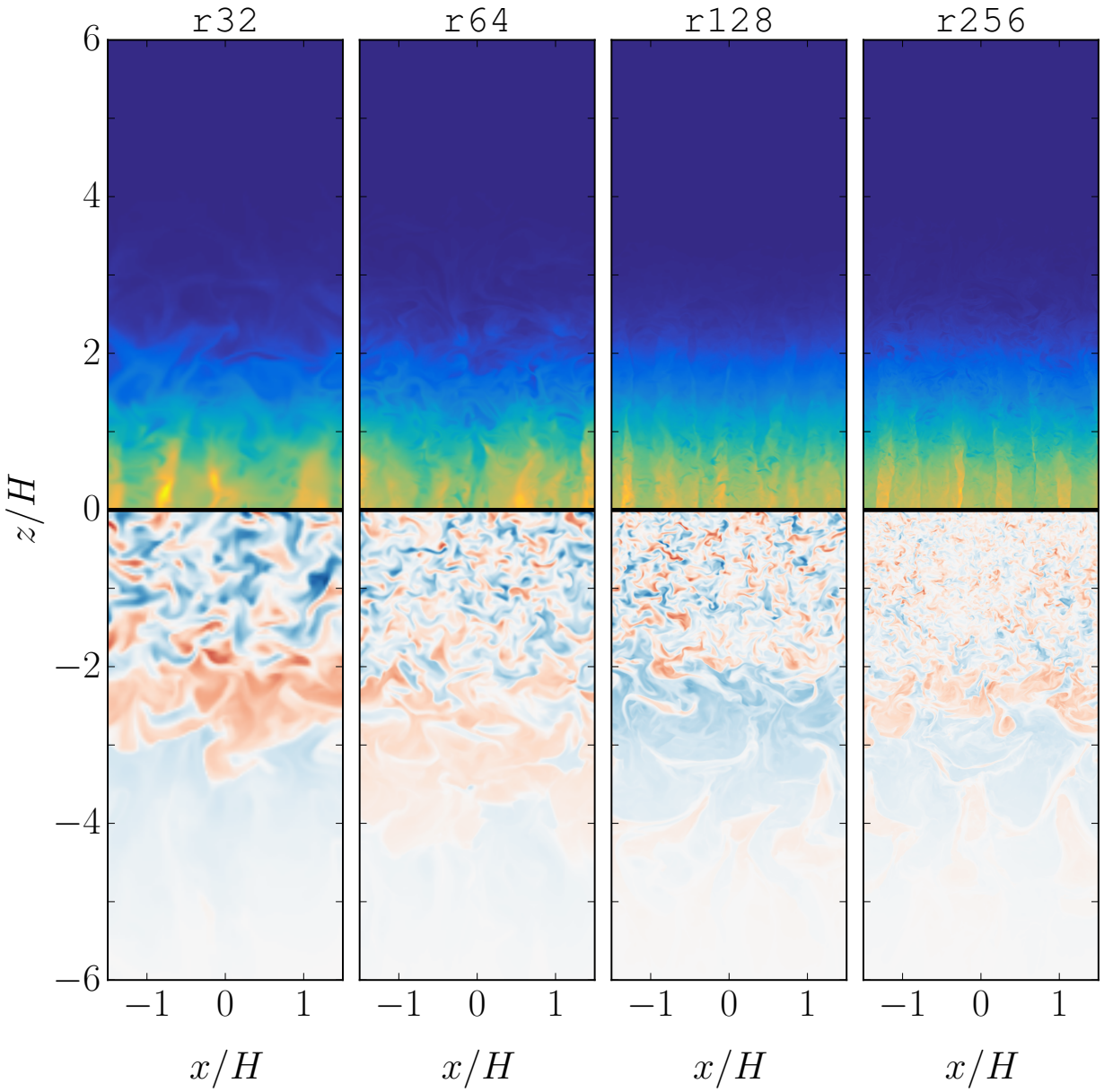

Figure 2.1: x-z slices of ρ (upper half) and B^y (lower half) for 32, 64, 128, and 256 zones per scaleheight. Note that as resolution increases, shocks become sharper and magnetic field structure becomes smaller. Color maps are linear and shared across resolutions.

function of the magnetic field.

2.4.1 Space and Time Averages

Does $\overline{\alpha}$ depend on resolution? Figure 2.2 shows α as a function of time and resolution. Average values are given in Table 2.3.2. Interestingly, the stress monotonically decreases with resolution and there is no evidence for convergence. The resolution dependence is well fit by $\overline{\alpha} \propto N^{-1/3}$.

How large are the error bars on our estimate of $\overline{\alpha}$, and is the observed variation with N significant? We assume that $\alpha(t)$ is a stationary process with mean $\overline{\alpha}$ and variance σ_α^2. We provide evidence in the Appendix that the fluctuations in $\alpha(t)$ decorrelate over large time intervals for a long-integration-time $N = 32$ model, and that the correlation time $\tau_c\Omega \approx 63$. A measurement of $\overline{\alpha}$ averaged over some interval T therefore consists of approximately $\sim T/\tau_c$ independent measurements, and one expects an rms error in evaluating $\overline{\alpha}$ of $\approx \sigma_\alpha (T/\tau_c)^{-1/2}$ (see Fig 4 of Longaretti & Lesur, 2010, which implies $\tau_c\Omega \sim 10$ in an unstratified local model).

In the Appendix we work out the relation between σ, τ_c and the rms error in evaluating $\overline{\alpha}$ for a class of model power spectra, assuming $\alpha(t)$ is a Gaussian process.[4] For a fit to the $N = 32$ run power spectrum, these imply that the expected rms error is $\approx 0.6\sigma_\alpha/\alpha_0 \approx 0.17$, assuming that σ_α/α_0 is independent of N, consistent with Table 2.3.2. This can be compared to $\overline{\alpha}(N)/\overline{\alpha}(2N) - 1 \approx 0.25$. Therefore the observed trend over a factor of 8 in N and ≈ 2 in $\overline{\alpha}$ is significant. A naive estimate of the probability that $d\log\overline{\alpha}/d\log N \geq 0$ gives $\approx 3\%$.

The run of magnetic field energy density $[E_B](z,t) = [\mathbf{B}\cdot\mathbf{B}/2]$ for all runs is shown in Figure 2.3. Evidently the "butterfly" or dynamo oscillations, which are independent, quasi-periodic enhancements in magnetic energy density on either side of the disk, followed by buoyant rise of magnetic field through $z \sim 2H$, are present at all resolutions.

Does the time-averaged vertical structure of the disk change with resolution? Figure 2.4 shows x,y-averaged quantities for all runs averaged over time. Also shown are fits to ρ and E_B from Guan & Gammie (2011), who study boxes of lower resolution but greater radial and azimuthal extent than we do here.[5] The density profile is consistent with an exponential profile (rather than Gaussian) at large $|z|$, with scale height $0.44H$. The magnetic energy density is also consistent with an exponential profile at large $|z|$, but with scale height $0.64H$. E_B has a feature close to the vertical boundaries, perhaps caused by field lines breaking as they intersect the boundary (Miller & Stone, 2000).

[4]The PDF of α *is not* consistent with a Gaussian. The PDF of $\log\alpha$ *is* consistent with a Gaussian. The analysis in the appendix does not change if carried out for $\log\alpha$ instead of α

[5]The fit is $\rho = 0.93\rho_0 \exp(-z^2/(2H^2))$ for $|z| < 2.55H$ and $\rho = 0.036\rho_0 \exp(-(|z|/H - 2.55)/0.44)$ otherwise, and $E_B = 0.012\rho_0 c_s^2$ for $|z| < 2.55H$ and $0.012\rho_0 c_s^2 \exp(-(|z|/H - 2.55)/0.64)$ otherwise.

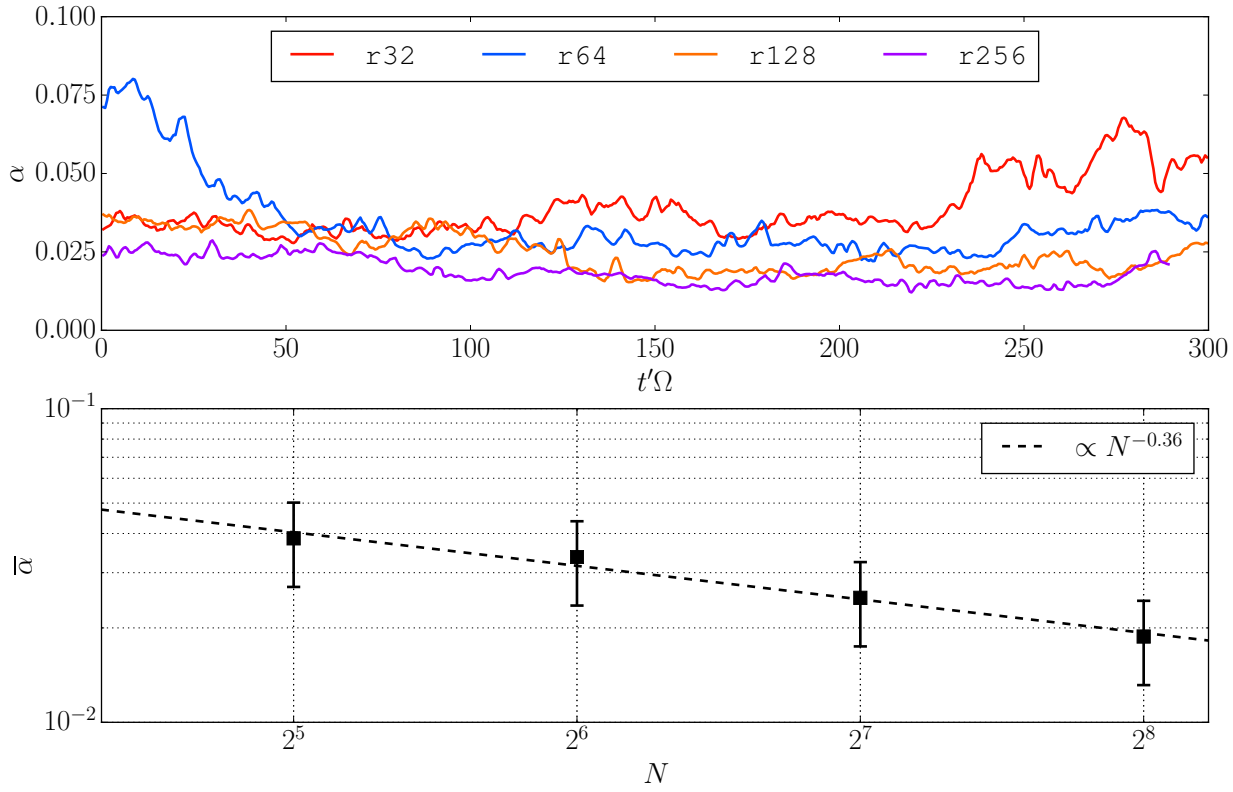

Figure 2.2: α for all runs. The top panel shows evolution over time (after boxcar smoothing of width $\Delta t = 2.5\Omega^{-1}$ for clarity), while the bottom panel shows the time averages as a function of resolution with a best-fit power law overlaid.

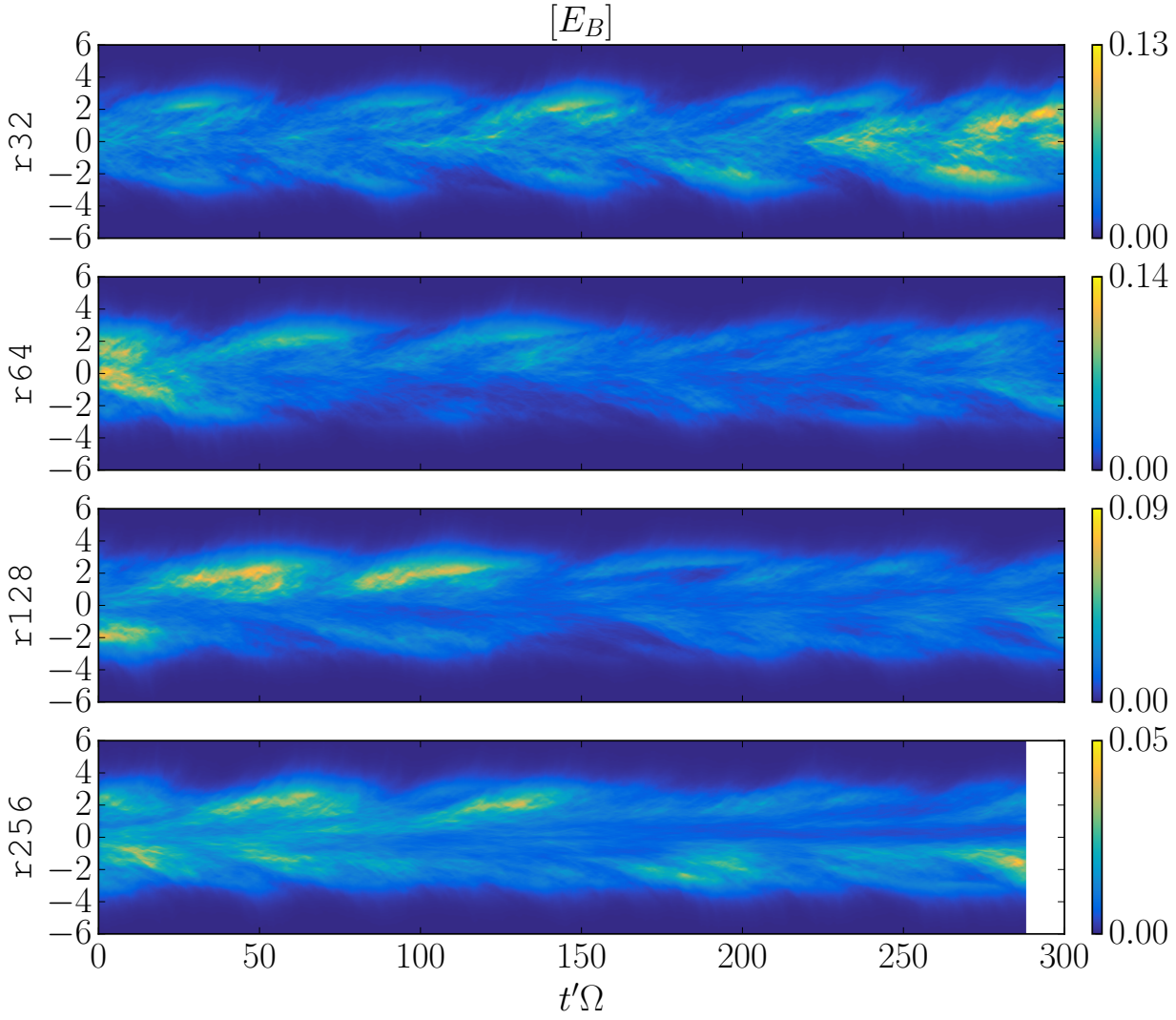

Figure 2.3: Spacetime diagram of $[E_B]$ for all runs. Color scales are specific to each panel. Note persistence of butterfly diagram across all resolutions.

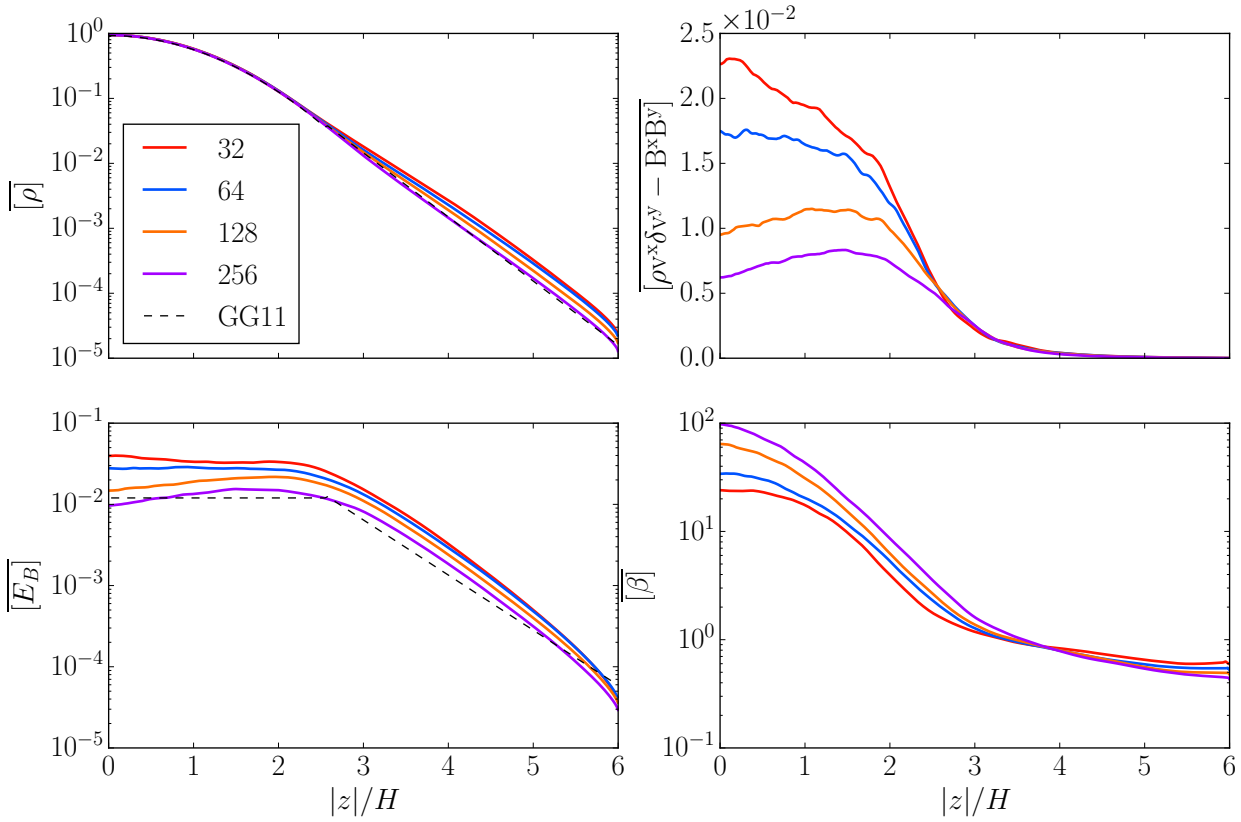

Figure 2.4: Time- and x,y-averaged quantities as a function of height. Fits to ρ and E_B from Guan & Gammie (2011) are overlaid.

The top right panel of Figure 2.4 shows the t,x,y-average of total stress. Little variation is seen at large $|z|$, and monotonic decrease of stress with resolution is seen near the midplane. Notice, however, that as resolution increases the structure of averaged stress develops a local minimum around $z = 0$ and a local maximum around $|z| \sim 2H$.

2.4.2 Magnetic Field Correlations

Earlier work (Guan et al., 2009) has shown that the magnetic field correlation length (defined below) scales as N^{-1} in zero-net-field, unstratified local ILES models where $\overline{\alpha} \sim N^{-1}$. How does the characteristic size of structures in MHD disk turbulence change with N for our stratified models?

The dimensionless magnetic field autocorrelation tensor is

$$T^{ij}(\delta x, \delta y, z, t) \equiv \frac{1}{[B^2]}[\delta B^i(x, y, z, t)\delta B^j(x + \delta x, y + \delta y, z, t)]. \tag{2.15}$$

The dimensionless scalar magnetic autocorrelation function $\xi_B \equiv Tr(T^{ij})$. Evidently $\xi_B(\delta x = 0, \delta y = 0) = 1$.

We consider only ξ_B; ξ_v and ξ_ρ contain comparatively larger contributions from the compressive disturbances evident in Figure 2.1 (see also Beckwith et al., 2011).

First we average $\xi_B(\delta x, \delta y, z, t)$ over $|z| < 2H$ and t, as did Davis et al. (2010). The result is shown in Figure 2.5. The correlation function is an ellipse swept back by the shear into a trailing spiral structure. The shape and orientation of the ellipse do not change significantly with resolution, but the scale of the correlation ellipse drops monotonically as resolution is increased.

Next we average $\xi_B(\delta x, \delta y, z, t)$ over time and over bins in z of width $\Delta z = 0.5H$, then fold around the midplane. We then evaluate the second moments of $\xi_B(z)$ in the contiguous region around $\delta x = \delta y = 0$ where $\xi_B > 0$. The eigenvectors of this moment tensor define a major and minor axis with major axis tilted at a small angle θ to the y axis. The correlation lengths $\lambda_{\rm minor}$ and $\lambda_{\rm major}$ are defined as the distance along each eigenvector at which $\xi_B = 1/e$. The shape of the correlation departs from an exponential at both small and large scales, although the correlations at large scale are weak and hard to measure accurately (although they must be present, as Guan & Gammie (2011) have shown that butterfly oscillations are coherent over large boxes). The correlation length is the outer scale of disk turbulence.

Figure 2.6 shows $\lambda_{\rm minor}(|z|)$, $\lambda_{\rm major}(|z|)$, and $\theta(|z|)$. All depend on height. The tilt rises toward $\approx 19^\circ$ for $|z| < 2.5H$. It declines out to $4.5H$ and then rises again toward the boundary (this rise may signal the influence of boundary conditions or the density floor). The major axis correlation length converges toward $\approx 0.5H$ for $|z| > 3H$, but is monotonically decreasing with N at $z = 0$. The minor axis correlation length is also monotonically decreasing with N at $z = 0$, and rises steadily with a bump at $\approx 3H$ toward the boundaries.

Figure 2.7 shows explicitly the resolution sensitivity $d\log\lambda/d\log N$ for the minor and major axis correlation lengths, along with the resolution sensitivity $d\log\overline{[w_{r\phi}]}/d\log N$ of the shear stress, as a function of $|z|$. Both correlation lengths are sensitive to resolution at the midplane, and far less sensitive (perhaps converged) at higher altitude. At the midplane, both correlation lengths scale as $N^{-1/2}$. $\overline{[w_{r\phi}]}$ exhibits a similar trend, especially for $|z| \lesssim 3H$.

Does this mean the outer scale of turbulence is unresolved, even at our highest resolution? Figure 2.6 also shows $\lambda_{\rm minor}(|z|)$, $\lambda_{\rm major}(|z|)$ in units of Δx in the right panels. Above $|z| = 3H$ even the minor axis is very well resolved, with in excess of 30 zones per correlation length. At the midplane $\lambda_{\rm minor}(N = 32)/\Delta x \approx 3$ and $\lambda_{\rm minor}(N = 256)/\Delta x \approx 10$. This differs from the nonconvergence observed in unstratified, zero-net-field ILES models, where $\lambda/\Delta x$ are independent of N; here, the outer scale is better resolved as resolution increases.[6]

[6]The ratio of correlation length to resolution $\lambda/\Delta x$ is related to, but not exactly the same as, the quality factor $Q \equiv \lambda_{MRI}/\Delta x$, where $\lambda_{MRI} \propto v_A/\Omega$ is a characteristic wavelength for the MRI (Sano et al., 2004; Noble et al., 2010; Hawley et

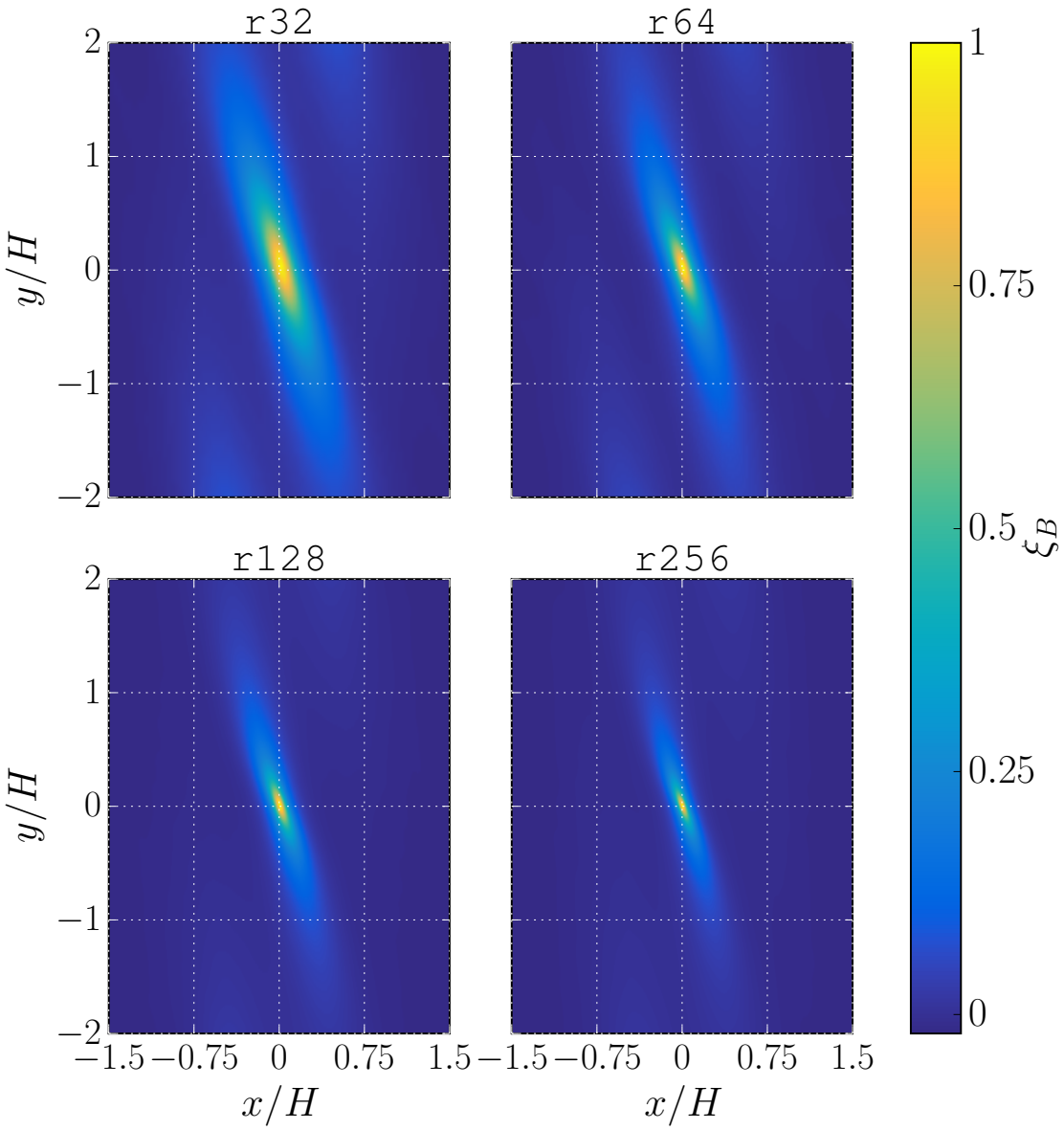

Figure 2.5: ξ_B averaged over time and the region $|z| < 2H$ for all runs.

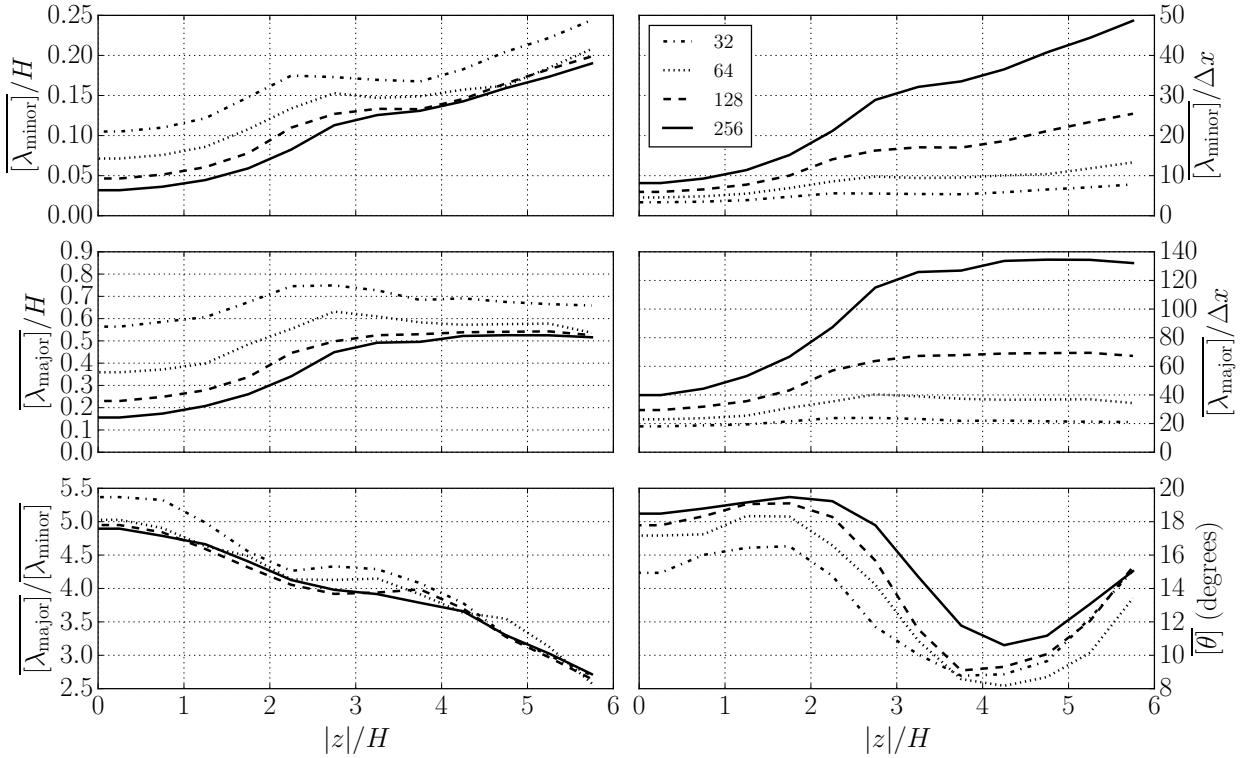

Figure 2.6: Minor axis correlation length, major axis correlation length, and tilt as a function of $|z|$ for each resolution. The correlation lengths are given in units of scale heights (left panels) and cell size Δx (right panels).

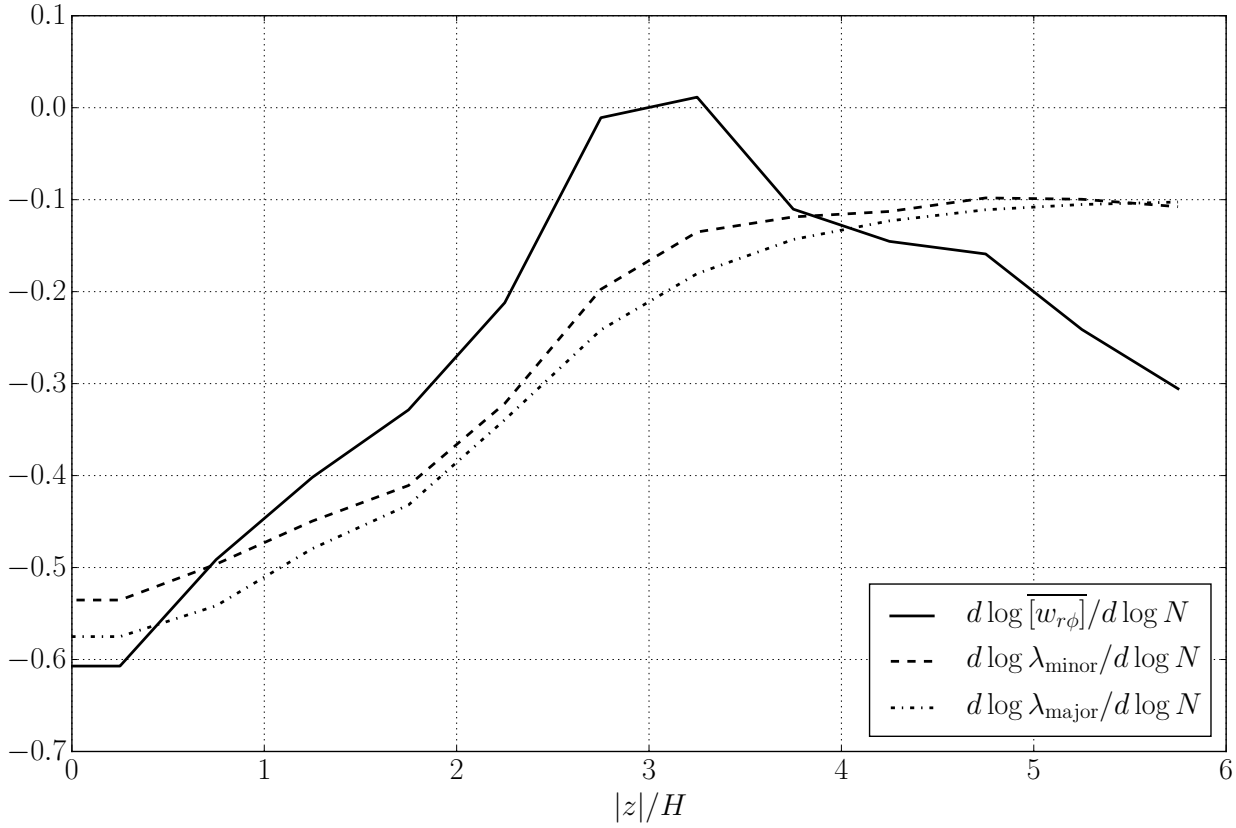

Figure 2.7: Resolution dependence of shear stress $d\log\overline{[w_{r\phi}]}/d\log N(z)$ and correlation lengths $d\log\lambda/d\log N(z)$ for λ the minor axis (middle) and major axis (bottom) magnetic field correlation lengths. Both λ are more strongly dependent on resolution at the midplane than at $|z| > 3H$.

2.4.3 Evolution of Net Magnetic Flux

Label	$\overline{\langle B^x \rangle}_{\rm RMS}$	$\sigma_{\langle B^x \rangle}$	$\overline{\langle B^y \rangle}_{\rm RMS}$	$\sigma_{\langle B^y \rangle}$	$\overline{\alpha}_{\rm NF}$
`r32`	7.0×10^{-4}	4.2×10^{-4}	3.6×10^{-2}	1.5×10^{-2}	1.1×10^{-2}
`r64`	4.0×10^{-4}	3.8×10^{-4}	1.8×10^{-2}	1.6×10^{-2}	5.6×10^{-3}
`r128`	4.3×10^{-4}	3.2×10^{-4}	2.0×10^{-2}	1.4×10^{-2}	6.2×10^{-3}
`r256`	3.7×10^{-4}	3.5×10^{-4}	1.1×10^{-2}	1.0×10^{-2}	3.4×10^{-3}

Table 2.4: RMS and standard deviation of net magnetic fluxes present for each run. Vertical magnetic flux is zero, conserved to machine precision.

Our choice of boundary conditions permit evolution of $\langle B^x \rangle$ and $\langle B^y \rangle$. How important is the mean field in driving the evolution?

The RMS and standard deviation of $\langle B^y \rangle$ and $\langle B^x \rangle$ are given in Table 2.4. Evidently $\langle B^y \rangle \gg \langle B^x \rangle$. We can estimate the effect of the mean field on $\overline{\alpha}$ using the saturation predictor of Hawley et al. (1995) for an unstratified shearing box with a net toroidal field[7]: $B^2 \sim 4\pi\sqrt{16/15}(0.012)\rho_0 L_y v_A \Omega$, where v_A is the Alfvén speed associated with the rms net toroidal field. Then using $\overline{\alpha}_{NF} \approx \int dz(1/(2\beta))/\int dz P = 0.25B^2(5H)/\sqrt{2\pi}$ (where $5H$ comes from assuming $B^2 = $ const for $|z| < 2.5H$, $B^2 = 0$ else), we find a predicted $\overline{\alpha}$ associated with the mean azimuthal field that is, for all models, at least a factor of 3 smaller than the measured $\overline{\alpha}$ (and nearly an order of magnitude for `r256`). This suggests that the boundary conditions are not controlling the saturation.

The mean field sensed locally by the turbulence may still control α locally. To illustrate this point, Figure 2.8 shows a sample estimate of a local mean field: the azimuthal field averaged over sheets at constant z. This fluctuates in sign, so to avoid cancellation we take the time average of the absolute value of this mean field. The resulting mean field is an order of magnitude larger than $\langle B_y \rangle$, which the unstratified box saturation predictor suggests would produce an $\overline{\alpha}$ comparable to what is measured. In sum: a localized mean field may play an important role in controlling the outcome, but the mean field over the entire computational domain does not.

al., 2011). The ratio of the two ratios is $\propto M \equiv v_A/\Omega\lambda$, which is the Alfvén Mach number of MRI-driven turbulence at the correlation length. Walker et al. (2016) demonstrated that in their unstratified models M is approximately constant in MRI driven turbulence. In our simulations M varies by a factor ~ 2 inside the disk.

[7]We emphasize that this predictor is for *unstratified* models; how well it recovers the behavior of stratified models is uncertain. We also use the mean field through the box as input; locally, the net field may vary.

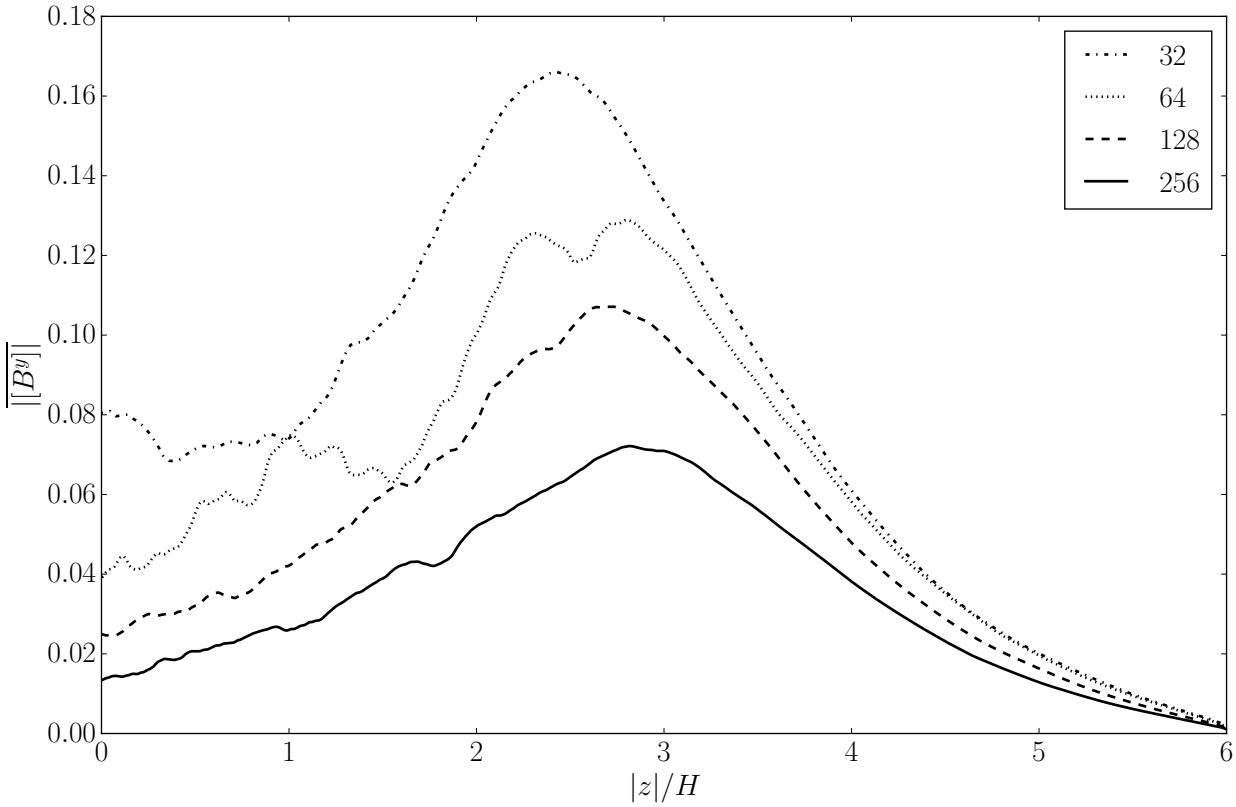

Figure 2.8: Time-averaged absolute value of the x,y-averaged magnetic flux.

2.5 Discussion

Our simulations have yielded several unexpected dependences on resolution: (1) $\overline{\alpha} \sim N^{-1/3}$ (2) $\lambda_{\rm minor} \propto \lambda_{\rm major} \sim N^{-1/2}$ in the midplane of the disk, and nearly $\sim N^0$ in the corona (3) The total stress, scaling similarly to λ with N, develops a local maximum at $|z| \sim 2H$ as resolution increases.

Surprisingly, we do not see convergence of the time-averaged, vertically integrated shear stress $\overline{\alpha}$ for resolution up to $N = 256$ zones per scale height in stratified, isothermal, local ILES models. This is broadly consistent with Bodo et al. (2014) and in tension with the results of Davis et al. (2010). Both Davis et al. (2010) and Bodo et al. (2014) find a plateau in $\overline{\alpha}$ between ≈ 45 and ≈ 90 zones per H. We do not find evidence for this behavior, but the plateau could be hidden in our measurement errors due to finite run time and finite computational volume.

Are our results consistent with earlier work? To compare, we need to convert to common units and a common measurement of stress, for which we will use α as defined in Eqn. (2.14).

Davis et al. (2010) report volume-and-time averaged stresses in units of the midplane pressure. This is equivalent to volume-averaged stress in our units. Notice that Davis et al. (2010) define $H = \sqrt{2}c_s/\Omega$. Then for $N \approx (23, 45, 91)$ their volume averaged stress (see their Table 1) is (0.0149, 0.0093, 0.0092). Converting to vertically integrated stress (multiply by $4\sqrt{2}$) and dividing by the vertically integrated gas pressure ($\sqrt{2\pi}$ in our units), we find (using our definition of α) $\overline{\alpha} = (0.034, 0.021, 0.021)$.

Bodo et al. (2014) also define $H = \sqrt{2}c_s/\Omega$, and set $c_s = 1/\sqrt{2}$, $\rho_0 = 1$, and $\Omega = 1$, so their unit of stress is a factor of 2 larger than ours. They consider models with $N \approx (23, 45, 91, 141)$. Since they do not report time-averaged stresses, we will estimate these from their Figure 2. We estimate that the volume integrated maxwell stress in their units is $\simeq (0.022, 0.017, 0.017, 0.01)$. We convert this vertically integrated stress to our units (multiply by $2\sqrt{2}$; the factor of 2 is for the stress unit and the factor of $\sqrt{2}$ is for the length unit), multiply by 1.25 to incorporate an assumed 25% Reynolds stress contribution, then divide by the vertically integrated pressure ($\sqrt{2\pi}$) in our units to find $\overline{\alpha} \simeq (0.031, 0.024, 0.024, 0.014)$.

To facilitate comparison, at a resolution of $N = (32, 64, 128, 256)$ we find $\overline{\alpha} = (0.039, 0.034, 0.025, 0.019)$. These results are shown in Figure 2.9. The overall offset of the Davis et al. and Bodo et al. series from ours is significant, but may be explained in part by the larger vertical extent of our models. The algorithms used also differ, possibly yielding different effective resolutions, and of course the vertical boundary conditions also differ. Nevertheless, it is reassuring that all simulations lead to values of $\overline{\alpha}$ that are within 1σ of our results. Indeed, least squares power-law fits to the Davis et al. and Bodo et al. series yield slopes (-0.35 and -0.37, respectively) consistent with ours (-0.36) and the relationship $\overline{\alpha} \sim N^{-1/3}$.

The correlation function in the $x - y$ plane is approximately ellipsoidal and characterized by the major

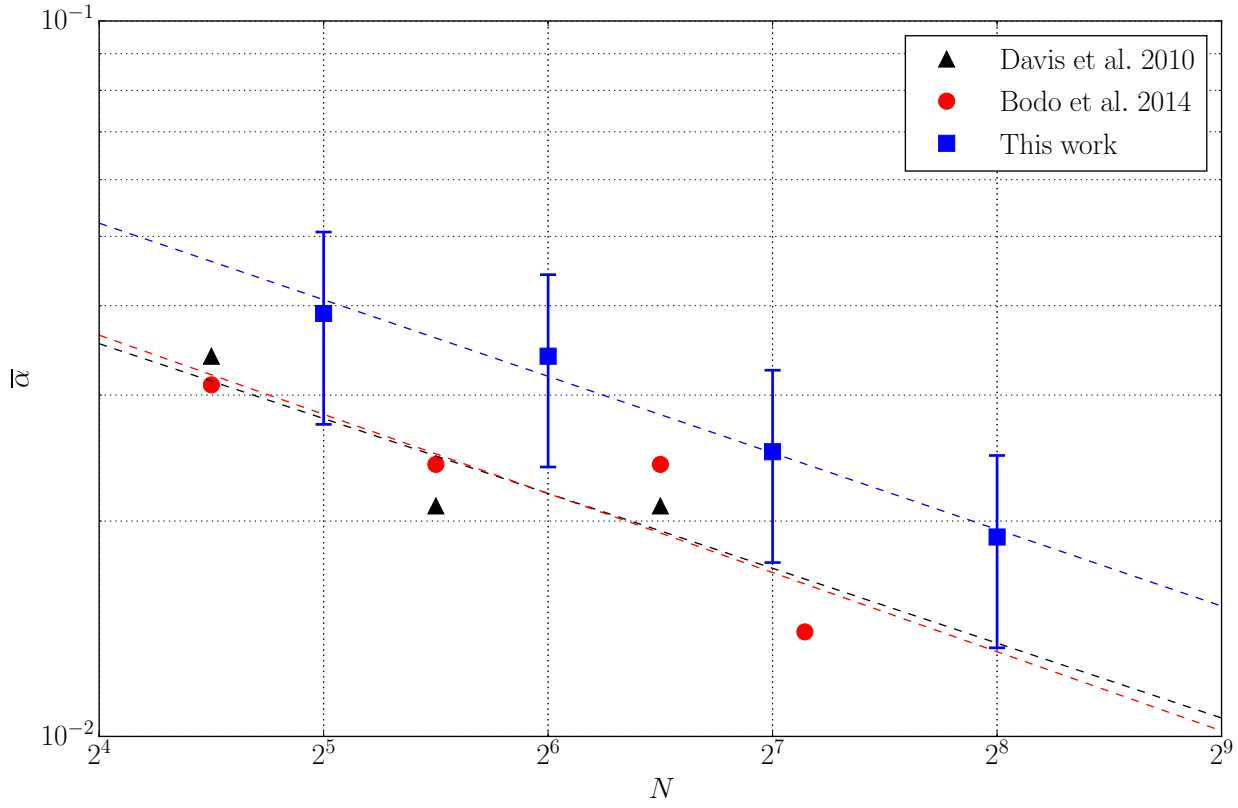

Figure 2.9: Time-averaged dimensionless shear stress $\overline{\alpha}$ for Davis et al. 2010, Bodo et al. 2014, and this work. Results are broadly consistent, and all show approximately the same scaling of stress with resolution. Fits to each dataset are shown as dashed lines.

axis length, minor axis length, and the "tilt angle" between the major axis and the y axis. The tilt angle $\theta_{\rm tilt}(N = 256) \sim 19^\circ$ is consistent with Davis et al. (2010) who find $\theta_{\rm tilt}(N \approx 91) \sim 18^\circ$. The increase in $\theta_{\rm tilt}$ with resolution was also reported by Guan et al. (2009). Although Davis et al. (2010) do not quote a value for $\lambda_{\rm minor}$, visual inspection of their $\xi_B(N \approx 64)$ slice yields a value comparable to what we find at similar resolution.

The sensitivity of stress to N depends on height (see Figure 2.7). The midplane shear stress decreases with N at a rate that is inconsistent with convergence, but the stress at $|z| \gtrsim 2H$ is much less sensitive to N and convergence is not excluded by our limited time- and volume-sampled data. One consequence of this is that a local minimum develops in the total stress at $z = 0$ and a local maximum develops at $|z| \simeq 2H$. A qualitatively similar local maximum in the stress is observed in stratified shearing boxes with self-consistent thermodynamics, at least when they are radiation pressure-dominated (Hirose et al. 2009, Jiang et al. 2016). This effect appears to be due to a convective process which also significantly enhances α in these models (e.g. Hirose et al., 2014).

Are our simulations run long enough? From a long-duration, low-resolution simulation we measured a correlation time of $\approx 60\Omega^{-1}$ (this is slightly shorter than the $90\Omega^{-1}$ correlation time seen in the $N = 90$ run of Davis et al. (2010) [8]), and our assessment of the error bars on $\bar{\alpha}$ relies on this measurement. Stratified shearing box models frequently give an impression of order-unity enhancements in α ("bursts") separated by long intervals, and rare bursts could change the correlation time. Our data are not sufficient to assess whether this impression is statistically well grounded or not. If it is, then the bursts might correspond to long-timescale power in the power spectrum of a Gaussian process that is undetectable in a short simulation, or non-Gaussianity associated with the flares. There is, however, no evidence for non-Gaussianity in our data; the probability distribution for $\log \alpha$, for example, is consistent with Gaussian. There is also no evidence to changes in the variance of $\log(\alpha)$ with N; the relative variance, shown in Table 3, shows no systematic trend.

Why no convergence? The cause may lie either with our numerical realization of the stratified isothermal zero-net-flux ILES shearing box model (A), or with assumptions made by the model itself (B). We have assembled an incomplete list of possible explanations:

(A1) The nonconvergence is physical and $\alpha_{MRI} \to 0$ in isothermal astrophysical disks with vanishing mean field. Although we cannot rule this out, it seems inconsistent with the result of Fromang (2010) for an unstratified model with explicit scalar viscosity and resistivity that converges to nonzero α, albeit only for $P_m = 4$.

[8] We thank S. Davis for kindly providing us with the data.

(A2) The apparent nonconvergence is a consequence of a combination of statistical errors associated with a finite sampling time and an initial transient that results from using resolution $N/2$ data to initialize resolution N models. Our analysis (see Appendix) suggests, however, that even though $\overline{\alpha}$ has a long correlation time this is improbable.

(A3) The nonconvergence is an artifact of the limited size of the model. Fluctuations in $\alpha(t)$ will depend on the volume of the simulation. Naively, they would scale as 1 over the square root of the number of correlation volumes. But there is coupling between correlation volumes via large-scale magnetic fields and this is connected to the butterfly oscillations. Furthermore, it is already known that in unstratified, local simulations the imposition of a mean field causes an ILES model to converge. Ultimately, it must be that turbulence is locally unable to distinguish between uniform fields and magnetic fields that have structure on a sufficiently large scale. Perhaps our models are simply too small to see this sufficiently large scale, and so they are analogous to the zero mean field unstratified models that do not converge.

The interaction between small and large scale fields has been explored by Sorathia et al. (2012) who measured the net magnetic flux in local regions of global unstratified ILES models. They found distributions of $\langle B^x \rangle$, $\langle B^y \rangle$, and $\langle B^z \rangle$ inconsistent with zero, with the linear MRI growth associated with these mean fields typically being well resolved in their simulations.

(A4) The model will converge at higher N, and we are simply not in the high resolution limit yet. The magnetic field correlation length is $\sim 10\Delta x$ in our highest resolution models, so there is only a dynamic range of $\simeq 2$ between the outer scale λ and the dissipation scale.

(A5) The model will *not* converge, with $\alpha \sim \lambda \sim N^{-1}$, in the complete absence of a mean magnetic field. Although we cannot account for the $\overline{\alpha}$ we measure from the net flux through our computational domain, our estimate is based on a fit to results from unstratified models. Mean fields in stratified boxes may behave differently. They may, for example, be playing a stronger role than we estimate in the magnetically-dominated corona, contributing to our near-convergence of λ above $|z| \sim 3H$. Nonetheless, Davis et al. (2010) *do* maintain zero net flux in a stratified model, and their results are inconsistent with $\alpha \sim N^{-1}$.

(B1) The nonconvergence is an artifact of our use of an ILES model. In models in which the numerical resolution and Reynolds numbers are increased together, there is numerical evidence that both unstratified and stratified models converge (Fromang 2010, Simon et al. 2011). It would be interesting to know whether this extends to larger N and the large Re_M, large Re limit relevant to astrophysical disks. There is also numerical evidence that computational models of the solar dynamo depend strongly on the dissipation model (see, e.g. Charbonneau, 2014, for a review).

(B2) The nonconvergence is an artifact of the absence of consistent vertical energy transport by radiation

and convection. It is now known that convective disks in models with consistent treatment of energy transport exhibit enhanced α (Hirose et al. 2014), which may enhance the amplitude of dwarf nova outbursts. The convective process may aid convergence (Bodo et al. 2015). It is not yet clear how well converged the energetically consistent models are; current model have $N \sim O(64)$.

(B3) The nonconvergence is an artifact of the symmetry of the local model. The local model is invariant under translations in the plane of the disk, and invariant under rotations by π around the z axis. The incorporation of higher order terms in H/r would break these symmetries and might qualitatively change the outcome. There is limited numerical evidence for convergence in unstratified global models (Sorathia et al., 2012), although with a tendency for $\overline{\alpha}$ (and hence $\dot{M}$ and β^{-1}) to increase with resolution (see also Shiokawa et al., 2012; Hawley et al., 2011, 2013).

What are the implications of nonconvergence? It is difficult to say without testing the hypotheses above with new numerical simulations. For example, if A4 is correct (insufficient resolution) then current lower resolution models may yield $\bar{\alpha}$ to within a factor of two. On the other hand, if A5 is correct (α is zero without a mean field) then the result would have profound implications for our understanding of disk structure and evolution, which would presumably be controlled by the generation and transport of large-scale magnetic field. No matter what the explanation for the nonconvergence seen here, future disk simulations need to be tested carefully for convergence.

2.6 Conclusion

The isothermal stratified zero-net-flux shearing box is a minimal model with zero physical parameters for the turbulent saturation of the magnetorotational instability and is thus central to accretion disk theory. We have attempted to sort out apparently conflicting reports of convergence in the literature using the `ramses-gpu` code on `blue waters` to probe convergence at an unprecedented resolution of $N = 256$ zones per scale height.

Our results imply that existing local and perhaps global zero-mean-field ILES models of disks are, at best, underresolved. We have found that $\overline{\alpha} \sim N^{-1/3}$. This is not convergent, but it differs from the sharp nonconvergence identified by Fromang et al. (2007) in unstratified ILES models, with $\overline{\alpha} \sim N^{-1}$.

We have also compared our results to earlier work by Davis et al. (2010) and Bodo et al. (2014). These earlier calculations are consistent with our to within the error bars, and all show a similar trend with resolution. Like Bodo et al. (2014) and unlike Davis et al. (2010), our models do not conserve net toroidal magnetic flux. Although first estimates suggest the net flux present in our model is not controlling our results,

this remains an uncertainty in performing comparisons. Box size effects may also confound comparisons.

We have reviewed possible physical and numerical causes of this nonconvergence. All of these are amenable to further numerical investigation when sufficient computational resources are available. One implication is clear, however: simulations of MHD turbulence in disks need to be tested carefully for convergence, and the attendant uncertainties need to be allowed for when weighing the results.

It is a pleasure to thank G. Bodo, M. Chandra, S. Davis, J. Dolence, J. Goodman, G. Lesur, V. Paschalidis, J. Simon, and J. Stone for useful discussions. We also thank the anonymous referee for a very useful report. The numerical calculations presented here were performed on the Blue Waters supercomputer at NCSA. BRR was supported by an Illinois Distinguished Fellowship and by NSF grant AST-1333612. Work at Los Alamos National Laboratory was done under the auspices of the National Nuclear Security Administration of the US Department of Energy. CFG's work was also supported in part by a Romano Professorial Scholar appointment, a Simons Fellowship in Theoretical Physics, and a Visiting Fellowship at All Souls College, Oxford.

2.A Measurement Error Estimates with a Gaussian Process Model

Shearing box simulations estimate the true, long-term average α_0 from $\overline{\alpha}$ measured over a finite time Δt. How long is long enough?

Note that in this section, $\langle\rangle$ denotes an expectation value for consistency with previous literature on Gaussian random fields, rather than the volume average of Equation 2.11. Suppose α has a correlation time τ_c and variance σ^2. Then our intuition is that $\langle(\overline{\alpha}-\alpha_0)^2\rangle$should be proportional to $\sigma^2\tau_c/\Delta t$, i.e. the rms error averaged over many realizations of α should scale as one over the square root of the number of correlation times. But with what coefficient?

We can estimate $\langle(\overline{\alpha}-\alpha_0)^2\rangle$ for a Gaussian process with known power spectrum over some long but finite time T. That is,

$$\alpha(t) = \alpha_0 + \sum_j a_j \cos(\omega_j t + \phi_j); \qquad \omega_j = \frac{2\pi j}{T} \tag{2.16}$$

The sum is taken only over $\omega_j > 0$, ϕ_j is uniformly distributed in $[0, 2\pi)$ (random phase) and a_j is Gaussian distributed:

$$P(a_j)da_j = \exp\left(-\frac{a_j^2}{2\langle a_j^2\rangle}\right)\frac{da_j}{(2\pi\langle a_j^2\rangle)^{1/2}} \tag{2.17}$$

The power spectrum $P_\omega \equiv T\langle a_j^2\rangle$. In the limit that T is large the modes are closely spaced and $\sum_j \rightarrow$

$\int d\omega T/(2\pi)$. The expected variance in α over the interval T is

$$\langle \sigma^2 \rangle = \langle (\alpha - \alpha_0)^2 \rangle = \frac{1}{2} \int_0^\infty \frac{d\omega}{2\pi} P_\omega. \tag{2.18}$$

where the factor of 2 comes from phase averaging. P_ω is independent of T if σ^2 is fixed.

The autocorrelation function is

$$\xi(\tau) \equiv \frac{1}{T} \int_0^T dt\, \alpha(t)\alpha(t+\tau) - \alpha_0^2 = \frac{1}{2} \int_0^\infty \frac{d\omega}{2\pi} P_\omega \cos \omega\tau. \tag{2.19}$$

The error in estimating α_0 from a finite interval Δt is

$$m = \frac{1}{\Delta t} \int_0^{\Delta t} dt\, (\alpha - \alpha_0) \tag{2.20}$$

Expanding and integrating,

$$m = \frac{1}{\Delta t} \int_0^{\Delta t} dt \sum_j a_j \cos(\omega_j t + \phi_j) = \sum_j a_j \frac{1}{\omega_j \Delta t} \left\{ \sin(\omega_j \Delta t + \phi_j) - \sin \phi_j \right\} \tag{2.21}$$

Then

$$\langle m^2 \rangle = \sum_j \langle a_j^2 \rangle \frac{1}{\omega_j^2 \Delta t^2} \left(1 - \cos(\omega_j \Delta t)\right) \to \int \frac{d\omega}{2\pi} \frac{P_\omega}{\omega^2 \Delta t^2} \left(1 - \cos(\omega \Delta t)\right). \tag{2.22}$$

To go further we need to know the power spectrum.

We consider model power spectra that decorrelate on long timescales, so that $P_\omega \propto \omega^0$ for ω small, and scale as a power law at high frequency. A suitable model is

$$P_\omega \propto (1 + (\omega/\omega_0)^2)^{-p/2}. \tag{2.23}$$

Evidently if the process is stationary then $p > 1$. The power spectrum can be normalized by σ^2:

$$P_\omega = \frac{\Gamma(p/2)\, 8\sqrt{\pi}}{\Gamma((p-1)/2)} \frac{\sigma^2}{\omega_0} \frac{1}{(1 + \omega^2/\omega_0^2)^{p/2}}. \tag{2.24}$$

Then

$$\xi(\tau) = \frac{2^{3/2-p/2}}{\Gamma((p-1)/2)}\ \sigma^2\ (\omega_0|\tau|)^{(p-1)/2} K_{(p-1)/2}(\omega_0|\tau|) \tag{2.25}$$

where K_n is a modified Bessel function of the second kind. It is easy to show that $\xi(0) \to \sigma^2$.

We estimate σ^2 from data taken over an interval Δt. This estimate is biased because it does not include

contributions to the variance from low frequency components. The expected value of σ^2 sampled over time Δt is

$$\langle(\alpha - \overline{\alpha})^2\rangle = \int_0^\infty \frac{d\omega}{2\pi} P_\omega \left(\frac{1}{2} + \frac{\cos(\omega\Delta t) - 1}{\omega^2 \Delta t^2}\right). \tag{2.26}$$

If p and ω_0 are known then this expression can be used to produce an debiased estimate of σ^2.

An auxiliary $N = 32$ run with $\Delta t = 2000\Omega^{-1}$ has a power spectrum consistent with $p \sim 2$. For this special case, $\xi(\tau) = \sigma^2 e^{-\omega_0|\tau|}$, $\tau_c = \omega_0^{-1}$, and

$$\langle m^2\rangle = \frac{\sigma^2}{\omega_0 \Delta t}\, 2\left(1 - \frac{1 - e^{-\omega_0 \Delta t}}{\omega_0 \Delta t}\right). \tag{2.27}$$

Consistent with expectations, this scales as $\sigma^2 \tau_c / \Delta t$. Also,

$$\langle(\alpha - \overline{\alpha})^2\rangle = \sigma^2 \left(1 - \frac{2}{\omega_0 \Delta t} + \frac{2(1 - e^{-\omega_0 \Delta t})}{\omega_0^2 \Delta t^2}\right). \tag{2.28}$$

The auxiliary $N = 32$ run has $\tau_c \Omega \simeq 60$, so $\omega_0 = 60^{-1}\Omega$, which we will assume is independent of N. Runs in Table 2 with $\Delta t = 300\Omega^{-1}$ therefore have $\omega_0 \Delta t \simeq 5$. Runs in Table 2 also have $\sigma_\alpha / \overline{\alpha} \simeq 0.25$. Then (2.28) implies the debiased $\sigma_\alpha / \alpha \simeq 0.30$. Combined with (2.27), we find $\langle m^2\rangle^{1/2} = 0.17\alpha$. This implies that the one-sigma error is small compared to the total change in $\overline{\alpha}$ over a factor of 8 in N.

Chapter 3

bhlight: General Relativistic Radiation Magnetohydrodynamics with Monte Carlo Transport

3.1 Summary

We present bhlight, a numerical scheme for solving the equations of general relativistic radiation magnetohydrodynamics (GRRMHD) using a direct Monte Carlo solution of the frequency-dependent radiative transport equation. bhlight is designed to evolve black hole accretion flows at intermediate accretion rate, in the regime between the classical radiatively efficient disk and the radiatively inefficient accretion flow (RIAF), in which global radiative effects play a sub-dominant but non-negligible role in disk dynamics. We describe the governing equations, numerical method, idiosyncrasies of our implementation, and a suite of test and convergence results. We also describe example applications to radiative Bondi accretion and to a slowly accreting Kerr black hole in axisymmetry[1].

3.2 Introduction

Many of the brightest objects in the universe, including quasars and the lesser active galactic nuclei, stellar-mass black hole binaries, and gamma-ray bursts, are likely the results of black hole accretion driven at least in part by the magnetorotational instability (MRI; Balbus & Hawley 1991). The structure of the luminous plasma surrounding the black hole remains uncertain (see the recent review of Begelman 2014), because it is difficult to resolve and because of physical complexity: relativistic gravity, turbulence in a magnetized plasma, and radiation transport all play some role in determining accretion flow structure.

Nonetheless, accreting black holes may be partially classified according to the ratio of their luminosity L to the Eddington luminosity, $L_{\rm Edd} \equiv 4\pi GMc/\kappa_{es}$.

For $L \gtrsim 10^{-2} L_{\rm Edd}$, radiation is dynamically important. Up to $L \sim L_{\rm Edd}$, this regime can be modeled by the aligned thin α disk model of Shakura & Sunyaev (1973), in which the disk is geometrically thin and optically thick, and in which radiation pressure exceeds gas pressure at radii where most of the disk

[1] This work appeared in publication as Ryan et al. (2015).

luminosity is produced. The radiative efficiency of the accretion flow, $\eta(a_*) \equiv L/(\dot{M}c^2)$, is expected to be approximately constant and determined by the dimensionless black hole spin $-1 < a_* < 1$. It is common to describe the accretion rate $\dot{M}$ in units of an Eddington rate defined using a nominal efficiency $\eta = 0.1$: $\dot{m} = \eta\dot{M}c^2/L_{\rm Edd}$. For $L \gtrsim L_{\rm Edd}$, the flow is expected to resemble the slim disk solution of Abramowicz et al. (1988), in which the flow becomes geometrically thick as a result of long radiation diffusion times. An obstacle to fully modeling the innermost, relativistic regions of flows with $\dot{m} \gtrsim 10^{-2}$ is the need for an efficient relativistic radiation hydrodynamics scheme that can operate in both the optically thick (disk midplane) and optically thin (disk atmosphere, corona, funnel) regimes.

For $L \ll L_{\rm Edd}$, or $\dot{m} \ll 1$, accretion is likely to occur through a radiatively inefficient accretion flow (RIAF or ADAF; see the recent review by Yuan & Narayan 2014), in which the cooling time of a parcel of plasma is much longer than the time required for it to fall into the black hole. Radiation plays no role in determining the flow structure. RIAFs are believed to be geometrically thick, optically thin, collisionless plasmas that are at least partially supported by rotation. RIAFs are commonly modeled numerically using relativistic magnetohydrodynamic (MHD) codes, but it is unclear how well the fluid model describes the dynamics of the magnetized, collisionless plasma. It is also unclear how best to model the electrons, which are collisionally decoupled from the ions and determine the radiative properties of the plasma. However, local models, particularly numerical kinetic calculations, are beginning to constrain the electron distribution function in this regime (e.g. Kunz et al. 2014, Riquelme et al. 2015, Sironi 2015).

Between thin disks and RIAFs lies an intermediate regime in which radiation plays a modest role in the accretion flow; this configuration may be thought of as a RIAF perturbed by radiative effects. ADAF solutions evaluated at these accretion rates indicate a flow that is optically thin to Compton scattering ($\tau \sim 10^{-5} - 10^{-3}$; Yuan et al. 2006), and optically thick only to synchrotron self-absorption at long wavelengths. As accretion rate increases the first non-negligible radiation-plasma interactions are expected to be Compton cooling and synchrotron cooling. For example, M87's central black hole, an object of interest for the Event Horizon Telescope (Doeleman et al. 2009), is expected to reside in this intermediate regime ($\dot{m} \lesssim 6.3 \times 10^{-6}$, based on a RIAF model; Kuo et al. 2014), in Mościbrodzka et al. (2011) and Dexter et al. (2012). Such systems exhibit nonlinear evolution of coupled gas and radiation in strong gravity; predictive modeling is our primary motivation for `bhlight`, a numerical scheme for general relativistic radiation magnetohydrodynamics.

In the nonrelativistic and $\mathcal{O}(v/c)$ regimes, many numerical methods have been developed to solve the radiation hydrodynamics equations (see the comprehensive review of Castor 2004), including flux-limited diffusion. Of particular relevance to black hole accretion flows is recent work on accretion in the near-

Eddington regime using flux-limited diffusion (Hirose et al. 2009, 2014) and using the more accurate short characteristics method, in which specific intensity is discretized in angle for each grid zone (Stone et al. 1992; Jiang et al. 2012, 2014a,b) and one obtains a full solution to the grey transfer equation.

Close to the event horizon special and general relativistic effects can produce order unity variations in the intensity. These effects are particularly important for rapidly rotating black holes. Numerical schemes for solving the equations of general relativistic radiation MHD (GRRMHD) have only been developed in the last few years. All are frequency-integrated and use approximate closure schemes, including the Eddington approximation (Farris et al. 2008, Zanotti et al. 2011, and Fragile et al. 2012) and low-order truncated moment closure (Shibata et al. 2011, Sądowski et al. 2013, and McKinney et al. 2014). These schemes are formally accurate at high optical depth, but not for general flows at the modest optical depths relevant to black holes in the intermediate accretion rate regime.

An alternative treatment of radiation, the Monte Carlo technique, has long been used for solving the full frequency-dependent transport equation without recourse to any closure model. Several radiation hydrodynamics schemes have recently been employed in astrophysics which couple a Monte Carlo representation of the radiation to a fluid model through interactions evaluated on a per-sample basis, yielding a Monte Carlo Radiation Hydrodynamics (MCRHD) scheme. This technique has received particular attention in the stellar physics community in Haworth & Harries (2012), Noebauer et al. (2012), Abdikamalov et al. (2012), Wollaeger et al. (2013), and Roth & Kasen (2015), which have variously investigated extensions such as implicit methods and interfacing the Monte Carlo representation with a continuum approximation in regions of large optical depth and/or large ratio of radiation to gas pressure, where the unadorned Monte Carlo technique fails. MCRHD schemes have also been implemented for studying star formation in Harries (2015), and have been used to model Compton cooling of accretion disks around black holes in flat space by Ghosh et al. (2011) and Garain et al. (2012). Monte Carlo techniques are particularly attractive for GRRMHD because they are algorithmically simple, naturally incorporate frequency dependence (useful for treating Compton scattering) and the potentially complicated angular dependence expected in an optically thin regime, and are easily modified to include special and general relativistic effects.

In what follows we develop a scheme for GRRMHD called `bhlight` that is designed to model accretion flows with modest to low optical depth. `bhlight` couples two existing schemes: the GRMHD code `harm`[2] (Gammie et al., 2003), and the Monte Carlo radiative transport scheme `grmonty`[3] (Dolence et al., 2009). The paper is organized as follows: §2 recounts the governing equations as they are solved in `bhlight`; §3 describes the numerical method; §4 demonstrates that `bhlight` converges on a set of test problems; §5

[2]Freely available; `http://rainman.astro.illinois.edu/codelib/codes/harm/harm.tgz`
[3]Freely available; `http://rainman.astro.illinois.edu/codelib/codes/grmonty/grmonty.tgz`

describes example applications to a radiating Bondi flow and an M87-like disk model; §6 concludes.

3.3 Basic Equations

We adopt a physical model in which emission, absorption, and scattering of photons couple an ideal, magnetized fluid to the radiation field. We consider the fluid and radiation sector in turn. The basic equations are identical to those integrated in the `harm` code (Gammie et al., 2003) and in the `grmonty` code (Dolence et al., 2009), but recounted here to define variables and expose physical assumptions.

3.3.1 Fluid

We assume particle number conservation, which in a coordinate basis is

$$\partial_t \left(\sqrt{-g}\rho_0 u^t\right) = -\partial_i \left(\sqrt{-g}\rho_0 u^i\right), \tag{3.1}$$

where ρ_0 is the comoving frame rest mass density and u^μ is the fluid four-velocity.

Energy and momentum conservation for the coupled fluid *and* radiation system are given by

$$\left(T^\mu_{\ \nu} + R^\mu_{\ \nu}\right)_{;\mu} = 0, \tag{3.2}$$

where $T^\mu_{\ \nu}$ is the magnetohydrodynamic stress-energy tensor, and $R^\mu_{\ \nu}$ is the radiation stress-energy tensor (not to be confused with the Ricci tensor). In a coordinate basis, Eq. 3.2 becomes

$$\partial_t \left(\sqrt{-g}T^t_{\ \nu}\right) = -\partial_i \left(\sqrt{-g}T^i_{\ \nu}\right) + \sqrt{-g}T^\kappa_{\ \lambda}\Gamma^\lambda_{\ \nu\kappa} + \sqrt{-g}G_\nu, \tag{3.3}$$

where the radiation four-force density

$$G_\nu \equiv -R^\mu_{\ \nu;\mu}. \tag{3.4}$$

In the ideal MHD limit $u_\mu F^{\mu\nu} = 0$ ($F^{\mu\nu} \equiv$ electromagnetic field tensor), and one can show that

$$T^\mu_{\ \nu} = (\rho_0 + u + P + b^2)u^\mu u_\nu + (P + \frac{1}{2}b^2)g^\mu_{\ \nu} - b^\mu b_\nu, \tag{3.5}$$

where $P \equiv$ fluid pressure, $u \equiv$ fluid internal energy density, and $b^2 = b^\mu b_\mu$, with b^μ the magnetic field four-vector,

$$b^\mu \equiv \frac{1}{2}\epsilon^{\mu\nu\kappa\lambda}u_\nu F_{\lambda\kappa}, \tag{3.6}$$

and $\epsilon^{\mu\nu\kappa\lambda} \equiv -[\mu\nu\kappa\lambda]/\sqrt{-g}$ is the Levi-Civita tensor.

Evidently $b^\mu u_\mu = 0$, so b^μ has only three degrees of freedom, expressed as $B^i \equiv {}^*F^{it}$, where

$$ {}^*F^{\mu\nu} = \frac{1}{2}\epsilon_{\mu\nu\kappa\lambda}F^{\kappa\lambda} = b^\mu u^\nu - b^\nu u^\mu. \tag{3.7}$$

Then

$$ b^t = B^i u^\mu g_{i\mu}, \tag{3.8}$$

$$ b^i = \frac{B^i + b^t u^i}{u^t}. \tag{3.9}$$

The magnetic field evolution is determined by

$$ \partial_t \left(\sqrt{-g}B^i\right) = \partial_j \left[\sqrt{-g}\left(b^j u^i - b^i u^j\right)\right] \tag{3.10}$$

subject to the no-monopoles constraint

$$ \partial_i \left(\sqrt{-g}B^i\right) = 0. \tag{3.11}$$

The equation of state is

$$ P = (\gamma - 1)u. \tag{3.12}$$

To summarize: the governing equations for the fluid evolution are equations 3.1, 3.3, and 3.10, together with 3.11 and 3.12.

3.3.2 Radiation

The radiation field consists of photons with wave four-vector k^μ and momentum $p^\mu = \hbar k^\mu$. The photons follow geodesics, with

$$ \frac{\mathrm{d}x^\mu}{\mathrm{d}\lambda} = k^\mu. \tag{3.13}$$

and

$$ \frac{\mathrm{d}k^\mu}{\mathrm{d}\lambda} = -\Gamma^\lambda{}_{\mu\nu}k^\mu k^\nu, \tag{3.14}$$

where $\Gamma^\lambda{}_{\mu\nu}$ is the connection and λ is an affine parameter along the geodesic. We assume that plasma dispersion effects are negligible, so photons travel on null geodesics, $k_\mu k^\mu = 0$. The frequency of a photon in a frame with four-velocity u^μ is $\omega = -k^\mu u_\mu$ ($\nu \equiv \omega/(2\pi)$).

In nonrelativistic radiative transfer one describes the radiation field with the specific intensity I_ν (here and throughout we ignore polarization), which is frame-dependent. However, $I_\nu/\nu^3 \propto f_R$ where f_R is the

radiation distribution function

$$f_R(x^\mu, p_i) = \frac{\mathrm{d}N}{\mathrm{d}^3x\mathrm{d}^3p}, \tag{3.15}$$

where $\mathrm{d}^3p = \mathrm{d}p_1\mathrm{d}p_2\mathrm{d}p_3$. Because $\mathrm{d}N$, $\mathrm{d}^3xp^t\sqrt{-g}$, and $\mathrm{d}^3p/(p^t\sqrt{-g})$ are invariant, f_R is also invariant.

The evolution of f_R is given by the Boltzmann equation,

$$\frac{\mathrm{D}f_R}{\mathrm{d}\lambda} = C[f_R] \tag{3.16}$$

where λ is an affine parameter along a photon trajectory (geodesic) and $C[f_R]$ accounts for interactions with matter: emission, absorption, and scattering of photons. The Liouville operator $\mathrm{D}/\mathrm{d}\lambda$ is a derivative along the photon trajectory in phase space.

One can rewrite the Boltzmann equation as the radiative transfer equation,

$$\frac{\mathrm{D}}{\mathrm{d}\lambda}\left(\frac{I_\nu}{\nu^3}\right) = \left(\frac{\eta_\nu}{\nu^2}\right) - (\nu\chi_\nu)\left(\frac{I_\nu}{\nu^3}\right). \tag{3.17}$$

Here the extinction coefficient

$$\chi_\nu \equiv \alpha_\nu + \sigma_\nu, \tag{3.18}$$

and the emission coefficient

$$\eta_\nu \equiv j_\nu + \eta^s_\nu(I_\nu), \tag{3.19}$$

where j_ν is the fluid emissivity, $\eta^s_\nu(I_\nu)$ is the scattering contribution to emissivity, σ_ν is the scattering extinction coefficient, and α_ν is the absorption coefficient. Each of the quantities in parentheses in (3.17) is invariant.

We neglect stimulated Compton scattering. The ratio of stimulated to spontaneous scattering is the photon occupation number in the scattered state. Models of highly sub-Eddington accretion onto supermassive black holes commonly feature: (1) relativistic electrons with $\Theta_e \equiv kT_e/(m_ec^2) > 1$, corresponding to a mean amplification factor after Compton scattering of $\approx 16\Theta_e^2$; (2) a low frequency (millimeter or far-IR) peak in the spectrum at ν_{pk} where the synchrotron absorption optical depth is $\mathcal{O}(1)$. The energetically important single scattering events therefore produce scattered photons with $\nu_{sc} \sim \nu_{pk}16\Theta_e^2$. For moderate accretion rates (i.e. scattering depth $\tau_s < 1$ for the disk), the photon occupation number at ν_{sc} is small, and so stimulated Compton scattering will be negligible.

A consequence of our neglect of stimulated Compton scattering is that in a purely scattering medium the radiation field will approach a Wien (Boltzmann) distribution rather than a Bose-Einstein distribution.

We verify this in Section 3.5.2.

To summarize: the governing equations for the radiation are (3.17), (3.14), and (3.13), together with appropriate expressions for the emission, scattering, and absorption coefficients.

3.3.3 Radiation-Fluid Interactions

In this section we adopt units such that $c = 1$ unless otherwise stated. It is apparent from Equations (3.3) and (3.17) that the fluid acts on the radiation through extinction and emission coefficients χ_ν and η_ν. The radiation acts on the fluid through the four-force density G_μ. We want to make these representations consistent. Begin with the manifestly covariant expression

$$R^{\mu\nu} = \int \frac{\mathrm{d}^3 p}{\sqrt{-g}p^t}\ p^\mu p^\nu f_R. \tag{3.20}$$

Then

$$G^\mu = -\nabla_\nu \int \frac{\mathrm{d}^3 p}{\sqrt{-g}p^t} p^\mu p^\nu f_R = -h \int \frac{\mathrm{d}^3 p}{\sqrt{-g}p^t} p^\mu \frac{\mathrm{D}f_R}{\mathrm{d}\lambda}. \tag{3.21}$$

The last equality follows from an expansion of $\mathrm{D}/\mathrm{d}\lambda$ and an integration by parts over momentum space (Lindquist 1966).

Using $f_R = I_\nu/(h^4\nu^3)$, and equations (3.17) and (3.21),

$$G^\mu = \frac{1}{h^3} \int \frac{\mathrm{d}^3 p}{\sqrt{-g}p^t} p^\mu \left[(\nu\chi_\nu)(I_\nu/\nu^3) - (\eta_\nu/\nu^2)\right] \tag{3.22}$$

where ν, χ_ν, I_ν, and η_ν are all evaluated in a frame with four-velocity u^μ.

G^μ can be evaluated in an orthonormal tetrad frame comoving with the fluid

$$e^\mu_{(a)}, \quad e^\mu_{(t)} = u^\mu \tag{3.23}$$

We will call this the "fluid frame." In the fluid frame,

$$G_{(a)} = \int \mathrm{d}\nu \mathrm{d}\Omega \left(\chi_\nu I_\nu - \eta_\nu\right) n_{(a)}, \tag{3.24}$$

where $n_{(a)} \equiv p_{(a)}/(h\nu)$. Then

$$G^\mu = e^\mu_{(a)} G^{(a)}. \tag{3.25}$$

which is manifestly consistent with energy-momentum gains and losses by the radiation field.

3.4 Numerical Method

`bhlight` combines a second order flux-conservative ideal GRMHD integrator (Gammie et al., 2003) with a Monte Carlo scheme for radiation transport (Dolence et al., 2009) through radiation-fluid interactions into a fully explicit GRRMHD scheme that is second order in space and first order in time for smooth flows. In this work we restrict ourselves to one- and two-dimensional flows, although the scheme can be trivially generalized to three spatial dimensions.

3.4.1 Fluid Integration

The fluid integrator in `bhlight` is taken from `harm`, a conservative second order shock-capturing scheme on a two-dimensional mesh with an arbitrary spacetime metric. Here we give a brief summary of the method. Also, we adopt units such that $c = 1$, and for black holes we set $GM = 1$.

The fluid sector in `bhlight` updates a set of conserved variables $\mathbf{U}$:

$$\mathbf{U} = \sqrt{-g} \left(\rho_0 u^t, T^t_{\ t}, T^t_{\ i}, B^i \right), \tag{3.26}$$

corresponding to the variables whose coordinate time derivatives are given in §3.3.1. These conserved variables are updated by fluxes $\mathbf{F}$:

$$\mathbf{F} = \sqrt{-g} \left(\rho_0 u^i, T^i_{\ t}, T^i_{\ j}, B^i \tilde{v}^j - B^j \tilde{v}^i \right), \tag{3.27}$$

which in turn are calculated from the primitive variables $\mathbf{P}$:

$$\mathbf{P} = \left(\rho_0, u, \tilde{v}^i, B^i \right), \tag{3.28}$$

where

$$\tilde{v}^i = v^i + \frac{\gamma \beta^i}{\alpha}, \tag{3.29}$$

where $v^i = u^i / u^0$ is the fluid spatial 3-velocity, $\gamma = \sqrt{1 + g_{ij} u^i u^j}$, $\alpha = \sqrt{-1/g^{00}}$ is the lapse, and $\beta^i = g^{0i}\alpha$ is the shift. Unlike v^i, $\tilde{v}^i$ ranges over $-\infty < \tilde{v}^i < \infty$. In the Newtonian formulation all transformations between the nonrelativistic analogs of $\mathbf{U}$, $\mathbf{F}$, and $\mathbf{P}$ are analytic, but in the covariant formulation there is no general analytic form for $\mathbf{P}(\mathbf{U})$.

The fluid update each timestep maps $\mathbf{P}^n$ to its updated value $\mathbf{P}^{n+1}$ by updating the conserved variables. Beginning with $\mathbf{P}^n$, the scheme calculates $\mathbf{U}^n = \mathbf{U}(\mathbf{P}^n)$ and $\mathbf{F}^n = \mathbf{F}(\mathbf{P}^n)$ via closed-form expressions, for $\mathbf{F}^n$

after a reconstruction step that estimates $\mathbf{P}^n$ at zone boundaries from values at zone centers. The update $\mathbf{U}^n \rightarrow \mathbf{U}^{n+1}$ over a timestep Δt is given by

$$\mathbf{U}^{n+1} = \mathbf{U}^n + \Delta t \left(-\frac{\mathbf{F}^{n+1/2}_{i+1,j} - \mathbf{F}^{n+1/2}_{i,j}}{\Delta x^1} - \frac{\mathbf{F}^{n+1/2}_{i,j+1} - \mathbf{F}^{n+1/2}_{i,j}}{\Delta x^2} + \dot{\mathbf{U}}^{n+1/2} \right), \tag{3.30}$$

where $\dot{\mathbf{U}}$ represents the source terms such as those associated with the spacetime connection, values at $n + 1/2$ are estimated from a similar first-order step to $\mathbf{U}^{n+1/2}$, and i, j here denote spatial indices in x^1 and x^2, respectively. This forms a second order, explicit timestepping scheme to $t + \Delta t$, and then $\mathbf{P}^{n+1}$ is found by numerically solving $\mathbf{U}(\mathbf{P}^{n+1}) = \mathbf{U}^{n+1}$ (see Noble et al. 2006 and Mignone & McKinney 2007).

The fluxes $\mathbf{F}(\mathbf{P})$ are evaluated at zone faces using Local Lax Friedrichs fluxes. Primitive variables on either side of the zone face are determined through slope-limited linear reconstruction. We typically use the monotonized central limiter for reconstruction, but it is trivial to use higher order methods as well.

Naively differencing the induction equation (3.10) will not preserve a numerical representation of the no-monopoles constraint (3.11); the monopole density will undergo a random walk from zero with a step size determined by truncation error. Unless directly controlled, the monopole density can grow quickly and corrupt the solution. A variety of techniques for avoiding or removing magnetic monopoles exist; `bhlight` employs the flux-interpolated constrained transport (flux-CT) scheme introduced by Tóth (2000). Although this introduces some additional diffusivity into the scheme, it is simple and effective. Details of the implementation are given in Gammie et al. (2003).

3.4.2 Radiation Transport

`bhlight` uses nearly the same Monte Carlo implementation as `grmonty`, with a few important differences. The Monte Carlo samples are referred to here as superphotons. Each superphoton has a weight w (the number of photons carried by the superphoton), a momentum p_μ ($p_\mu = \hbar k_\mu$ and $p_\mu p^\mu = 0$), and a position x^μ.

The Monte Carlo representation of the the photon distribution function is

$$f_{R,MC} = \sum_k w_k \, \delta^3(x^i - x^i_k) \delta^3(p_j - p_{j,k}) \tag{3.31}$$

where $\delta^3(x^i - x^i_k) = \delta(x^1 - x^1_k)\delta(x^2 - x^2_k)\delta(x^3 - x^3_k)$, etc. The sum is taken over all photon samples in the model, labeled by the index k, and w_k are the weights. Like f_R, $f_{R,MC}$ is invariant because w_k, $\delta^3(x^i - x^i_k)/(\sqrt{-g}p^t)$, and $\delta^3(p_j - p_{j,k})\sqrt{-g}p^t$ (with p_j *covariant*) are all invariant.

Using equation (3.20), the stress-energy tensor is

$$R^{\mu\nu} = \sum_k \frac{p_k^\mu p_k^\nu}{\sqrt{-g}p_k^t} w_k \delta^3(x^i - x_k^i) \tag{3.32}$$

This can be averaged over a three-volume $\Delta^3 x = \Delta x^1 \Delta x^2 \Delta x^3$ to obtain an estimate for $\bar{R}^{\mu\nu}$:

$$\bar{R}^{\mu\nu} \approx \frac{1}{\Delta^3 x} \int d^3x R^{\mu\nu} = \frac{1}{\sqrt{-g}\Delta^3 x} \sum_k \frac{p_k^\mu p_k^\nu}{p_k^t} w_k \tag{3.33}$$

where now the sum is taken only over photons within the three-volume (zone) in question.

Initializing the radiation field

How should one initialize $f_{R,MC}$? In `bhlight`'s target applications this question usually does not arise because f_R relaxes rapidly to a quasi-equilibrium, so one can set $f_R = 0$ in the initial conditions. In test problems, however, an accurate initial f_R may be required. In this case one wants to sample a set of photons in a single zone centered at x_c, that is, we want to sample $\Delta^3 x f_R(x_c)$.

One strategy is to sample f_R directly in a coordinate frame, using the invariance of f_R. For example, if f_R is thermal in the fluid frame, then the distribution function in any coordinate frame is $c^2 B_\nu/(h^4\nu^3)$, where B_ν is the Planck function, and $\nu = -u^\mu k_\mu/(2\pi)$.

A second strategy, which we adopt, is to sample f_R in the fluid frame (comoving indices are denoted by parentheses). Then we must take care: $\Delta^3 x f_R(x_c)$ is not invariant, because the volume element $\Delta^3 x$ is not invariant. But $\Delta^3 x \sqrt{-g} p^t$ *is* invariant, so $(\Delta^3 x'/\Delta^3 x) = \sqrt{-g}p^t/p^{(t)}$, where $\Delta^3 x'$ is a fluid frame volume element, and $\sqrt{-g} = 1$ in the fluid frame. Then $\Delta^3 x f_R(x_c) = (\Delta^3 x/\Delta^3 x')\Delta^3 x' f_R = (p^{(t)}/(\sqrt{-g}p^t))\Delta^3 x' f_R$. This suggests that we can sample $\Delta^3 x' f_R$ in the fluid frame and then multiply the photon number $\mathrm{d}N$ by the corresponding $p^{(t)}/(\sqrt{-g}p^t)$ to obtain a fair sample of $\Delta^3 x f_R$ in the coordinate frame[4].

This second strategy can be described more explicitly in terms of the Monte Carlo samples as follows. A list of photons in a single zone is obtained by taking

$$\int_{\Delta^3 x} d^3x \, f_{R,MC} = \sum_k w_k \, \delta^3(p_j - p_{j,k}) \tag{3.34}$$

where the sum is over photon samples in a single zone. This is not invariant because $\delta^3(p_j - p_{j,k})$ is not invariant, so one must take care in sampling $p_{j,k}$ and w_k. Suppose we sample $f_R \Delta^3 x'$ in the tetrad frame. This gives us a list of weights and momenta. We can transform back to the fluid frame using the invariance

[4]We are indebted to F. Foucart for identifying a typographical error in this paragraph.

of $\sqrt{-g}p^t\delta(p_j - p_{j,k})$, so that each $w_k\delta(p_j - p_{j,k})$ in the tetrad frame becomes $w_k\sqrt{-g}(p^t/p^{(t)})\delta(p_j - p_{j,k})$ in the coordinate frame. We can therefore obtain a fair sample by adjusting the weights by a factor of $\sqrt{-g}p^t/p^{(t)}$ in transforming from the fluid frame to the coordinate frame.

Geodesic integration

The position and wavevector of each superphoton is evolved individually by integrating Equations (3.13) and (3.14) numerically. Since evaluation of Christoffel symbols is costly, it is sensible to minimize the number of evaluations per timestep.

We use the Verlet algorithm, a second order method that requires only one evaluation of the connection (number of evaluations is typically the order of the scheme). The algorithm as used in `bhlight` is identical to that used in `grmonty` and is described explicitly in Dolence et al. (2009).

The Verlet method may be applied iteratively *without re-evaluating the Christoffel symbols*. For a fractional tolerance of 10^{-3} and the timesteps (corresponding to the $\Delta\lambda$) taken in `bhlight`, the scheme always converges. Although as of this writing we integrate all four components of k^μ, one could potentially integrate three components and use $k^\mu k_\mu = 0$ to evaluate the fourth, suppressing numerical errors and computational expense by a factor of 4/3.

Units

The radiation sector uses cgs units, except that photon wavevector components are measured in units of the electron rest mass energy. We therefore have to convert between units in the fluid sector and units in the radiation sector. For black hole spacetimes, this is done by choosing a cgs value for the fluid length unit and the fluid time unit, here

$$\mathcal{L} = \frac{GM}{c^2}, \tag{3.35}$$

and

$$\mathcal{T} = \frac{GM}{c^3}, \tag{3.36}$$

respectively. We also need a mass unit. Notice that the mass unit is *not* provided by the black hole mass in the test fluid ($\rho\mathcal{L}^3 \ll M$) approximation used here. Instead we must scale the density, or equivalently the mass accretion rate, by choosing a cgs value for the mass unit $\mathcal{M}$. Then, e.g., $\rho_{\rm CGS} = \rho_{\rm FLUID}\mathcal{M}/\mathcal{L}^3$.

The components of the code photon wavevector k^μ are measured in units of $m_e c^2$. One might then be concerned about consistency between the transfer equation and the geodesic equation. The only condition for consistency is that the differential optical depth $d\tau_\nu = (\nu\kappa_\nu)d\lambda$, which in turn requires that the $\nu d\lambda = ds$,

i.e. that the units used in defining ν and $d\lambda$ be consistent and that the correct conversion be made from fluid sector units to cgs. In practice, then, we evaluate $\nu\kappa_\nu$ in cgs units in the fluid frame and set $d\tau_\nu = \mathcal{N}(\nu\kappa_\nu)d\lambda$, with $\mathcal{N} \equiv h\mathcal{L}/(m_e c^2)$.

Superphoton Weighting

The passive Monte Carlo code `grmonty` is designed to maximize the signal to noise in the final spectrum, which is measured in logarithmic intervals in frequency at spatial infinity. The optimum allocation of weights would then place equal numbers of superphotons in each bin in $\log \nu$. This requires an estimate of the final spectrum; `grmonty` estimates the final spectrum by integrating over the simulation volume, assuming the flow is optically thin at all frequencies, neglecting gravitational redshift and Doppler shift, and setting the weights accordingly.

In `bhlight`, by contrast, the weights should be designed to minimize errors in the dynamical evolution, i.e. in G_μ. The momentum and energy exchange associated with each radiation-fluid interaction is proportional to $wh\nu$, where ν is the fluid frame frequency. This suggests that we should distribute energy uniformly among superphotons (as in Abbott & Lucy 1985) to minimize the interaction noise, and thus set $w \propto 1/\nu$. This is not generally possible because the four-velocity fluctuates across the simulation domain, but we will not do too badly if we ignore Doppler shift and gravitational redshift and thus set $w \propto 1/\nu$ when sampling the emissivity.

`bhlight`'s constant-energy-per-superphoton weighting scheme limits spectral resolution at low and high frequencies where the specific energy density is small prior to scattering. These parts of the spectrum have little impact on the dynamical evolution, however, and higher quality spectra can be extracted in post-processing using `grmonty`.

Emissivity

At each timestep we sample the emissivity in the invariant four-volume $\sqrt{-g}\Delta t \Delta^3 x$ of each zone based on the fluid values at the half-step. It is easiest to sample the fluid emission in a comoving tetrad, where we have a simple expression for the emissivity.

The emissivity is

$$j_\nu = \frac{1}{\sqrt{-g}} \frac{dE}{d^3x dt d\nu d\Omega}. \tag{3.37}$$

Using $dE = h\nu dN$ where N is the number of photons, we can write

$$\int d\Omega \, j_\nu = \frac{h}{\sqrt{-g}} \frac{dN}{d^3x dt d\log\nu}. \tag{3.38}$$

Since $dN = w dN_s$ where N_s is the number of superphotons, we can then write for the number of superphotons produced per logarithmic interval in a single zone with volume $\Delta^3 x$:

$$\frac{dN_s}{d\log\nu} = \sqrt{-g}\Delta t \Delta^3 x \frac{1}{hw(\nu)} \int \mathrm{d}\Omega \, j_\nu. \tag{3.39}$$

In writing (3.39) we have made use of the invariance of $\sqrt{-g}d^3x dt$. Here $w(\nu) \propto 1/\nu$, and the constant of proportionality is set dynamically to keep the number of superphotons in the computational domain approximately constant.

`bhlight` samples equation 3.39 between minimum and maximum frequencies $\nu_{\rm min}$ and $\nu_{\rm max}$, where the limits are set so that νj_ν is small outside this region in frequency space. It then uses a rejection scheme, sampling a uniform distribution in $\log\nu_{min} < \log\nu < \log\nu_{max}$ and a uniform distribution in $0 < r < (\mathrm{d}N_s/\mathrm{d}\log\nu)_{\rm max}$, where $(\mathrm{d}N_s/\mathrm{d}\log\nu)_{\rm max}$ is the maximum of Equation 3.39. A sample is rejected when $r > \mathrm{d}N_s/\mathrm{d}\log\nu$.

The angular distribution of photons is also sampled by rejection. The photon direction is given by (θ, ϕ), where θ is the angle between the magnetic field and photon direction in the fluid frame and ϕ is the corresponding azimuthal angle. `bhlight` samples a uniform distribution in $0 \leq \cos\theta < 1$, and a uniform distribution in $0 \leq r < 1$. A sample is rejected if $r > j_\nu(\theta)/j_{\nu,\rm max}$. It then samples a uniform distribution in $0 \leq \phi < 2\pi$. To ensure that the net force due to emission in the fluid frame is zero to machine precision, photons are generated in pairs. Thus, a second photon is generated with the same frequency and $\cos\theta' = -\cos\theta$ and $\phi' = \phi + \pi$. In the fluid frame, $k^{(t)} = \omega$, $k^{(x)} = \omega\sin\theta\cos\phi$, $k^{(y)} = \omega\sin\theta\sin\phi$, and $k^{(z)} = \omega\cos\theta$, where $e^{(z)}$ is parallel to the magnetic field. Once we have a superphoton sample in the comoving frame it is transformed to the coordinate frame using a pre-constructed orthonormal tetrad $e^\mu_{(a)}$. The superphoton x^μ is set to the zone center to avoid additional orthonormal tetrad construction.[5]

Sampling is a subdominant computational expense in `bhlight`, so although one could develop more efficient sampling schemes, a simple rejection scheme is adequate.

Four-momentum is locally conserved and so superphoton emission implies a back-reaction on the emitting fluid. A pair of emitted superphotons with wavevectors k^μ_1, k^μ_2 correspond to a change in four-momentum Δp^μ (in fluid code units):

$$\Delta p^\mu = \mathcal{P} w \left(k^\mu_1 + k^\mu_2\right), \tag{3.40}$$

[5]Because photons are created at zone centers, our scheme will fail when individual zones become optically thick. Should this become a problem the scheme can be modified so that new superphotons are distributed within a zone.

where $\mathcal{P} = m_e/\mathcal{M}$, which in turn specifies the contribution to the four-force density ΔG_μ:

$$\Delta G_\mu = -\frac{1}{\sqrt{-g}\Delta^3 x \Delta t}\Delta p_\mu, \tag{3.41}$$

where all geometric quantities are evaluated at zone centers. Because photons are emitted in pairs, the spatial components of k^μ cancel in the fluid frame, and $\delta p_\mu \propto u_\mu$.

Absorption

`grmonty` treats absorption deterministically by continuously decrementing w along a ray. A similar deterministic procedure has been shown to suppress noise in Monte Carlo radiation hydro schemes (e.g. Noebauer et al. 2012) in flat space. However, formulating such a scheme in general relativity, where photons move along geodesics, is more complicated because the photons follow curved trajectories through each zone.

In `bhlight` we treat absorption probabilistically. While stepping a superphoton by $\Delta\lambda$ along a geodesic, the incremental optical depth to absorption $\Delta\tau_a = \mathcal{N}\kappa_{\nu,abs}\nu\Delta\lambda$. Here $\nu\kappa_{\nu,abs}$ is the invariant absorption coefficient, evaluated in the fluid frame and interpolated to x^μ. An absorption occurs if

$$\Delta\tau_a > -\log r_a, \tag{3.42}$$

where $0 < r_a < 1$ is sampled uniformly; the absorption occurs at $\Delta\tau_a = -\log r_a$. To process the event we push the superphoton back, $\lambda \rightarrow \lambda + \Delta\lambda(\log r_a/\Delta\tau_a)$, put the superphoton four-momentum into the fluid at that location, and annihilate the superphoton.

The four-momentum change in the fluid Δp^μ due to absorption of a superphoton with wavevector k^μ is

$$\Delta p^\mu = \mathcal{P} w k^\mu. \tag{3.43}$$

This can be expressed as a contribution to the radiation four-force density ΔG_μ:

$$\Delta G_\mu = \frac{\Delta p_\mu}{\sqrt{-g}\Delta^3 x \Delta t}, \tag{3.44}$$

where $\sqrt{-g}$ is evaluated at the zone center.

Scattering

We treat scattering probabilistically in `bhlight`, as in `grmonty`. Scattering is similar to absorption, i.e. scattering occurs when

$$\Delta\tau_s > -(\log r_s)/b_s, \tag{3.45}$$

where $0 < r_s < 1$ is sampled uniformly, $\Delta\tau_s = \mathcal{N}\kappa_{\nu,s}\nu\Delta\lambda$, and $\nu\kappa_{\nu,s}$ is the invariant scattering opacity. Because scattering events are rare but energetically important we have introduced a bias parameter $b_s > 1$ to enhance the probability of sampling scattering events. To process the event, we push the photon back along the geodesic from $\lambda + \Delta\lambda$ to $\lambda + \Delta\lambda \log r_s/(b_s\Delta\tau_s)$. To preserve photon number a scattered superphoton is created with weight $w_s = w/b_s$ and the original superphoton has weight set to $w' = w - w_s$.

In general, a superphoton is subject to both absorption and scattering simultaneously. In a deterministic treatment, the code must dynamically choose which process, if any, to apply to the superphoton. To handle this in an unbiased manner, for each photon we, assuming that at least one of the inequalities Eqns. 3.42 and 3.45 has been satisfied, choose which interaction to process according to a similar weighted sampling. That is, for

$$\frac{-\log r_a}{\Delta\tau_a} < \frac{-\log r_s}{b_s\Delta\tau_s}, \tag{3.46}$$

the absorption interaction is chosen; else, scattering is chosen. With this method, large optical depth or bias in one interaction will not serve to decrease the physical effect of the other interaction, although it will increase the number of superphotons required to resolve both interactions simultaneously.

How should we set b_s? Most of our models have $\tau_s \ll 1$, so only $\approx \tau_s$ superphotons would produce scattering events if $b_s = 1$, and the energy per superphoton would increase by the mean amplification factor $A \approx 1 + 4\Theta_e + 16\Theta_e^2$.[6] This suggests that we should set $b_s \sim A$ to maintain constant energy per superphoton. There are two failure modes to be avoided, however. First, if $b_s \gtrsim 1/\tau_s$ then each superphoton will scatter more than once and the number of superphotons on the grid will grow exponentially. Second, if $Awh\nu$ is larger than the total internal energy in the zone where the scattering occurs then the zone energy will be negative after scattering (more on this in the next subsection). Together, this suggests that we set

$$b_s = A\,\mathrm{MAX}\left(\mathcal{C}, \frac{wh\nu}{u\sqrt{-g}\Delta^3 x}\right). \tag{3.47}$$

Here $\mathcal{C}$ depends only on t and is dynamically adjusted to control the number of scattered superphotons in the simulation. The requirement $b_s\tau_s \sim 1$ is equivalent to each superphoton scattering once between emission

[6] This approximate expression overestimates A by 16% at $\Theta_e \approx 1/2$. A better estimate, which underestimates A by 4% at $\Theta_e \approx 0.02$, is $A - 1 \approx 4\Theta_e - 2\Theta_e^{3/2} + 16\Theta_e^2$.

and escape through the boundary (neglecting absorption). Over a timestep Δt, one can estimate the number of photons which escape through the boundaries of a domain with linear dimension L as $Nc\Delta t/L$, where N is the desired total number of superphotons (which sets the weights for emission as described previously). To enforce the requirement that each superphoton scatter once, $\mathcal{C}$ is calculated dynamically as the ratio of this estimate to the real number of scattering events per timestep, averaged over some timescale.

Each scattered superphoton is generated from an incident superphoton wavevector k^μ as follows. The four-momentum p^μ of the scattering electron is sampled from a thermal (Maxwell-Jüttner) distribution according to the procedure described in Canfield et al. (1987). The scattered superphoton wavevector k_s^μ is sampled from the Klein-Nishina differential scattering cross section in the rest frame of the scattering electron and boosted to the fluid frame and then transformed to the coordinate frame. It is then assigned a weight and entered in the list of active superphotons.

Each scattering event generates a change in fluid four-momentum,

$$\Delta p^\mu = \mathcal{P}\frac{w}{b_s}\left(k^\mu - k_s^\mu\right) \tag{3.48}$$

and a corresponding contribution to the fluid through the four-force density G_μ,

$$\Delta G_\mu = \frac{\Delta p_\mu}{\sqrt{-g}\Delta^3 x \Delta t} \tag{3.49}$$

where $\sqrt{-g}$ is evaluated at the zone center.

3.4.3 Radiation Force in Fluid Evolution

The radiation force is treated in an operator-split fashion. The fluid integrator initially updates the conserved variables $\mathbf{U}$ from step n to $n+1$ over the entire timestep Δt without radiation, i.e. it performs $\mathbf{U}^n \rightarrow \mathbf{U}^{n+1'}$ as described in Section 3.4.1. This fluid integration generates half-step fluid primitive variables $\mathbf{P}^{n+1/2}$; these values are sent to the radiation sector and used to evaluate the total radiation four-force density $G_\mu(\mathbf{P}^{n+1/2})$ for each zone. The fluid integrator then updates the fluid variables with the radiation interaction $\mathbf{U}^{n+1'} \rightarrow \mathbf{U}^{n+1}$ by considering only the radiation contribution to the conserved energy and momentum variables:

$$\left(\sqrt{-g}T^t{}_\nu\right)^{n+1} = \left(\sqrt{-g}T^t{}_\nu\right)^{n+1'} + \Delta t\sqrt{-g}G_\nu. \tag{3.50}$$

$\mathbf{U}^{n+1}$ then are the final conserved fluid variables at the $(n+1)^{\text{th}}$ step. The evolution is therefore first order in time.

The evolution is explicit and the radiation and fluid share a common timestep Δt, which we set to the minimum grid zone light crossing time $\approx \Delta x/c$, where Δx is a characteristic zone lengthscale. As is well known, the radiation source terms are stiff when the timescale for exchange of energy-momentum between the fluid and radiation is smaller than a timestep. The cooling time $\tau_{cool} \equiv u/\Lambda$, where $\Lambda \equiv$ cooling rate per unit volume, $= u_\mu G^\mu \sim u_{rad} c/\lambda_{mfp}$, where λ_{mfp} is a suitably frequency-averaged absorption mean free path and $u_{rad} = R^{\mu\nu} u_\mu u_\nu$ is the radiation energy density in the fluid frame (one can perform a similar estimate for Compton cooling). Thus the source term is stiff if $u/\Lambda < \Delta x/c$ or $(u_{rad}/u)(\Delta x/\lambda_{mfp}) > 1$, or when the optical depth across a zone exceeds u/u_{rad}.

For our scheme we must also consider robustness in the presence of Monte Carlo noise. Even if $\tau_{cool}/\Delta t > 1$ the cooling rate may fluctuate upward so that a zone loses all its thermal energy in a single timestep. This can happen if $u/\langle \Lambda^2 \rangle^{1/2} \lesssim \Delta x/c$. This will differ from the usual stiffness condition only when the number of absorption events per timestep in a zone is small compared to one. The condition for robustness against this failure mode, "supercooling," where a single photon causes the zone to lose all its internal energy, is that $wh\nu < u\Delta^3 x$ (where we have left out geometric factors).

Where, then, will `bhlight` fail? The radiation force source terms are stiff when the optical depth across a single zone exceeds u/u_{rad}. For black hole accretion applications we expect this only for models in the high accretion rate regime, $\dot{M} \gtrsim 10^{-3} \dot{M}_{Edd}$, although the precise condition will depend on details of the evolution and the numerical setup. This problem could be remedied by using an implicit update, but Monte Carlo is probably not the optimal method for studying this regime anyway. The supercooling problem is more relevant for our target application to intermediate accretion rate black holes, and arises if the internal energy content of a zone is small compared to the typical superphoton energy. This can occur in low density regions over the poles of the black hole, but the fluid evolution is inaccurate there in any case (because the truncation error in internal energy is dominated by the magnetic field evolution, to which it is coupled via the total energy density), and negative internal energies are dealt with by `harm`'s floor routines, resulting in a small nonconservation of energy.

3.4.4 Parallelization

`bhlight` is a hybrid MPI/OpenMP scheme in which a single node handles the fluid integration, multiple nodes evolve the radiation, and a single additional node acts as gatekeeper between the fluid and radiation sectors. During each timestep, the only exchanges are an array of radiation four-force densities to the fluid sector and an array of fluid variables to the radiation sector via the gatekeeper node. The gatekeeper node distributes the fluid variables to all radiation nodes, and reduces the four-force density contributions from

each radiation node.

We evolve radiation on each node independently from other radiation nodes. After globally scaling the emission weights and scattering bias to yield approximately the desired number of superphotons at saturation, the code samples emission events on each radiation node, each of which has access to the entire array of fluid variables and maintains its own set of superphoton samples. Emission, absorption, and scattering events generate a four-force density contribution. At the end of every timestep, these contributions are reduced by the primary radiation node over MPI. Each radiation node is individually parallelized under OpenMP, further dividing the superphoton calculations across individual compute cores. We parallelize the main compute loops for the fluid sector with OpenMP, which enables completion in a reasonable clock time for an axisymmetric calculation.

3.4.5 Implementation Details

In attempting to describe our numerical implementation in a coherent narrative we have omitted certain secondary topics, which we now collect here.

- The radiation sector in `bhlight` makes extensive use of random numbers. We use the Mersenne Twister algorithm from the GNU Scientific Library, with a different random seed for each MPI node and each OpenMP thread.

- In axisymmetric disk calculations, we implement a form of static mesh refinement by using modified Kerr-Schild (MKS) coordinates $\{t, x^1, x^2\}$. x^1 and x^2 are related to the Kerr-Schild r, θ by $r = \exp\left(x^1\right) + r_0$ and $\theta = \pi x^2 + ((1 - h_s)/2)\sin(2\pi x^2)$, where $r_0 \in [0, \infty)$ and $h_s \in (0, 1]$ are free parameters.

- Truncation error in the geodesic integration causes k^μ to drift off the lightcone (this is a consequence of our decision to integrate all four components). We destroy superphotons with negative frequency in the fluid frame; for torus runs as in Section 3.6.2, we find $\sim 1.1 \times 10^{-6}$ destructions per geodesic update. This problem does not occur in Cartesian coordinates in Minkowski space.

- Scattered superphotons may scatter any number of additional times during the same timestep, provided sufficient optical depth to do so.

- `bhlight` does not conserve momentum and energy to machine precision because of truncation error in the geodesic integrator. However, for the integrator tolerance and typical superphoton resolutions this is not significant (for torus runs as in Section 3.6.2). At some time, the average fractional error

in energy relative to the initial energy at emission is $\sim$ few $\times 10^{-7}$; if this were to become a leading source of error, increasing the integrator tolerance is not a significant expense.

3.5 Test Suite

We have developed a suite of test problems for `bhlight`. Since the fluid and radiation sectors of `bhlight` use well tested codes, we focus on problems with coupling between the two sectors. Good test problems are hard to find, since there are few known exact solutions to the equations of radiation MHD in either Newtonian or relativistic contexts. We substitute approximate solutions to the full equations, such as some of the shocks we consider below. We do not consider pure transport tests that are trivially satisfied by a Monte Carlo scheme, such as shadow tests, expanding pulses, and dynamic diffusion[7].

3.5.1 Optically Thin Cooling

We consider the temperature evolution of an optically thin, radiating, stationary, ideal, and homogeneous gas initially at temperature T_0. The gas obeys a γ-law equation of state i.e. $p = (\gamma - 1)u$. The density and velocity of the gas are fixed; only the temperature is allowed to evolve. The bremsstrahlung-like emissivity is

$$j_\nu = N n^2 T^{-1/2} \exp\left(-h\nu/k_B T\right), \tag{3.51}$$

where $N = 5.4 \times 10^{-39}$ cm^3 K$^{1/2}$ s^{-1} Sr^{-1} Hz^{-1} is a constant. The associated cooling rate Λ is given by

$$\Lambda = -\frac{\mathrm{d}u}{\mathrm{d}t} = \int \mathrm{d}\nu \mathrm{d}\Omega j_\nu = 4\pi \frac{k_B n^2 N}{h} T^{1/2}, \tag{3.52}$$

which implies a temperature evolution

$$T(t) = T_0 \left(1 - \frac{t}{t_f}\right)^2 \tag{3.53}$$

valid from $t_i = 0$ to $t_f = h T_0^{1/2}/((\gamma - 1)\pi N n)$, the time at which the temperature of the fluid reaches zero.

For this realization we choose $\gamma = 5/3$, $t_f = 10^8$ s, and $T_0 = 10^8$ K. Figure 3.1 shows the resulting numerical evolution plotted against the analytic solution. Convergence in the L^1 norm,

$$L^1(f) \equiv \sum_i |f_{\mathrm{num},i} - f_{\mathrm{reference},i}| \tag{3.54}$$

is expected to scale as $N_s^{-1/2}$; this can be seen in Figure 3.2, which is evaluated near $t = t_f$.

[7]Such tests can be performed with the freely available `grmonty` code.

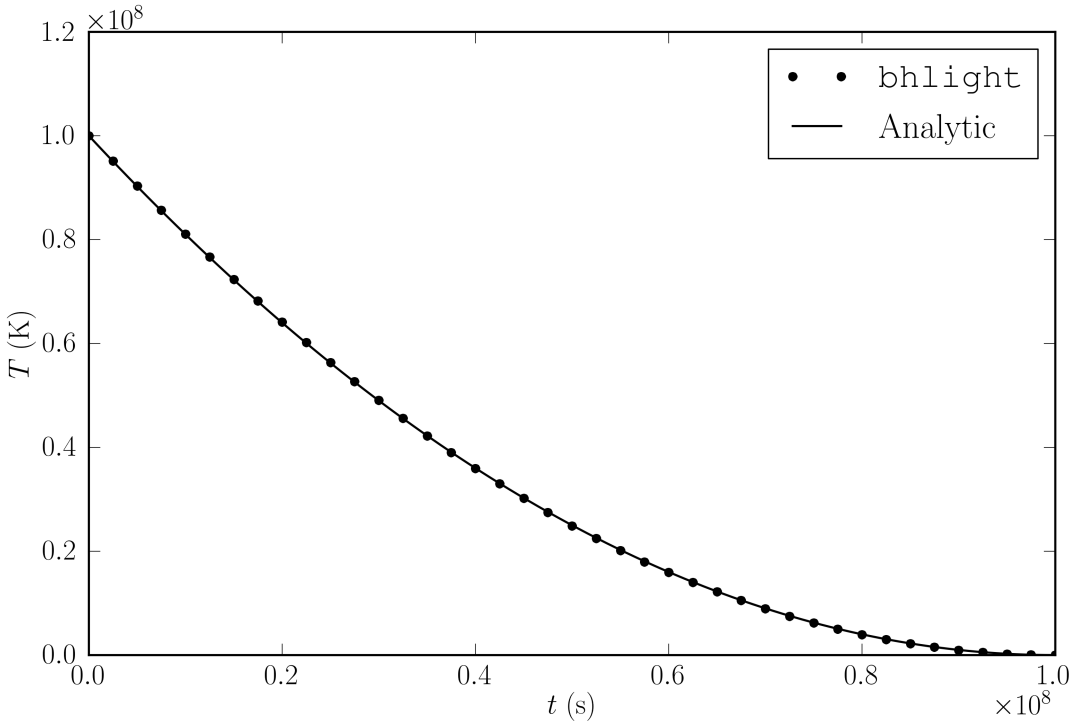

Figure 3.1: Optically thin cooling of one static fluid zone. Approximately 5×10^8 superphotons were created.

3.5.2 Compton Cooling

Consider a closed, one-zone model in which Compton scattering is the only permitted interaction between an ideal, $\gamma = 5/3$ gas initially at temperature $T_{g,i}$ and a swarm of photons all with initial frequency $\nu = \nu_0$. Fluid motion is suppressed; only the internal energy is allowed to evolve. The number of photons is conserved, and in thermal equilibrium $T_{g,f} = T_{r,f} = T_f$, the radiation approaches the Wien distribution,

$$f_R = \frac{n_\gamma}{8\pi} \left(\frac{c}{kT_f} \right)^3 \exp\left(-h\nu/(k_B T_f)\right), \tag{3.55}$$

where n_γ is the number density of photons. This tests the scattering kernel and Compton heating and cooling of the fluid.

We set the electron number density $n = 2.5 \times 10^{17}$ cm^{-3}, $T_{g,i} = 5 \times 10^7$ K, $\nu_0 = 3 \times 10^{16}$ Hz, and $n_\gamma = 2.38 \times 10^{18}$ cm^{-3}. The characteristic (Compton) relaxation time is the photon mean free time $(n_e \sigma_T c)^{-1}$ divided by the fractional energy change per scattering, $\sim kT/(m_e c^2)$, yielding a Comptonization timescale $\simeq$ 0.02 s. We can predict the final state using: (1) thermal equilibrium; (2) conservation of photon number; (3) that the final photon distribution is Boltzmann; (4) conservation of total energy. This yields $T_f = 5.19 \times 10^6$

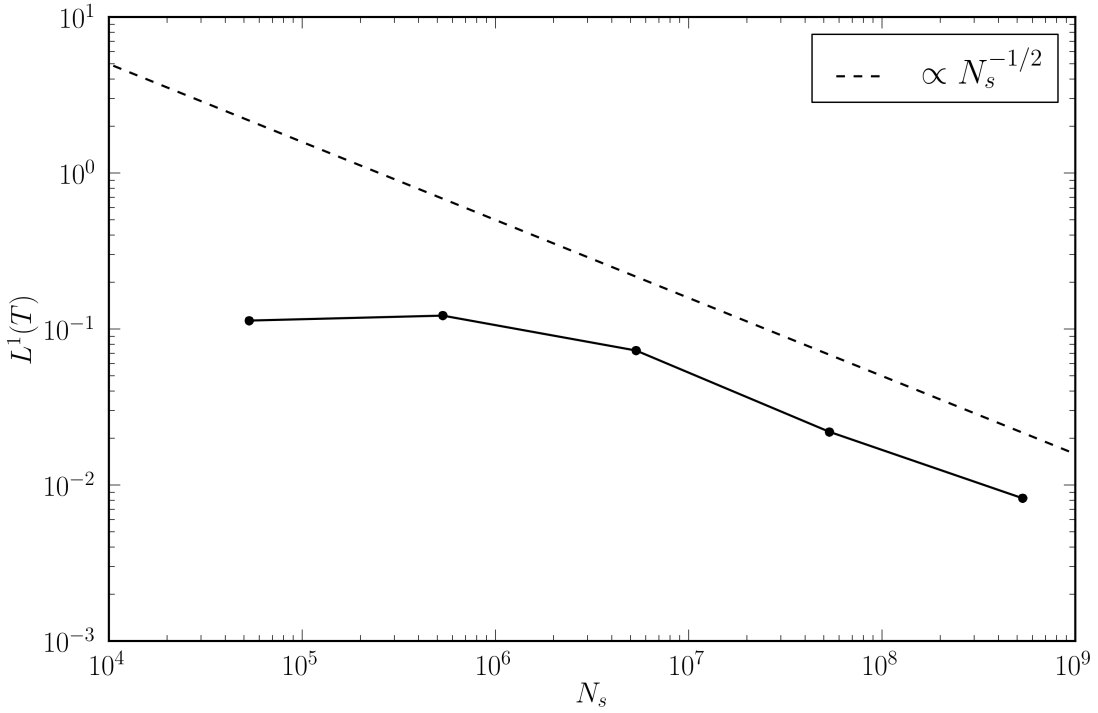

Figure 3.2: Convergence of the optically thin cooling test. N_s is directly proportional to the number of superphotons created.

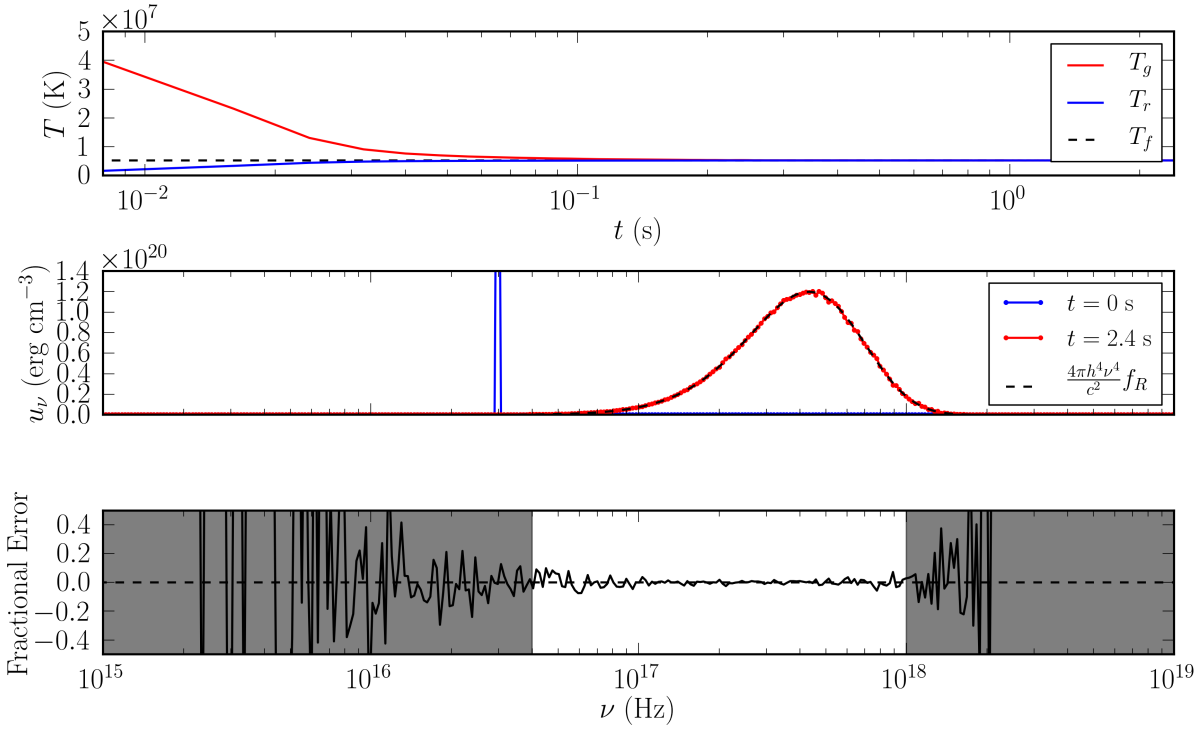

Figure 3.3: Evolution of the Comptonization problem. The top panel shows radiation and gas temperatures approaching the analytic final temperature. The middle panel shows the initial and final u_ν for the radiation, along with the analytic result for the final state. The bottom panel shows the residuals for the final spectrum; the numerical spectrum is apparently unbiased even at frequencies with low sampling resolution (shaded regions).

K. Figure 3.3 shows fluid and gas temperatures equilibrating at the correct temperature on approximately the estimated timescale, and $u_\nu \equiv \mathrm{d}E/(\mathrm{d}^3x\,\mathrm{d}\log\nu)$ plotted against the anticipated distribution along with associated residuals. Note that we define $T_r \equiv E_r/(3n_\gamma k_B)$ (E_r is the radiation energy density), which assumes a Wien distribution, and so this value is strictly valid only at late time.

3.5.3 Linearized Transfer and Energy Equations

As a test of the full transfer equation in 1D with gray absorption, consider a sinusoidal temperature perturbation in a static gas. Mihalas & Mihalas (1984) show that in this case the full transfer equation plus gas energy equation admit damped solutions. The eigenmode has perturbations $\propto \exp(i(kx - t/t_{RR}))$ for wavenumber k and decay time t_{RR}. The dispersion relation is

$$t_{RR}(k) = \left[\frac{16\sigma\kappa T_0^3}{\rho c_v}\left(1 - \frac{\alpha_0}{k}\cot^{-1}\left(\frac{\alpha_0}{k}\right)\right)\right]^{-1}, \tag{3.56}$$

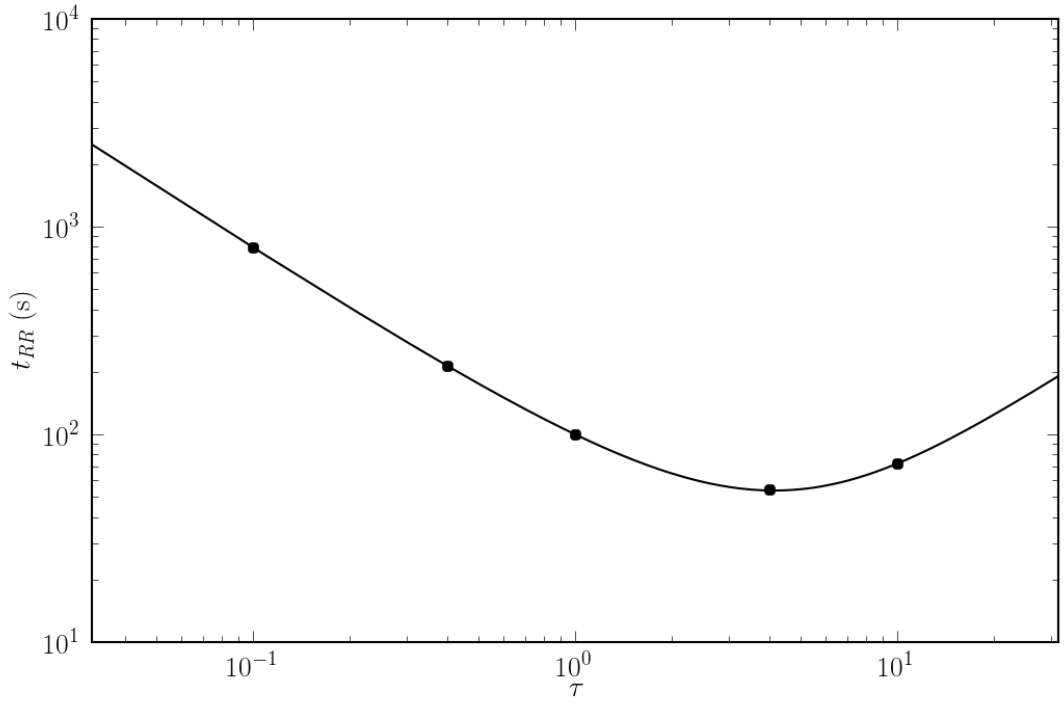

Figure 3.4: Dispersion relation for eigenmode of the transfer and energy equations as a function of optical depth per wavelength. Solid line shows analytic expectation, while points show `bhlight` results. At this resolution, the fractional error is $\approx 10^{-3}$.

where T_0 is the mean temperature, ρ is the material density, α_0 is the frequency-integrated extinction coefficient, and c_v is the specific heat capacity. We simulate this problem in `bhlight` by initializing one wavelength in a 1D box in local radiative equilibrium with 64 grid zones and periodic boundary conditions. The amplitude of the initial perturbation is $0.05T_0$. We evolve this system for a variety of optical depths per wavelength τ by varying α_0. We obtain a decay time from the amplitude of the best fit sinusoid at $t = t_{RR}$. We find good agreement with Equation 3.56 in both optically thin and optically thick regimes, as shown in Figure 3.4.

We also examine convergence for $\tau = 1$ (with 100 grid zones); this result is shown in Figure 3.5. Evidently the errors scale as $N_s^{1/2}$, as expected.

3.5.4 Relativistic Radiation MHD Linear Modes

We now also consider linear modes of the full equations of one-dimensional radiation magnetohydrodynamics; that is, we now include momentum exchange and magnetic fields. Acquiring even a linear solution to these equations with full transport is challenging, and so we resort to the approximate, relativistic

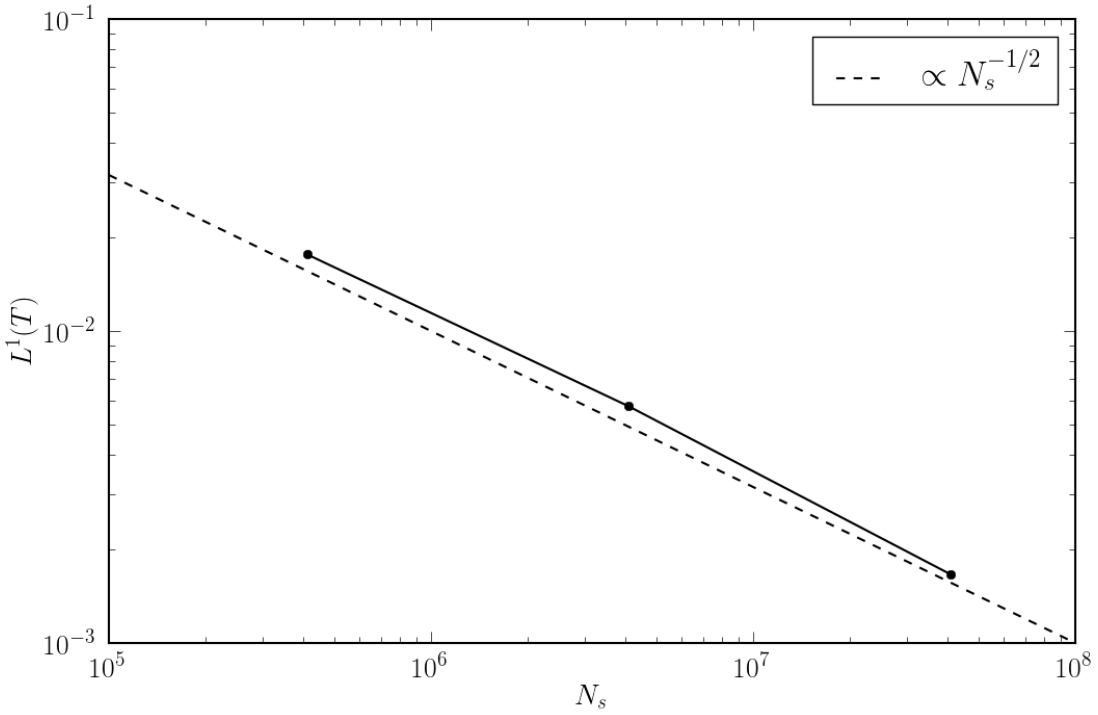

Figure 3.5: Convergence for the linear mode of the transfer and energy equations, with N_s directly proportional to the number of superphotons.

Eddington closure scheme of Farris et al. (2008) with gray opacity κ from which to extract plane-wave solutions $\mathbf{P}$. Details of our calculation for a perturbation $\delta\mathbf{P}$ for $\delta \sim \exp(\omega t - ikx)$ about a thermal equilibrium $\mathbf{P}_0$ are given in Appendix 3.C. With a magnetic field $B^i = (B_0, B_0, 0)$ we follow the non-relativistic treatment of Jiang et al. (2012) by confining variation to a plane (suppressing Alfvèn waves): $\mathbf{P} = (\rho, u, u^1, u^2, B^1, B^2, E, F^1, F^2) = (\rho_0+\delta\rho, u_0+\delta u, \delta u^1, \delta u^2, B_0, B_0+\delta B^2, E_0+\delta E, \delta F^1, \delta F^2)$. `bhlight` is not designed to evolve perturbed equilibria; we focus on cases which accomodate both `bhlight`'s numerical limitations as well as the discrepancy between the Eddington closure and `bhlight`'s full transport (i.e. we consider only many optical depths per wavelength). We study convergence of two specific cases with significant radiation pressure: a nonrelativistic radiation-modified slow MHD mode, and a relativistic radiation-modified fast MHD mode. In this section, $c = k_B = 1$. For all calculations, we use a box of length $L = 1$ with 128 grid zones, evolve to final time t_f, set the wavenumber of the perturbation $k = 2\pi$, and normalize the $\delta\mathbf{P}$ to be $\lesssim 1\%$ of the $\mathbf{P}_0$ for all $\mathbf{P}$.[8] The ratio of radiation to gas pressure $\beta_r \equiv a_R P^3/(3\rho^4)$, and the optical depth per wavelength $\tau \equiv \kappa\rho L$.

Radiation-Modified Slow Mode

For a magnetized fluid in the presence of radiation, the MHD modes are damped in a similar fashion to the radiation hydrodynamic case. We first consider the radiation-modified slow mode solution. We set $\gamma = 5/3$, $\rho = 1$, $u = 0.01$, $B_0 = \sqrt{5/6}$, $\beta_r = 1$, and $\tau = 20$ and evolve the initial conditions in `bhlight` to $t_f = 2.5$, nearly half an e-folding time. The eigenmode is given in Table 3.1. Expected convergence at t_f in the average number of extant superphotons N_s for Monte Carlo-dominated error is shown in Figure 3.6.

ω	$-0.155954250795 + 0.506371984839i$
$\delta\rho$	0.992522043854
δu	$0.0115437955397 + 0.00253571930238i$
δu^1	$-0.0799889439467 - 0.024635280384i$
δu^2	$-0.0804556011602 - 0.0252291311891i$
δB^2	$-0.00672014035309 - 0.00465692766557i$
δE	$0.0129233747759 + 0.0201394332108i$
δF^1	$0.00205715652365 - 0.00136719504591i$
δF^2	$-3.27455464963 \times 10^{-5} + 5.02957595074 \times 10^{-5}i$

Table 3.1: Radiation-Modified Slow Mode.

Radiation-Modified Fast Mode

We now consider the radiation-modified fast mode solution, for a relativistic equilbrium. We set $\gamma = 4/3$, $\rho = 1$, $u = 10$, $B_0 = \sqrt{5/6}$, $\beta_r = 1$, and $\tau = 20$ and evolve the initial conditions in `bhlight` to $t_f = 1.7$,

[8] The SageMath notebook used to evaluate these modes may be accessed via SageMathCloud at `http://bit.ly/1CCi82y`

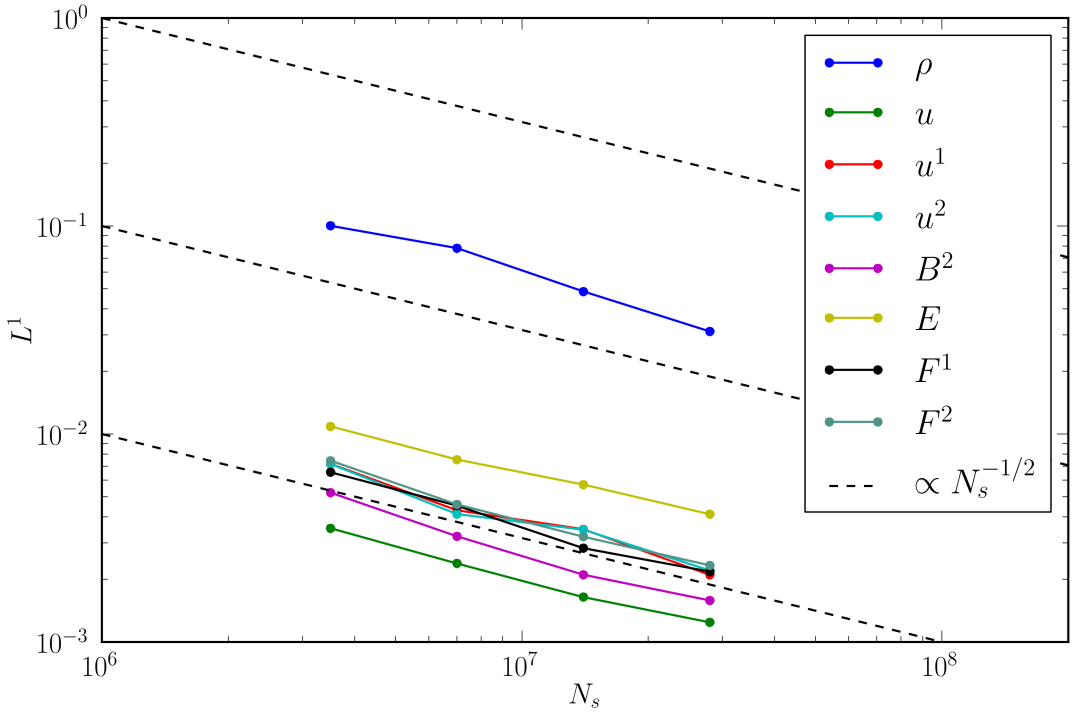

Figure 3.6: Convergence for the radiation-modified slow mode.

approximately a wave period. Note that radiation damping is not significant during this time. The eigenmode is given in Table 3.2. Expected convergence at t_f in the average number of extant superphotons N_s for Monte Carlo-dominated error is shown in Figure 3.7.

ω	$-0.155954250795 + 0.506371984839i$
$\delta\rho$	$0.0528655837266 - 0.000203781373769i$
δu	$0.704834313006 - 0.00203965222393i$
δu^1	$0.0309307265333 - 0.000125078175647i$
δu^2	$-0.00191512771962 + 0.000183786243559i$
δB^2	$0.0512475714061 - 0.000472212042911i$
δE	0.704838422737
δF^1	$-4.41864621469 \times 10^{-5} + 0.00198608271502i$
δF^2	$0.000397994468532 - 0.00462049532989i$

Table 3.2: Radiation-Modified Fast Mode.

3.5.5 Su-Olson Problem

Su & Olson (1996) found a solution in terms of integrals to the coupled energy balance and radiative transport equations in the diffusion approximation for a semi-infinite slab of static, initially cold fluid (with

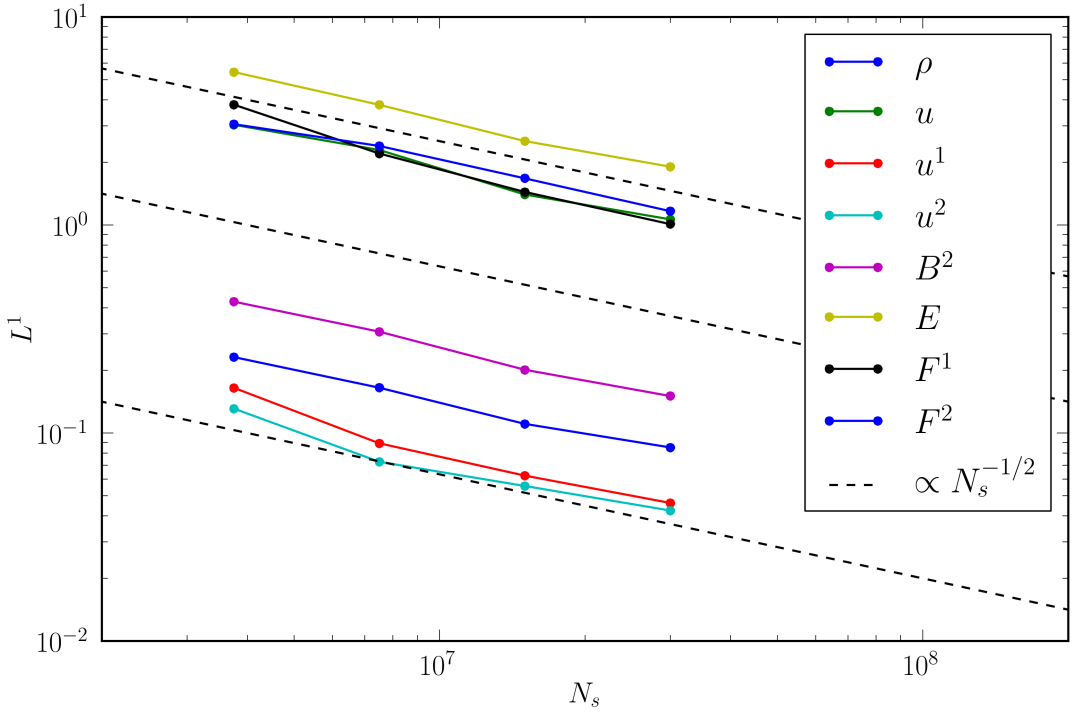

Figure 3.7: Convergence for the radiation-modified fast mode.

heat capacity $c_v = \mathscr{C}T^3$) with gray absorption coefficient α, and a Marshak (isotropic incident radiation) condition at the left boundary with incident flux F. The solution is given in terms of dimensionless gas and radiation energy densities u and v, respectively, versus the dimensionless spatial coordinate $x = \sqrt{3}\alpha z$ and dimensionless time coordinate $t = 4a_R c\alpha t'/\mathscr{C}$, where a_R is the radiation constant. u and v are defined as:

$$u(x,t) \equiv \left(\frac{c}{4}\right)\left(\frac{E(x,t)}{F}\right), \tag{3.57}$$

$$v(x,t) \equiv \left(\frac{c}{4}\right)\left(\frac{a_R T^4(x,t)}{F}\right), \tag{3.58}$$

where E is the radiation energy density.

In replicating this solution with `bhlight`, we adopt parameters such that the solution remains optically thick, without being so optically thick across a grid zone that our Monte Carlo transport scheme fails. We use 1024 grid zones on $x = [0, 50\sqrt{3}]$ and evolve the system to $t = 500$ (when the solution is approximately in equilibrium). Results are shown in Figure 3.8.

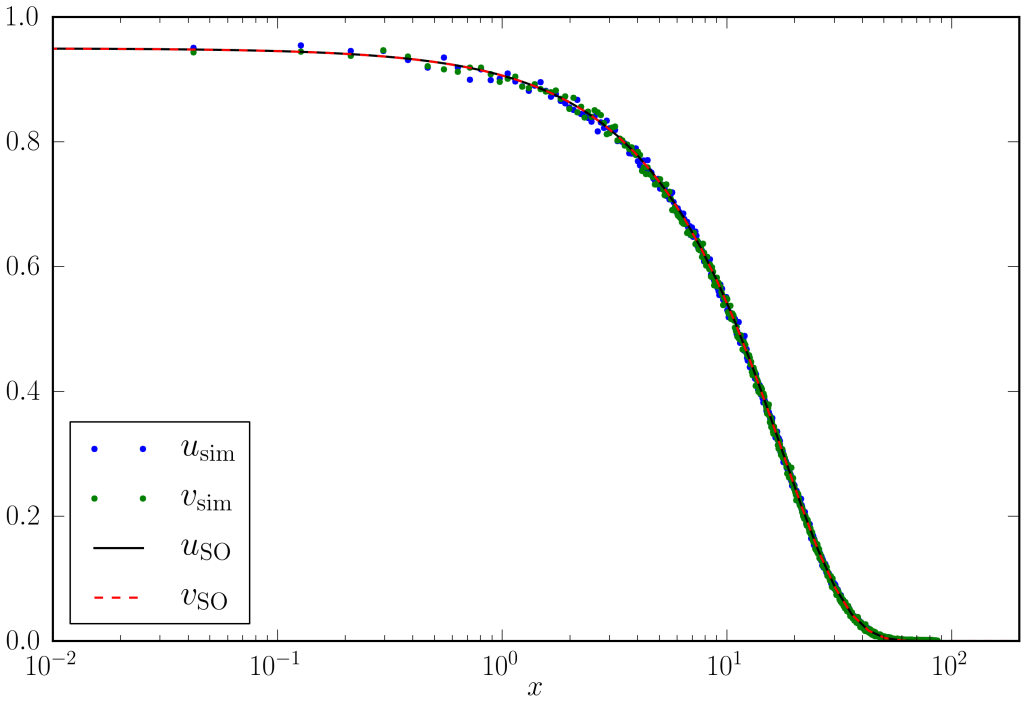

Figure 3.8: Numerical gas and radiation energy densities versus analytic gas and radiation energy densities. The `bhlight` calculation and Su-Olson results show excellent correspondence at this late time.

3.5.6 Radiative Shocks

We now turn to dynamical tests: here, 1D radiative shocks. We will use nearly the same suite of relativistic, radiative shocks considered by Farris et al. (2008) in testing their GRRMHD code, which was based on a nonequilibrium Eddington closure. Because we solve the full transfer equation, we expect disagreement on scales of order the photon mean free path.

The Farris et al. tests assume a grey opacity κ and are set in Minkowski space. The solutions are described by ρ_0, the x component of the fluid four velocity u^x, the gas pressure P, and the comoving-frame radiation energy density E and x-component of the radiation flux four-vector F^x. The latter vanishes far from the shock. We consider only the shock-frame (unboosted) version of the tests, initialized as shock tubes. All tests are purely hydrodynamic: the magnetic field plays no role.

Our tests are identical to those given in Farris et al. (2008) except that we modify case (4), which has radiation pressure a factor of 10 larger than gas pressure upstream from the shock. Due to this large radiation pressure, `bhlight` cannot integrate this case stably with the numerical resources available to us. Instead, we set the upstream radiation pressure equal to the gas pressure, and call this case (4a). The shock parameters are listed in Table 3.3. Units are such that $c = 1$; a_R (equivalently, $\hbar$) is determined by enforcing thermal equilibrium $E = a_R(P/\rho_0)^4$ far from the shock.

Case	γ	κ	Left State	Right State
1	5/3	0.4	$\rho_0 = 1.0$	$\rho_0 = 2.4$
			$P = 3.0 \times 10^{-5}$	$P = 1.61 \times 10^{-4}$
			$u^x = 0.015$	$u^x = 6.25 \times 10^{-3}$
			$E = 1.0 \times 10^{-8}$	$E = 2.51 \times 10^{-7}$
2	5/3	0.2	$\rho_0 = 1.0$	$\rho_0 = 3.11$
			$P = 4.0 \times 10^{-3}$	$P = 0.04512$
			$u^x = 0.25$	$u^x = 0.0804$
			$E = 2.0 \times 10^{-5}$	$E = 3.46 \times 10^{-3}$
3	2	0.3	$\rho_0 = 1.0$	$\rho_0 = 8.0$
			$P = 60.0$	$P = 2.34 \times 10^3$
			$u^x = 10.0$	$u^x = 1.25$
			$E = 2.0$	$E = 1.14 \times 10^3$
4a	5/3	0.4	$\rho_0 = 1.0$	$\rho_0 = 1.165$
			$P = 0.1$	$P = 0.1233$
			$u^x = 0.5$	$u^x = 0.4292$
			$E = 0.3$	$E = 0.3763$

Table 3.3: Parameters for Farris shocks.

Case 1 is a nonrelativistic strong shock with gas pressure much greater than radiation pressure, and consequently the fluid variable profiles resemble a nonrelativistic shock. `bhlight` output and the analytic solution are shown in Figure 3.9. Correspondence is good except for small deviations in the radiation

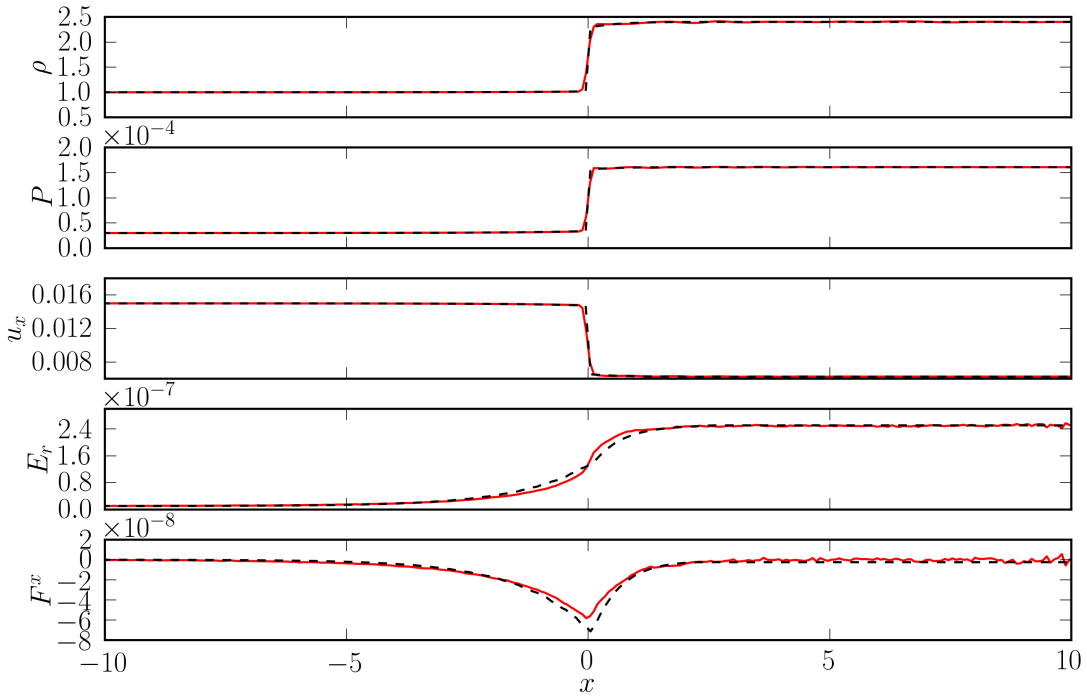

Figure 3.9: Gas and radiation variables for radiative shock Case 1. The result from `bhlight` is shown as a red solid line, and the analytic solution is shown as a dashed line.

variables near the shock interface, as expected for our full transfer solution.

Case 2 is a mildly relativistic shock with somewhat larger radiation pressure than in Case 1. `bhlight` output and the analytic solution are shown in Figure 3.10. The profiles of E and F^x show qualitative differences between the `bhlight` result and the analytic solution: a discontinuity in the analytic solution does not appear for the case of full transfer. This is unsurprising given the approximate nature of the Farris solutions. Note that for this case the approximate Eddington solution contains an unphysical discontinuity in the coordinate frame radiation energy density.

Case 3 is a highly relativistic shock with dynamically important radiation field. `bhlight` output and the analytic solution are shown in Figure 3.11. We find significant differences within a few photon mean free paths of the shock, particularly for the radiation flux. Figure 3.12 shows the expected $N^{-1/2}$ self-convergence in the radiation variables. A similar self-convergence trend also appears in the fluid variables until grid resolution becomes the dominant source of error.

Case 4a is a modestly relativistic wave with upstream radiation and gas pressure nearly equal. `bhlight` output and the analytic solution are shown in Figure 3.13. We find good agreement in all variables, despite the relatively strong radiation field. Note also that even with a large number of samples it is difficult to suppress

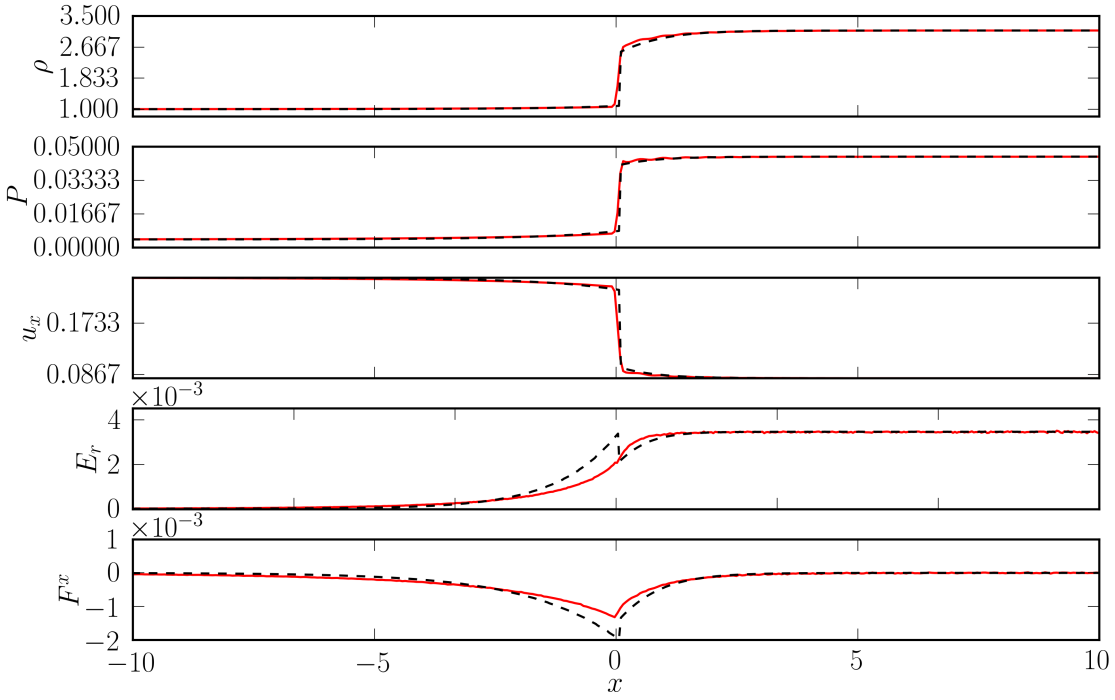

Figure 3.10: as and radiation variables for radiative shock Case 2. The result from `bhlight` is shown as a red solid line, and the analytic solution is shown as a dashed line.

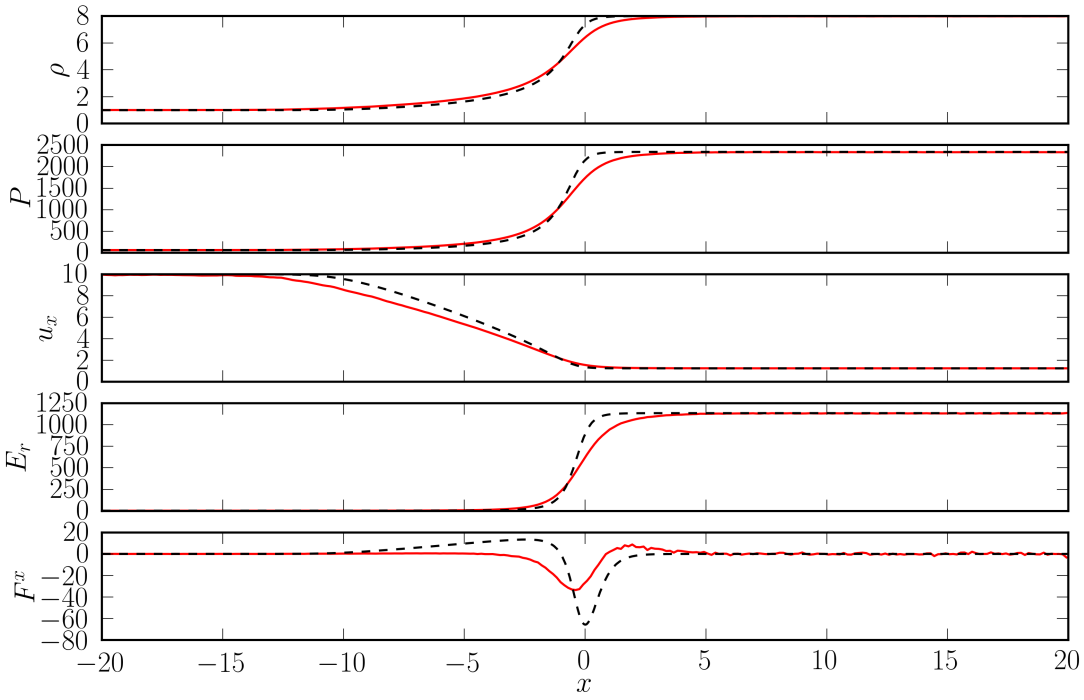

Figure 3.11: Gas and radiation variables for radiative shock Case 3. The result from `bhlight` is shown as a red solid line, and the analytic solution is shown as a dashed line.

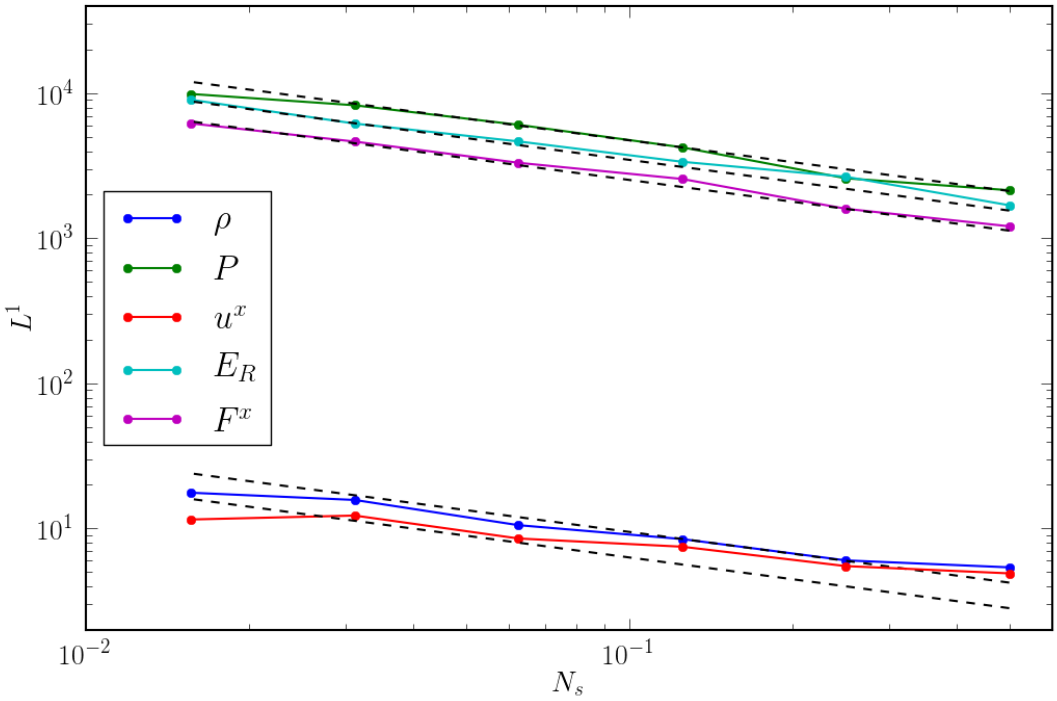

Figure 3.12: Self-convergence of all variables in radiative shock Case 3. N_s is directly proportional to the number of extant photons in the simulation. Dashed lines correspond to the $N_s^{-1/2}$ trend expected for Monte Carlo integration in the absence of resolution errors in the hydrodynamics solver.

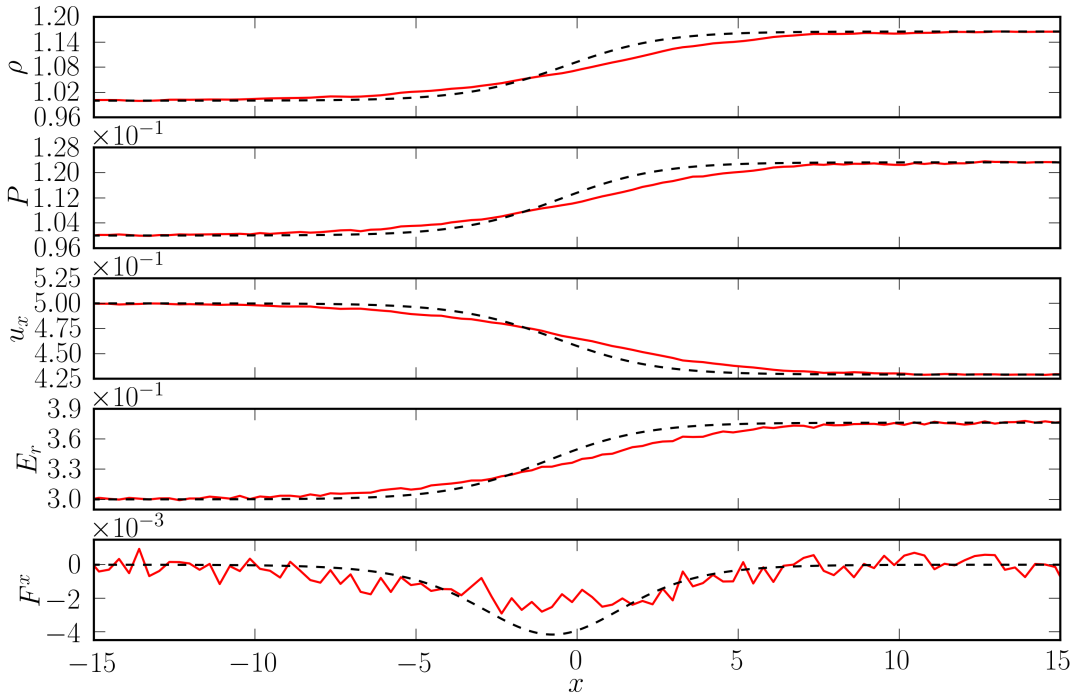

Figure 3.13: Gas and radiation variables for radiative shock Case 4a. The result from `bhlight` is shown as a red solid line, and the analytic solution is shown as a dashed line.

noise in F^x when it is much smaller than E.

3.5.7 Black Hole Atmosphere

Next we turn to a general relativistic equilibrium test. Consider a Schwarzschild black hole surrounded by a static atmosphere. The atmosphere is bounded by static, concentric spherical shells at $r_i > 2GM/c^2$ and $r_o > r_i$, and is in radiative equilibrium. The shells are reflecting boundaries and exchange no heat with the atmosphere, which has a grey opacity κ and adiabatic index $\gamma = 5/3$.

In the Newtonian limit radiative conduction would drive the atmosphere toward $T = $ const. In a relativistic atmosphere the gravitational field causes the atmosphere to come into a different equilibrium in which redshifted temperature, $T_\infty \equiv T\sqrt{-g_{00}}$, is constant.

In the Eddington approximation the atmospheric structure is determined by the conditions $T_\infty = $ const, and mechanical equilibrium, $T^{rr}{}_{;r} = 0$. Note that any radiation source terms vanish in thermal equilibrium; in fact, the Eddington approximation solution turns out to be an exact solution to the transfer equation, as we show in Appendix 3.B.

Once the inner and outer radii are specified, there are three dimensionless parameters that describe the

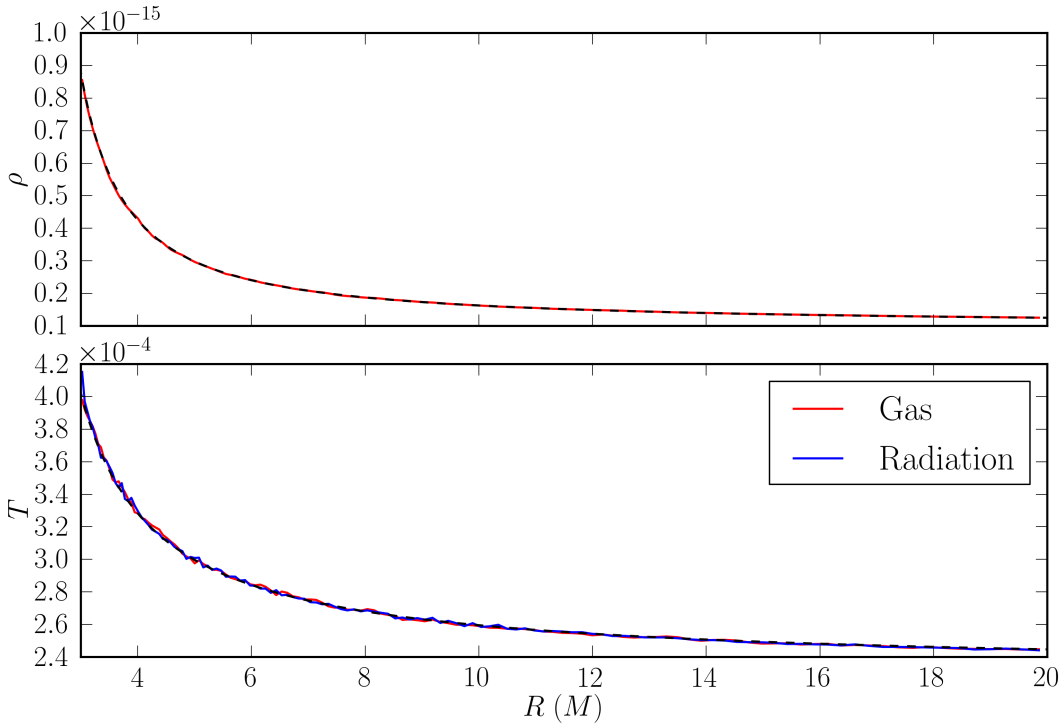

Figure 3.14: Rest-mass density and both gas and radiation temperatures for the static atmosphere test at $t = 150M$. Dashed lines represent the analytic solutions.

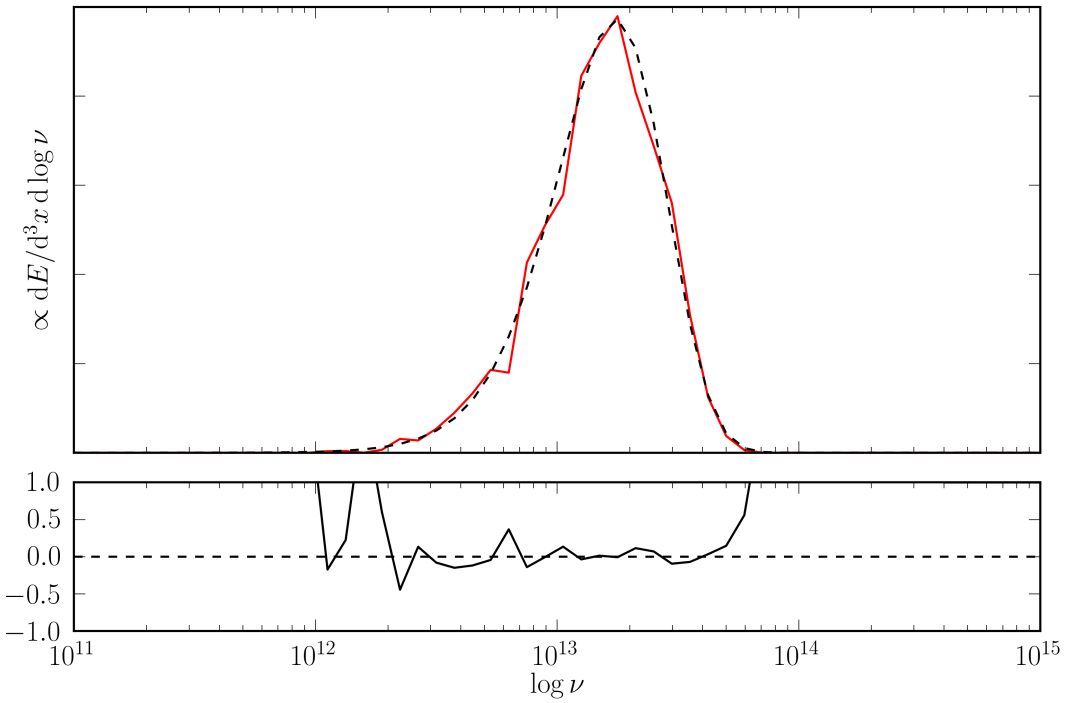

Figure 3.15: Spectrum of superphotons at $r \approx r_i$ for the radiating atmosphere test, showing good correspondence to the expected Planck spectrum.

solution (although their interpretation is purely Newtonian): the ratio of the atmospheric scale height at the inner boundary to the local radius $h_i \equiv \gamma k_B T_i r_i/(\mu m_p GM)$ (where μ is the mean molecular weight), the ratio of radiation pressure to gas pressure at the inner boundary $\beta_r \equiv \mu m_p a_R T_i^3/(3\rho_i k_B)$, and the characteristic optical depth $\tau \equiv \kappa\rho_i(r_o - r_i)$.

We set $r_i = 3GM/c^2$, $r_o = 20GM/c^2$. We set $h \approx 2.66$, $\beta_r \approx 0.23$, and $\tau \approx 5.0$. We use a 1D domain with 128 zones; the errors are dominated by Monte Carlo noise. The solution is shown in Figure 3.14. We also find the comoving spectrum at fiducial radius $r \approx r_i$ to match our expectation for thermalized radiation (with free vertical scale), as shown in Figure 3.15. Evidently the redshifted temperature is indeed constant.

3.6 Applications

3.6.1 Radiating Bondi Accretion

Here we report a preliminary investigation of spherically symmetric accretion onto a Schwarzschild black hole with radiative coupling. The fully dynamical problem has been studied analytically (although not with a full transport solution, frequency dependence, or magnetic fields) by Vitello (1984), Park (1990), and Nobili et al. (1991). Frequency-integrated numerical studies have also been performed in Fragile et al. (2012), Roedig et al. (2012), and McKinney et al. (2014) over many GM/c^2. Here we obtain a full transport solution with frequency dependence and magnetic fields. We include synchrotron emission, synchrotron absorption, and Compton scattering, with associated heating and cooling.

We set $M = 6.6 \times 10^9 M_\odot$ and describe the spacetime with modified Kerr-Schild (MKS) coordinates (Section 3.4.5). All simulations are performed in 1D, with $r \in [1.5M, 50M]$ for 64 zones. As initial conditions for the fluid, we adopt the nonradiative Bondi solution of Hawley et al. (1984) (which we hold constant at the outer boundary), except we set $\gamma = 13/9$ and place the sonic point at $r = 200M$. We vary the accretion rate by varying the density (or equivalently the mass unit $\mathcal{M}$) of the flow.

The magnetic field is initialized as a radial, monopolar field, which has no effect on the fluid motion. We set $B^1 = \alpha/r^3$, where α is chosen such that $\beta \equiv 2P/b^2 \approx 130$ at $r = 2M$ in the initial (GRMHD) conditions. No radiation is present initially. The radiation is allowed to flow freely out of the computational domain at the radial boundaries, with no inflow of radiation.

The luminosity $L(r)$, evaluated once the flow has settled and become almost time-independent, is

$$L(r) \equiv \int \sqrt{-g}\, \mathrm{d}x^2 \mathrm{d}x^3 R^1{}_0. \tag{3.59}$$

We average $L(r)$ over radial shells between $r = 30GM/c^2$ and $r = 50GM/c^2$ to obtain an average luminosity L. This is equivalent to time-averaging at a single radius.

We perform five calculations at different accretion rates. We evolve each system until the luminosity becomes stable. At high accretion rate this can take as long as $400GM/c^3$. The characteristic number density for each simulation, mass accretion rate

$$\dot{M} \equiv -\int \sqrt{-g}\, \mathrm{d}x^2 \mathrm{d}x^3 \rho u^1 \tag{3.60}$$

(evaluated at the event horizon), and L are given in Table 3.4. The resulting profiles of these five cases, along with that of Case 5 with Compton scattering disabled, are shown in Figure 3.16. The lack of cooling in the pure synchrotron case indicates that Compton cooling dominates over synchrotron cooling for the highest accretion rate model. The relationship between luminosity and accretion rate when Compton scattering is active is shown in Figure 3.17.

We have checked self-convergence of a solution with $n = 1.51 \times 10^{10}$ cm^{-3} (between Cases 4 and 5 in Table 3.4) in steady state at $t = 200M$. The expected convergence behavior for Monte Carlo-dominated error is shown in Figure 3.18.

Our models show that Compton cooling is important for Bondi accretion near the Eddington rate, and that – for our assumed field configuration – synchrotron cooling is comparatively unimportant. Although here we find appreciable cooling only close to the Eddington rate, we expect that for near-Keplerian accretion flows Compton scattering will become dynamically important at lower accretion rates, as individual fluid elements will have more time to cool (their radial velocity is lower) before accreting onto the black hole.

Case	n (cm^{-3})	$\dot{m}$	L ($L_{\rm Edd}$)
1	3.0×10^{6}	4.01×10^{-7}	2.03×10^{-14}
2	3.0×10^{7}	4.01×10^{-6}	1.46×10^{-12}
3	3.0×10^{8}	4.01×10^{-5}	2.08×10^{-10}
4	3.0×10^{9}	4.01×10^{-4}	5.81×10^{-7}
5	3.0×10^{10}	4.01×10^{-3}	3.05×10^{-4}

Table 3.4: Parameters for radiating Bondi accretion.

3.6.2 Axisymmetric Radiating Kerr Black Hole Accretion

As another preliminary application of `bhlight` we consider the effect of radiation on an intermediate accretion rate black hole accretion flow. Recall that for systems with $L \sim 10^{-9} L_{\rm Edd}$ (like Sgr A*) radiation will have little effect since the cooling timescale is long compared to the accretion timescale. This is the classical

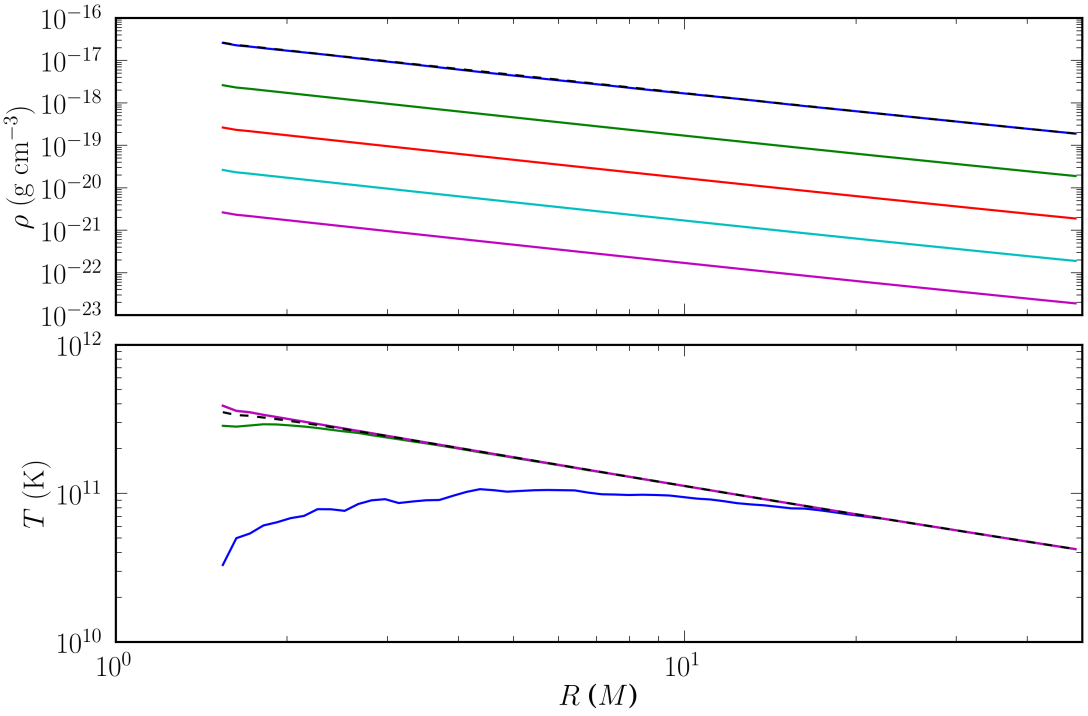

Figure 3.16: Fluid and radiation profiles for the radiating Bondi problem. Case 1 is shown in purple, Case 2 in teal, Case 3 in red, Case 4 in green, and Case 5 in blue. The dashed line shows Case 5 without Compton scattering.

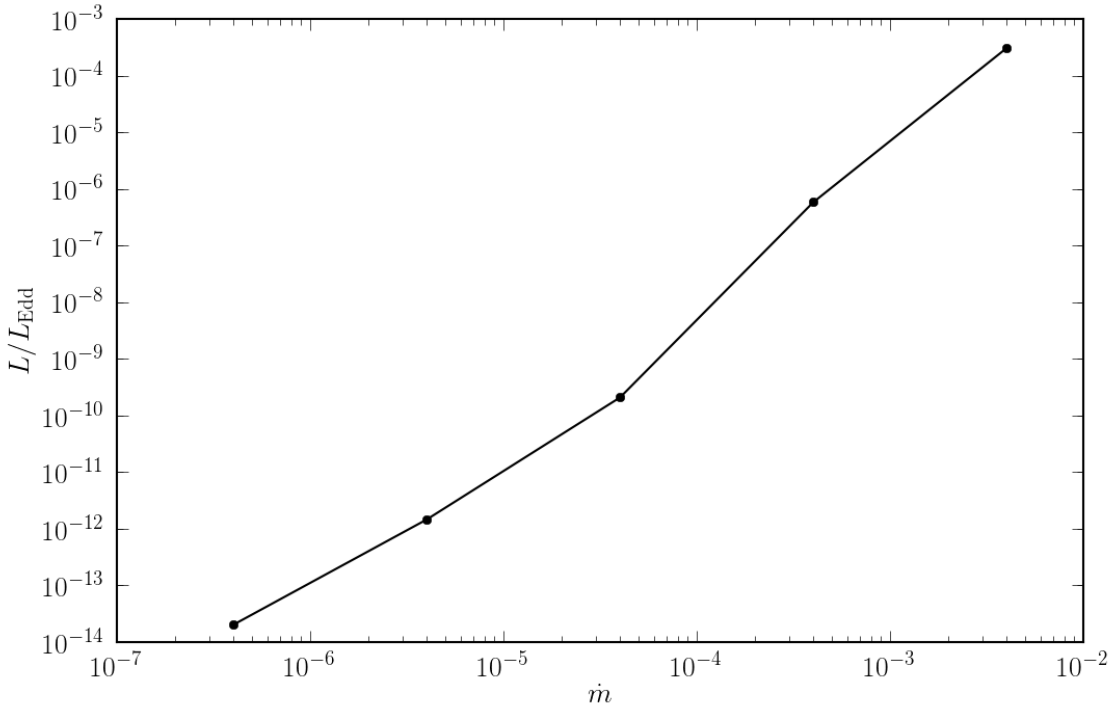

Figure 3.17: Efficiency of accretion for the radiating Bondi problem.

RIAF regime. For systems with $L \sim 10^{-5} L_{\rm Edd}$ (like M87) the effect of radiation depends on temperature and the distribution function of the electrons, but in certain circumstances radiation interactions – especially Compton cooling – can cool the flow on timescales comparable to or shorter than the accretion timescale.

Here we consider an axisymmetric accretion flow with parameters inspired by M87. We set black hole mass $M = 6.6 \times 10^9 M_\odot$ following Gebhardt et al. (2011) and dimensionless spin $a_* = 0.9375$, and we adjust $\mathcal{M}$ so that $\dot{m} \approx 6.3 \times 10^{-6}$ (Kuo et al., 2014). Although the distribution functions for ions and electrons in M87-like systems probably contains multiple components, we adopt thermal distributions for both and set the ion and electron temperatures $T_i = 3T_e$. T_i/T_e may strongly affect the dynamics of this system; essentially, it controls the cooling rate. We set the adiabatic index $\gamma = 13/9$, appropriate for ionized hydrogen when $kT_i \ll m_p c^2$ and $kT_e \gg m_e c^2$. We include synchrotron emission for a relativistic, thermal distribution of electrons (emissivity given by Equation 72 of Leung et al. 2011), thermal absorption, and Compton scattering. Bremsstrahlung is neglected, as it is a small correction to the emissivity within $\sim 10^3 M$ of the black hole for such intermediate accretion rate systems (e.g. Narayan & Yi 1995).

The initial conditions are a Fishbone-Moncrief torus (Fishbone & Moncrief 1976) with an inner radius at $6GM/c^2$ and pressure maximum at $12GM/c^2$. We extend this configuration by adding a weak poloidal

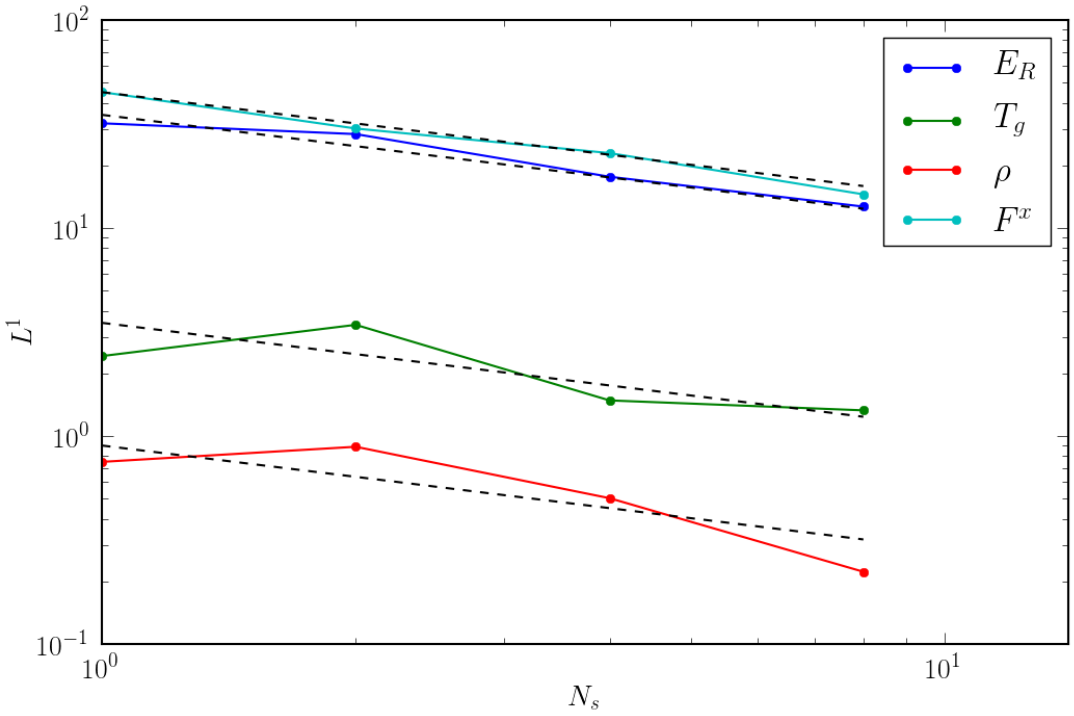

Figure 3.18: Self-convergence for the radiating Bondi problem near the Eddington limit. Dashed lines show convergence $\propto N_s^{-1/2}$.

magnetic field that follows isodensity contours, using the same procedure as in McKinney & Gammie (2004), but with the vector potential modified by a $\cos\theta$ factor to produce a two-loop configuration. The field strength is normalized so that β has a global minimum value of 100. Small perturbations are applied to the internal energy to efficiently initiate the magnetorotational instability. No radiation is present in the initial conditions.

We use the modified Kerr-Schild coordinates (see §3.4.5), with $r_0 = 0$ and $h_s = 0.3$. The grid runs from $r = 0.98(1 + \sqrt{1 - a_*^2})GM/c^2$ to $r = 40GM/c^2$, and from $\theta = 0$ to $\theta = \pi$. We impose outflow boundary conditions on both the fluid and radiation at the inner and outer radial boundaries, and reflecting polar boundary conditions. In this instance we adopt the piecewise parabolic method for reconstruction. We set the CFL number to 0.7, and evolve the system until $t = 2000M$.

To accurately sample cooling due to scattering events, we bias the scattering via the method given in Section 3.4.2 such that $b_s \propto \Theta_e^2$. To determine the absolute number of superphotons in steady state, we require only that the bolometric light curve be satisfactorily resolved (here, $\sim 1.1 \times 10^6$ superphotons at any one time). In the future we will more carefully consider the resolution requirement for these models.

We find qualitative differences between the radiative torus simulated in `bhlight` and the same model evolved with ideal GRMHD due mainly to Compton cooling in the hot, dense regions of the flow. Figure 3.19 shows fluid temperature and comoving radiation energy density at $t = 2000M$. Figure 3.20 shows density contours at $t = 2000M$ for the two models. Figure 3.21 shows shell-averaged density-weighted temperature,

$$\langle \Theta_e \rangle \equiv \frac{\int \sqrt{-g} \mathrm{d}x^2 \mathrm{d}x^3 \rho \Theta_e}{\int \sqrt{-g} \mathrm{d}x^2 \mathrm{d}x^3 \rho}, \tag{3.61}$$

as a function of radius for both `bhlight` and ideal GRMHD calculations; evidently the plasma is significantly cooler in the model with radiation interactions. Notice, however, that our single temperature model may be having an unrealistically strong dynamical effect; at these accretion rates the ions are likely imperfectly coupled to the electrons.

We evaluate the luminosity L, Equation 3.59, at large radius by integrating over all zones in a spherical shell. Figure 3.22 shows L and the radiative efficiency $\eta = L/\dot{M}c^2$. The mean η we find between $t = 1750M$ and $t = 2000M$, $\langle \eta \rangle = 0.51$, where

$$\langle \eta \rangle \equiv \frac{\int \mathrm{d}t\, L}{\int \mathrm{d}t\, \dot{M}c^2}, \tag{3.62}$$

is high compared to the thin disk value, ≈ 0.18 (for this a_*). Most of this energy is extracted by Compton scattering at $r \sim 10 - 15GM/c^2$. This high efficiency is a consequence of the flow having not yet reached steady state.

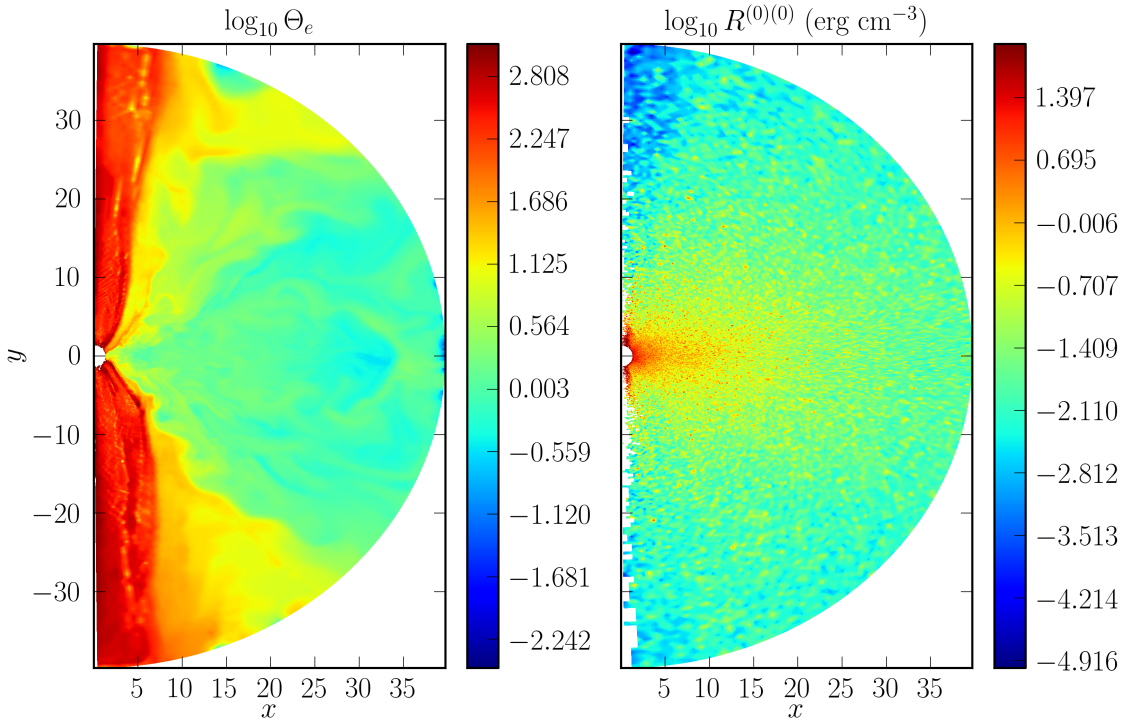

Figure 3.19: Torus temperature Θ_e and comoving radiation energy density $R^{\mu\nu}u_\mu u_\nu$ at $t = 1500M$.

We plan to explore radiative flows at intermediate accretion rates with more sophisticated treatments of the electron physics in future work.

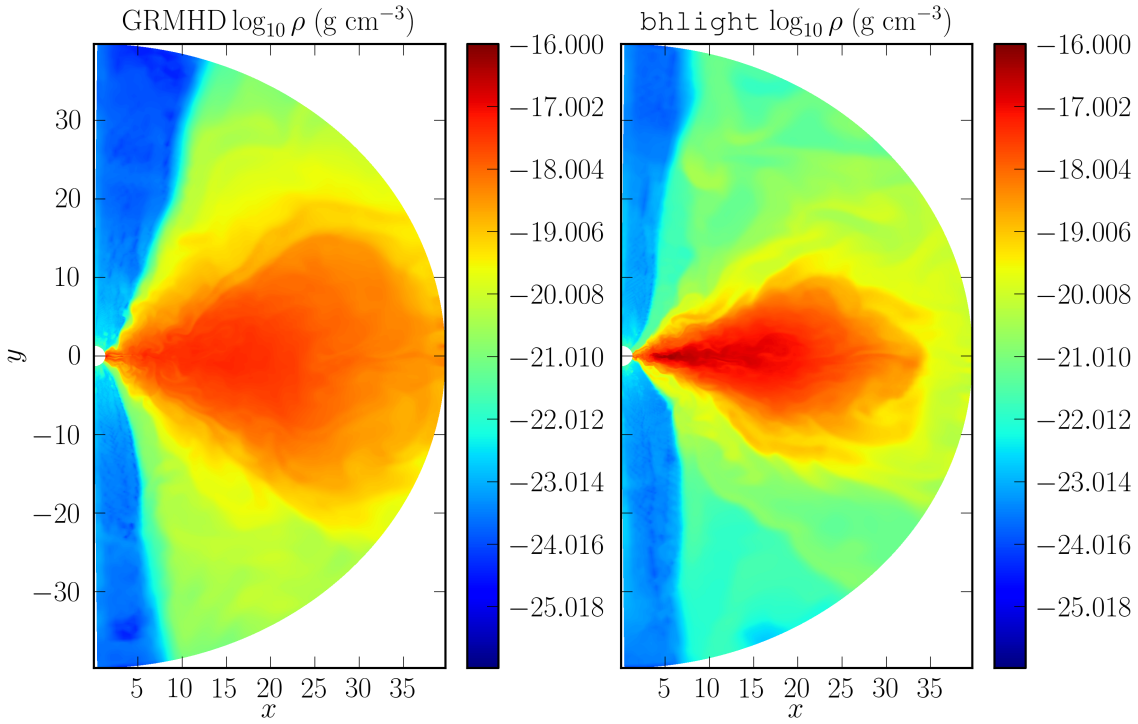

Figure 3.20: Comparison of gas density ρ between GRMHD and `bhlight` torus calculations. Note especially that for the `bhlight` result, the disk is relatively thin and the funnel is poorly developed.

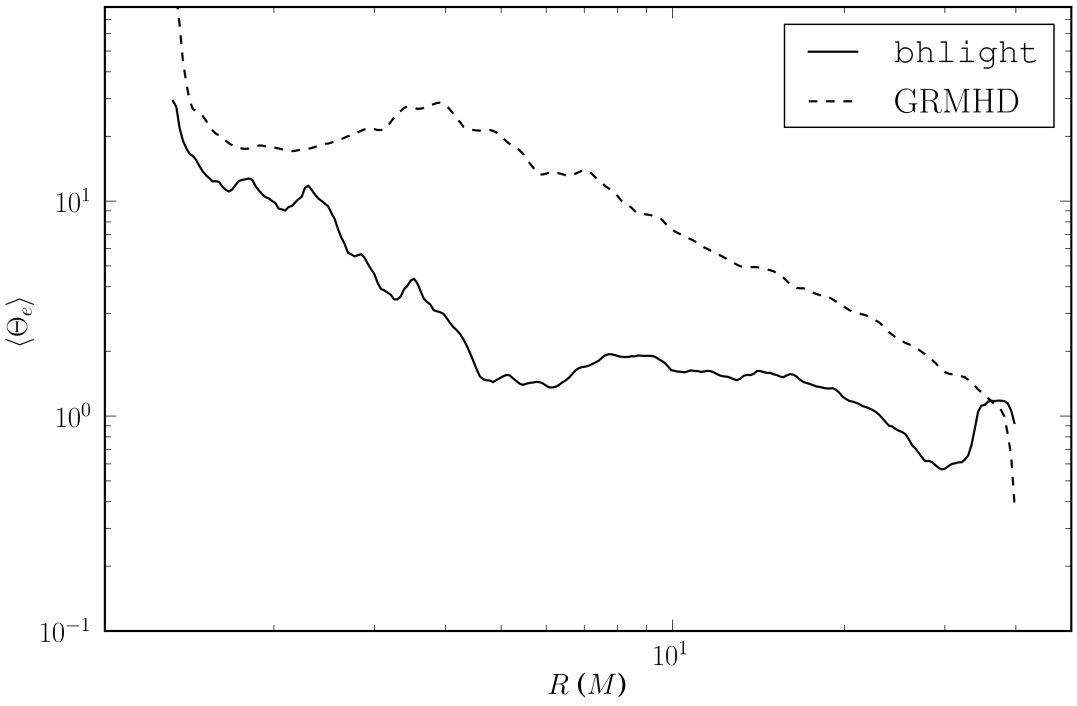

Figure 3.21: Shell-averaged density-weighted temperature for the torus problem in `bhlight` and ideal GRMHD at $t = 2000M$.

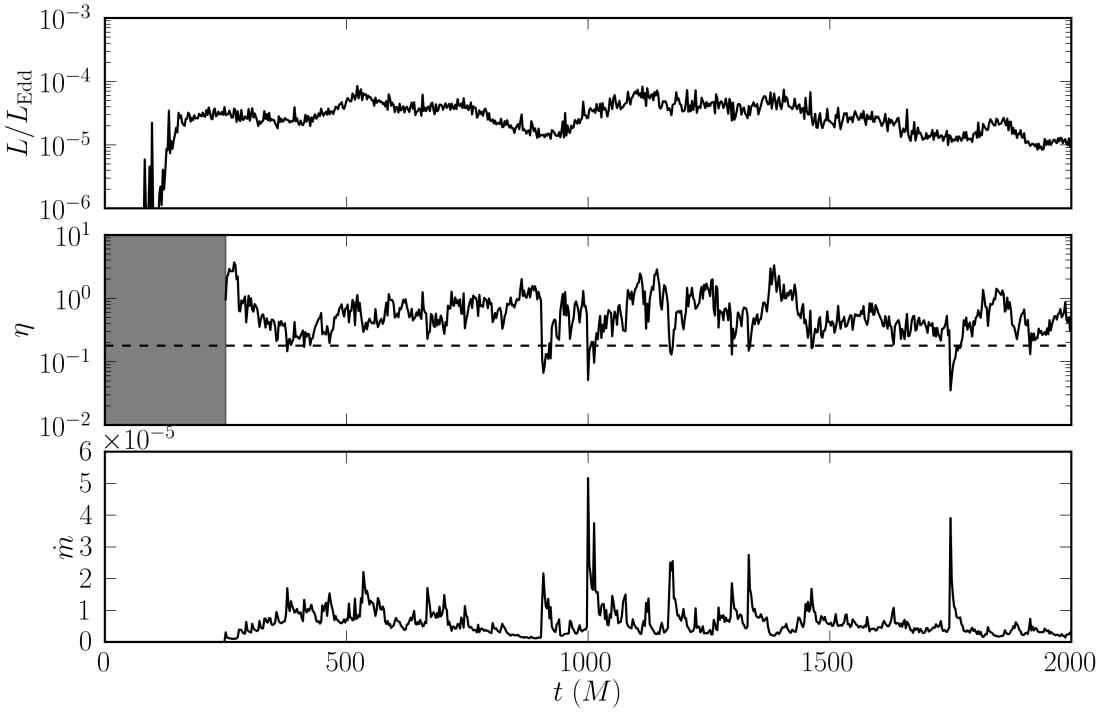

Figure 3.22: Torus luminosity, instantaneous efficiency η, and mass accretion rate as a function of time. The dashed line denotes the thin disk efficiency at this spin. The grey region indicates the portion of η prior to the onset of accretion across the horizon which we omit.

3.7 Conclusion

We have introduced `bhlight` which, in coupling a second order Godunov scheme to a frequency-dependent Monte Carlo radiative transfer scheme, provides a full solution to the equations of GRRMHD. `bhlight` displays convergence on a number of test problems, and we have demonstrated evolution of our target application: relativistic accretion flows at moderate accretion rate. `bhlight` enables more nearly *ab initio* study of flows in this regime, which have historically proven resistant to other methods of inquiry.

Numerical schemes have limitations. Apart from failure modes related to large optical depths and large radiation pressures mentioned previously (which prohibit near-Eddington studies as of this writing), Monte Carlo techniques are simply expensive, particularly when geodesics are nontrivial. The axisymmetric torus problem we reported was performed on one 8-core node (using `mpirun` to alternate between fluid and radiation MPI sectors) for 146 hours, achieving approximately 9.5×10^4 superphoton updates (interactions and geodesic steps) per core-second. In comparison, the pure GRMHD torus run required only 69 core-hours, about 17 times less expensive even at this low superphoton resolution. The true minimum relative cost of `bhlight` over `harm`, however, will depend on the required resolution in the specific intensity for the particular problem at hand.

This work was supported by NSF grant AST 13-33612 and NASA grant NNX10AD03G, by a NASA GSRP fellowship to JCD, an Illinois Distinguished Fellowship to BRR, a Metropolis Fellowship to JCD, and a Romano Professorial Scholarship to CFG. We thank B. Farris, C. Roedig, and particularly M. Chandra and S. Shapiro for discussions, as well as J. Stone, E. Quataert, and all the members of the horizon collaboration (`horizon.astro.illinois.edu`). We also thank the anonymous referee for a very useful report. A portion of the analytic results presented here were obtained using the SageMath software package running on SageMathCloud (https://cloud.sagemath.com). A portion of the numerical results presented here were obtained on Princeton's `tiger` cluster. This research is part of the Blue Waters sustained-petascale computing project, which is supported by the National Science Foundation (awards OCI-0725070 and ACI-1238993) and the state of Illinois. Blue Waters is a joint effort of the University of Illinois at Urbana-Champaign and its National Center for Supercomputing Applications.

3.A Radiation Boundary Conditions

In the general coordinate frame, certain boundary conditions on the superphotons required for test problems in `bhlight` are more complex than in the nonrelativistic case. Here we review such boundaries as used.

3.A.1 Reflecting Boundary Conditions

The static atmosphere test in Section 3.5.7 uses reflecting boundaries that are aligned with the coordinates. How should one apply the reflecting boundary conditions to the radiation field? This is not trivial in Kerr-Schild coordinates where the naive approach of simply changing the sign of the radial component of the wavevector is wrong, because the radial component of the shift does not vanish.

When a photon crosses the boundary, we build an orthonormal tetrad with time component $e^{\mu}_{(t)} = (u^t, 0, 0, 0)$ (i.e. the tetrad is stationary in the coordinate, and hence the boundary, frame) and one spatial component that is normal to the boundary. We transform the wavevector to the tetrad frame, reverse the normal component of the wavevector, and transform back to the coordinate frame.

3.A.2 Equilibrium Boundary Conditions

For problems with fluid inflow across the boundary (e.g. the relativistic shocks in Section 3.5.6) the fluid advects a thermal radiation field with it across the boundary. How should one sample the incoming photons on the boundary? The problem is that one is sampling a *flux* rather than the distribution function itself.

We have found that the simplest procedure is to sample the distribution function and multiply the weights in the sample by $\cos\theta$, where θ is the angle between the wavevector and the normal to the boundary.

3.B The Radiating Atmosphere Under Full Transfer

We revisit the analytic solution to the radiating atmosphere problem described in Section 3.5.7, in which fluid and radiation confined in the Schwarzschild spacetime between two reflective spherical shells maintain a static atmosphere, without resorting to any closure for describing the radiation.

Consider the relativistic transfer equation in invariant form (ignoring scattering),

$$\frac{\mathrm{D}}{\mathrm{d}\lambda}\left(\frac{I_\nu}{\nu^3}\right) = \left(\frac{j_\nu}{\nu^2}\right) - (\nu\alpha_\nu)\left(\frac{I_\nu}{\nu^3}\right), \tag{3.63}$$

which may be rewritten in terms of the invariant differential optical depth $\mathrm{d}\tau \equiv \nu\alpha_\nu \mathrm{d}\lambda$ (and noting that the Planck function $B_\nu = j_\nu/\alpha_\nu$, i.e. Kirchoff's law applies) to give

$$\frac{\mathrm{d}}{\mathrm{d}\tau}\left(\frac{I_\nu}{\nu^3}\right) = \left(\frac{B_\nu}{\nu^3}\right) - \left(\frac{I_\nu}{\nu^3}\right), \tag{3.64}$$

where all quantities in brackets are again invariant.

We adopt the ansatz for the fluid temperature distribution $\sqrt{-g_{00}}T(r) = T_\infty$ from Section 3.5.7. Consider also the frequency $\omega = -k_\mu u^\mu$ of a superphoton at radius r in the Schwarzschild spacetime. The four-velocity of a local frame not moving with respect to the coordinate system is $u^\mu = (1/\sqrt{-g_{00}}, 0, 0, 0)$: then, $\omega = -k_0/\sqrt{-g_{00}}$. The invariant Planck function $B_\nu/\nu^3 = (h^4/c^2)f(h\nu/k_BT)$. However, $h\nu/k_BT = -hk_0/2\pi k_BT_\infty$ is constant along geodesics; B_ν/ν^3 is therefore also constant along every ray.

For reflecting boundary conditions, rays of the intensity I_ν do not terminate; they instead repeatedly reflect off the boundaries all the way back to $\mathrm{d}\tau \to \infty$. Because B_ν/ν^3 is constant along every ray, for the stationary system we have $I_\nu/\nu^3 = B_\nu/\nu^3$ everywhere. Our assumed temperature distribution is therefore consistent with the full transfer equation, and the solution presented in Section 3.5.7 is exact for all optical depths.

3.C Linear Modes in Relativistic Radiation Magnetohydrodynamics

We present the linearized equations of radiation magnetohydrodynamics in flat spacetime, assuming the Eddington closure (Farris et al., 2008) with a gray absorption opacity κ and setting $k_B = c = 1$. The governing equations are then given in terms of divergences of the matter four-current and the MHD and radiation stress-energy tensors, along with the magnetic induction equation. In plane-parallel symmetry, we search for wave solutions of the form $\mathbf{P} = (\rho, u, u^1, u^2, B^1, B^2, E, F^1, F^2) = (\rho_0+\delta\rho, u_0+\delta u, \delta u^1, \delta u^2, B_0, B_0+\delta B^2, E_0+\delta E, \delta F^1, \delta F^2)$ (i.e. we confine variation to a plane), where $\delta \propto \exp(\omega t - ikx)$ is a small perturbation, and $E_0 = a_R((\gamma-1)u_0/\rho_0)^4$ to enforce radiative equilibrium of the background state. We write the linearized systems in the form $\omega\delta\mathbf{P} = \mathbf{A}\delta\mathbf{P}$; the dispersion relation is then $\det(\mathbf{A} - \mathbb{I}\omega) = 0$. We find that the matrix $\mathbf{A}$ is

$$\begin{pmatrix}
0 & 0 & -ik\rho_0 & 0 & 0 & 0 & 0 & 0 \\
4\kappa E_0 & \frac{-4\kappa E_0\rho_0}{u_0} & -ik\gamma u_0 & 0 & 0 & \kappa\rho_0 & 0 & 0 \\
0 & \frac{-ik(\gamma-1)C_2}{C_1} & 0 & 0 & \frac{-iB_0k}{C_2+B_0^2} & 0 & \frac{\kappa\rho_0 C_2}{C_1} & \frac{B_0^2\kappa\rho_0}{C_1} \\
0 & \frac{-ik(\gamma-1)B_0^2}{C_1} & 0 & 0 & \frac{iB_0k}{C_2+B_0^2} & 0 & \frac{B_0^2\kappa\rho_0}{C_1} & \frac{\kappa\rho_0 C_2}{C_1} \\
0 & 0 & -ikB_0 & ikB_0 & 0 & 0 & 0 & 0 \\
-4\kappa E_0 & \frac{4E_0\kappa\rho_0}{u_0} & -\frac{4}{3}ikE_0 & 0 & 0 & -\kappa\rho_0 & -ik & 0 \\
0 & \frac{4ikC_2E_0(\gamma-1)}{3C_1} & 0 & 0 & \frac{4ikB_0E_0}{3\left(C_2+B_0^2\right)} & -\frac{1}{3}ik & \frac{-C_3\kappa\rho_0}{3C_1} & \frac{-4B_0^2E_0\kappa\rho_0}{3C_1} \\
0 & \frac{4ikB_0^2E_0(\gamma-1)}{3C_1} & 0 & 0 & \frac{-4ikB_0E_0}{3\left(C_2+B_0^2\right)} & 0 & \frac{-4\kappa\rho_0B_0^2E_0}{3C_1} & \frac{-C_3\kappa\rho_0}{3C_1}
\end{pmatrix},$$

where

$$C_1 = \gamma^2 u_0^2 + 2(\gamma u_0 + \rho_0)B_0^2 + 2\gamma\rho_0 u_0 + \rho_0^2,$$

$$C_2 = B_0^2 + \gamma u_0 + \rho_0,$$

$$C_3 = 3C_1 + 4E_0 C_2.$$

Chapter 4

Two-Temperature GRRMHD Simulations of Slowly Accreting Supermassive Black Holes

4.1 Summary

We present axisymmetric numerical simulations of radiatively inefficient accretion flows onto black holes combining general relativity, magnetohydrodynamics, self-consistent electron thermodynamics, and frequency-dependent radiation transport. We investigate a range of accretion rates up to $10^{-5}\dot{M}_{\rm Edd}$ onto a $10^8 M_\odot$ black hole with spin $a_\star = 0.5$. We report on averaged flow thermodynamics as a function of accretion rate. We present the spectra of outgoing radiation and find that it varies strongly with accretion rate, from synchrotron-dominated in the radio at low $\dot{M}$ to inverse Compton-dominated at our highest $\dot{M}$. In contrast to canonical analytic models, we find that by $\dot{M} \approx 10^{-5}\dot{M}_{\rm Edd}$, the flow approaches $\sim 1\%$ radiative efficiency, with much of the radiation due to inverse Compton scattering off Coulomb-heated electrons far from the black hole. These results have broad implications for modeling of accreting black holes across a large fraction of the accretion rates realized in observed systems[1].

4.2 Introduction

At low mass accretion rates $\dot{m} \equiv \dot{M}/\dot{M}_{\rm Edd}$[2] $\lesssim 10^{-3}$, thermally stable accretion onto black holes is generally believed to form a geometrically thick, optically thin, radiatively inefficient accretion flow (RIAF, or ADAF[3]; Ichimaru 1977, Narayan & Yi 1994, Yuan & Narayan 2014). Due in part to the two-temperature nature (e.g. Shapiro et al. 1976, Mahadevan & Quataert 1997, Ressler et al. 2015) of such flows, RIAFs are nearly virial and the liberated gravitational energy is either advected across the event horizon or lost through mechanical outflows. Such accretion flows are probably well-represented across the range of astrophysical black hole masses (McClintock & Remillard 2006, Ho 2009).

Analytic and semi-analytic RIAF models have been profitably applied in the study of low-luminosity

[1] This work appeared in publication as Ryan et al. (2017b).

[2] $\dot{M}$ is the accretion rate. $\dot{M}_{\rm Edd} \equiv 4\pi G M m_p/\eta\sigma_T c$, where M is the black hole mass and η is the nominal efficiency. We adopt $\eta = 0.1$; $\dot{M}_{\rm Edd} = 1.4 \times 10^{18}(M/M_\odot)$ g/s $= 2.2 \times 10^{-8}(M/M_\odot)\ M_\odot$/yr.

[3] Advection-Dominated Accretion Flow

accretion flows (e.g. Narayan et al. 1997, Narayan et al. 1998). However, a limitation of such studies is the reliance on an α viscosity (Shakura & Sunyaev 1973) to represent angular momentum transport, probably due to magnetohydrodynamic (MHD) turbulence generated by the magnetorotational instability (MRI; Balbus & Hawley 1991). Additionally, analytic models typically neglect or approximate general relativity, with potential consequences for interpreting observations as much of a RIAF's outgoing radiation may originate near the black hole (e.g. Mościbrodzka et al. 2009).

Global general relativistic numerical simulations have been widely used to study RIAFs driven self-consistently by magnetorotational turbulence (e.g. Koide et al. 1999, De Villiers et al. 2003b, McKinney & Gammie 2004, Narayan et al. 2012). In the absence of significant mean fields and cooling, such calculations generically recover the hot, nearly Keplerian, nearly axisymmetric (but see Fragile et al. 2007) accretion disk anticipated by analytic models. Nonetheless, electron thermodynamics in such calculations has remained a challenge. These flows are collisionless and likely two-temperature (Quataert 1998). Historically, constant proton to electron temperature ratios, or other local prescriptions mapping the fluid state to electron temperature (e.g. Mościbrodzka et al. 2009, Shcherbakov et al. 2012, Mościbrodzka et al. 2014, Chan et al. 2015) have been employed. Recently, however, Ressler et al. (2015) introduced a method to track numerical dissipation in conservative relativistic MHD schemes, interpret it according to local kinetic plasma studies, and thus separately evolve the electron temperature (see also Sądowski et al. 2017 for a similar method). While this provides for physically motivated electron heating, it still assumes a thermal distribution of electrons, whereas these collisionless flows may have a significant population of nonthermal electrons (e.g. Kunz et al. 2016, Chael et al. 2017).

Radiative losses are negligible at sufficiently low accretion rates. Towards the Eddington rate, however, radiative processes become important to the dynamics of the flow. Significantly below Eddington, the flow is still optically thin and the electrons are relativistic near the black hole. The dominant energy loss mechanisms are synchrotron emission and Compton upscattering. Ohsuga et al. (2009) first demonstrated that radiation leads to thick/thin disk transitions in numerical models. Fragile & Meier (2009) found a cooling state inconsistent with either a pure RIAF or a thin disk, and compared it to a magnetically-dominated accretion flow in the inner disk. Mościbrodzka et al. (2011) studied accretion rates targeting the supermassive black hole at the center of M87. Dibi et al. (2012) identified $\dot{m} \approx 10^{-7}$ as a critical accretion rate above which radiative losses matter in GRMHD simulations. Wu et al. (2016) targeted the near-Eddington state transition in X-ray binaries in Newtonian MHD with local cooling. Recently, Sądowski et al. (2017) addressed cooling in RIAFs with self-consistent electron heating and a gray M1 radiation closure, while Sądowski & Gaspari (2017) use a similar model except with constant proton-to-electron temperature ratios to study the transition

to radiatively efficient flows.

These studies integrate over frequency and adopt a local cooling function or approximate the radiation as a fluid. In this paper we do not use either of these approximations. Instead, we introduce a scheme that couples a global, albeit axisymmetric, model with electron heating (Ressler et al. 2015) for the flow to a Monte Carlo radiation MHD scheme (Ryan et al. 2015), yielding a frequency-dependent, full transport solution to the equations of two-temperature relativistic radiation MHD.

We apply this new scheme, `ebhlight`, to RIAFs across a range of accretion rates. Section 4.3 presents the governing equations. Section 4.4 describes our numerical implementation. Section 4.5 contains our results. Section 4.6 concludes.

4.3 Governing Equations

We solve the equations of general relativistic radiation ideal magnetohydrodynamics with full radiation transport. We include a separate electron energy equation (Ressler et al. 2015) and electron-photon interactions. Hereafter, we adopt units such that $c = k_B = 1$ and absorb a factor $\sqrt{4\pi}$ into definitions of magnetic field strength.

The radiation and fluid are coupled through exchange of four-momentum. The electron energy density is sourced by numerical dissipation, and electrons and protons exchange energy through Coulomb interactions, as in Sądowski et al. (2017), allowing transfer of energy between protons and electrons according to the transrelativistic rate of Stepney & Guilbert (1983). Although we track electron and proton temperatures separately, we assume a single four-velocity for the fluid dynamics (Ressler et al. 2015).

The dynamical variables in our model are the fluid rest-mass density ρ_0, the fluid four-velocity u^μ, the fluid internal energy u (equivalently, the fluid pressure $P = (\gamma - 1)u$), the magnetic field three-vector B^i, $\kappa_e \equiv \exp((\gamma_e - 1)s_e) = P_e/\rho_0^{\gamma_e}$ ($s_e \equiv$ electron entropy), and the radiation specific intensity I_ν. We adopt three adiabatic indices: $\gamma_e = 4/3$ for the (relativistic) electrons, $\gamma_p = 5/3$ for the (non-relativistic) protons, and $\gamma = 13/9$ for the total fluid. Although our approximation of three constant γ is likely not valid everywhere, previous studies (Shiokawa et al. 2012, Sądowski et al. 2017) suggest that variable γ do not significantly alter conclusions drawn from numerical (GRMHD, GRRMHD) calculations.

Our full set of governing equations is (written in a coordinate basis):

$$\partial_t \left(\sqrt{-g}\rho_0 u^t\right) = -\partial_i \left(\sqrt{-g}\rho_0 u^i\right), \tag{4.1}$$

$$\begin{aligned}\partial_t \left(\sqrt{-g}T^t{}_\nu\right) = \partial_i \left(\sqrt{-g}T^i{}_\nu\right) + \sqrt{-g}T^\kappa_\lambda \Gamma^\lambda{}_{\nu\kappa} \\ - \sqrt{-g}R^\mu{}_{\nu;\mu},\end{aligned} \tag{4.2}$$

$$\partial_t \left(\sqrt{-g}B^i\right) = \partial_j \left[\sqrt{-g}\left(b^j u^i - b^i u^j\right)\right], \tag{4.3}$$

$$\partial_i \left(\sqrt{-g}B^i\right) = 0, \tag{4.4}$$

$$\frac{dx^\mu}{d\lambda} = k^\mu, \tag{4.5}$$

$$\frac{dk^\mu}{d\lambda} = -\Gamma^\lambda{}_{\mu\nu} k^\mu k^\nu, \tag{4.6}$$

$$\frac{D}{d\lambda}\left(\frac{I_\nu}{\nu^3}\right) = \frac{\eta_\nu(T_e)}{\nu^2} - \frac{I_\nu \chi_\nu(T_e)}{\nu^2}, \tag{4.7}$$

$$\frac{\rho^{\gamma_e}}{\gamma_e - 1} u^\mu \partial_\mu \kappa_e = f_e Q_H + Q_C(T_e, T_p) - u^\nu R^\mu{}_{\nu;\mu}, \tag{4.8}$$

where $D/d\lambda$ is the convective derivative in phase space, the GRMHD stress-energy tensor

$$\begin{aligned}T^\mu{}_\nu = \left(\rho_0 + u + P + b^\lambda b_\lambda\right) u^\mu u_\nu \\ + \left(P + \frac{b^\lambda b_\lambda}{2}\right) g^\mu{}_\nu - b^\mu b_\nu\end{aligned} \tag{4.9}$$

with b^μ the magnetic field four-vector (see Gammie et al. 2003), and the radiation stress-energy tensor

$$R^\mu{}_\nu = \int \frac{d^3p}{\sqrt{-g}p^t} p^\mu p_\nu \left(\frac{I_\nu}{h^4\nu^3}\right). \tag{4.10}$$

Q_H and Q_C are, respectively, dissipative and Coulomb volumetric heating rates. Temperature dependencies of interaction terms are shown for clarity. Note that T_e is calculated not from P and ρ_0 as in Ryan et al. (2015), but rather from ρ_0 and κ_e as $T_e = \rho_0^{\gamma_e - 1}\kappa_e$. $T_p = (\gamma_p - 1)(u - u_e)/\rho$ is the proton temperature, only needed for Coulomb coupling. For $T_e = (\gamma_e - 1)u_e/\rho_0$, $\Theta_e = m_p T_e/m_e$ where $\Theta_e \equiv$ electron temperature in units of $m_e c^2$. Note that the radiation four-force $R^\mu{}_{\nu;\mu}$ is applied to both the electron and total energy equations; $T^\mu{}_\nu$ incorporates both electrons and protons.

We consider synchrotron emission and absorption. We also include Compton scattering, which for $\Theta_e \gg 1$ and $h\nu \ll k_b T_e$ has a mean amplification factor $\delta E_\gamma / E_\gamma \approx 16\Theta_e^2$.

4.4 Numerical Method

Our calculations are performed with `ebhlight`, an extension of `bhlight` (Ryan et al. 2015) that includes the electron heating model of Ressler et al. (2015). `ebhlight` solves the equations of GRMHD (Equations 4.1 - 4.4) with the flux-conservative second-order-accurate `harm` scheme (Gammie et al. 2003). The radiative transfer and photon-electron interactions (Equations 4.5 - 4.7) are evaluated with the Monte Carlo scheme `grmonty` (Dolence et al. 2009; we term radiation samples "superphotons"). The electron heating (Equation 4.8) is evaluated as in Ressler et al. (2015), with Coulomb heating introduced in a separate explicit second-order step. We neglect electron and ion conduction, as RIAF simulations have found both to be suppressed by misaligned magnetic fields and temperature gradients (Ressler et al. 2015, Foucart et al. 2017). The radiation four-force is evaluated with time-centered fluid quantities, and applied to the total fluid and the electron energy in a first-order operator-split fashion. Emission, absorption, and scattering are treated probabilistically as in Ryan et al. (2015).

4.4.1 Coordinates

We perform our calculation in horizon-penetrating Modified Kerr-Schild (MKS) coordinates (McKinney & Gammie 2004). The inner boundary is placed inside the event horizon, the outer boundary at $r = 200GM/c^3$. The MKS h parameter is 0.3. To avoid wasting computational resources advancing many superphotons in the outer region where radiative interactions are relatively unimportant ($\Theta_e \lesssim 1$), we evaluate the radiation sector only inside a smaller outer radius, either 40 or $100GM/c^2$, as required to capture at least 95% of the bolometric luminosity. We employ a spatial resolution 388×256 zones.

4.4.2 Initial Conditions

`ebhlight` is currently axisymmetric; useful time integrations are thus of the order $t \sim 1000GM/c^3$, after which MRI turbulence decays (see Guan & Gammie 2008 for details of MRI-driven turbulence in axisymmetry). The timescale for viscous electron heating to equilibrate is longer than this beyond $10 - 15GM/c^2$. To address this issue, we initialize our simulation with axisymmetrized data from a 3D *nonradiative* GRMHD run with electron heating using the method described in Ressler et al. 2017. We consider a low net magnetic flux configuration (i.e. SANE rather than MAD; see e.g. Narayan et al. 2012). For ρ_0, u, κ_e, and u^i, axisymmetrization is a straightforward average in ϕ. For B^i, we construct a vector potential from the 3D data, average that, and then evaluate the axisymmetric field.

No radiation is present initially; the radiation field equilibrates on the light crossing time. We set the

black hole mass to $10^8 M_\odot$ (near the turnover of the supermassive black hole mass function; e.g. Kelly & Merloni 2012) and dimensionless black hole spin $a_\star = 0.5$. The accretion rate is controlled by varying the mass of the torus.

4.4.3 Pathologies

We employ the drift-frame floors described in Ressler et al. (2017) to repair unphysical total fluid densities and energies. Capturing numerical dissipation for electron heating is especially challenging: `harm`-like schemes can violate the second law of thermodynamics locally at the truncation error level, and in our scheme the electrons may also be *cooled* anomalously near large fluid entropy gradients, such as at the funnel wall. See Ressler et al. (2017) for more details. We enforce $\Theta_{e,\max} < 1000$ in the radiation sector, and $T_p/T_e > 0.01$.

Explicit radiation-fluid coupling may yield negative electron energies. This is difficult to prevent except by increasing superphoton resolution. We monitor such "supercooling" events to ensure that they are negligible to the total radiation energy budget. This diagnostic is used to set superphoton resolution, which is related to the cooling time of the flow.

4.5 Results

$\overline{\dot{m}}$	$\overline{L}/L_{\rm Edd}$	$\overline{\epsilon}$	$\langle\overline{\Theta_e}\rangle_J$	$\overline{L_{\rm em}}/\overline{L_{\rm sc}}$
1.25×10^{-9}	3.01×10^{-14}	2.45×10^{-6}	13.1	1.51×10^4
1.08×10^{-8}	4.27×10^{-12}	4.45×10^{-5}	14.9	1.07×10^3
1.18×10^{-7}	2.86×10^{-10}	2.60×10^{-4}	12.4	1.42×10^2
9.33×10^{-7}	1.39×10^{-8}	1.61×10^{-3}	12.2	1.79×10^1
1.01×10^{-5}	4.89×10^{-7}	5.07×10^{-3}	7.64	1.74

Table 4.1: Accretion rate, luminosity, radiative efficiency, emission-weighted electron temperature, and ratio of emission to scattering processes for all simulations. Throughout, models are identified by $\overline{\dot{m}}$ rounded to the nearest power of 10.

We consider the same initial conditions except at five accretion rates: $\dot{m} \sim (10^{-9}, 10^{-8}, 10^{-7}, 10^{-6}, 10^{-5})$. Each calculation extends for $1000GM/c^3$. To gauge the importance of cooling, we run these models both with and without radiative cooling. Luminosities from models without cooling are post-processed using `grmonty` with a $5GM/c^3$ cadence.

Each superphoton records the i, j indices of the zone of its last interaction; over a time interval Δt, superphotons captured at the outer radial boundary are used to compute volumetric radiative energy exchange rates in each zone $J_{i,j} \equiv \sum_n -w_n k_{0,n}/(\sqrt{-g}\Delta t \Delta x^1 \Delta x^2 \Delta x^3)$ with the sum taken over the n recorded photons tagged with i, j. $J_{\rm em}$ is that due to emission (with self-absorption subtracted) and $J_{\rm sc}$ is that due to

scattering. As above, heating rates are $Q \equiv du/d\tau$ due to each process. Luminosities L are $\int R^1{}_0 \sqrt{-g} dx^2 dx^3$ evaluated at the outer radial radiation boundary. The mass accretion rate $\dot{M} = \int \rho_0 u^1 \sqrt{-g} dx^2 dx^3$ is evaluated at the inner radial boundary. Radiative efficiency $\epsilon \equiv L/\dot{M}$.

We begin time averages at the time at which global quantities ($\dot{m}$, L, ϵ) appear relatively steady; time averages (denoted as $\overline{f}$ for a quantity f) are always for $600 \leq tc^3/GM \leq 1000$. We also consider weighted spatial averages,

$$\langle f \rangle_\phi \equiv \frac{\int dx^1 dx^2 dx^3 \sqrt{-g} f \, \phi}{\int dx^1 dx^2 dx^3 \sqrt{-g} \, \phi}. \tag{4.11}$$

For simple volume averages inside a radius r denoted $\langle f \rangle_r$, $\phi = 1$ and r sets the upper radial bound of the integrals. $r = 10GM/c^2$ is a natural choice , as it is approximately the radius inside of which viscous equilibrium is achieved.

Figure 1 compares the radiative efficiency ϵ for radiative and nonradiative models versus $\dot{m}$. Up to $\dot{m} \approx 10^{-6}$, the models are equivalent. At higher $\dot{m}$, however, radiative cooling significantly affects the bolometric luminosity. Therefore, for $\dot{m} \gtrsim 10^{-6}$, self-consistency requires the inclusion of radiative cooling. Note that this value is somewhat higher than the condition $\dot{m} \gtrsim 10^{-7}$ identified by Dibi et al. (2012), possibly due to differing prescriptions for T_e. Additionally, our ϵ are a factor ~ 5 larger at comparable $\dot{m}$ than the $T_p/T_e = 10$, $a_\star = 0$, 3D models of Sądowski & Gaspari (2017). Compton scattering becomes commensurate with synchrotron emission at $\dot{m} \approx 10^{-5}$, and Coulomb heating becomes energetically significant at the $\sim 10\%$ level. The emission-weighted electron temperature $\langle \overline{\Theta_e} \rangle_J$ decreases significantly for $\dot{m} \approx 10^{-5}$. Electrons inside $r \sim 15GM/c^2$ achieve thermal equilibrium in our models. These are the radiating electrons for all but the $\dot{m} \approx 10^{-5}$ model, where electrons out to $\sim 30GM/c^2$ contribute to the luminosity. At $t = 1000GM/c^3$, these electrons are still heating slightly due to Coulomb coupling. Hereafter we ignore the $\dot{m} \approx 10^{-9}$ model, as flow properties are nearly independent of $\dot{m}$ at such low rates in our model since radiation is negligible.

Figure 4.2 shows $\dot{m}$, luminosity L, and radiative efficiency ϵ as a function of time. L scales superlinearly with $\dot{m}$ for all simulations reported here ($L \sim \dot{m}^2$, and therefore $\epsilon \sim \dot{m}$, for low $\dot{m}$, as expected for synchrotron-dominated weak cooling), consistent with the increase in ϵ with $\dot{m}$ seen in Figure 4.1. Across this range of $\dot{m}$ the flow transitions from very radiatively inefficient to a nearly radiatively efficient luminous state.

Figure 4.3 shows the global structure of the electron temperature $\overline{\Theta_e}$ in the accretion flows near the black hole. The electron heating model used here leads to hotter electrons in the more magnetized corona and cooler electrons in the less-magnetized disk midplane (see Ressler et al. 2015, 2017 for more details). At the

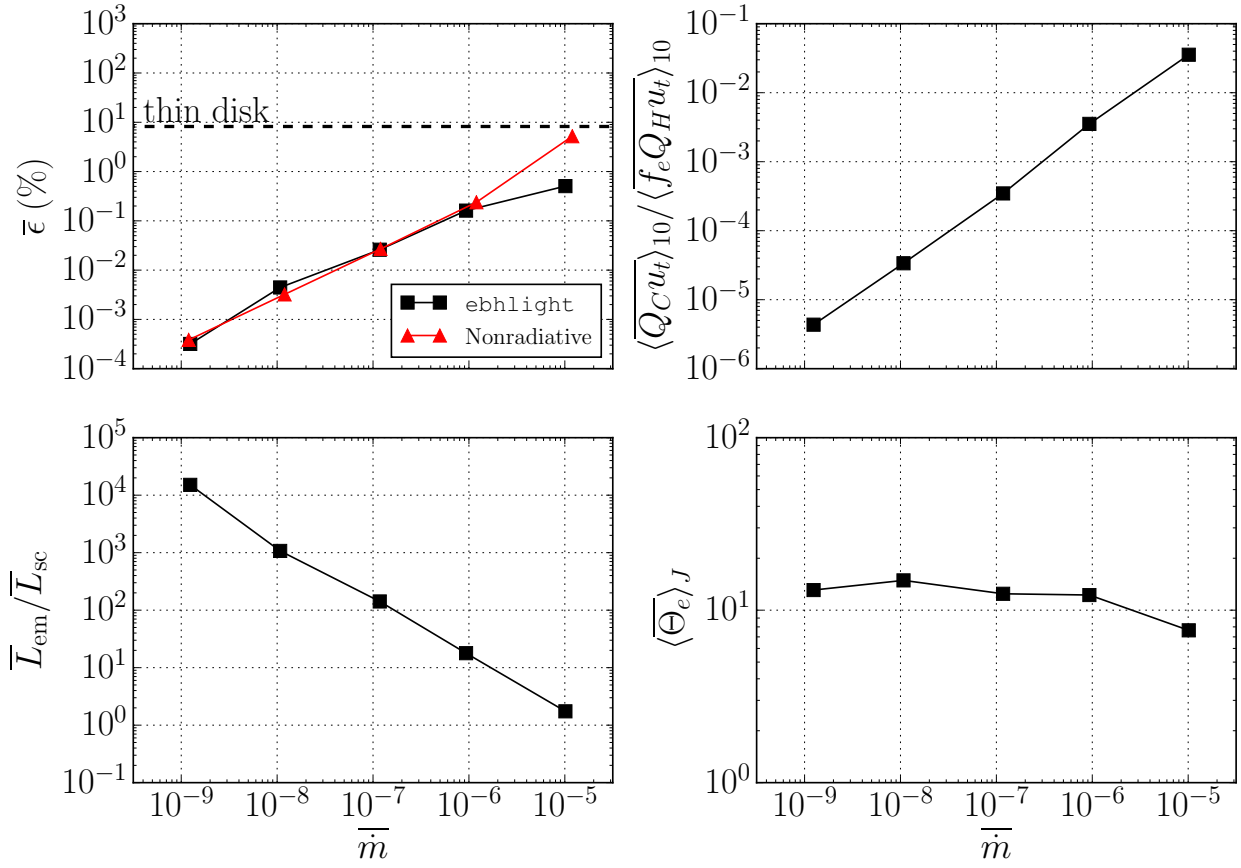

Figure 4.1: Globally averaged quantities. The top left panel shows radiative efficiency ϵ versus $\overline{\dot{m}}$ for models with and without radiative cooling, along with the thin disk efficiency ($\epsilon = 8.2\%$ for $a_\star = 0.5$; Novikov & Thorne 1973). The top right panel shows the ratio between viscous and Coulomb heating. The bottom right panel shows the emissivity-weighted electron temperature, and the bottom left panel shows the ratio of outgoing radiation due to synchrotron and Compton processes.

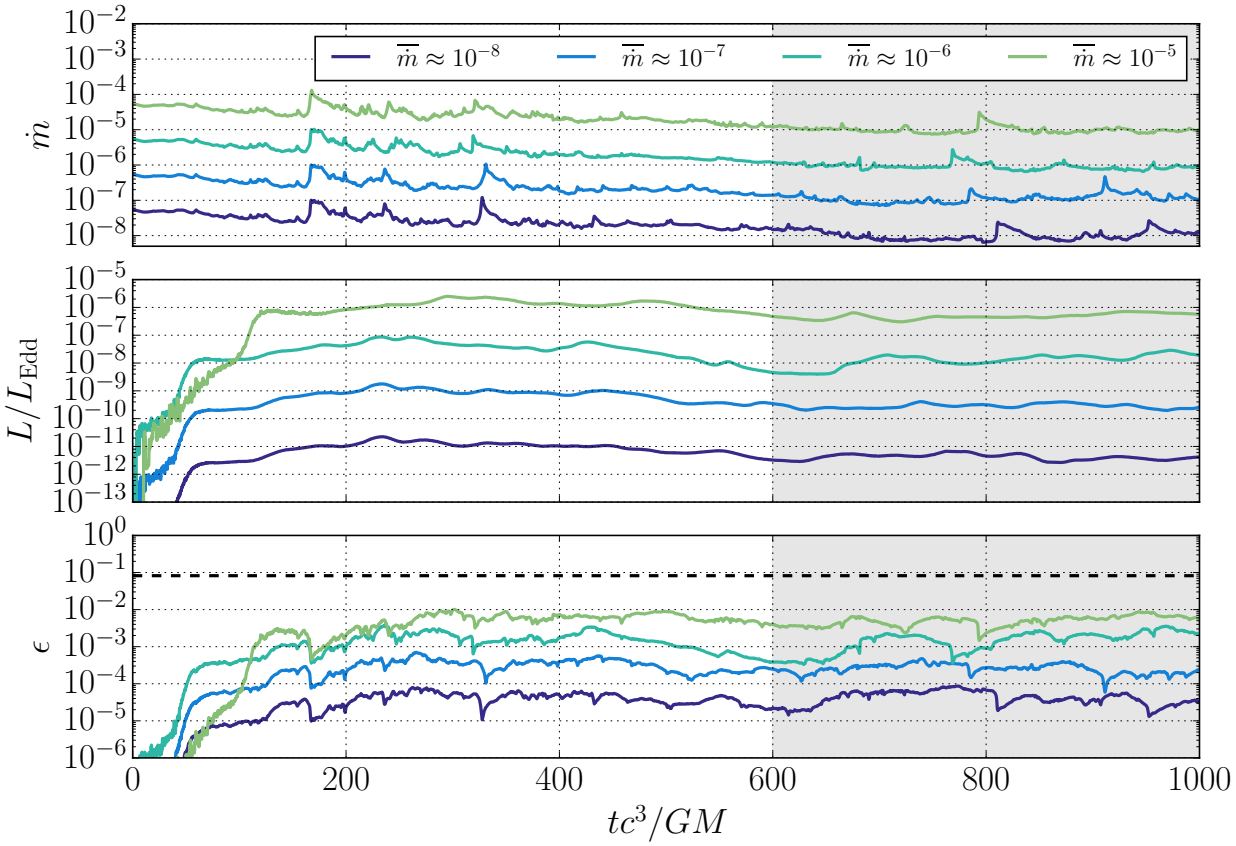

Figure 4.2: Accretion rate, luminosity, and radiative efficiency as a function of time. Time-averaging window is shown as the shaded region. Thin disk efficiency is shown as dashed line in the bottom panel.

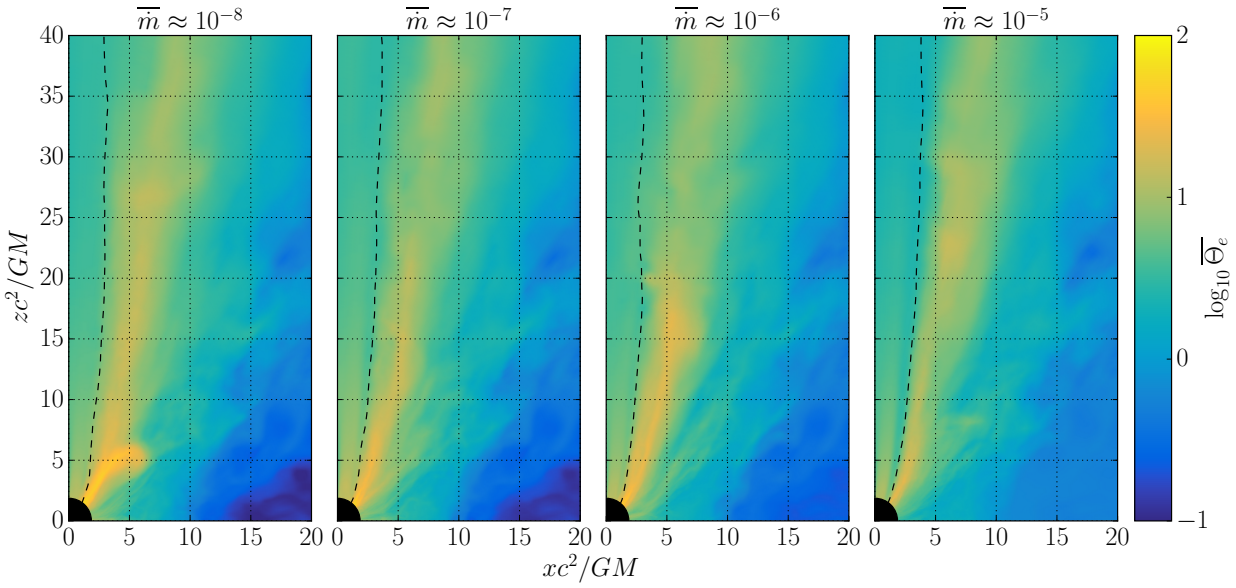

Figure 4.3: Time-averaged electron temperature for all models, also averaged about the midplane. Coulomb collisions heat up the disk at higher $\dot{m}$. The dashed line shows the funnel wall, defined as $b^2/\rho = 1$.

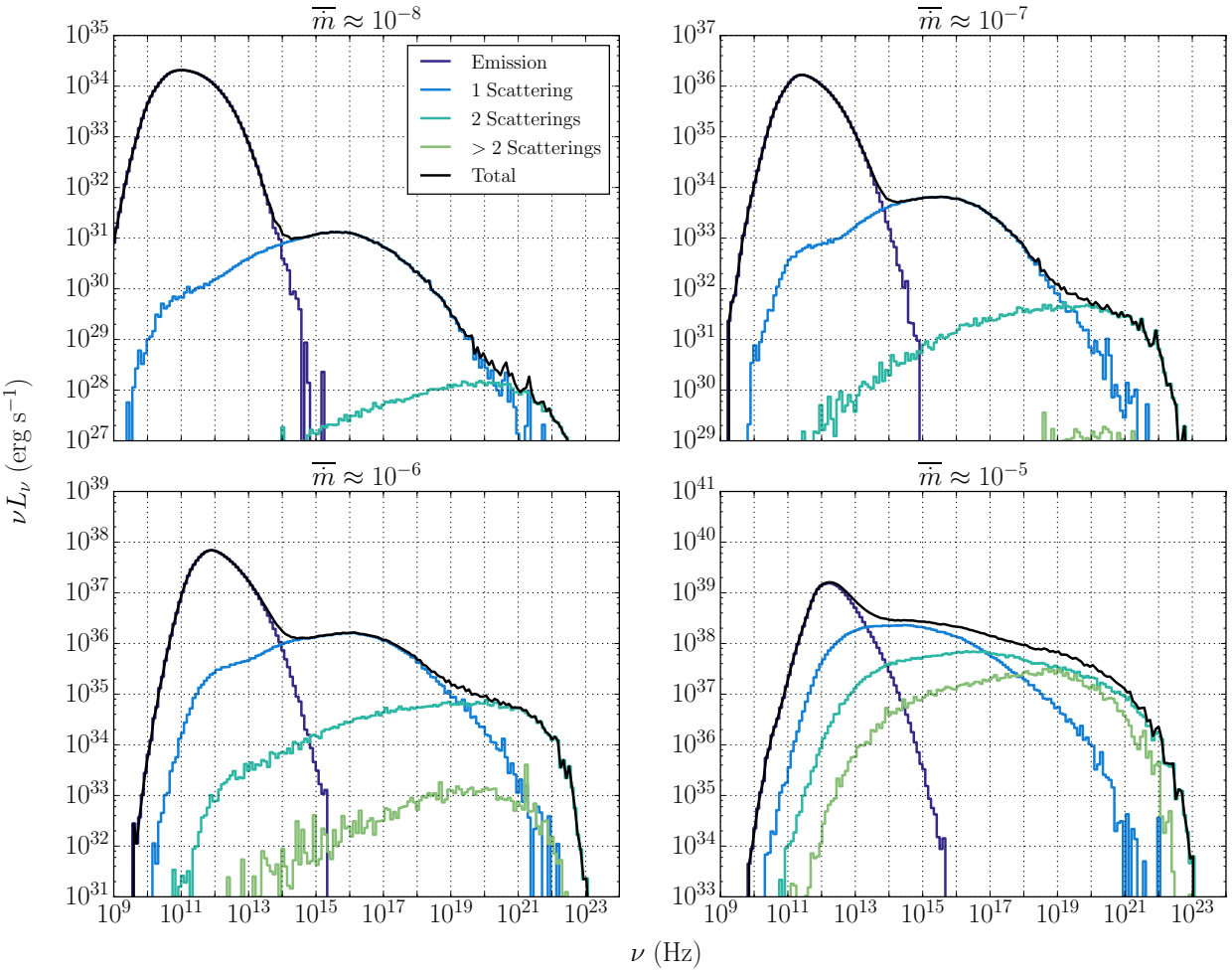

Figure 4.4: Spectral energy distributions for all models. Both total νL_ν and that due to individual interactions (emission, one scattering event, etc.) are shown. The logarithmic interval in νL_ν is common to all panels. At high $\dot{m}$, multiple Compton scattering events form a high-energy, nearly power-law spectral component

highest accretion rates, however, the midplane electrons are significantly hotter (at $r = 20GM/c^2$, in the midplane, $\Theta_e(\dot{m} = 10^{-5})/\Theta_e(\dot{m} = 10^{-8}) \approx 8$) due to Coulomb heating, and cooling lowers Θ_e in the inner regions of the flow.

Figure 4.4 shows the spectra of emergent radiation for an observer nearly in the midplane of the disk. These are evaluated from the same superphotons present in the simulations. At low accretion rates the spectrum is very soft, with distinct Compton bumps, consistent with previous models where radiation was calculated in post-processing without solving self-consistently for the electron temperature (e.g. Mościbrodzka et al. 2009). As the accretion rate increases, the slope of the high energy tail shifts upwards. These trends are consistent with spectral models of 1D RIAFs (e.g. Esin et al. 1997, Yuan et al. 2004).

4.6 Conclusion

We have presented general relativistic radiation magnetohydrodynamic simulations of radiatively inefficient black hole accretion flows. We have considered a black hole of mass $10^8 M_\odot$ and spin $a_\star = 0.5$, and accretion rates up to and including those for which radiative cooling is important. In particular, our inclusion of frequency-dependent full radiation transport addresses an important uncertainty in simulations of RIAFs.

We have found that RIAF models depart from self-consistency at an accretion rate $\dot{m} \approx 10^{-6}$, in the sense that self-consistent calculations with cooling are needed to predict the radiative efficiency and spectrum. By $\dot{m} \approx 10^{-5}$, the cooling of these flows becomes dominated by Compton scattering, rather than emission, and the flow achieves nearly 1%-level radiative efficiency.

Our results suggest that Coulomb collisions will become as important as viscous heating at an accretion rate of $\dot{m} \approx 10^{-4}$ (extrapolating Figure 4.1 to somewhat higher $\dot{m}$). This is well below what is traditionally assumed in semi-analytic models (for example, Esin et al. (1997) assume that Coulomb collisions dominate for $\dot{m} \gtrsim 0.1$). This is probably due to the different density and temperature profiles for analytic models and numerical simulations (e.g. Narayan et al. 2012). Future work should study this in 3D simulations and assess the implications of this behavior for observations, including the phenomenology of state transitions in X-ray binaries.

Our study is limited to axisymmetry. To minimize this weakness, we have used as initial conditions long-duration 3D nonradiative two-temperature GRMHD simulations. Nonetheless, we achieve viscous and inflow equilibria only within $r \sim 15GM/c^2$. This has potential consequences mostly for the $\dot{m} \sim 10^{-5}$ model, for which $\sim 20\%$ of the luminosity is generated beyond $15GM/c^2$. In this model the electrons at large radius are still heating up; thermal equilibrium would imply a slightly higher radiative efficiency. Should the flow change after viscous equilibration (probably towards reduced proton pressure), the luminosity could be suppressed by $\sim 20\%$, mostly in the high-energy tail of the spectrum.

Our survey is not comprehensive. Black hole mass, spin, accretion disk tilt, and net magnetic flux may all significantly affect these results. We will study these dependencies in future work.

We have directly demonstrated that radiative cooling plays an important role in RIAFs. The whole range of accretion rates considered in this work is probably populated by astrophysical sources, and the technique presented here will be valuable in interpreting observations of both stellar mass and supermassive black holes from the mm to the γ-ray.

It is a pleasure to thank M. Chandra, A. Sądowski, and J. Stone for useful discussions, as well as the anonymous referee for a very useful report. Work at Los Alamos National Laboratory was done under the auspices of the National Nuclear Security Administration of the US Department of Energy. SMR is

supported in part by the NASA Earth and Space Science Fellowship. JD acknowledges support from the Laboratory Directed Research and Development program at Los Alamos National Laboratory. Support for AT was provided by NASA through Einstein Postdoctoral Fellowship grant number PF3-140131 awarded by the Chandra X-ray Center, which is operated by the Smithsonian Astrophysical Observatory for NASA under contract NAS8-03060, and the TAC fellowship, and by NSF through an XSEDE computational time allocation TG-AST100040 on TACC Stampede. This work was made possible by computing time granted by UCB on the Savio cluster. CFG's work was also supported in part by a Romano Professorial Scholar appointment, a Simons Fellowship in Theoretical Physics, and a Visiting Fellowship at All Souls College, Oxford. EQ is supported in part by a Simons Investigator Award from the Simons Foundation and the David and Lucile Packard Foundation. This work was supported in part by NSF grant AST 13-33612. This research used resources provided by the Los Alamos National Laboratory Institutional Computing Program, which is supported by the U.S. Department of Energy National Nuclear Security Administration under Contract No. DE-AC52-06NA25396.

Chapter 5

Two-Temperature GRRMHD Simulations of M87

5.1 Summary

We present axisymmetric two-temperature general relativistic radiation magnetohydrodynamic (GRRMHD) simulations of the inner region of the accretion flow onto the supermassive black hole at the center of M87. We address uncertainties from previous modeling efforts through inclusion of models for (1) self-consistent viscous and Coulomb electron heating (2) radiation transport (3) frequency-dependent synchrotron emission, self-absorption, and Compton scattering. We adopt a distance $D = 16.7$ Mpc, an observer angle $\theta = 20°$, and consider black hole masses $M/M_\odot = (3.3 \times 10^9, 6.2 \times 10^9)$ and dimensionless black hole spin parameters $a_\star = (0.5, 0.9375)$ in a four-simulation suite. For each $(M, a_\star)$, we identify the accretion rate that recovers the 230 GHz flux from resolved VLBI measurements. We report on disk thermodynamics at these accretion rates ($\dot{M}/\dot{M}_{\rm Edd} \sim 10^{-5}$) and identify several universal features. The disk remains geometrically thick; cooling does not lead to a thin disk component. While electron heating is dominated by Coulomb rather than viscous dissipation for $r \gtrsim 10GM/c^2$, the accretion disk remains two-temperature. Radiative cooling of electrons is not negligible, especially for $r \lesssim 10GM/c^2$. The Compton y parameter is of order unity. We then compare synthetic and observed spectra, derive mm images in the context of upcoming EHT measurements, and compare jet power to inferred values. Simulations with $M/M_\odot = 3.3 \times 10^9$ are in conflict with observations. For both values of spin they produce mm images that are too small, while the low-spin simulation also overproduces X-rays. For $M/M_\odot = 6.2 \times 10^9$, both simulations agree with observational constraints on radio/IR/X-ray emission and imaging. Jet power is a factor $10^2 - 10^4$ below observationally inferred values for all models, a possible consequence of the modest net magnetic flux in our simulations[1].

[1]This work is in preparation for submission to ApJ; Ryan et al. (2018).

5.2 Introduction

The supermassive black hole (SMBH) at the center of the massive elliptical galaxy M87, hereafter simply M87, has been a classic observational target from the mm to the γ ray for decades. M87 is a valuable laboratory for studying Radiatively Inefficient Accretion Flows (RIAF; Ichimaru 1977; Narayan & Yi 1994; Yuan & Narayan 2014), jet launching, and the phenomenology of low-luminosity active galactic nuclei (LLAGN), which dominate the population of local SMBHs (Greene & Ho 2007).

Apart from details of the accretion disk, the appearance of a black hole is set by its mass M and dimensionless spin parameter $a_\star$. The two leading methods for determining the mass of M87, stellar-dynamical measurements (e.g. Gebhardt et al. 2011, who find $M = 6.6 \times 10^9 M_\odot$ for distance $D = 17.9$ Mpc) and gas-dynamical measurements (e.g. Walsh et al. 2013, who find $M = 3.5 \times 10^9 M_\odot$, also for $D = 17.9$ Mpc) currently disagree by a factor ≈ 2. The spin of M87 is uncertain (although see Doeleman et al. 2012 for an argument based on very long baseline interferometry (VLBI) favoring $a_\star \gtrsim 0.5$).

M87 is detectable at essentially all observed wavelengths: the radio (e.g. Hada et al. 2011; de Gasperin et al. 2012; Doeleman et al. 2012), IR (e.g. Shi et al. 2007; Asmus et al. 2014), optical/UV (e.g. Sparks et al. 1996), X-ray (e.g. Böhringer et al. 2001; Wilson & Yang 2002; Di Matteo et al. 2003), and γ-ray (e.g. Abdo et al. 2009; Abramowski et al. 2012). Constructing broadband spectra of LLAGN, however, leads to difficulties: (1) different frequency bands use different observational techniques, leading to inconsistent aperture sizes and spectral resolution (2) LLAGN exhibit variability, often on the timescale at which observations at different frequencies may be performed (3) The jet of M87 exhibits several bright knots, especially HST-1 (e.g. Perlman et al. 2011). Prieto et al. (2016) have addressed these issues for M87, creating an optimal set of contemporaneous measurements that led to the identification of two states of accretion: quiescence and outburst. In both cases, the spectrum is nearly flat and featureless across almost 10 decades in frequency, in contrast to typical RIAF models which contain distinct Compton bumps, at least for a thermal electron distribution function (e.g. Narayan et al. 1998; Mościbrodzka et al. 2009).

Along with Sagittarius A* (Sgr A*), the Milky Way's supermassive black hole, M87 is one of the two event horizons sufficiently large on the sky for resolved VLBI imaging by the Event Horizon Telescope (EHT, e.g. Doeleman et al. 2012). Sgr A* and M87 form a serendipitous pair for studying RIAFs. Despite masses and accretion rates (in Eddington units) differing by several orders of magnitude, and Sgr A* possibly being nearly edge-on (e.g. Mościbrodzka et al. 2009; Dexter et al. 2010; Shcherbakov et al. 2012) while M87 is nearly face-on (e.g. Heinz & Begelman 1997), the two sources have approximately the same synchrotron peak frequency. Although Sgr A*'s event horizon is somewhat larger on the sky, particularly if lower measurements for the M87 mass are correct, M87 remains an attractive target for two reasons: (1) intrinsic variability is

long compared to the timescale of a global VLBI observation (2) there is only modest interstellar scattering between Earth and M87, in contrast to Sgr A* (Bower et al. 2006). Radio VLBI observations of M87 have already achieved beam sizes of the order of a few Schwarzschild radii (Doeleman et al. 2012), implying a compact population of hot electrons near the black hole, in agreement with previous RIAF models (e.g. Esin et al. 1997, Mościbrodzka et al. 2009; Yuan & Narayan 2014).

Accretion onto black holes is probably mediated at least in part by angular momentum transport due to the turbulent state resulting from the saturation of the magnetorotational instability (MRI; Balbus & Hawley 1991). Together with magnetized coronae (Miller & Stone, 2000), correlations in the magnetic field (Guan & Gammie, 2011), and magnetized jets (Blandford & Znajek, 1977) all in a relativistic environment, general relativistic magnetohydrodynamic models are strongly motivated. As an example of the important of general relativity, for M87 Dexter et al. (2012) have argued that emission is counterjet-dominated through gravitational lensing, a purely relativistic effect. Significant progress in RIAFs has been made through numerical simulations (e.g. De Villiers et al. 2003b; McKinney & Gammie 2004; Narayan et al. 2012), which allow for a self-consistent treatment of the turbulent stress, as well as capturing the effects of large-scale components of the magnetic field (Tchekhovskoy et al. 2011; McKinney et al. 2012).

At very low accretion rates, $\dot{m} \equiv \dot{M}/\dot{M}_{\rm Edd} \ll 1$ (where the Eddington rate $\dot{M}_{\rm Edd} \equiv 2.2 \times 10^{-8}$ $(M/M_\odot)$ $M_\odot$ yr^{-1}, i.e. we adopt a nominal efficiency $\eta = 0.1$), RIAFs are Coulomb collisionless (Mahadevan & Quataert, 1997; Sądowski et al., 2017; Ryan et al., 2017b). Even for such collisionless flows, simple fluid model closures may be sufficient to accurately evolve the total fluid (Foucart et al., 2017). However, the electron thermodynamics are probably set by Larmor-scale velocity space instabilities (Quataert 1998; Sironi & Narayan 2015) which are not captured in ideal MHD. Magnetic reconnection may also play a role in electron heating (Rowan et al. 2017), as well as accelerating nonthermal electrons (e.g. Sironi & Spitkovsky 2014) which may have observational consequences for infrared variability and low-frequency radio emission (Özel et al. 2000; Yuan et al. 2003; Chael et al. 2017).

The generic consequence of electron heating through kinetic turbulent dissipation is probably hot protons and somewhat cooler electrons (Quataert 1998), with each population nonetheless approximately thermal due to kinetic instabilities that feed off distribution function anisotropies (Kunz et al. 2014; Riquelme et al. 2015; Kunz et al. 2016). The electron heating probably depends on the local plasma conditions, especially the plasma $\beta \equiv nk_BT/8\pi B^2$ (Howes 2010). While the electron temperature in RIAF simulations is often set to a prescribed fraction of the total internal energy (Mościbrodzka et al. 2009; Drappeau et al. 2013; Chan et al. 2015; Mościbrodzka et al. 2016), Ressler et al. (2015) have developed a method to combine advection and heating based on implicit dissipation in GRMHD schemes to self-consistently evolve the electron temperature,

which we extended to include Coulomb coupling in Ryan et al. (2017b) (see also Sądowski et al. 2017 for a similar method).

A significant challenge to numerical models of M87 has been the apparent importance of radiative processes to the thermodynamics of the accretion flow. Previous efforts applying nonradiative GRMHD simulations to M87 have had difficulty demonstrating self-consistency (Mościbrodzka et al., 2011; Dexter et al., 2012). Near the black hole, both synchrotron emission and Compton upscattering cool the electrons. More recently, Mościbrodzka et al. (2016) achieved reasonable radiative efficiencies, but required a proton-to-electron temperature ratio $T_p/T_e = 100$ in the midplane, relatively high compared to those preferred for unambiguously nonradiative models (e.g. Sgr A*, Mościbrodzka et al. 2014), but for $T_p/T_e < 40$ in the midplane, the models overproduced X-ray emission. While optically thin synchrotron emission is easily incorporated, the Compton y parameter is probably ~ 1 for M87 (e.g. Dexter et al. 2012). Compton scattering globally couples the disk electrons through the radiative transfer equation. Global relativistic MHD models with self-consistent radiation transport are therefore strongly motivated.

The importance of radiative cooling to electron temperatures and observable radiation in RIAFs above some $\dot{m}$ has long been recognized (e.g. Esin et al. 1997; Xie et al. 2010; Niedźwiecki et al. 2012). However, computational expense and algorithmic complexity have restricted the inclusion of radiative transport into GRMHD calculations. Ohsuga et al. (2009) and Ohsuga & Mineshige (2011) studied the first global radiation magnetohydrodynamics models of accretion disks, using a diffusion model for radiation transport to demonstrate the anticipated transition from RIAFs to radiation-dominated thin disks (Shakura & Sunyaev 1973) with increasing $\dot{m}$. Subsequent work used local models for radiative cooling (Fragile & Meier 2009; Dibi et al. 2012; Wu et al. 2016), or a fluid model for radiation to yield a general relativistic radiation magnetohydrodynamics (GRRMHD) model in axisymmetry (Sądowski et al. 2017) and 3D (Sądowski & Gaspari 2017). Simulations have generally confirmed the picture of a RIAF perturbed by radiative cooling, although details of the transition to radiative efficiency are still uncertain.

We have developed a numerical method, `bhlight`, for solving the GRRMHD equations with a Monte Carlo method to provide a direct solution to the frequency-dependent radiative transport equation including emission, absorption, and Compton scattering (Ryan et al. 2015). We introduced `ebhlight` to include the electron heating scheme of Ressler et al. (2015) with Coulomb coupling in Ryan et al. (2017b). Surveying $\dot{m}$ for $M = 10^8 M_\odot$, Ryan et al. (2017b) found radiative cooling to be significant for $\dot{m} \gtrsim 10^{-5}$, with high-energy spectra progressively hardening and previously distinct Compton bumps merging to form a smooth power-law tail with increasing $\dot{m}$. `ebhlight` allows us to model optically thin RIAFs in axisymmetry without substantial approximation to the radiation physics, although our model remains sensitive to the electron

thermodynamics, and to our assumption that the electron distribution function is thermal.

Post-processing of GRMHD simulations is now a standard technique for interpreting LLAGN observations, particularly for Sgr A* where the accretion rate is so low that radiative feedback on the flow dynamics and energetics is negligible (Dibi et al. 2012). GRMHD models, electron physics, accretion rate, black hole spin, and observer angle are all constrained through spectra, variability, polarization, and imaging (e.g. Mościbrodzka et al. 2009; Dexter et al. 2012; Dolence et al. 2012; Shcherbakov et al. 2012; Shcherbakov & McKinney 2013; Drappeau et al. 2013; Mościbrodzka et al. 2014; Chan et al. 2015; Ball et al. 2016; Ressler et al. 2017; Medeiros et al. 2017).

In this work we apply standard GRMHD post-processing techniques to a suite of global axisymmetric GRRMHD `ebhlight` simulations to interpret time-averaged spectral and imaging observations of M87. In Section 5.3 we describe the governing equations, and in Section 5.4 we describe our numerical implementation and present a test of our code. Section 5.5 presents our models and results. Section 5.6 discusses these results in the context of current and upcoming observations, and Section 5.7 concludes.

5.3 Governing Equations

`bhlight` solves the equations of GRRMHD in stationary spacetimes with frequency dependent radiative transport. Electron temperatures are evolved self-consistently according to a plasma-dependent heating prescription. Photon-electron emission, absorption, and scattering couple the matter and radiation. In this section, we adopt units such that $GM = c = 1$.

5.3.1 Magnetohydrodynamics

The equations of GRMHD for conservation of mass, energy-momentum, and magnetic flux along with the no-monopoles constraint (e.g. Gammie et al. 2003) take the forms, respectively,

$$\partial_t \left(\sqrt{-g}\rho_0 u^t\right) = -\partial_i \left(\sqrt{-g}\rho_0 u^i\right), \tag{5.1}$$

$$\begin{aligned}\partial_t \left(\sqrt{-g}T^t{}_\nu\right) = &-\partial_i \left(\sqrt{-g}T^i{}_\nu\right) + \sqrt{-g}T^\kappa{}_\lambda \Gamma^\lambda{}_{\nu\kappa} \\ &- \sqrt{-g}R^\mu{}_{\nu;\mu},\end{aligned} \tag{5.2}$$

$$\partial_t \left(\sqrt{-g}B^i\right) = \partial_j \left[\sqrt{-g}\left(b^j u^i - b^i u^j\right)\right], \tag{5.3}$$

$$\partial_i \left(\sqrt{-g}B^i\right) = 0. \tag{5.4}$$

with ρ_0 the rest-mass density, u^μ the fluid four-velocity, $\Gamma^\mu_{\ \nu\lambda}$ the Christoffel symbols, the total fluid stress-energy tensor

$$T^\mu_{\ \nu} = \left(\rho_0 + u + P + b^\lambda b_\lambda\right) u^\mu u_\nu + \left(P + \frac{b^\lambda b_\lambda}{2}\right) g^\mu_{\ \nu} - b^\mu b_\nu, \tag{5.5}$$

b^μ the magnetic field four-vector, u the total fluid internal energy density, $P = (\gamma - 1)u$ the total fluid pressure, and the radiation stress-energy tensor

$$R^\mu_{\ \nu} = \int \frac{d^3p}{\sqrt{-g}p^t} p^\mu p_\nu \left(\frac{I_\nu}{h^4\nu^3}\right), \tag{5.6}$$

($p^\mu \equiv$ photon four-momentum, $I_\nu \equiv$ specific intensity) the four-divergence of which ($G_\nu \equiv R^\mu_{\ \nu;\mu}$) gives the radiation four-force applied to the total fluid.

5.3.2 Two-Temperature Thermodynamics

To obtain both proton and electron temperatures, we solve for the electron entropy in addition to the total fluid energy as in Ressler et al. (2015). The first law of thermodynamics for the electrons in a coordinate basis is

$$\frac{\rho^{\gamma_e}}{\gamma_e - 1} u^\mu \partial_\mu \kappa_e = f_e Q_H + Q_C - u^\nu R^\mu_{\ \nu;\mu}, \tag{5.7}$$

where $\kappa_e \equiv \exp((\gamma_e - 1)s_e) = P_e/\rho_0^{\gamma_e}$ ($s_e \equiv$ electron entropy), Q_H and Q_C are, respectively, dissipative (viscous/resistive) and Coulomb (Stepney & Guilbert, 1983) volumetric heating rates. The last term represents exchange of energy between photons and electrons.

Typically in hot accretion disks, the electrons are relativistic while the protons are nonrelativistic; the two species thus have different adiabatic indices. We adopt three constant values: $\gamma_p = 5/3$ for protons, $\gamma_e = 4/3$ for electrons, and $\gamma = 13/9$ for the total fluid. The proton internal energy density (needed for the Coulomb heating rate) is $u_p = u - u_e$.

5.3.3 Covariant Radiation Transport

We solve the radiative transfer equation in invariant form

$$\frac{d}{d\lambda}\left(\frac{I_\nu}{\nu^3}\right) = \frac{\eta_\nu}{\nu^2} - (\nu\chi_\nu)\frac{I_\nu}{\nu^3}, \tag{5.8}$$

along geodesics described by

$$\frac{dx^\mu}{d\lambda} = k^\mu, \tag{5.9}$$

$$\frac{dk^\mu}{d\lambda} = -\Gamma^\lambda{}_{\mu\nu} k^\mu k^\nu, \tag{5.10}$$

where x^μ is the spacetime coordinate of a photon, k^μ the corresponding wavevector, and $d\lambda$ the affine parameter along the geodesic. η_ν and χ_ν are the emission and absorption coefficients, respectively, and include contributions from scattering. We consider thermal synchrotron emission and absorption, and Compton scattering.

5.4 Numerical Method

`ebhlight` (Ryan et al. 2017b) solves the equations of general relativistic radiation magnetohydrodynamics with frequency dependent radiation transport. Here we provide an overview of the numerical implementation, emphasizing the interplay between the electron thermodynamics (Ressler et al., 2015) and the radiation. The one-temperature GRRMHD method `bhlight` is described in detail in Ryan et al. (2015).

5.4.1 GRMHD

`ebhlight`'s fluid sector is based on the GRMHD scheme `harm` (Gammie et al., 2003). `harm` is a relativistic second-order explicit shock-capturing scheme for stationary spacetimes. Magnetic monopoles are suppressed to roundoff error through flux-interpolated constrained transport (Tóth, 2000).

The radiation four-force, the cumulative representation of emission, absorption, and scattering (equivalently, the divergence of the radiation stress-energy tensor), is applied in a first-order operator-split fashion to the total energy and momentum of the MHD sector. While this is inferior to the second-order accuracy elsewhere in the GRMHD sector, `ebhlight` is designed for RIAF problems for which the radiative cooling time is long compared to the timestep.

5.4.2 Radiation

The radiation field is discretized into Monte Carlo samples, hereafter "superphotons", based on the relativistic radiative transfer scheme `grmonty` (Dolence et al., 2009). Each superphoton possesses the usual properties of a photon (position x^μ, wavevector k^μ) along with a weight w corresponding to the number of constituent photons. In contrast to `grmonty`, each superphoton is emitted with equal total energy, i.e. $h\nu w = \text{const}$ (Abbott & Lucy 1985), which tends to provide highest accuracy at fixed computational expense for Monte Carlo radiation hydrodynamics. The radiation boundary is typically further in than the fluid boundary. This allows us to place the outer boundary of GRMHD evolution far from the black hole to avoid spurious fluid boundary effects while avoiding the computational expense of integrating large numbers of superphotons along nearly straight geodesics through regions with negligible radiation-matter interactions.

`ebhlight` integrates superphotons along geodesics using a second-order explicit step on the fluid timestep. Although our second-order scheme requires only one evaluation of the Christoffel symbols per geodesic update, in practice this is the dominant computational cost in accretion disk simulations.

Superphotons are created by sampling the total emissivity of the plasma in the fluid frame over frequency and angle. `ebhlight` is physics-agnostic in this regard. While we have implemented the synchrotron emissivity of Leung et al. (2011), new emissivities are readily introduced.

Absorption and scattering are incorporated probabilistically. Following integration along geodesics, optical depths to absorption and scattering are calculated based on the traversed affine parameter $\Delta\lambda$. These optical depths are sampled to determine if an interaction has taken place, and if so whether it was absorption or scattering. If so, the superphoton is pushed back along its geodesic to the site of the interaction and the interaction is processed. For absorption, the superphoton is completely absorbed. For scattering, a bias parameter is used such that superphotons are scattered more frequently, but only with a fraction of their weight w. This process generates an additional superphoton for each biased scattering, and greatly enhances resolution in the radiation field when the optical depth to scattering is small but the amplification factor due to scattering is large.

The desired number of superphotons per MPI process is specified as a runtime parameter in `ebhlight`. Superphoton resolution (i.e. weight w) is controlled dynamically in two ways so as to recover this desired number of superphotons in a time-averaged sense. First, the energy per superphoton is adjusted to control the emitted number of superphotons, based on the difference in emitted and absorbed superphotons relative to the light crossing time of the radiation region. Second, the scattering bias is adjusted such that each emitted superphoton scatters approximately once. With less frequent scattering, resolution is lost at higher photon frequencies. With more frequent scattering, the numerics go critical, analogous to a fission reactor

meltdown.

The usual signature of insufficient superphoton resolution for our RIAF models is "supercooling", in which superphoton weights are too large to accurately sample emission and scattering; there are too few interactions per cooling time. Zones may then be cooled to negative internal energies, which after GRMHD fixup routines results in energy nonconservation, or at least spurious electron heating. We monitor supercooling to ensure that this anomalous energy is not a significant part of the radiation energy budget, i.e. that we have a sufficient number of superphotons per MPI process and a sufficient number of MPI processes. Supercooling could also result from local cooling timescales shorter than the global simulation timestep. Although we do not encounter such short cooling timescales in our target application, implicit Monte Carlo methods (e.g. Roth & Kasen 2015) have been developed to address this issue.

5.4.3 Electron thermodynamics

We model the electron temperature with the self-consistent electron heating scheme of Ressler et al. (2015). Viscous heating in ideal MHD schemes such as `harm` is present as grid-scale dissipation. Here we evaluate that heating by advecting the total entropy of the fluid simultaneously with the traditional GRMHD update of conserved mass, energy, and momentum. After the step, the advected and evolved total entropies are compared; this difference is the heating rate. A fraction of this heating, evaluated based on the local plasma prescription of Howes (2010), is then applied the electron entropy, which is itself advected and which provides the electron temperature.

In `ebhlight`, the electron entropy variable provides the electron temperature used in evaluating emissivities, absorptivities, and scattering events. In addition, the radiation exchanges energy directly with this electron entropy, rather than with the total fluid internal energy. We apply the timelike component of the radiation four-force in the comoving frame, $u^\mu G_\mu$, to the electron entropy in a similar first-order operator split fashion as we apply G_μ to the total fluid stress-energy tensor.

We now also include Coulomb heating as a second-order operator-split explicit update to the electron entropy. Evaluating electron and proton temperatures from the total fluid internal energy and the electron entropy, we calculate the Coulomb heating rate of Stepney & Guilbert (1983). We then update the electron entropy in accordance with this heating; the total internal energy is unchanged.

`harm`-like codes require fixup routines, which enforce minimum densities of rest mass and energy, to avoid instability during the fluid integration. Similar fixup routines are used for the electron entropy by Ressler et al. (2015). Our inclusion of Coulomb heating, which requires positive proton and electron temperatures, motivates somewhat different fixup routines than those in Ressler et al. (2015). In particular, we enforce

the ratio of proton to electron temperature $(T_p/T_e)_{\rm min} > 0.01$. In the radiation sector, we enforce $\Theta_e \equiv k_B T_e/m_e c^2 < 1000$ to avoid failures in sampling Compton scattering. Additionally, we forbid radiation interactions in the highly magnetized funnel region ($b^2/\rho > 1$), where `harm`-like total energy codes cannot accurately represent even total fluid thermodynamics[2].

5.4.4 e-p-γ Thermalization

We now present a test verifying our implementation, emphasizing Coulomb coupling and electron-photon interactions. Additional tests of the electron heating and radiation MHD sectors may be found in Ressler et al. (2015) and Ryan et al. (2015) We consider a one-zone model for the thermalization of electrons, protons, and photons. Electrons and protons interact through Coulomb collisions, while (only in this test) electrons and photons interact through a bremsstrahlung-like emissivity,

$$j_\nu = N n_e n_p T_e^{-1/2} \exp\left(\frac{-h\nu}{k_B T_e}\right), \tag{5.11}$$

where $n_e = n_p$ are the electron and ion number densities and $N = 5.4 \times 10^{-39}$ cm^3 K$^{1/2}$ s^{-1} Sr^{-1} Hz^{-1}. Thermal absorption is included. This test is similar to the thermalization problem in Sadowski 2016, except that we consider the full multifrequency problem through a frequency-dependent opacity.

We set the mass density $\rho = 2 \times 10^{-4}$ g cm^{-3} and initial proton and electron temperatures $T_{p,0} = 10^8$ K and $T_{e,0} = 10^7$ K. No radiation is present initially. We set the Coulomb logarithm $\log \Lambda = 0.01$ (present in $Q_{\rm coul}$) to enforce comparable Coulomb and emission timescales for an equilibrium temperature at which the radiation pressure does not overwhelm the gas pressure. We set $\gamma = 13/9$, $\gamma_e = 4/3$, and $\gamma_p = 5/3$.

We construct a semianalytic solution by solving the integro-differential equations

$$\frac{dT_e}{dt} = \frac{\gamma_e - 1}{n_e k_B}\left(Q_{\rm coul} - \int d\nu \frac{du_\nu}{dt}\right), \tag{5.12}$$

$$\frac{dT_p}{dt} = -\frac{\gamma_p - 1}{n_p k_B} Q_{\rm coul}, \tag{5.13}$$

$$\frac{du_\nu}{dt} = 4\pi j_\nu(T_e)\left(1 - \frac{c u_\nu}{4\pi B_\nu(T_e)}\right), \tag{5.14}$$

where the specific radiation energy density u_ν is discretized over frequency. We compare numerical output with this semianalytic solution in Figure 5.1, and find good agreement.

[2]At least within the GRMHD model, densities in the funnel region seem to have no lower limit; material either falls onto the black hole or is ejected to infinity, and the funnel wall itself is apparently stable to long-wavelength instabilities, at least for steady dipolar fields and an ideal fluid (McKinney & Blandford 2009). As a result, densities in the funnel are usually set by the numerical floor required for stability. Without additional physics such as pair production (e.g. Mościbrodzka et al. 2011), our model constrains us to suppose that densities in the funnel are too low to lead to significant radiation.

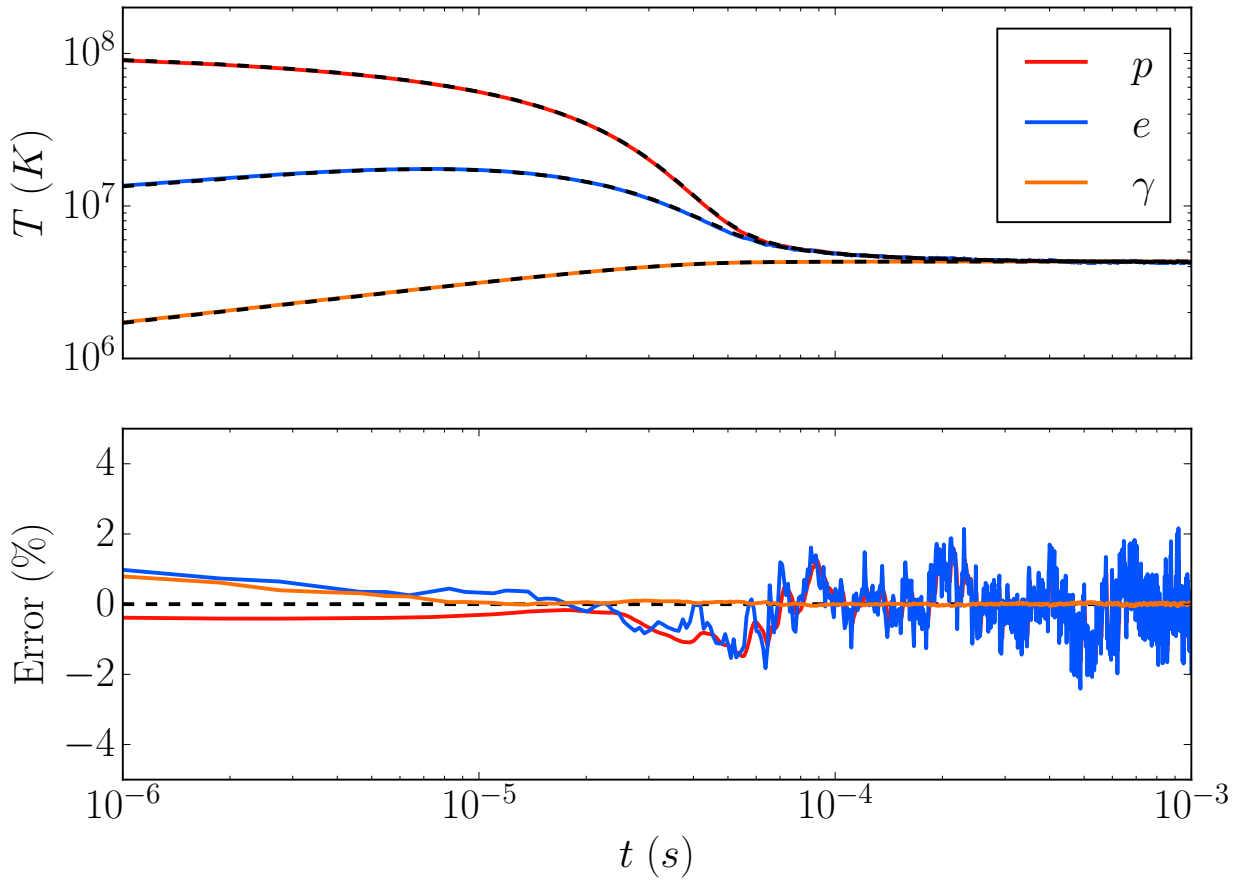

Figure 5.1: Proton, electron, and radiation temperatures for the thermalization test, along with relative errors. Solid lines denote `ebhlight` solution, while dashed lines give the semianalytic solution. Relative error is small, and at late time is dominated by Monte Carlo noise.

5.5 Results

We set out to model M87 for several parameter choices in order to identify which, if any, are consistent with observations. Our simulations are the four combinations of black hole masses $M/M_\odot = (3.3 \times 10^9, 6.2 \times 10^9)$ and spins $a_\star = (0.5, 0.9375)$. We assume a distance $D = 16.7$ Mpc (Blakeslee et al. 2009). The accretion rate is chosen such that we recover the 230 GHz flux measured for M87 from Doeleman et al. (2012), who found $F_{\nu,230\mathrm{GHz}} = 0.98 \pm 0.04$ Jy. Of all observed frequencies, this is probably the best choice for normalizing our models; the source is probably optically thin at 230 GHz, 230 GHz synchrotron emission is dominated by relativistic electrons near the black hole (as opposed to IR and X-ray emission, which may have contributions from outside our simulation domain), and Doeleman et al. (2012) demonstrated that at least some of this emission originates in a from a compact region at $r \lesssim 10GM/c^2$. Observer inclination angle is fixed at $\theta = 20^\circ$ (e.g. Heinz & Begelman 1997)[3].

5.5.1 Initial conditions

We use the horizon-penetrating Modified Kerr-Schild coordinates of McKinney & Gammie (2004), with θ-refinement parameter $h = 0.3$. We adopt a spatial resolution 388×256 zones. We target $\sim 10^7$ superphotons at saturation. The inner boundary is placed such that five zones (one fluid reconstruction stencil) are inside the event horizon, while the outer fluid boundary is placed at $200GM/c^2$. The outer radiation boundary is set to $40GM/c^2$ for $M/M_\odot = 6.2 \times 10^9$ and $100GM/c^2$ for $M/M_\odot = 3.3 \times 10^9$, beyond which radiative interactions are negligible in our model (there are radiative contributions at larger radii in our lower-mass simulations).

We initialize our torii using axisymmetrized 3D data from two 3D two-temperature SANE[4] GRMHD simulations ($a_\star = 0.5$ and $a_\star = 0.9375$, otherwise similar) run for $10,000\ GM/c^3$. This allows the electron temperatures to saturate due to viscous heating through a larger region of the disk ($r \lesssim 12GM/c^2$) than is possible with the limited runtimes available in axisymmetric models. Fluid mass, internal energy, and velocity, along with electron entropy, are averaged in ϕ, while the magnetic field is first converted to a magnetic vector potential, which is averaged in ϕ and then differentiated to recover an axisymmetric divergence-free magnetic field. No radiation is present initially, and the radiation field and superphoton number density equilibrate on the light crossing time. Each simulation is run for 1000 GM/c^3; time averages are begun at 600 GM/c^3, by which time bolometric luminosity L and radiative efficiency ϵ are relatively steady (see

[3]Dexter et al. 2012 found, for mm images of M87 derived from GRMHD simulations, that decreasing θ caused images to be more ring-shaped and less Gaussian. Image size was less sensitive to θ.

[4]SANE: Standard and Normal Evolution, i.e. net magnetic flux far below the Magnetically Arrested Disk limit at which the MRI-driven turbulence picture of angular momentum transport breaks down. See e.g. Narayan et al. (2012) for a comparison.

Figure 5.2).

The accretion rate for which the time-averaged 230 GHz flux agrees with the EHT result is determined by rootfinding. For each mass and spin, `ebhlight` simulations are performed in sequence at different $\dot{m}$ until the simulation and EHT $F_{\nu,230\mathrm{GHz}}$ agree to within 5%, roughly the error reported by Doeleman et al. (2012). This fully specifies the accretion disk for each mass and spin.

5.5.2 Diagnostics

We employ weighted shell averages $\langle f \rangle_w$ such that

$$\langle f \rangle_w = \frac{\int f w \sqrt{-g} dx^2 dx^3}{\int w \sqrt{-g} dx^2 dx^3}. \tag{5.15}$$

We use similar notation to denote unweighted averages inside a maximum radius $r_{\rm out}$:

$$\langle f \rangle_{r_{\rm out}} = \frac{\int^{r_{\rm out}} f \sqrt{-g} dx^2 dx^3}{\int^{r_{\rm out}} \sqrt{-g} dx^2 dx^3}; \tag{5.16}$$

see appendix in Farris et al. 2010 for a discussion of the transformation properties of integrals over $\sqrt{-g}dx^2dx^3$. For quantities representing ratios (T_p/T_e, β, $Q_{\rm coul}/Q_{\rm visc}$, $t_* \equiv u_*/Q_*$), $\langle A/B \rangle$ implies $\langle A \rangle / \langle B \rangle$. We do this so that isolated, small values of the denominators do not overly bias the averages.

We define a disk aspect ratio $H/R = \tan\theta_d$, where we follow McKinney et al. (2012) and define

$$\theta_d^2 \equiv \langle (\theta - \theta_0)^2 \rangle_\rho, \tag{5.17}$$

with $\theta_0 = \langle \theta \rangle_\rho$. Additionally, we define an accretion rate

$$\dot{M} = -\int \rho u^1 \sqrt{-g} dx^2 dx^3, \tag{5.18}$$

and a bolometric luminosity

$$L = -\int R^1{}_0 \sqrt{-g} dx^2 dx^3, \tag{5.19}$$

with a corresponding radiative efficiency $\epsilon \equiv L/\dot{M}$. Here, L and $\dot{M}$ are evaluated at the outer radiation and inner fluid radial boundaries, respectively, and ϵ therefore contains a delay corresponding to the light crossing time and ignores the effects of outflows. $R_{95} \equiv$ the radius inside of which 95% of the bolometric luminosity is generated. Averaged quantities for our simulations are summarized in Table 5.1.

Label	$\dot{m}$	ϵ	$\langle\Theta_e\rangle_J$	$L_{\rm em}/L_{\rm sc}$	$\frac{\langle Q_{\rm coul}\rangle_{10}}{\langle Q_{\rm visc}\rangle_{10}}$	$\langle H/R\rangle_{10}$	$R_{95}(GM/c^2)$	$P_{\rm J}$ (erg s^{-1})
M3a05	2.2×10^{-5}	1.6×10^{-2}	5.1	0.33	0.03	0.26	67	1.8×10^{40}
M3a09	8.2×10^{-6}	2.4×10^{-2}	8.7	0.75	0.04	0.32	88	4.7×10^{41}
M6a05	9.2×10^{-6}	6.7×10^{-3}	9.3	1.4	0.013	0.26	31	1.6×10^{40}
M6a09	5.2×10^{-6}	1.2×10^{-2}	14	1.5	0.024	0.32	12	5×10^{41}

Table 5.1: For each simulation, time-averaged fluid and radiation quantities: accretion rate, radiative efficiency, emissivity-weighted electron temperature, ratio of emitted and scattered photon contributions to bolometric luminosity (roughly the inverse of Compton y), ratio of Coulomb to viscous heating inside $r = 10GM/c^2$, radius of region contributing to luminosity, and jet power.

5.5.3 Intrinsic Model Properties

Our models, at $\dot{m} \sim 10^{-5}$, occupy an interesting range in accretion rate, and at black hole masses somewhat higher than the low spin ($a_\star = 0.5$), $M/M_\odot = 10^8$ black hole considered in Ryan et al. (2017b). Therefore, in this section we elaborate on the thermodynamic state of the accretion disk in our models. Note that care should be taken in extracting trends with mass and spin from this simulation suite, as the accretion rate for each simulation is set by the 230 GHz flux.

Accretion rate, luminosity, and radiative efficiency are shown as a function of time for all models in Figure 5.2. For the black hole masses and spins considered here, $\dot{m}$ varies by a factor ~ 20 across models. Radiative efficiency, on the other hand, varies by $\lesssim 4$. While axisymmetry probably enhances the variability of GRMHD simulations, there is no dramatic secular trend in $\dot{m}$, L, or ϵ over our time integration window ($600 < t < 1000$).

Time-averaged density, plasma β, dimensionless electron temperature Θ_e, and proton-to-electron temperature ratio T_p/T_e from M3a05 are shown in Figure 5.3. Despite cooling, for this accretion rate and runtime the ions in the torus continue to resemble a nonradiative hot, geometrically thick accretion flow. Consistent with the pure GRMHD calculations of self-consistent electron heating of Ressler et al. (2015), midplane electrons are generally cold while coronal electrons are hot. Notice however that the inclusion of Coulomb heating in this model enhances electron temperatures preferentially in the midplane, where collision times are shorter. The variable two-temperature nature of the flow is shown explicitly in the spatial dependence of T_p/T_e, which is approximately unity at the funnel wall and $\sim 10 - 30$ in the midplane.

Figure 5.4 shows time-averaged radial profiles from all simulations. To interpret the role of radiation physics, we have performed *nonradiative* (hereafter 'GRMHD') simulations at the two spin values from our axisymmetrized 3D data. Notice that black hole mass and accretion rate have no meaning in scale-free GRMHD simulations. Except for disabling radiation and Coulomb physics, all simulation properties are identical for GRMHD and GRRMHD simulations at each spin.

The top left panel of Figure 5.4 shows scaleheight H/R for each simulation relative to the equivalent

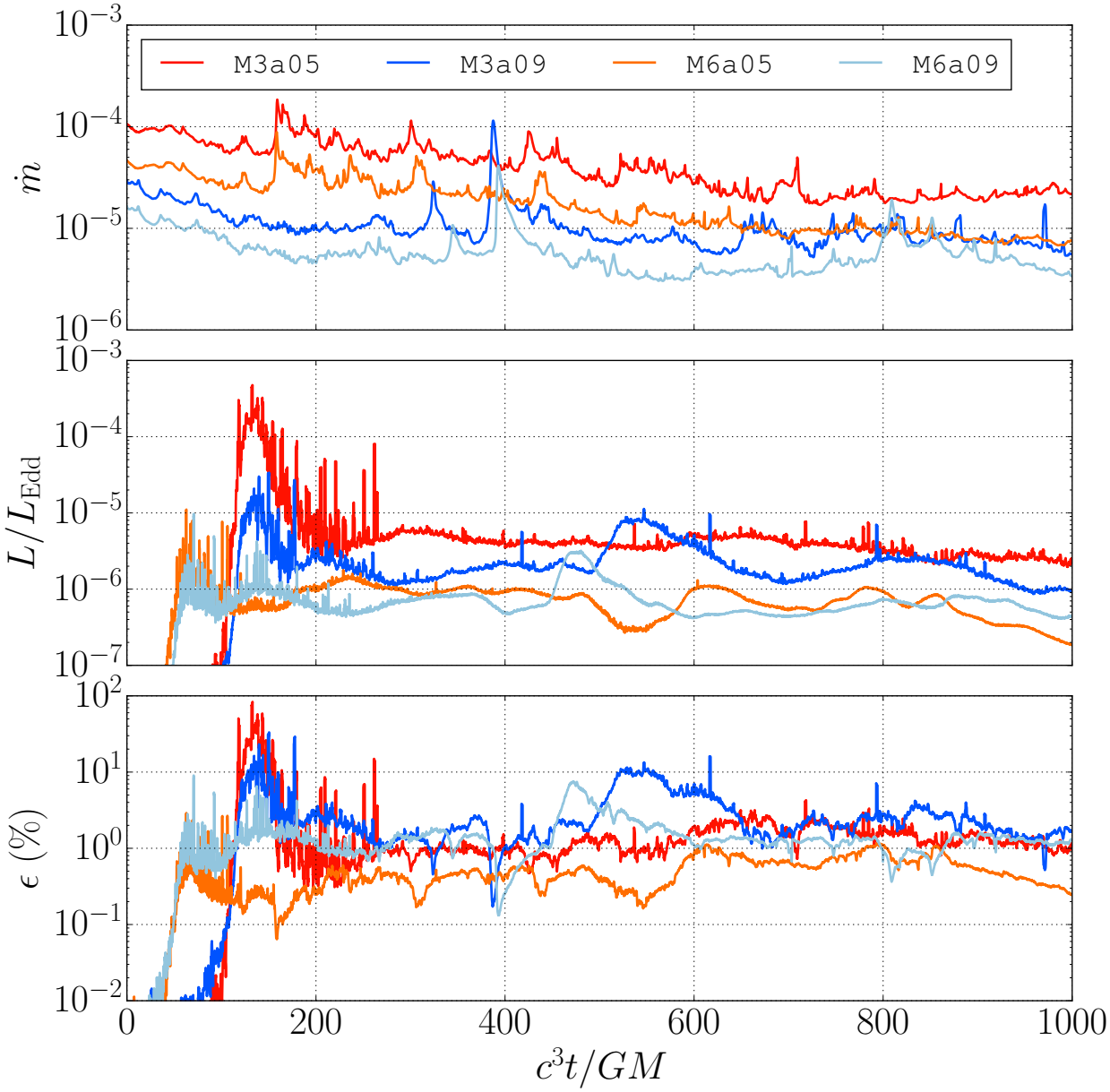

Figure 5.2: Accretion rate, luminosity, and radiative efficiency as a function of time for all models.

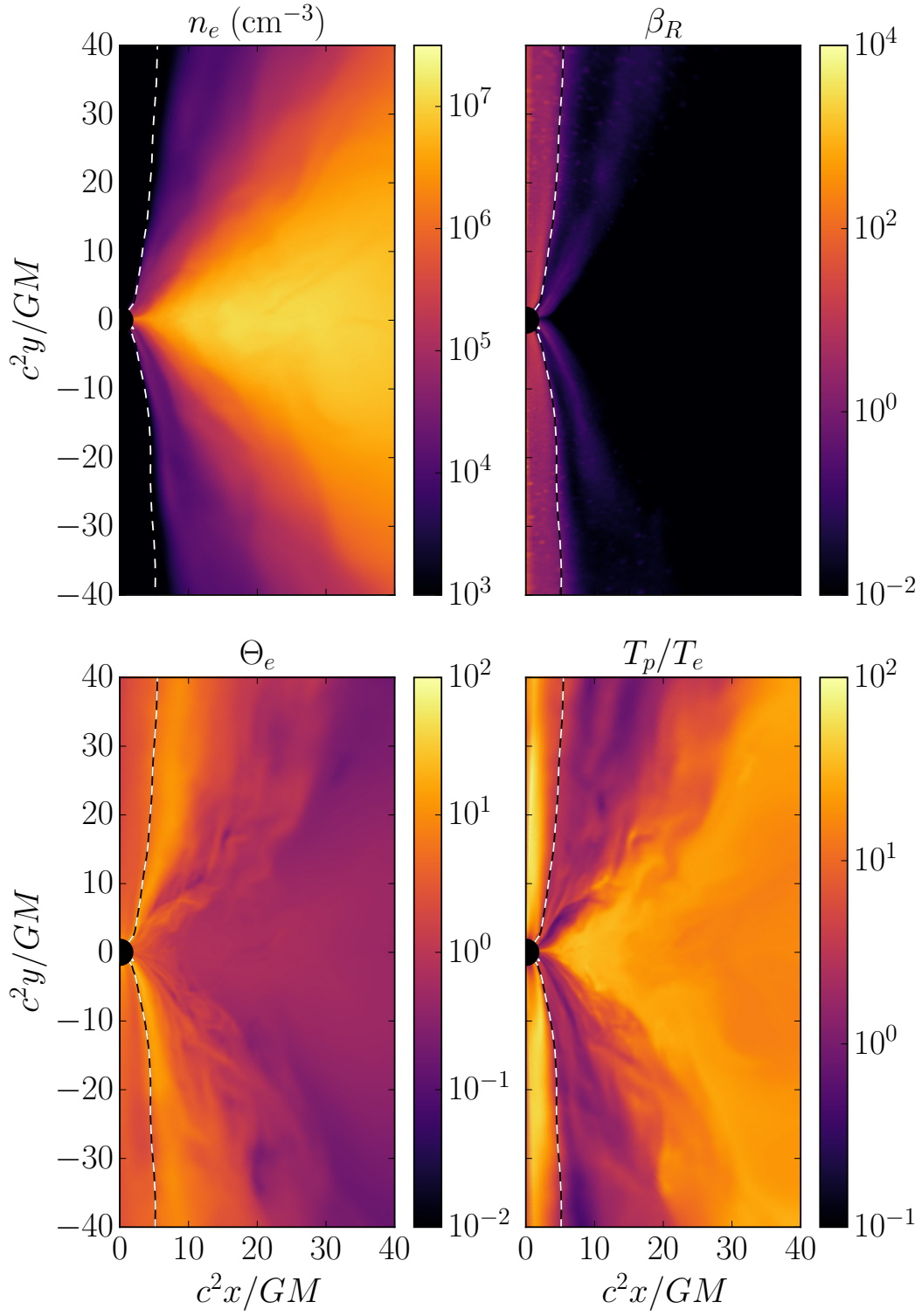

Figure 5.3: Azimuthal slices of time-averaged density, radiation to gas pressure ratio β_R, electron temperature, and proton to electron temperature ratio for simulation `M3a05`. Dashed lines denote the boundary of the magnetized funnel, where $b^2/\rho > 1$.

GRMHD simulation. Evidently H/R changes by $\lesssim 5\%$, and only near the black hole. Radiative losses do not change the accretion flow geometry. In particular, there is no clear evidence for the development of a thin, radiatively efficient disk anywhere in our simulations.

The top right panel of Figure 5.4 shows the ratio of Coulomb and turbulent heating for electrons. For $r \gtrsim 10GM/c^2$, Coulomb interactions dominate the electron heating. Note that for simulations with $a_\star = 0.9375$, Coulomb heating is an order of magnitude higher relative to (plasma β-dependent) viscous heating for $r \lesssim 10GM/c^2$. This is likely a consequence of the change in radius of the innermost stable circular orbit with spin, which in turn influences the accretion disk magnetization out to some radius.

Figure 5.4 also shows proton and electron temperatures relative to their respective GRMHD simulations. Proton temperatures decrease relative to GRMHD values by $\lesssim 10\%$ very close to the black hole, and $\lesssim 10\%$ at larger radii. For $r \gtrsim 10GM/c^2$, the small change in H/R combined with the $\sim 5-10\%$ drop in Θ_p implies the disk is receiving more electron pressure support at these radii in GRMHD models.

Electron temperatures vary significantly between radiative and GRMHD models. Near the black hole, mean electron temperatures are a factor $\sim 2-3$ lower than in similar nonradiative models. For $r \gtrsim 10$, however, electrons are a factor $\sim 5-10$ hotter than in similar models that neglect Coulomb coupling. Note, however, that in the absence of fully developed turbulence far from the black hole in these simulations, viscous heating is suppressed in this region. Therefore, despite the greatly enhanced electron heating for $r \gtrsim 10$, $\langle T_p/T_e \rangle$ is always $\gtrsim 20$ in this region.

When recording superphotons at the outer radiation boundary, we record whether they have undergone scattering events. Assuming large Compton amplification factors, i.e. $\Theta_e \gtrsim 1$, we can calculate the Compton y parameter, the relative importance of Compton scattering to photon emission. Total luminosity is related to luminosity from emission by $L \sim L_{\rm em}(1+y)$. Table 5.1 reports $L_{\rm em}/L_{\rm sc}$, roughly $1/y$, for each model. Compton y ranges from ~ 0.6 to 3; Compton scattering is an important contribution to the total luminosity, and to radiative cooling.

5.5.4 Spectra

We now return to comparing simulated and observed quantities for M87. We first consider flux across the observed electromagnetic spectrum. The mm flux is fixed by EHT measurements, which resolve the source to within the computational volume we consider here (Doeleman et al. 2012). Lower frequency measurements are from progressively larger structures due to increasing optical depth to synchrotron self-absorption.

The next lowest-frequency data comes from IR and optical observations (Prieto et al. 2016). These measurements have an angular resolution $\sim 0.15''$; for a black hole mass $M = (3.3 \times 10^9, 6.2 \times 10^9)$, this

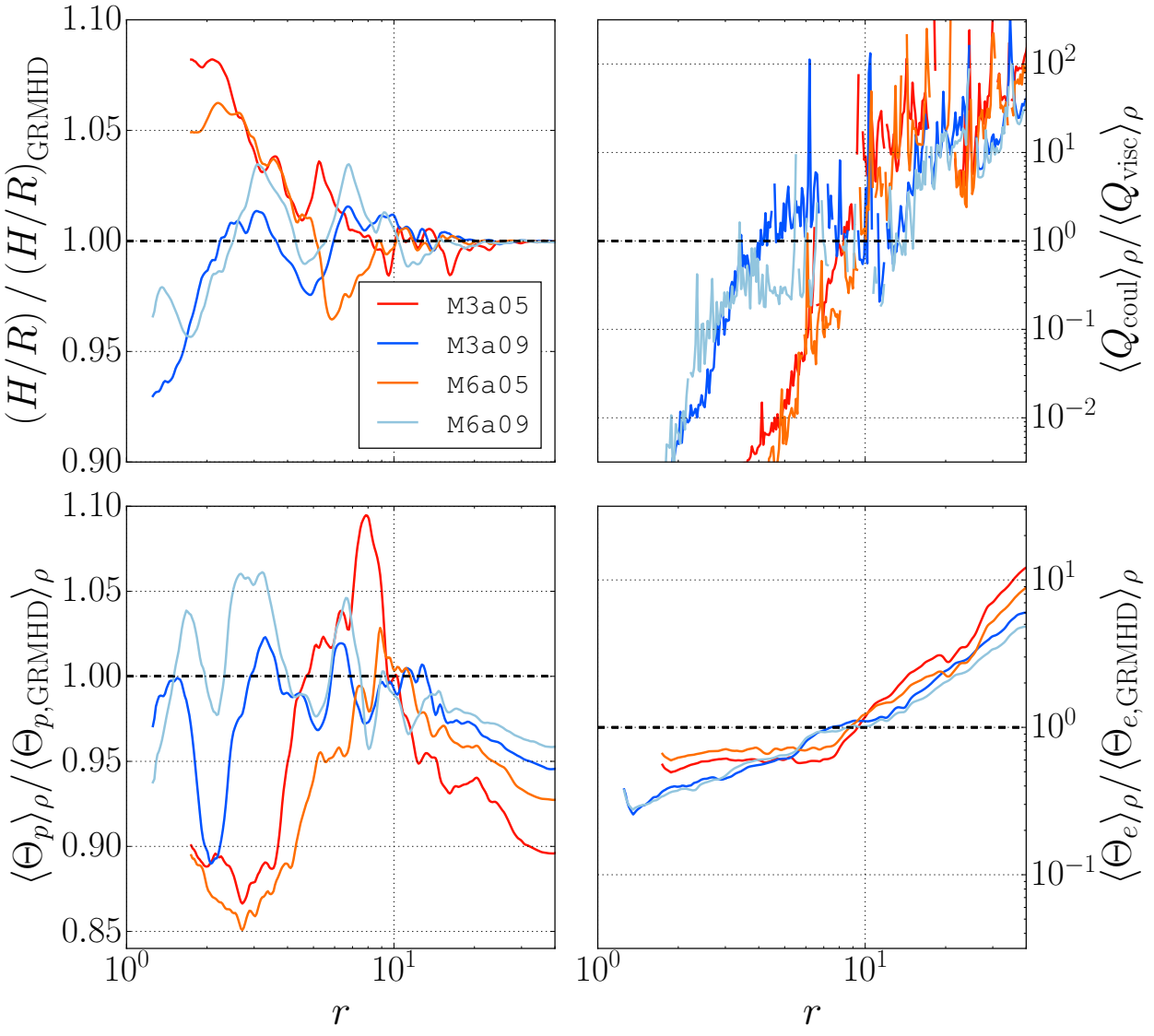

Figure 5.4: Clockwise from top left: H/R, ratio of Coulomb to viscous heating, dimensionless electron temperature Θ_e, and dimensionless proton temperature $\Theta_p \equiv k_B T_p/(m_p c^2)$. H/R, Θ_e, and Θ_p are shown relative to the same quantities from equivalent nonradiative GRMHD simulations. Dashed lines correspond to no change between radiative and nonradiative models. $Q_{\rm coul}/Q_{\rm visc}$ is boxcar averaged for clarity.

corresponds to a radius $r = (7.7 \times 10^4, 4.1 \times 10^4) GM/c^2$, outside our simulation volume. X-ray data has a slightly lower resolution, $\sim 0.4''$. With these angular resolution, flux from the brightest M87 jet knot, HST-1, is excluded.

We cannot guarantee that we are capturing the emission region for frequencies outside of ~ 230 GHz. Spectra from our `ebhlight` models are thus best interpreted as lower limits on the emission; while larger radii may contribute to the luminosity, optical depth is low past the synchrotron peak. R_{95}, the radius inside of which 95% of the luminosity is generated, for our models is always contained by the radiative region of each simulation. However, our models may not be in equilibrium at large radius, and do not include bremsstrahlung emission, which may contribute, especially in the X-ray, far from the black hole.

Spectra are taken directly from `ebhlight` simulations by recording superphotons crossing the outer radial radiation boundary, binned in elevation θ. For M87, we consider the bin closest to the polar axis, corresponding to angles $\lesssim 35^\circ$ from the polar axes, averaged about the midplane. The time-averaged result for all models is shown in Figure 5.5. Also shown are quiescent state observations from Prieto et al. (2016), given for $0.15''$ and $0.4''$ maximum angular resolutions.

While all models recover similar mm slopes broadly consistent with high angular resolution measurements, no model reproduces both the optical/IR and X-ray data simultaneously. In this regard the best performer is `M3a09`, which only slightly underproduces both IR and X-ray data (thereby not excluding itself). We find agreement between simulation and high-resolution observations down to ~ 43 GHz, but at lower frequencies our models underpredict the flux.

Our models do not produce much γ-ray flux, which may in any case be dominated by emission from HST-1. In addition, we do not include non-thermal electrons; a power-law tail extending to high electron energies may be responsible for extreme Compton scattering events and higher energy synchrotron emission.

5.5.5 Imaging

We used escaping superphotons binned in angle to evaluate $F_{\nu,230\mathrm{GHz}}$ for the purpose of choosing $\dot{m}$ to recover the EHT flux (Doeleman et al. 2012). Images, however, are created with post-processed raytracing along particular lines of sight (Noble et al. 2007). Throughout, for imaging we set θ to either 20° or 160°. Images are calculated with 1024×1024 pixels and a 70 GM/c^2 field of view. We adopt a position angle of 288° (Reid et al., 1982). For generating images, we choose a timeslice and $\theta = (20^\circ, 160^\circ)$ for each simulation at which imaging-derived flux agrees with the EHT flux to within a few percent. These times and θ are given in Table 5.2.

230 GHz images are shown in Figure 5.6. The size of the event horizon on the sky (the black hole shadow)

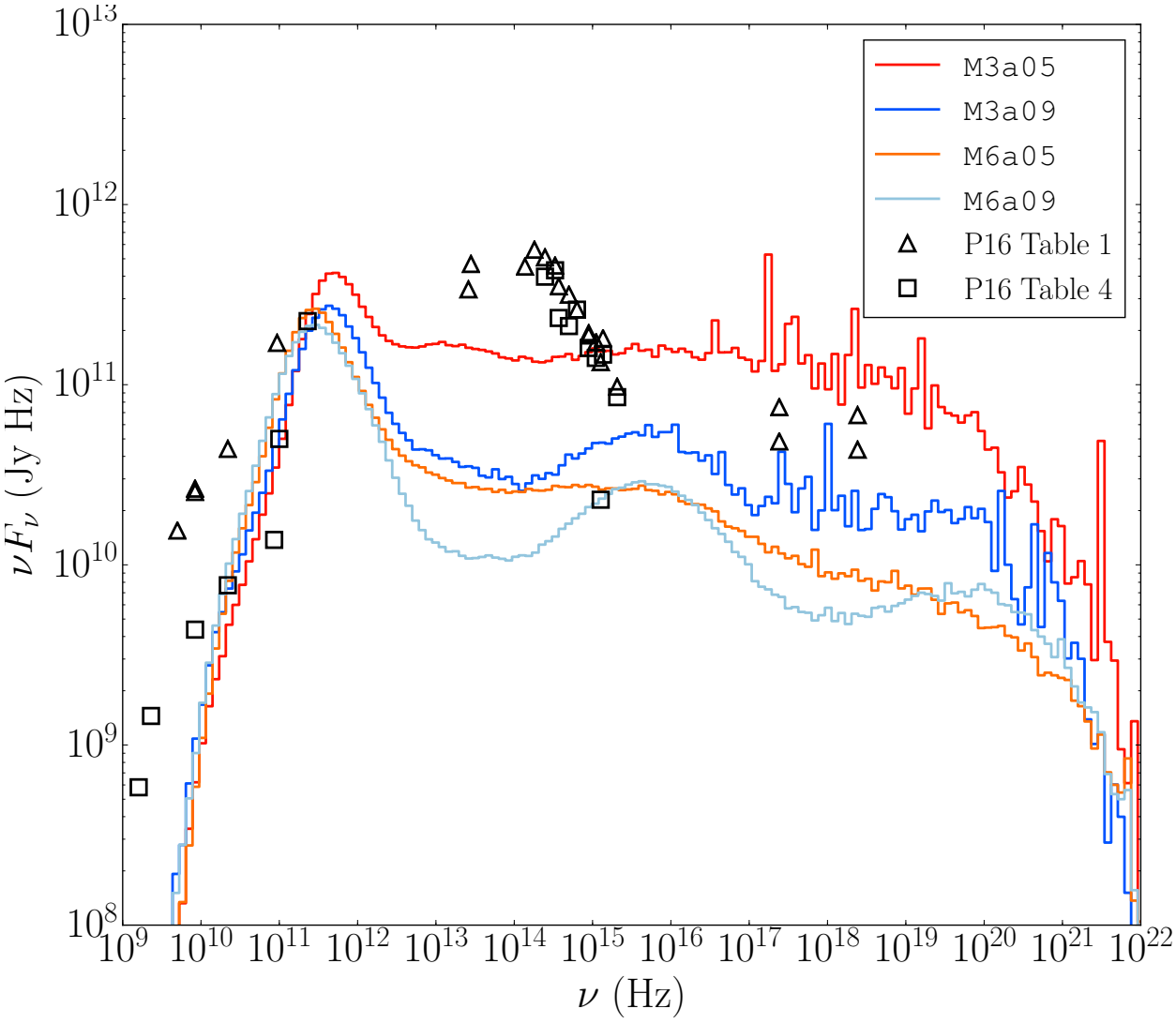

Figure 5.5: Time-averaged face-on spectra for all models. Data points taken from quiescent period measurements in Prieto et al. (2016) (P16). Triangles show observations for angles ($\leq 0.4''$), while squares show higher resolution observations ($\leq 0.15''$).

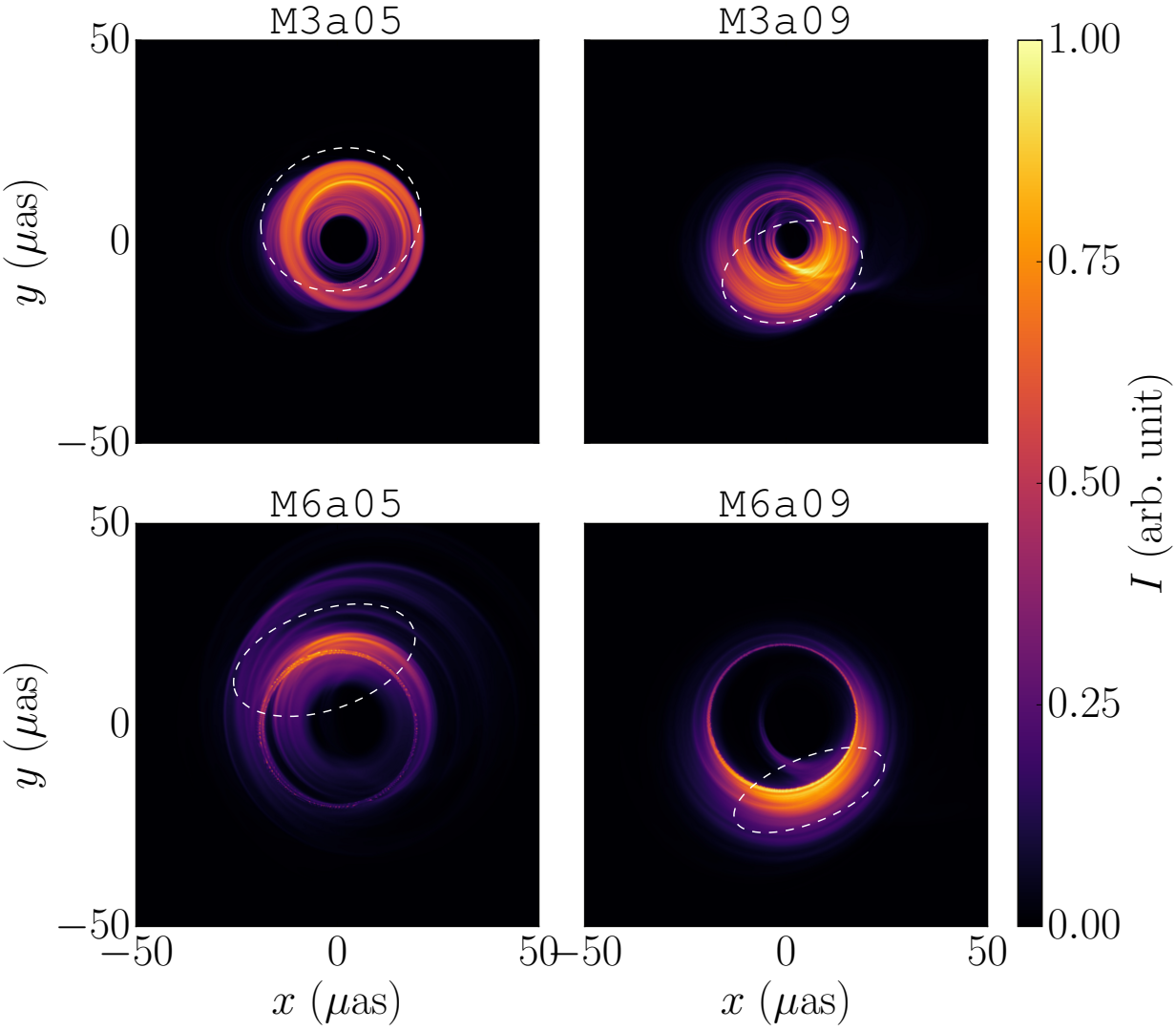

Figure 5.6: 230 GHz images from each model, evaluated at times for which the image-derived flux is nearly the value measured by the EHT (0.92 Jy; Doeleman et al. 2012). Color scheme is common to all panels. Also shown are $1/e$ contours of the best-fit 2D Gaussians.

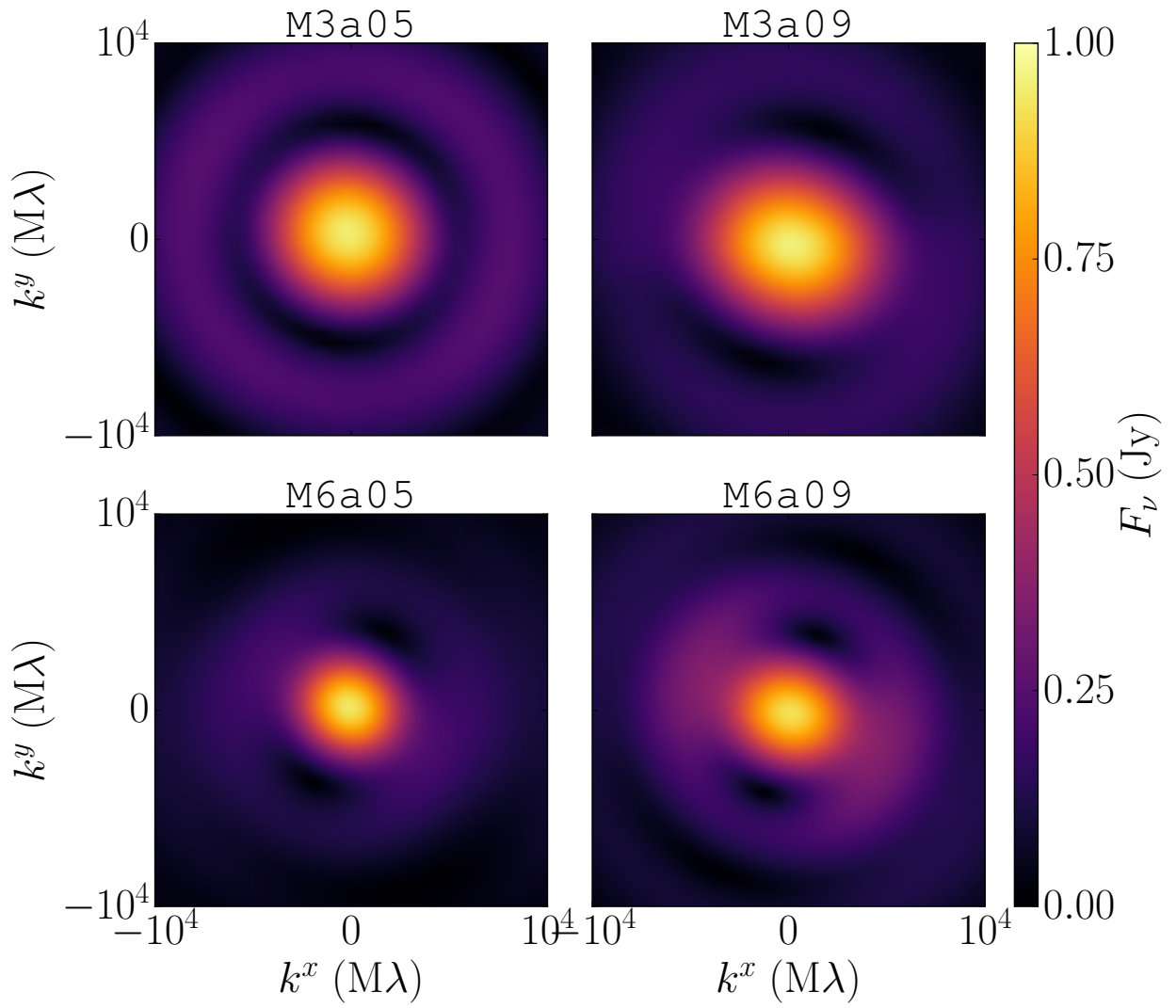

Figure 5.7: Visibilities calculated from 230 GHz images. Images from high-mass black holes are somewhat larger on the sky, while those form low-mass black holes are more rotationally symmetric.

is proportional to the black hole mass. Note that the relative brightness of the upper or lower half-plane (set by our choice of θ) is not a prediction of our model. These images may be mirrored about the $\phi = 288°$ axis; equivalently, the orbital angular velocity of the accretion disk may be pointed either towards or away from the observer.

We calculate the contribution from the counterjet by setting emissivities (but not absorptivities and rotativities) to zero above and below the disk midplane (relative to the observer) to capture counter and forward jet contributions, respectively. The ratio of intensity produced below the midplane to total intensity gives the counterjet fraction $f_{\rm CJ}$, which is also given in Table 5.2. Counterjet fraction increases with both mass and spin.

Label	t/M	θ	$f_{\rm CJ}$	$\sigma_{\rm G,maj}$ (μas)	$\sigma_{\rm G,min}$ (μas)
M3a05	850	20°	25%	14.2	12.4
M3a09	700	160°	70%	12.6	8.5
M6a05	705	20°	34%	16.6	8.7
M6a09	745	160°	81%	14.1	5.7

Table 5.2: Chosen times, inclination angles, counterjet fractions, and standard deviations along major and minor axes of 2D Gaussian fits to mm images.

Increased black hole spin increases the counterjet fraction in our models by a factor ~ 3. The sense of this effect is expected; higher spin means more emission at smaller r, where gravitational lensing is stronger. Our $a_\star = 0.5$ models show only a $\sim 30\%$ counterjet contribution to mm flux. In agreement with Dexter et al. (2012), who study an $a_\star = 0.92$ GRMHD model of M87, our high-spin models are counterjet-dominated. Increased black hole mass (equivalently, decreased accretion rate) increases the counterjet fraction by a factor $\sim 10 - 20\%$.

Figure 5.6 also shows contours of least squares 2D Gaussian fits to the mm images. The major and minor axes, $\sigma_{\rm G,maj}$ and $\sigma_{\rm G,min}$, are given in Table 5.2. These Gaussians vary from nearly circularly symmetric to heavily skewed; the eccentricity $e \equiv 1 - \sigma_{\rm G,min}/\sigma_{\rm G,maj}$ varies from 0.13 for M3a05 to 0.60 for M6a09. e increases with both mass and spin, and is probably at least partially associated with enhanced counterjet fraction; offset circular bands of emission will be partially clipped by the black hole shadow when produced by the counterjet.

Figure 5.7 shows visibility maps corresponding to the images in Figure 5.6. The black hole shadow (smaller in the low-mass models) is clearly visible in all cases as zeroes in the visibilities. However, the low-mass models are nearly rotationally symmetric, whereas the high-mass models show a strong asymmetry.

We compare to the measured visibilities in Doeleman et al. (2012) in Figure 5.8 by extracting fluxes from our measured visibilities at the same baselines. These observations were taken over the course of three days (about 16 and 8.5 GM/c^3 for black hole masses $M/M_\odot = 3.3 \times 10^9$ and 6.2×10^9, respectively; note, however that our simulated visibilities are each calculated at a single simulation timeslice). All simulations do a reasonable job of reproducing the short baseline fluxes. The low-mass simulations, however, overproduce flux at longer baselines; these images are too small, at least for our electron physics model. M6a09 overproduces flux at the longest baselines and marginally underproduces at short baselines.

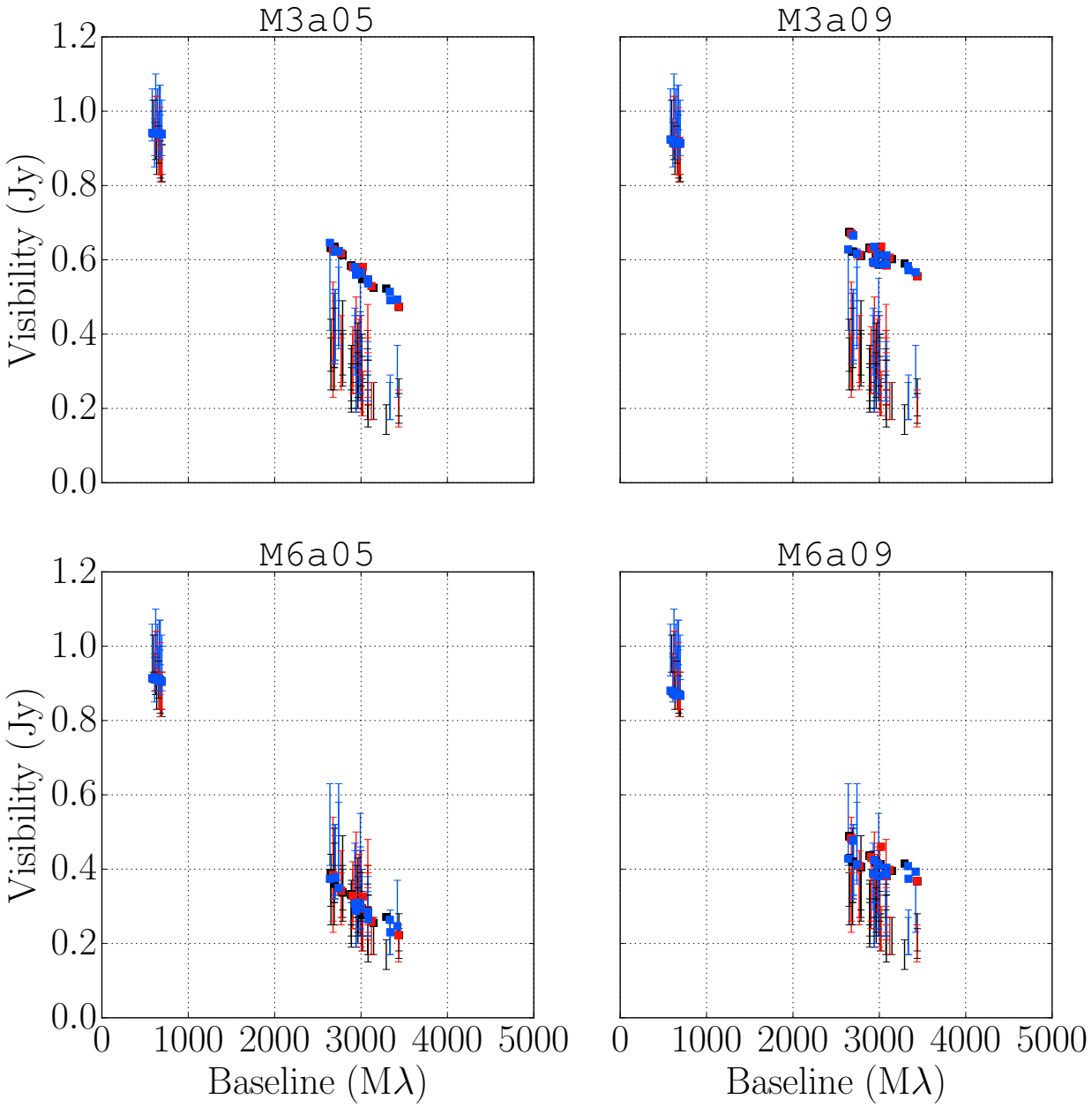

Figure 5.8: Visibilities from EHT observations (error bars; (Doeleman et al., 2012)) and `ebhlight` models (squares) for the same baselines. EHT measurements were taken over the course of three days, designated as black, red, and blue, respectively.

5.5.6 Jet Power

We compute jet power by separately integrating matter and electromagnetic fluxes in the jet region where $b^2/\rho > 1$, yielding matter and electromagnetic jet powers,

$$P_{\rm J,M} = \int (\rho + \gamma u) u^1 u_0 \sqrt{-g} dx^2 dx^3, \tag{5.20}$$

$$P_{\rm J,EM} = \int (b^2 u^1 u_0 - b^1 b_0) \sqrt{-g} dx^2 dx^3 \tag{5.21}$$

respectively (this procedure omits any fluxes outside the Poynting jet, e.g. Blandford & Payne 1982). These integrals are evaluated at $r = 40GM/c^2$. In all cases we find the matter flux is negligible, $P_{\rm J,M}/P_{\rm J,EM} \approx 10^{-3}$ (this ratio is set by our treatment of floors in the funnel region); hereafter we consider only the electromagnetic flux, and set $P_{\rm J} = P_{\rm J,EM}$. $P_{\rm J}$ is given in Table 5.1, and is $\sim 10^{40} - 10^{41}$ erg s^{-1} for all simulations.

5.6 Discussion

Provided a robust measurement of the 230 GHz flux from the inner region of M87's accretion flow, we have tested synthetic observations from `ebhlight` simulations against fluxes at other wavelengths and interferometric imaging, as well as comparing measured and inferred jet powers. `M3a05` significantly overproduced X-ray emission. IR/optical emission is uniformly underproduced in our models. A strong constraint comes from the resolved visibilities of Doeleman et al. (2012), which are relatively insensitive to both observational confusion and systematic uncertainties in our models. These observations are inconsistent with the compact emission from both low-mass models, `M3a05` and `M3a09`. The `M6a09` mm image was slightly too small, although with only marginal significance. All our models significantly underproduce the jet power inferred from observations. Despite uncertainties, multiple techniques for inferring the jet power, such as VLBI observations of the radio core (e.g. de Gasperin et al. 2012 and internal pressure in a reconfinement shock (e.g. Stawarz et al. 2006), recover a similar jet power $P_{\rm J} \sim 10^{43} - 10^{44}$ erg s^{-1}.

Our study prefers the high-mass, low-spin model `M6a05`. While one or both of `M3a05` and `M3a09` disagree with one or more observational constraints, `M6a05` is only marginally preferable to `M6a09` and our study does not provide much ability to constrain black hole spin. We now turn to future directions, particular in the context of uncertainties in this work.

5.6.1 Multifrequency Observations

We find that high spin leads to more distinct Compton bumps, whereas low-spin models are nearly power-laws between synchrotron emission and the high frequency cutoff. This conclusion is probably sensitive to our assumption of a thermal electron distribution function. Although resolving the inner $\sim 100GM/c^2$ of M87 is challenging at these wavelengths, additional frequency measurements filling out the spectrum could help constrain the spin of M87 by identifying or ruling out Compton bumps.

Our models do not produce much radiation beyond $\sim 10^{22}$ Hz. This may be a consequence of our assumption of thermal electron distributions everywhere (in contrast at least with ion distributions in larmor-scale studies, e.g. Kunz et al. 2016). The high energy emission that we observe, however, may need to originate in highly relativistic outflows (i.e. in the jet) to circumvent the opacity to pair production (Begelman et al., 2008). TeV fluxes are probably also sensitive to the population of nonthermal electrons.

M87 is a powerful emitter of TeV photons (e.g. Aharonian et al. 2006). The high energy emission that we observe, however, may need to originate in highly relativistic outflows (i.e. in the jet) to circumvent the opacity to pair production (Begelman et al., 2008). Observations cannot separate the inner region of the accretion flow with jet knots, most notably HST-1. TeV fluxes are probably also sensitive to the population of nonthermal electrons. Identifying the origin of TeV photons in M87 is an important future direction.

Bremsstrahlung emission is not considered in our model; it is subdominant to synchrotron emission near the black hole. At larger radii, however, it may be a significant source of X-ray emission. Exploring a very large dynamic range in radius (and therefore time) is challenging for simulations; modeling emission from the entire region subtended by the resolution of X-ray observations is consequently difficult.

Equilibration

Axisymmetry limits the duration of our simulations. We are therefore not able to achieve inflow equilibrium at all radii for which radiation is (thermo)dynamically important; the disk structure may tend towards smaller scaleheights and ion and electron temperatures at these radii. While such a change would leave 230 GHz emission and images largely unchanged, it could sap energy from the spectrum throughout the region dominated by Compton upscattering.

Electron heating

The electron temperature is simultaneously perhaps the most important and most uncertain component of our simulations. While Ressler et al. (2015) represents a significant advance from *ad hoc* models, it is vulnerable to numerical challenges in accurately capturing grid-scale dissipation, and uncertainties in the

underlying kinetic physics itself.

Ressler et al. (2017) provide a discussion of difficulties in measuring dissipation due to truncation error. For one, dissipation can be either positive or negative (total energy-conserving schemes locally obey the second law of thermodynamics only to truncation error). At least for uniform low Mach number turbulence, such as generally obtains near the midplane in MRI-driven RIAF simulations, dissipation acts as heating on average. In the presence of large entropy gradients, however, dissipation can have a net cooling effect. The funnel wall is such a configuration, and our funnel wall electrons may be artificially cool. This has potential consequences for the low-frequency radio slope; artificial electron cooling will suppress low-frequency emission.

We employ the state-of-the-art electron heating fraction model of Howes (2010). For this model, Howes (2011) found agreement within experimental uncertainty with the electron-ion temperature ratio in the solar wind, probably the best accessible analog of RIAFs. However, uncertainties are non-negligible, and the data do not cover the entire range of plasma β present in our simulations. In addition, electrons may be heated by more than electron Larmor scale instabilities (e.g. Rowan et al. 2017). Our understanding of microscale electron heating is incomplete, and new results (as well as nonthermal electron distributions) may substantially change the results of global simulations.

5.6.2 Net Magnetic Flux

M87 sources a powerful relativistic jet, and such jets may be associated with black holes accreting at the Magnetically-Arrested Disk limit (MAD; Narayan et al. 2003, Tchekhovskoy et al. 2011, McKinney et al. 2012). In MADs, strong vertical magnetic fields qualitatively change the accretion flow. The interchange instabilities which govern angular momentum transport in this case are probably inaccessible to axisymmetric fluid models, such as we study here, and hence we avoid consideration of MADs. Nonetheless, this is a viable model for the M87 accretion flow. The $\sim 100\%$ efficiencies in the electromagnetic jet luminosity would, all else being equal, bring our measured $P_{\rm J}$ in line with inferred values, as our current jet efficiencies are $\sim 0.02\%$ and $\sim 1\%$ for low- and high-spin models, respectively.

The funnels in our models have relatively narrow opening angles compared to MAD simulations (e.g. Tchekhovskoy et al. 2011). The consequences of a wider jet in our model, especially for coronal electron temperatures, is uncertain (although see Ressler et al. 2017 for a semi-MAD calculation with electron heating).

Whether MAD models with self-consistent radiative cooling are a viable alternative for M87 is an interesting question we plan to explore in future work. Along with spectra, MADs may exhibit quite different

variability and polarization (e.g. Gold et al. 2017).

5.6.3 Variability

Our axisymmetric model has limited duration and probably overestimates variability. Additionally, nonaxisymmetric fluctuations may imprint characteristic frequencies onto lightcurves, e.g. Dolence et al. (2012), Shcherbakov & McKinney (2013). Hence, we leave study of variability to future work. Studies of variability in 3D GRRMHD simulations of M87, and RIAFs subject to cooling more generally, are a promising future direction for constraining accretion flows.

After compiling separate observed spectra for M87 in quiescent and active states, Prieto et al. (2016) argue that the spectral shape seems independent of state; the entire spectrum simply shifts up or down. Given that the accretion rates we study already show the effects of radiative cooling, increasing $\dot{m}$ to match the active state of Prieto et al. (2016), assuming an increase in accretion rate in the source is responsible for the outburst, would presumably serve to increase radiative cooling. Cooling tends to alter spectral shape; for example, when distinct Compton bumps are present, their separation is $\sim A$, the amplification factor. Requiring that a single model recovers both quiescent and active spectra could act as a powerful discriminant in the future.

5.7 Conclusion

We have presented two-temperature general relativistic radiation magnetohydrodynamic models of the inner accretion flow of M87. Along the way, we considered the interplay of viscous heating, Coulomb coupling, and radiative cooling in RIAFs at $\dot{M}/\dot{M}_{\rm Edd} \sim 10^{-5}$. We found Compton y parameters ~ 1 for these models, consistent with previous estimates. We find that Coulomb heating dominates viscous heating for electrons for $r \gtrsim 10GM/c^2$. We have demonstrated that radiative cooling is important for the inner region of the M87 accretion flow in our model.

For black hole masses bracketing the observationally preferred values and high and low black hole spins, we have derived synthetic observations of spectra and 230 GHz images. Acknowledging uncertainties in our chosen net magnetic field and electron heating model, we exclude a low black hole mass, $M/M_\odot = 3.3 \times 10^9$, through radio image sizes, and the low-mass, low-spin model through overproduction of X-rays. $M/M_\odot = 6.2 \times 10^9$ simulations satisfy radio/IR/X-ray emission and image size. However, jet power is always a factor $10^2 - 10^3$ lower than previously inferred values.

Our model is axisymmetric, which not only limits our time integration window but also renders variability

information unreliable. Similar modeling in three spatial dimensions is a critical future direction, albeit much more expensive, especially given our procedure for determining optimal accretion rate through a series of simulations.

It is a pleasure to thank J. Dexter, M. Moscibrodzka, A. Tchekhovskoy, and Fu-Guo Xie for useful discussions. Work at Los Alamos National Laboratory was done under the auspices of the National Nuclear Security Administration of the US Department of Energy. SMR is supported in part by the NASA Earth and Space Science Fellowship. JD acknowledges support from the Laboratory Directed Research and Development program at Los Alamos National Laboratory. CFG's work was also supported in part by a Romano Professorial Scholar appointment. EQ is supported in part by a Simons Investigator Award from the Simons Foundation and the David and Lucile Packard Foundation. This work was supported in part by NSF grant AST 13-33612. This research used resources provided by the Los Alamos National Laboratory Institutional Computing Program, which is supported by the U.S. Department of Energy National Nuclear Security Administration under Contract No. DE-AC52-06NA25396.

References

Abbott, D. C., & Lucy, L. B. 1985, ApJ, 288, 679

Abbott, B. P., Abbott, R., Abbott, T. D., et al. 2016a, Physical Review Letters, 116, 061102

Abbott, B. P., Abbott, R., Abbott, T. D., et al. 2016b, Physical Review Letters, 116, 241103

Abbott, B. P., Abbott, R., Abbott, T. D., et al. 2017a, Physical Review Letters, 118, 221101

Abbott, B. P., Abbott, R., Abbott, T. D., et al. 2017b, ApJL, 851, L35

Abbott, B. P., Abbott, R., Abbott, T. D., et al. 2017c, Physical Review Letters, 119, 141101

Abdikamalov, E., Burrows, A., Ott, C. D., et al. 2012, ApJ, 755, 111

Abdo, A. A., Ackermann, M., Ajello, M., et al. 2009, ApJ, 707, 55

Abramowicz, M. A., Czerny, B., Lasota, J. P., & Szuszkiewicz, E. 1988, ApJ, 332, 646

Abramowski, A., Acero, F., Aharonian, F., et al. 2012, ApJ, 746, 151

Agol, E., & Krolik, J. H. 2000, ApJ, 528, 161

Aharonian, F. A. 2000, New Astron., 5, 377

Aharonian, F., Akhperjanian, A. G., Bazer-Bachi, A. R., et al. 2006, Science, 314, 1424

Asmus, D., Hönig, S. F., Gandhi, P., Smette, A., & Duschl, W. J. 2014, MNRAS, 439, 1648

Bai, X.-N., & Stone, J. M. 2013, ApJ, 767, 30

Balbus, S. A., & Hawley, J. F. 1991, ApJ, 376, 214

Balbus, S. A., Hawley, J. F., & Stone, J. M. 1996, ApJ, 467, 76

Balbus, S. A., & Hawley, J. F. 1998, Reviews of Modern Physics, 70, 1

Balbus, S. A., & Hawley, J. F. 2002, ApJ, 573, 749

Ball, D., Özel, F., Psaltis, D., & Chan, C.-k. 2016, ApJ, 826, 77

Bardeen, J. M., Press, W. H., & Teukolsky, S. A. 1972, ApJ, 178, 347

Barth, A. J., Sarzi, M., Rix, H.-W., et al. 2001, ApJ, 555, 685

Beckwith, K., Hawley, J. F., & Krolik, J. H. 2009, ApJ, 707, 428

Beckwith, K., Armitage, P. J., & Simon, J. B. 2011, MNRAS, 416, 361

Begelman, M. C., & Meier, D. L. 1982, ApJ, 253, 873

Begelman, M. C., Fabian, A. C., & Rees, M. J. 2008, MNRAS, 384, L19

Begelman, M. C. 2014, arXiv:1410.8132

Begelman, M. C., & Armitage, P. J. 2014, ApJL, 782, L18

Blakeslee, J. P., Jordán, A., Mei, S., et al. 2009, ApJ, 694, 556

Blandford, R. D., & Znajek, R. L. 1977, MNRAS, 179, 433

Blandford, R. D., & McKee, C. F. 1982, ApJ, 255, 419

Blandford, R. D., & Payne, D. G. 1982, MNRAS, 199, 883

Blandford, R. D., & Begelman, M. C. 1999, MNRAS, 303, L1

Bodo, G., Cattaneo, F., Ferrari, A., Mignone, A., & Rossi, P. 2011, ApJ, 739, 82

Bodo, G., Cattaneo, F., Mignone, A., & Rossi, P. 2014, ApJL, 787, L13

Bodo, G., Cattaneo, F., Mignone, A., & Rossi, P. 2015, ApJ, 799, 20

Böhringer, H., Belsole, E., Kennea, J., et al. 2001, A&A, 365, L181

Bolton, C. T. 1972, Nature Physical Science, 240, 124

Boris, J. P. 1970, NRL Memorandum Report 2167

Bower, G. C., Goss, W. M., Falcke, H., Backer, D. C., & Lithwick, Y. 2006, ApJL, 648, L127

Brandenburg, A., Nordlund, A., Stein, R. F., & Torkelsson, U. 1995, ApJ, 446, 741

Broderick, A. E., Loeb, A., & Narayan, R. 2009, ApJ, 701, 1357

Brown, G. E., & Bethe, H. A. 1994, ApJ, 423, 659

Canfield, E., Howard, W. M., & Liang, E. P. 1987, ApJ, 323, 565

Capellupo, D. M., Haggard, D., Choux, N., et al. 2017, ApJ, 845, 35

Carter, B. 1971, Physical Review Letters, 26, 331

Castor, J. I. 2004, Radiation Hydrodynamics, by John I. Castor, pp. 368. ISBN 0521833094. Cambridge, UK: Cambridge University Press, November 2004., 368

Chael, A. A., Narayan, R., & Saḍowski, A. 2017, MNRAS, 470, 2367

Chan, C.-k., Psaltis, D., & Özel, F. 2013, ApJ, 777, 13

Chan, C.-K., Psaltis, D., Özel, F., Narayan, R., & Saḍowski, A. 2015, ApJ, 799, 1

Chandrasekhar, S., Kaufman, A. N., & Watson, K. M. 1958, Proceedings of the Royal Society of London Series A, 245, 435

Charbonneau, P. 2014, ARA&A, 52, 251

Chirenti, C., & Rezzolla, L. 2016, PhRvD, 94, 084016

Chokshi, A., & Turner, E. L. 1992, MNRAS, 259, 421

Coppi, P. S. 1999, High Energy Processes in Accreting Black Holes, 161, 375

Davis, S. W., & Hubeny, I. 2006, ApJS, 164, 530

Davis, S. W., Stone, J. M., & Pessah, M. E. 2010, ApJ, 713, 5

Davies, S. J., & White, C. M. 1928, Proceedings of the Royal Society of London Series A, 119, 92

de Gasperin, F., Orrú, E., Murgia, M., et al. 2012, A&A, 547, A56

De Villiers, J.-P., & Hawley, J. F. 2003a, ApJ, 589, 458

De Villiers, J.-P., Hawley, J. F., & Krolik, J. H. 2003b, ApJ, 599, 1238

Dexter, J., Agol, E., Fragile, P. C., & McKinney, J. C. 2010, ApJ, 717, 1092

Dexter, J., McKinney, J. C., & Agol, E. 2012, MNRAS, 421, 1517

Dexter, J. 2016, MNRAS, 462, 115

Di Matteo, T., Allen, S. W., Fabian, A. C., Wilson, A. S., & Young, A. J. 2003, ApJ, 582, 133

Dibi, S., Drappeau, S., Fragile, P. C., Markoff, S., & Dexter, J. 2012, MNRAS, 426, 1928

Doeleman, S., Agol, E., Backer, D., et al. 2009, astro2010: The Astronomy and Astrophysics Decadal Survey, 2010, 68

Doeleman, S. S., Fish, V. L., Schenck, D. E., et al. 2012, Science, 338, 355

Dolence, J. C., Gammie, C. F., Mościbrodzka, M., & Leung, P. K. 2009, ApJS, 184, 387

Dolence, J. C., Gammie, C. F., Shiokawa, H., & Noble, S. C. 2012, ApJL, 746, L10

Drappeau, S., Dibi, S., Dexter, J., Markoff, S., & Fragile, P. C. 2013, MNRAS, 431, 2872

Dressler, A., & Richstone, D. O. 1988, ApJ, 324, 701

Eckart, A., & Genzel, R. 1997, MNRAS, 284, 576

Elbert, O. D., Bullock, J. S., & Kaplinghat, M. 2018, MNRAS, 473, 1186

Esin, A. A., McClintock, J. E., & Narayan, R. 1997, ApJ, 489, 865

Evans, C. R., & Hawley, J. F. 1988, ApJ, 332, 659

Fabian, A. C., Rees, M. J., Stella, L., & White, N. E. 1989, MNRAS, 238, 729

Fabian, A. C., Lohfink, A., Kara, E., et al. 2015, MNRAS, 451, 4375

Farris, B. D., Li, T. K., Liu, Y. T., & Shapiro, S. L. 2008, PhRvD, 78, 024023

Farris, B. D., Liu, Y. T., & Shapiro, S. L. 2010, PhRvD, 81, 084008

Fender, R. P., Belloni, T. M., & Gallo, E. 2004, MNRAS, 355, 1105

Ferrarese, L., & Merritt, D. 2000, ApJL, 539, L9

Ferrarese, L., & Ford, H. 2005, SSRv, 116, 523

Fish, V. L., Doeleman, S. S., Beaudoin, C., et al. 2011, ApJL, 727, L36

Fishbone, L. G., & Moncrief, V. 1976, ApJ, 207, 962

Flock, M., Ruge, J. P., Dzyurkevich, N., et al. 2015, A&A, 574, A68

Foucart, F., Chandra, M., Gammie, C. F., Quataert, E., & Tchekhovskoy, A. 2017, MNRAS, 470, 2240

Fragile, P. C., Blaes, O. M., Anninos, P., & Salmonson, J. D. 2007, ApJ, 668, 417

Fragile, P. C., & Meier, D. L. 2009, ApJ, 693, 771

Fragile, P. C., Gillespie, A., Monahan, T., Rodriguez, M., & Anninos, P. 2012, ApJS, 201, 9

Fragile, P. C., Olejar, A., & Anninos, P. 2014, ApJ, 796, 22

Fromang, S., Hennebelle, P., & Teyssier, R. 2006, A&A, 457, 371

Fromang, S., Papaloizou, J., Lesur, G., & Heinemann, T. 2007, A&A, 476, 1123

Fromang, S. 2010, A&A, 514, L5

Fromang, S., Latter, H., Lesur, G., & Ogilvie, G. I. 2013, A&A, 552, A71

Gammie, C. F. 1996, ApJ, 457, 355

Gammie, C. F. 1999, ApJL, 522, L57

Gammie, C. F., McKinney, J. C., & Tóth, G. 2003, ApJ, 589, 444

Garain, S. K., Ghosh, H., & Chakrabarti, S. K. 2012, ApJ, 758, 114

Gebhardt, K., & Thomas, J. 2009, ApJ, 700, 1690

Gebhardt, K., Adams, J., Richstone, D., et al. 2011, ApJ, 729, 119

Ghez, A. M., Klein, B. L., Morris, M., & Becklin, E. E. 1998, ApJ, 509, 678

Ghez, A. M., Hornstein, S. D., Lu, J. R., et al. 2005, ApJ, 635, 1087

Ghez, A. M., Salim, S., Weinberg, N. N., et al. 2008, ApJ, 689, 1044-1062

Ghosh, H., Garain, S. K., Giri, K., & Chakrabarti, S. K. 2011, MNRAS, 416, 959

Gillessen, S., Eisenhauer, F., Trippe, S., et al. 2009, ApJ, 692, 1075

Gold, R., McKinney, J. C., Johnson, M. D., & Doeleman, S. S. 2017, ApJ, 837, 180

Goldreich, P., & Lynden-Bell, D. 1965, MNRAS, 130, 125

Gou, L., McClintock, J. E., Reid, M. J., et al. 2011, ApJ, 742, 85

Greene, J. E., & Ho, L. C. 2007, ApJ, 667, 131

Greene, J. E., Peng, C. Y., Kim, M., et al. 2010, ApJ, 721, 26

Gressel, O. 2013, ApJ, 770, 100

Guan, X., & Gammie, C. F. 2008, ApJS, 174, 145-157

Guan, X., Gammie, C. F., Simon, J. B., & Johnson, B. M. 2009, ApJ, 694, 1010

Guan, X., & Gammie, C. F. 2011, ApJ, 728, 130

Guilbert, P. W., Fabian, A. C., & Rees, M. J. 1983, MNRAS, 205, 593

Hada, K., Doi, A., Kino, M., et al. 2011, Nature, 477, 185

Harms, R. J., Ford, H. C., Tsvetanov, Z. I., et al. 1994, ApJL, 435, L35

Harries, T. J. 2015, arXiv:1501.05754

Hawking, S. W., & Ellis, G. F. R. 1973, The large-scale structure of space-time., by Hawking, S. W.; Ellis, G. F. R.. Cambridge (UK): Cambridge University Press, 11 + 391 p.,

Hawley, J. F., Smarr, L. L., & Wilson, J. R. 1984, ApJ, 277, 296

Hawley, J. F., Gammie, C. F., & Balbus, S. A. 1995, ApJ, 440, 742

Hawley, J. F., Guan, X., & Krolik, J. H. 2011, ApJ, 738, 84

Hawley, J. F., Richers, S. A., Guan, X., & Krolik, J. H. 2013, ApJ, 772, 102

Haworth, T. J., & Harries, T. J. 2012, MNRAS, 420, 562

Heinz, S., & Begelman, M. C. 1997, ApJ, 490, 653

Herdeiro, C. A. R., & Radu, E. 2014, Physical Review Letters, 112, 221101

Herrnstein, J. R., Moran, J. M., Greenhill, L. J., & Trotter, A. S. 2005, ApJ, 629, 719

Hirose, S., Krolik, J. H., & Blaes, O. 2009, ApJ, 691, 16

Hirose, S., Blaes, O., Krolik, J. H., Coleman, M. S. B., & Sano, T. 2014, ApJ, 787, 1

Ho, L. C., Filippenko, A. V., & Sargent, W. L. W. 1997, ApJ, 487, 568

Ho, L. 1999, Observational Evidence for the Black Holes in the Universe, 234, 157

Ho, L. C. 2008, ARA&A, 46, 475

Ho, L. C. 2009, ApJ, 699, 626

Howes, G. G. 2010, MNRAS, 409, L104

Howes, G. G. 2011, ApJ, 738, 40

Ichimaru, S. 1977, ApJ, 214, 840

Igumenshchev, I. V., Chen, X., & Abramowicz, M. A. 1996, MNRAS, 278, 236

Igumenshchev, I. V., & Abramowicz, M. A. 1999, MNRAS, 303, 309

Ji, H., Burin, M., Schartman, E., & Goodman, J. 2006, Nature, 444, 343

Jiang, Y.-F., Stone, J. M., & Davis, S. W. 2012, ApJS, 199, 14

Jiang, Y.-F., Stone, J. M., & Davis, S. W. 2013a, ApJ, 767, 148

Jiang, Y.-F., Stone, J. M., & Davis, S. W. 2013b, ApJ, 778, 65

Jiang, Y.-F., Stone, J. M., & Davis, S. W. 2014a, ApJS, 213, 7

Jiang, Y.-F., Stone, J. M., & Davis, S. W. 2014b, ApJ, 796, 106

Jiang, Y.-F., Davis, S. W., & Stone, J. M. 2016, ApJ, 827, 10

Jiang, Y.-F., Stone, J., & Davis, S. W. 2017, arXiv:1709.02845

Johnson, B. M., Guan, X., & Gammie, C. F. 2008, ApJS, 177, 373-387

Ju, W., Stone, J. M., & Zhu, Z. 2016, ApJ, 823, 81

Ju, W., Stone, J. M., & Zhu, Z. 2017, ApJ, 841, 29

Kalogera, V., & Baym, G. 1996, ApJL, 470, L61

Kelly, B. C., & Merloni, A. 2012, Advances in Astronomy, 2012, 970858

Kerr, R. P. 1963, Physical Review Letters, 11, 237

Kestener, P., Château, F., & Teyssier, R. 2010, Accelerating Euler Equations Numerical Solver on Graphics Processing Units, ed. C.-H. Hsu, L. T. Yang, J. H. Park, & S.-S. Yeo (Berlin, Heidelberg: Springer Berlin Heidelberg), 281–288

Kestener, P., Fromang, S., Kritsuk, A., & Hennebelle, P. 2014, in NVIDIA GPU Technology Conference 2014

King, A. R., Pringle, J. E., & Livio, M. 2007, MNRAS, 376, 1740

Klahr, H. H., & Bodenheimer, P. 2003, ApJ, 582, 869

Klahr, H., & Hubbard, A. 2014, ApJ, 788, 21

Klein, O., & Nishina, T. 1929, Zeitschrift fur Physik, 52, 853

Koide, S., Shibata, K., & Kudoh, T. 1999, ApJ, 522, 727

Kormendy, J. 1988, ApJ, 325, 128

Kormendy, J., & Richstone, D. 1995, ARA&A, 33, 581

Kormendy, J., & Ho, L. C. 2013, ARA&A, 51, 511

Kunz, M. W., Schekochihin, A. A., & Stone, J. M. 2014, Physical Review Letters, 112, 205003

Kunz, M. W., Stone, J. M., & Quataert, E. 2016, Physical Review Letters, 117, 235101

Kuo, C. Y., Braatz, J. A., Condon, J. J., et al. 2011, ApJ, 727, 20

Kuo, C. Y., Asada, K., Rao, R., et al. 2014, ApJL, 783, L33

Lesur, G., & Longaretti, P.-Y. 2007, MNRAS, 378, 1471

Lesur, G., & Papaloizou, J. C. B. 2010, A&A, 513, A60

Lesur, G. R. J., & Latter, H. 2016, MNRAS, 462, 4549

Leung, P. K., Gammie, C. F., & Noble, S. C. 2011, ApJ, 737, 21

Levermore, C. D. 1984, J. Quant. Spec. Radiat. Transf., 31, 149

Lightman, A. P. 1974, ApJ, 194, 419

Lightman, A. P. 1974, ApJ, 194, 429

Liska, M., Hesp, C., Tchekhovskoy, A., et al. 2018, MNRAS, 474, L81

Livadiotis, G., & McComas, D. J. 2013, SSRv, 175, 183

Lo, K. Y. 2005, ARA&A, 43, 625

Longaretti, P.-Y., & Lesur, G. 2010, A&A, 516, A51

Lynden-Bell, D. 1969, Nature, 223, 690

Lynden-Bell, D., & Pringle, J. E. 1974, MNRAS, 168, 603

Macchetto, F., Marconi, A., Axon, D. J., et al. 1997, ApJ, 489, 579

Magorrian, J., Tremaine, S., Richstone, D., et al. 1998, AJ, 115, 2285

Mahadevan, R. 1997, ApJ, 477, 585

Mahadevan, R., & Quataert, E. 1997, ApJ, 490, 605

Marcus, P. S., Pei, S., Jiang, C.-H., et al. 2015, ApJ, 808, 87

Marrone, D. P., Moran, J. M., Zhao, J.-H., & Rao, R. 2006, Journal of Physics Conference Series, 54, 354

Masset, F. 2000, A&AS, 141, 165

Matsumoto, R., & Tajima, T. 1995, ApJ, 445, 767

Matteini, L., Landi, S., Hellinger, P., & Velli, M. 2006, Journal of Geophysical Research (Space Physics), 111, A10101

McClintock, J. E., & Remillard, R. A. 2006, Compact stellar X-ray sources, 39, 157

McClintock, J. E., Remillard, R. A., Rupen, M. P., et al. 2009, ApJ, 698, 1398

McClintock, J. E., Narayan, R., & Steiner, J. F. 2014, SSRv, 183, 295

McKinney, J. C., & Gammie, C. F. 2002, ApJ, 573, 728

McKinney, J. C., & Gammie, C. F. 2004, ApJ, 611, 977

McKinney, J. C., & Blandford, R. D. 2009, MNRAS, 394, L126

McKinney, J. C., Tchekhovskoy, A., & Blandford, R. D. 2012, MNRAS, 423, 3083

McKinney, J. C., Tchekhovskoy, A., Sadowski, A., & Narayan, R. 2014, MNRAS, 441, 3177

McKinney, J. C., Dai, L., & Avara, M. J. 2015, MNRAS, 454, L6

McKinney, J. C., Chluba, J., Wielgus, M., Narayan, R., & Sadowski, A. 2017, MNRAS, 467, 2241

Medeiros, L., Chan, C.-k., Özel, F., et al. 2017, ApJ, 844, 35

Meheut, H., Fromang, S., Lesur, G., Joos, M., & Longaretti, P.-Y. 2015, A&A, 579, A117

Méndez, M., & van der Klis, M. 1997, ApJ, 479, 926

Miesch, M., Matthaeus, W., Brandenburg, A., et al. 2015, SSRv, 194, 97

Mignone, A., & McKinney, J. C. 2007, MNRAS, 378, 1118

Mihalas, D., & Mihalas, B. W. 1984, New York, Oxford University Press, 1984, 731 p.

Miller, K. A., & Stone, J. M. 2000, ApJ, 534, 398

Miller, J. M. 2007, ARA&A, 45, 441

Misner, C. W., Thorne, K. S., & Wheeler, J. A. 1973, San Francisco: W.H. Freeman and Co., 1973,

Miyoshi, T., & Kusano, K. 2005, Journal of Computational Physics, 208, 315

Morris, M. R., Meyer, L., & Ghez, A. M. 2012, Research in Astronomy and Astrophysics, 12, 995

Mościbrodzka, M., Gammie, C. F., Dolence, J. C., Shiokawa, H., & Leung, P. K. 2009, ApJ, 706, 497

Mościbrodzka, M., Gammie, C. F., Dolence, J. C., & Shiokawa, H. 2011, ApJ, 735, 9

Mościbrodzka, M., Falcke, H., Shiokawa, H., & Gammie, C. F. 2014, A&A, 570, A7

Mościbrodzka, M., Falcke, H., & Shiokawa, H. 2016, A&A, 586, A38

Mościbrodzka, M., & Gammie, C. F. 2018, MNRAS, 475, 43

Narayan, R., & Yi, I. 1994, ApJL, 428, L13

Narayan, R., & Yi, I. 1995, ApJ, 444, 231

Narayan, R., Barret, D., & McClintock, J. E. 1997, ApJ, 482, 448

Narayan, R., Mahadevan, R., Grindlay, J. E., Popham, R. G., & Gammie, C. 1998, ApJ, 492, 554

Narayan, R., Igumenshchev, I. V., & Abramowicz, M. A. 2000, ApJ, 539, 798

Narayan, R., & Heyl, J. S. 2002, ApJL, 574, L139

Narayan, R., Igumenshchev, I. V., & Abramowicz, M. A. 2003, PASJ, 55, L69

Narayan, R., SÄ dowski, A., Penna, R. F., & Kulkarni, A. K. 2012, MNRAS, 426, 3241

Narayan, R., Zhu, Y., Psaltis, D., & Saḍowski, A. 2016, MNRAS, 457, 608

Nauman, F., & Blackman, E. G. 2014, MNRAS, 441, 1855

Neilsen, J., Nowak, M. A., Gammie, C., et al. 2013, ApJ, 774, 42

Nelson, R. P., Gressel, O., & Umurhan, O. M. 2013, MNRAS, 435, 2610

Niedźwiecki, A., Xie, F.-G., & Zdziarski, A. A. 2012, MNRAS, 420, 1195

Nobili, L., Turolla, R., & Zampieri, L. 1991, ApJ, 383, 250

Noble, S. C., Gammie, C. F., McKinney, J. C., & Del Zanna, L. 2006, ApJ, 641, 626

Noble, S. C., Leung, P. K., Gammie, C. F., & Book, L. G. 2007, Classical and Quantum Gravity, 24, S259

Noble, S. C., Krolik, J. H., & Hawley, J. F. 2010, ApJ, 711, 959

Noebauer, U. M., Sim, S. A., Kromer, M., Röpke, F. K., & Hillebrandt, W. 2012, MNRAS, 425, 1430

Novikov, I. D., & Thorne, K. S. 1973, Black Holes (Les Astres Occlus), 343

Ohsuga, K., Mineshige, S., Mori, M., & Kato, Y. 2009, PASJ, 61, L7

Ohsuga, K., & Mineshige, S. 2011, ApJ, 736, 2

Oishi, J. S., & Mac Low, M.-M. 2011, ApJ, 740, 18

Orosz, J. A., McClintock, J. E., Aufdenberg, J. P., et al. 2011, ApJ, 742, 84

Orszag, S. A., & Kells, L. C. 1980, Journal of Fluid Mechanics, 96, 159

Oppenheimer, J. R., & Snyder, H. 1939, Physical Review, 56, 455

Özel, F., Psaltis, D., & Narayan, R. 2000, ApJ, 541, 234

Paczyńsky, B., & Wiita, P. J. 1980, A&A, 88, 23

Padmanabhan, T. 2000, Theoretical Astrophysics - Volume 1, Astrophysical Processes, by T. Padmanabhan, pp. 622. Cambridge University Press, December 2000. ISBN-10: 0521562406. ISBN-13: 9780521562409. LCCN: QB461 .P33 2000, 622

Parkin, E. R., & Bicknell, G. V. 2013, MNRAS, 435, 2281

Penna, R. F., Kulkarni, A., & Narayan, R. 2013, A&A, 559, A116

Pessah, M. E., Chan, C.-k., & Psaltis, D. 2007, ApJL, 668, L51

Petersen, M. R., Julien, K., & Stewart, G. R. 2007, ApJ, 658, 1236

Petersen, M. R., Stewart, G. R., & Julien, K. 2007, ApJ, 658, 1252

Park, M.-G. 1990, ApJ, 354, 64

Parker, E. N. 1958, Physical Review, 109, 1874

Perlman, E. S., Adams, S. C., Cara, M., et al. 2011, ApJ, 743, 119

Peterson, B. M., Ferrarese, L., Gilbert, K. M., et al. 2004, ApJ, 613, 682

Peterson, B. M. 2014, SSRv, 183, 253

Piran, T. 1978, ApJ, 221, 652

Pozdnyakov, L. A., Sobol, I. M., & Syunyaev, R. A. 1983, Astrophysics and Space Physics Reviews, 2, 189

Prieto, M. A., Fernández-Ontiveros, J. A., Markoff, S., Espada, D., & González-Martín, O. 2016, MNRAS, 457, 3801

Pringle, J. E. 1981, ARA&A, 19, 137

Quataert, E. 1998, ApJ, 500, 978

Quataert, E., & Gruzinov, A. 1999, ApJ, 520, 248

Quataert, E., & Gruzinov, A. 2000, ApJ, 545, 842

Quataert, E., Dorland, W., & Hammett, G. W. 2002, ApJ, 577, 524

Rees, M. J. 1978, The Observatory, 98, 210

Rees, M. J. 1984, ARA&A, 22, 471

Reid, M. J., Schmitt, J. H. M. M., Owen, F. N., et al. 1982, ApJ, 263, 615

Reid, M. J., McClintock, J. E., Narayan, R., et al. 2011, ApJ, 742, 83

Remillard, R. A., & McClintock, J. E. 2006, ARA&A, 44, 49

Ressler, S. M., Tchekhovskoy, A., Quataert, E., Chandra, M., & Gammie, C. F. 2015, MNRAS, 454, 1848

Ressler, S. M., Tchekhovskoy, A., Quataert, E., & Gammie, C. F. 2017, MNRAS, 467, 3604

Reynolds, C. S. 2014, SSRv, 183, 277

Riquelme, M. A., Quataert, E., & Verscharen, D. 2015, ApJ, 800, 27

Robinson, D. C. 1975, Physical Review Letters, 34, 905

Roedig, C., Zanotti, O., & Alic, D. 2012, MNRAS, 426, 1613

Ross, J., Latter, H. N., & Guilet, J. 2016, MNRAS, 455, 526

Roth, N., & Kasen, D. 2015, ApJS, 217, 9

Rowan, M. E., Sironi, L., & Narayan, R. 2017, arXiv:1708.04627

Ryan, B. R., Dolence, J. C., & Gammie, C. F. 2015, ApJ, 807, 31

Ryan, B. R., Gammie, C. F., Fromang, S., & Kestener, P. 2017a, ApJ, 840, 6

Ryan, B. R., Ressler, S. M., Dolence, J. C., et al. 2017b, ApJL, 844, L24

Ryan, B. R., Ressler, S. M., Dolence, J. C., Gammie, C. F., & Quataert, E. 2018, in prep.

Rybicki, G. B., & Lightman, A. P. 1979, New York, Wiley-Interscience, 1979. 393 p.,

Ryu, D., & Goodman, J. 1992, ApJ, 388, 438

Sądowski, A., Narayan, R., Tchekhovskoy, A., & Zhu, Y. 2013, MNRAS, 429, 3533

Sądowski, A., Narayan, R., McKinney, J. C., & Tchekhovskoy, A. 2014, MNRAS, 439, 503

Sądowski, A., Narayan, R., Tchekhovskoy, A., et al. 2015a, MNRAS, 447, 49

Sądowski, A., & Narayan, R. 2015b, MNRAS, 453, 3213

Sądowski, A., Wielgus, M., Narayan, R., et al. 2017, MNRAS, 466, 705

Sądowski, A., & Gaspari, M. 2017, MNRAS, 468, 1398

Sagaut, P. 2006, Large Eddy Simulation for Incompressible Flows: An Introduction, Scientific Computation. ISBN 978-3-540-26344-9. Springer-Verlag Berlin Heidelberg, 2006,

Salpeter, E. E. 1964, ApJ, 140, 796

Salvesen, G., Simon, J. B., Armitage, P. J., & Begelman, M. C. 2016, MNRAS, 457, 857

Sano, T., Inutsuka, S.-i., Turner, N. J., & Stone, J. M. 2004, ApJ, 605, 321

Sargent, W. L. W., Young, P. J., Lynds, C. R., et al. 1978, ApJ, 221, 731

Schmidt, M. 1963, Nature, 197, 1040

Schnittman, J. D., & Krolik, J. H. 2013, ApJ, 777, 11

Shafee, R., McKinney, J. C., Narayan, R., et al. 2008, ApJL, 687, L25

Shakura, N. I., & Sunyaev, R. A. 1973, A&A, 24, 337

Shakura, N. I., & Sunyaev, R. A. 1976, MNRAS, 175, 613

Shapiro, S. L., Lightman, A. P., & Eardley, D. M. 1976, ApJ, 204, 187

Shapiro, S. L., & Teukolsky, S. A. 1983, Research supported by the National Science Foundation. New York, Wiley-Interscience, 1983, 663 p.,

Shcherbakov, R. V., Penna, R. F., & McKinney, J. C. 2012, ApJ, 755, 133

Shcherbakov, R. V., & McKinney, J. C. 2013, ApJL, 774, L22

Shen, J., & Gebhardt, K. 2010, ApJ, 711, 484

Shen, Y., & Ho, L. C. 2014, Nature, 513, 210

Shi, Y., Rieke, G. H., Hines, D. C., Gordon, K. D., & Egami, E. 2007, ApJ, 655, 781

Shi, J., Krolik, J. H., & Hirose, S. 2010, ApJ, 708, 1716

Shi, J.-M., Stone, J. M., & Huang, C. X. 2016, MNRAS, 456, 2273

Shibata, M., Kiuchi, K., Sekiguchi, Y., & Suwa, Y. 2011, Progress of Theoretical Physics, 125, 1255

Shiokawa, H., Dolence, J. C., Gammie, C. F., & Noble, S. C. 2012, ApJ, 744, 187

Simon, J. B., Hawley, J. F., & Beckwith, K. 2009, ApJ, 690, 974

Simon, J. B., Hawley, J. F., & Beckwith, K. 2011, ApJ, 730, 94

Simon, J. B., Beckwith, K., & Armitage, P. J. 2012, MNRAS, 422, 2685

Simon, J. B., Hughes, A. M., Flaherty, K. M., Bai, X.-N., & Armitage, P. J. 2015, ApJ, 808, 180

Sincell, M. W., & Krolik, J. H. 1994, ApJ, 430, 550

Sironi, L., & Spitkovsky, A. 2014, ApJL, 783, L21

Sironi, L., & Narayan, R. 2015, ApJ, 800, 88

Sironi, L. 2015, ApJ, 800, 89

Soltan, A. 1982, MNRAS, 200, 115

Sorathia, K. A., Reynolds, C. S., Stone, J. M., & Beckwith, K. 2012, ApJ, 749, 189

Sparks, W. B., Biretta, J. A., & Macchetto, F. 1996, ApJ, 473, 254

Stawarz, Ł., Aharonian, F., Kataoka, J., et al. 2006, MNRAS, 370, 981

Steiner, J. F., McClintock, J. E., Remillard, R. A., et al. 2010, ApJL, 718, L117

Stepney, S., & Guilbert, P. W. 1983, MNRAS, 204, 1269

Stone, J. M., Mihalas, D., & Norman, M. L. 1992, ApJS, 80, 819

Stone, J. M., Hawley, J. F., Gammie, C. F., & Balbus, S. A. 1996, ApJ, 463, 656

Stone, J. M., & Balbus, S. A. 1996, ApJ, 464, 364

Stone, J. M., Pringle, J. E., & Begelman, M. C. 1999, MNRAS, 310, 1002

Su, B., & Olson, G. L. 1996, J. Quant. Spec. Radiat. Transf., 56, 337

Suzuki, T. K., Muto, T., & Inutsuka, S.-i. 2010, ApJ, 718, 1289

Tanaka, Y., & Lewin, W. H. G. 1995, X-ray Binaries, 126

Tchekhovskoy, A., Narayan, R., & McKinney, J. C. 2011, MNRAS, 418, L79

Tchekhovskoy, A., McKinney, J. C., & Narayan, R. 2012, Journal of Physics Conference Series, 372, 012040

Thorne, K. S. 1981, MNRAS, 194, 439

Tóth, G. 2000, Journal of Computational Physics, 161, 605

Urpin, V. 2003, A&A, 404, 397

Urry, C. M., & Padovani, P. 1995, PASP, 107, 803

van den Bosch, R. C. E., & de Zeeuw, P. T. 2010, MNRAS, 401, 1770

Veilleux, S., & Osterbrock, D. E. 1987, ApJS, 63, 295

Vincent, F. H., Paumard, T., Gourgoulhon, E., & Perrin, G. 2011, Classical and Quantum Gravity, 28, 225011

Vitello, P. 1984, ApJ, 284, 394

Wagner, J., Roy, A. L., Krichbaum, T. P., et al. 2015, A&A, 581, A32

Walker, J., Lesur, G., & Boldyrev, S. 2016, MNRAS, 457, L39

Walsh, J. L., Barth, A. J., Ho, L. C., & Sarzi, M. 2013, ApJ, 770, 86

Webster, B. L., & Murdin, P. 1972, Nature, 235, 37

Wilson, A. S., & Yang, Y. 2002, ApJ, 568, 133

Wollaeger, R. T., van Rossum, D. R., Graziani, C., et al. 2013, ApJS, 209, 36

Wong, G., Ryan, B. R., & Gammie, C. F. 2018, in prep.

Wu, M.-C., Xie, F.-G., Yuan, Y.-F., & Gan, Z. 2016, MNRAS, 459, 1543

Xie, F.-G., Niedźwiecki, A., Zdziarski, A. A., & Yuan, F. 2010, MNRAS, 403, 170

Yuan, F., Quataert, E., & Narayan, R. 2003, ApJ, 598, 301

Yuan, F., Quataert, E., & Narayan, R. 2004, ApJ, 606, 894

Yuan, F., Taam, R. E., Xue, Y., & Cui, W. 2006, ApJ, 636, 46

Yuan, F., & Narayan, R. 2014, ARA&A, 52, 529

Zanotti, O., Roedig, C., Rezzolla, L., & Del Zanna, L. 2011, MNRAS, 417, 2899

Zhang, S. N., Cui, W., & Chen, W. 1997, ApJL, 482, L155